2011

Geomechanical Stability Analysis for Co2 Sequestration in Carbonate Formation

Xue J. Zhou
University of North Dakota

GEOMECHANICAL STABILITY ANALYSIS FOR CO2 SEQUESTRATION IN CARBONATE FORMATION

by

Xue Jun Zhou
Bachelor of Science, XiDian University, 1990
Master of Science, Montana Tech of the University of Montana, 2007

A Dissertation
Submitted to the Graduate Faculty
of the
University of North Dakota
In partial fulfillment of the requirements

for the degree of
Doctor of Philosophy

Grand Forks, North Dakota
May
2011

This dissertation, submitted by Xue Jun Zhou in partial fulfillment of the requirements for the Degree of Doctor of Philosophy from the University of North Dakota, has been read by the Faculty Advisory Committee under whom the work has been done and is hereby approved.

_____
Chairperson

_____

_____

_____

_____

This dissertation meets the standards for appearance, conforms to the style and format requirements of the Graduate School of the University of North Dakota, and is hereby approved.

_____
Dean of the Graduate School

_____
Date

PERMISSION

Title Geomechanical Stability Analysis for CO2 Sequestration in Carbonate Formation

Department Engineering

Degree Doctor of Philosophy

In presenting this dissertation in partial fulfillment of the requirements for a graduate degree from the University of North Dakota, I agree that the library of this University shall make it freely available for inspection. I further agree that permission for extensive copying for scholarly purposes may be granted by the professor who supervised my dissertation work or, in his absence, by the chairperson of the department or the dean of the Graduate School. It is understood that any copying or publication or other use of this dissertation or part thereof for financial gain shall not be allowed without my written permission. It is also understood that due recognition shall be given to me and to the University of North Dakota in any scholarly use which may be made of any material in my dissertation.

Signature _____

Date _____

TABLE OF CONTENTS

LIST OF FIGURES

LIST OF TABLES

ACKNOWLEDGMENTS

The financial assistance and academic support provided by the University of North Dakota (Department of Geology and Geological Engineering, School of Engineering and Mines, Graduate School, Petroleum Research, Education and Entrepreneurship Center of Excellence, Energy & Environmental Research Center, etc), government agencies (US DOE, NDIC, NDDoC, NDGS Core library), and industrial partners (Denbury Resources Inc., Hess Corp., Marathon Oil Co., St. Mary Land & Exploration Co., Whiting Petroleum Corp) are greatly acknowledged.

I would like to express my deepest appreciation to my advisor Dr. Zheng-Wen Zeng for his help and suggestions in conducting the research work for this dissertation. Thanks are also due to other members of my advisory committee: Dr. William Gosnold, Dr. Scott Korom, Dr. Yeo Howe Lim, and Dr. Isaac Schlosser. I learned structural geology and geothermics from Dr. Gosnold, hydrogeology and geochemistry from Dr. Korom, and fluid mechanics from Dr. Lim. Their thoughtful comments and their taking the time to be involved in my research are greatly appreciated.

I am extremely grateful to some previous students in this group who devoted their enthusiasm, intelligence and time in setting up the laboratory facilities. They are: Andi Jakupi, Matthew Belobraydic, Justin Kringstad, Soren Hampton, and Benjamin Huffman. Even though I did not have the chance to meet some of them, their works are greatly appreciated. This dissertation could not be the document as it is without their work.

I owe special thanks to Hong Liu, who has assisted the laboratory tests from the very beginning of my research. I thank Salowah Ahmed for her help in the laboratory work, good sense of humor and willingness to collaborate. Big thanks go out to Dr. Luke Huang for spending time to teach me and generously allowing me to use the facility at his lab for the preparation of rock samples with specific requirements. I am very grateful to Mr. Hanying Xu from the Environmental Analytical Research Lab for providing support whenever needed.

I appreciate J.A. LeFever and other staff members of the Laird Core library for being constant and reliable resources. I appreciate Darin Buri for his sense of humor and other staff members of the UND library systems helping me locate many reference materials. I appreciate the fruitful discussions with several visiting scholars, Dr. Fengfeng Zhou, Prof. Annan Jiang, Prof. Lin Fa, Dr. Chenghu Wang, Mr. Jun He and Dr. Yunyong Wang. I would like to thank some people whom I met at different points during my research: Dr. Randolph Martin, Dr. Gregory Boitnott, Peter Gale, and James Noel from New England Research Lab; Gordy Carlson and Jon Giannonatti from Continental Resources; Rich Brierley from Whiting Oil & Gas Corp; Everett Walker from Rocky MT oilfield testing center; Yanhui Han from Itasca Group, etc. I owe many thanks to many other people of UND and Grand Forks, North Dakota. I cannot list them all but their kindness will be in my mind for the years to come.

Last but certainly not least, I would like to thank my wife Hongwen and my children Doudou and Dengdeng. Their love enlightened my way and enabled me to overcome many difficulties.

ABSTRACT

Geomechanical analysis is one of the fundamental pillars to build up the confidence of geological sequestration of CO_2. Large scale CO_2 sequestration in deep carbonate formation is a complicated geological process, which will non-reversibly transform the presumed equivalent and stable status of a sedimentary basin that formed over millions of years: chemically, hydraulically, geothermally, and geomechanically. In this dissertation, thermoporoelasticity guides the theoretical establishment of a conservative baseline for the geomechanical stability analysis of CO_2 sequestration.

Extensive laboratory tests, including CO_2 flooding tests, permeability tests, uniaxial and triaxial tests, Brazilian tensile strength tests, poroelasticity tests, point load tests, and fracture toughness tests, etc, were conducted on Indiana limestone and Pierre shale to investigate the effects of CO_2 sequestration on storage rock and caprock. Numerical simulations using finite difference method of FLAC3D were also conducted to understand the mechanism of strain localization due to pore pressure fluctuation.

Based on these laboratory and numerical tests, it is concluded that two mechanisms are competing for rock failures in deep carbonate formations during CO_2 sequestration. One is the faulting induced by pore-pressure buildup, and another is the compaction failure because of rock quality deterioration due to exposure to CO_2 enriched solution.

Fracture toughness measurements on limestone and shale suggest that the fracture toughness of target formation may not be necessarily lower than that of cap rock formation; then the fractures developed in target formation may be easily extended to the cap rock formation, ruining the sealing mechanism. As such, preventing extensive fracturing, and monitoring the seismicity in target formation are essential.

Finally, the potential problems of CO_2 sequestration in the Williston Basin were investigated. The in-situ stress regime of the Williston Basin was estimated as a mixture of normal and strike-slip faulting regimes, in favor of a vertical or sub-vertical fracture development pattern, which is negative to the CO_2 sequestration. However, as the basin is not very close to an incipient failure, compaction failures are expected to be more pronounced, and naturally occurred geological phenomena, stylolites, will help to understand the CO_2 sequestration in deep carbonate formation in the long run.

CHAPTER I

INTRODUCTION

1.1 Motivations

The geological storage of carbon dioxide (CO_2) has been proposed as a method of reducing greenhouse gas emissions. However, the acceptance of this approach requires the confidence that geological sequestration is safe and environmentally sound. The large scales, long timeframes, multi-disciplinary features, etc., make the evaluation of CO_2 sequestration more difficult and delicate, in comparison with many other geological problems.

The consequence of potential leakage of CO_2 from the storage site has been demonstrated or implicated by some natural disasters or environmental problems. For example, a sudden release of about 1.6 million tonnes of CO_2 from Lake Nyos, Cameroon, on August 21, 1986 caused many fatalities of people and livestock (Kling et al., 1987). Carbon dioxide, being about 1.5 times denser than air, resulted in the CO_2-enriched cloud to "hug" the ground and descend down to lower elevations.

Large scale disturbances of originally intact rock formations by mining activities have caused a world wide environmental problem: acid rock drainage (ARD). For example, the Berkeley Pit, Butte, Montana, formed a lake. As of December 2001, the lake was 220 m deep at its center, strongly acidic with a pH of 2.63, and was extremely enriched in heavy metals (Gammons et al., 2003). Obviously, ARD is troublesome, and

its treatment is very costly (Johnson and Hallberg, 2005). As an acidic gas, the potentially slow, but large scale upward diffusion of stored CO_2 may reduce the pH of the groundwater and further environmental issues will follow, which may be comparable with ARD.

A lesson learned from ARD is that the environmental problems were not recognized, or at least paid enough attention to, at the time of mining, but rather long after the cessation of mining activities. Many mines might not have been opened if the environmental costs were ever taken into account.

So far there are a few CO_2 sequestration projects world wide, and optimistic evaluations seem to be present (Herzog, 2001; Sengul, 2006). However, these pilot sites generally have low injection rates and volumes compared to potential practical projects (Michael et al., 2010). In addition, the timeframe is short, only ten or twenty years, or at best a half century with the addition of experiences gained from the oil industry. Thus, it is needed to conduct more research to understand the coupled process of CO_2 sequestration under controlled conditions.

1.2. Scope of the Dissertation

Whether the earth is under global warming or cooling (Macdougall, 2004) is beyond the scope of this dissertation. Whether CO_2 is the culprit of global climatic change because of today's atmospheric CO_2 concentrations never attained during the past 20 million years (Prentice et al., 2001) is also beyond the scope of this dissertation. Further, whether the operation of CO_2 capture and separation is financially sound is also beyond the scope of this dissertation. Thus, all the issues related with the topics above will be excluded.

The fact is that CO_2 has already been pumped into deep rock formations either for the sake of climatic concern, or enhanced hydrocarbon recovery, or both; and this practice will continue, or more likely increase, in the foreseeable future. Thus, its impact to the underground system is the focus of this dissertation. This study seeks to increase the understanding of this practice, which is a coupled thermo-hydro-chemo-mechanical process.

To manage the complexity of this research, the study focuses on the geo-mechanical aspect, and addresses other factors with respect to their influence on the geo-mechanical part. Since further sequestration of CO_2 is planned to be conducted in the Williston Basin, this study uses the Williston Basin for the geological setting. The focus is on the estimation of the in-situ stress regime in this basin, from which potential rock failure behavior associated with CO_2 sequestration may be derived.

Most of the world's sedimentary formations that are potential candidates for CO_2 sequestration are comprised of carbonate rocks, including the Williston Basin. Actually, CO_2 flooding has been used as one of the major methods of enhanced oil recovery (EOR) for several decades in many carbonate oil reservoirs (Manrique et al., 2007). Carbonate rocks, mainly consist of $CaCO_3$, $MgCO_3$, and $CaMg(CO_3)_2$, are inclined to react with CO_2, thus, the mechanical strength change (deterioration) due to these chemical reactions is of the primary concern upon the formation stability analysis.

1.3. Dissertation Outline

Following this introductory chapter, Chapter 2 is a literature review. It first provides an overview of the geological storage, the trapping mechanisms, and the coupled thermal-hydro-chemo-mechanical approaches that have been applied to this

topic. Then, reviews on the CO_2 sequestration from three different perspectives were made: the geochemistry, the hydrogeology, and the geothermics. All these combined form a broad background for the succeeding chapters.

Based on poro-thermal-elasticity, Chapter 3 sets up the theoretical foundation for this dissertation. The correlations among rock strength, in-situ stress, pore pressure buildup, and failure behavior were developed. From the geomechanical standpoint, the major concern is the pore-pressure buildup induced rock fracture (earthquake), as sealing mechanisms might be ruined by such fracturing, leading to catastrophic consequences. Thus as a result of this chapter, the correlation between pore pressure buildup and faulting was investigated.

Chapter 4 details the laboratory work on the host formation by using Indiana limestone as a reference. Rock strengths before and after CO_2 flooding were tested. Permeability and its stress dependency were measured. Fracture toughness was also measured.

Similarly, Chapter 5 details the laboratory work on the cap rock formation by using Pierre shale. A technique to measure the permeability of low permeable rock such as shale was developed, and a non-destructive method to measure mechanical strengths of weak rock was introduced.

In parallel with laboratory works numerical analysis was launched in Chapter 6. Based on the finite difference method, a commercial software suite, FLAC3D, was used as a tool to simulate rock behavior under different scenarios. Different tests, such as uniaxial and triaxial compression tests, and the Brazilian (indirect tensile) test were simulated in comparison with the actual laboratory tests. Fluid injection induced faulting

was simulated to correlate with the inferences of Chapter 3.

Chapter 7 develops the methodology to access the geo-mechanical stability of the Williston Basin upon CO_2 sequestration. The in-situ stress and pore pressure were estimated based on extensive literature review and justification of some geological information. The major potential rock failure behavior due to CO_2 sequestration was verified by numerical simulation.

Finally, conclusions of the study are presented in Chapter 8. The last chapter also gives recommendations for future work.

CHAPTER II

LITERATURE REVIEW

2.1. Geological Sequestration of Carbon Dioxide

Carbon sequestration, broadly defined, is a term that includes the removal of CO_2 from the atmosphere by agricultural modifications and reforestation, as well as the reduction of CO_2 emissions by capture and storage (USGS, 2003). The overarching goal of carbon geological storage research is to ensure that CO_2 storage in geologic formations is safe and environmentally secure (US DOE, 2002).

2.1.1. Overview of Geological Storage Capacity and Trapping Mechanisms

Three forms of CO_2 storage have been identified: in deep geological media, through surface mineral carbonation, and in oceans (Bachu et al., 2007).

Surface mineral carbonation is to react CO_2 with calcium or magnesium silicate minerals to form solid carbonate products that are ready for disposal. Little effort is needed to verify the successful storage of carbon dioxide as CO_2 is permanently stored in an environmentally benign form (Seifritz, 1990; Lackner et al., 1995; Goff and Lackner, 1998). However, this technology is not currently considered competitive with other sequestration technologies because of high energy consumption (Krevor, 2009).

The oceans represent a huge natural reservoir for carbon dioxide disposal. CO_2 has to be injected below the thermocline, 1000 m or deeper, to ensure both the solution and hydrate to sink to the ocean floor. However, the acidic plume may have adverse

effects on mesopelagic organisms with potential negative ecosystem consequences, thus ocean storage is an immature technology at present (Golomb, 1993; IPCC, 2005).

In contrast, CO_2 storage in geological media is a technology immediately applicable as a result of the experience gained in oil and gas exploration and production, deep waste disposal. This technology is achieved through a combination of physical and chemical trapping mechanisms that are effective over different timeframes and scales (Bachu, 2001; IPCC, 2005). CO_2 global geological storage potential ranges from 1,000 to over 10,000 gigatonne (Gt) in depleted oil reservoirs, saline aquifers and unminable coal seams (Davison et al., 2001). This represents more than 26 to 260 times the amount of projected energy-related CO_2 emissions in 2030 (IEA, 2004).

Table 2.1. Estimates of storage capacities for different geological reservoirs (Davison et al., 2001)

Storage option	Global capacity	
	Gt CO_2	% of emissions to 2050
Depleted oil and gas fields	920	45
Deep saline aquifers	400- 10,000	20-500
Unminable coal seams	20	<2

The ultimate CO_2 sequestration capacity (UCSCS) in solution of an aquifer is the difference between the maximum capacity and the current carbon content in the in-situ solution, as given by Bachu and Adams (2003):

$$UCSCS = \iiint \phi\left(\rho_s \chi_s^{co_2} - \rho_0 \chi_0^{co_2}\right) dxdydz \qquad 2.1.1$$

where ϕ is porosity, ρ is the density of the formation water, χ^{co_2} is the carbon content (mass fraction), and the subscripts 0 and S stand for current carbon content and at saturation, respectively. The mass fraction of CO_2 at saturation, $\chi_s^{co_2}$, is a function of the formation water salinity, temperature and pressure.

Zhou et al. (2008) proposed a simple analytical method for the quick assessment of the CO_2 storage capacity in closed or semi-closed systems. It was important to recognize the influences of upper- and lower- seal permeability on pressure buildup in the storage formation. Their results indicated that a semi-closed system with seal permeability of 10^{-17} m^2 is essentially an open system as the rate of displaced brine leaking through the seals equals the rate of injected CO_2 at a later time of injection.

Different trapping mechanisms present in rock formations (McKee, 2005; White et al, 2005). These include (1) structural and statigraphic trapping: a fluid in gas or liquid phase is contained in a static position beneath an impermeable layer; (2) residual gas trapping: CO_2 migrating through the rock is trapped between the interstices of the grains as a result of the surface tension of the CO_2 phase; (3) dissolution trapping: CO_2 dissolves into the formation water or oil as it passes through the pores in the rock; (4) mineral trapping: CO_2 reacts with the rock and formation water and precipitates carbonate minerals in the rock; (5) hydrodynamic trapping: CO_2's lateral movement is impeded by regional and basin scale flow systems, even without structural or stratigraphic traps; (6) coal adsorption: coals have higher affinity to adsorb CO_2 than other hydrocarbon gases; (7) mined salt caverns: a technology developed and applied for underground storage of petroleum, natural gas and compressed air.

Different trapping mechanisms have different advantages and limitations. For example, mineral trapping is the most desired, but might operate on much longer time frames (100s to 100,000s of years) than other trapping mechanisms; also, it strongly depends on the mineralogy of the host formation. Coal adsorption has a substantially greater capacity; however, CO_2 storage in coals is effective as long as the pressure regime

is not lowered, otherwise, it will be released. In addition, coals that are deemed today as uneconomic may become economic for mining or in-situ gasification in the future. The associated costs for mined salt caverns storage are too high; and the environmental problems relating to rock and brine disposal are significant (Bradley et al., 1991; Crossley, 1998).

In short, sequestration of CO_2 in geological media is technically feasible on a large scale. Depending on reservoir temperature and original pressure, CO_2 can be stored either as a compressed gas, liquid or in supercritical phase (Turkenburg, 1997).

2.1.2. Characterization of the Sequestration Medium

The selection of strata and site for CO_2 sequestration in geological media depends on specific criteria to be met to satisfy the general requirements of safety, benign environmental impact and public acceptance (Bachu and Gunter, 1999). The sequestration medium requires full characterization in terms of depth, geometry, lithology and mineralogy, porosity and permeability, etc. The sealing unit requires characterization in terms of thickness, areal extent, permeability, integrity, etc (Bachu, 2000).

The criteria for site characterization include: tectonic setting, hydrodynamic regimes, geothermal regimes, hydrocarbon potential and basin maturity, and site-specific characterization, etc. In-situ conditions, such as temperature, pressure, stress, rock lithology, formation water salinity, oil density and viscosity (in the case of oil reservoirs) and coal rank and gas content (in the case of coal beds), are essential for CO_2 sequestration (Bachu and Gunter, 1999).

The data that may be required include: (1) seismic profiles across the area of interest; (2) structure contour maps of reservoirs, seals and aquifers; (3) detailed maps of

the structural boundaries of the trap; (4) predicted pathway from the point of injection; (5) documentation of faults; (6) lateral facies changes in the reservoirs and seals; (7) core and drill cuttings samples from the reservoir and seal intervals; (8) well logs; (9) fluid analyses and tests from downhole sampling and production testing; (10) oil and gas production data (if a hydrocarbon field); (11) pressure transient tests for measuring reservoir and seal permeability; (12) petrophysical measurements (porosity, permeability, mineralogy, petrography, seal capacity, etc); (13) in-situ stress analysis; (14) hydrodynamic analysis to identify the magnitude and direction of water flow; (15) seismological data; (16) geomorphologic data and (17) tectonic investigation, etc (Bachu, 2000).

One can see that site characterization for CO_2 sequestration is multidisciplinary.

2.1.3. CO_2 Sequestration: a Coupled Thermal-Hydro-Chemo-Mechanical Process

Injection of CO_2 into deep sedimentary formations will cause a series of physical and chemical reactions extending from a local scale to regional scale depending on the time scale that is considered. The ultimate fate of the injected CO_2 will be determined by the interrelationship between multiple processes (Johnson et al., 2004).

For example, as stated by Morris et al. (2009), the large volume of injection will change stress gradients within the host formation that may activate existing faults, or create new fractures and flow paths. Reactions with CO_2 may modify the pore space thus changing the permeability. Furthermore, the flow in many target reservoirs is fracture-dominated, and fractures can exaggerate the interactions among different processes. A small change in aperture may result in a big change in permeability and relatively small changes in in-situ stress may induce big changes in fracture permeability.

Celia and Nordbotten (2009) proposed a set of seven simplifications to allow for a range of reductions in complexity for the mathematical models for CO_2 sequestration. For example, during the stage when CO_2 remains in a separate and mobile phase, two-phase flow physics is the dominant process while geochemical reactions and dissolution could be ignored.

Kumar et al. (2004) presented the results of compositional reservoir simulation of a prototypical CO_2 sequestration project in a deep saline aquifer. Their emphasis was on those mechanisms that would immobilize the CO_2. It was found that both aquifer dip and permeability anisotropy have a significant effect on gas migration, which in turn affects gas dissolution and mineralization.

Rutqvist et al. (2007, 2008, 2010) conducted a series of coupled reservoir-geomechanical analysis of CO_2 sequestration under different scenarios. They found that a fully coupled numerical analysis is needed for a more accurate estimation of the maximum sustainable CO_2 injection pressure (Rutqvist et al., 2007). It is also essential to have an accurate estimate of the three-dimensional in-situ stress field to support the design of CO_2 sequestration (Rutqvist et al., 2008). The uplift of ground surface caused by CO_2 sequestration might be more obvious if the target formation has a relatively low permeability (Rutqvist et al., 2010).

Sasaki et al. (2008) investigated CO_2 injection into rock masses with the emphasis on reservoir hydrostatic pressure and temperature effects. Because the controlling factors for CO_2 density are pressure and temperature, CO_2 at different densities will have different physical and chemical properties, and further rock mechanical effects will be induced.

Jimenez-Gomez (2006) made a geomechanical assessment for the Weyburn CO_2 storage project with an emphasis on the hydro-thermal-mechanical behavior of the cap rock system. A comprehensive understanding of the geology, structure and hydrogeology of the field is essential. In the Weyburn Field, hydraulic fractures may control the volume of CO_2 that could be potentially stored.

Chiaramonte (2008) conducted CO_2 sequestration research on a fractured Pennsylvanian age eolian sandstone formation at Teapot dome, Wyoming. She found that raising pore pressure during sequestration may activate minor faults but not the reservoir-bounding fault. The potential for slip on these minor fractures could compromise the top seal capacity if they extend up into the cap rock. It is also suggested that many deep saline aquifers of the mid-continental U.S. appear to have very low porosity and permeability, which results in limited injectivity and storage capacities.

Lucier (2007) performed CO_2 storage analysis on the Ohio River Valley project. The results of the geomechanical analysis were incorporated with a geo-statistical aquifer model to test the effects of injection rate on the initiation of hydraulic fractures. It is shown that geomechanical analysis provided critical information required to evaluate sequestration potential and associated risks.

Carneiro (2009) applied dual porosity concept model into CO_2 sequestration in carbonate formations, and found that due to molecular diffusion of CO_2 into the rock matrix, dissolution trapping and hydrodynamic trapping are more effective in comparison with an equivalent single porous media. However, if the aquifer is hydrodynamic, instead of hydrostatic, the leaking potential is even higher, as fluids may move faster in the fissured media, thus reaching the discharge zones sooner.

Vidal-Gibert et al. (2009, 2010) conducted geomechanical analysis for both the Paris Basin and the Otway Basin, Australia. It was found that the in-situ stress field may evolve with respect to the pore pressure change. The critical pore pressures for fault reactivation were estimated for both basins.

Mathias et al. (2009) investigated the correlation between pore pressure buildup and fracture development. The pore pressure buildup was approximated by accounting for two-phase Forchheimer flow of supercritical CO_2 and brine in a compressible porous medium. Fracture development was assumed to occur when pore pressures exceed the minimum principal stress, which is related with the Poisson's ratio of the rock formation.

Although many researches are not directly related with CO_2 sequestration, they are still valuable by considering the application of coupled hydro-thermal-chemo-mechanical analysis concept.

The coupling between fluid and porous solid, i.e., poroelasticity, was first introduced by Biot (1941), and further developed by many people including Skempton (1954), Geertsma (1966), Detournay and Cheng (1993), Gueguen and Bouteca (2004), etc.

When external loads are applied to a rock-mass, a new state of stress would be established, resulting in opening or closing of the pores. These processes can lead to either an increase or decrease in the hydraulic conductivity of the rock-mass. Wang (2000, Page 5) defined that the subject of poroelasticity is formed by the coupling between changes in stress of porous medium and changes in fluid pressure. He observed two basic phenomena underlie poro-elastic behavior: "Solid-fluid coupling occurs when a change in applied stress produces a change in fluid pressure or fluid mass; fluid-to-solid

coupling occurs when a change in fluid pressure or fluid mass produces a change in the volume of the porous material."

Dean et al. (2006) compared three techniques for coupling multiphase flow in porous media and geomechanics. Explicitly-coupled, iteratively-coupled and fully-coupled techniques produce similar results when a tight tolerance was used for the nonlinear iterations for the iteratively-coupled technique, and when small time steps were used for the explicitly-coupled technique.

Arbitrary orientation and spatial distribution of fractures in naturally fractured reservoirs is likely to create a complex flow path that must be represented using full tensor permeability field. Bagheri (2006) used joint mechanics theory to develop general, rigorous coupling between fluid flow equation and deformation of fractured media. The geomechanics solution is decomposed into matrix and fracture parts and used to compute their dynamic porosity and permeability separately.

Nguyen (1995) treated geo-materials, such as rock, basically as porous multiphase materials. The rock matrix or solid skeleton is pervaded by discontinuities such as pores, cracks and micro-cracks. These discontinuities, simply referred to as pores, can be filled with some type(s) of fluid(s) either in a liquid or gaseous state. During thermal, hydraulic and mechanical loading, the various components respond individually and also interact with one another. It is this mutual interaction between various phases of the geo-materials that makes its behavior distinct from the behavior of single phase materials.

Nguyen (2010) conducted a study of anisotropic dual-porosity and dual-permeability poro-mechanics through generalized analytical solutions for selected problems in laboratory and field applications. Because naturally fractured rock

formations are well-known to present a dual-porosity nature, the work on this field extends the fundamental concept of poroelasticity.

Thermoporoelasticity combines the theory of heat conduction with the stress field of porous medium. The concept was developed by many works published by McTigue (1986), Zimmerman (2000), Hudson et al. (2005), Ghassemi et al. (2008), etc.

Heat is transferred by the processes of conduction and convection. The convective component is due to the bulk movement of the fluid, and is directly proportional to the fluid velocity. Heat transfer is influenced by two basic effects: buoyancy and thermal expansion. Many thermal conductivity models have been proposed for common soils, clays and engineered geological materials, but most of them are characterized by a single value of the thermal conductivity, under conditions of being fully saturated or dry (Sakashita and Kumada, 1998). The coupling of reactions to convection depends upon the reaction altering either the fluid density (through changes in temperature or solute concentration) or the properties of the porous medium (porosity and permeability) (Ennis-King and Paterson, 2007).

Zhang (2004) developed a two-dimensional transient, indirect boundary element method (BEM) to solve the coupled thermal-mechanical problems. The indirect BEM has two sub-formulations: the displacement discontinuity method and the fictitious stress method. Effects of thermal loading and pore pressure loading were compared in different geo-problems.

In general, mechanical processes directly influence heat transfer process by changing the length of the heat transport paths. Since the displacement field in the porous

medium is expected to be small compared to the original dimensions of the system, this direct influence is negligible. Thus, the mechanical-thermal coupling could be neglected.

On the other hand, the thermal-mechanical coupling is one process that has been examined quite extensively in the literature in geomechanics. Thermally induced stresses and deformation in the rock mass possibly leads to the disturbance of existing joints, or the formation of new joints (Nguyen, 1995).

The fully coupled thermo-hydro-chemo-mechanical analysis integrates the influences of all processes (Coussy, 2004). It is the most complex combination, where both experimental (laboratory and numerical) and theoretical developments are needed. Porosity and permeability evolutions due to chemical reaction and thermal-hydro process ensure the communication between fluid(s) and solid(s) phases.

Leem (1999) developed a finite element model to simulate thermo-hydro-chemo-mechanical (THCM) coupling effects in rocks. The basis for the model was the growth of cracks. The hypothesis was that if the growth of cracks in rock could be accurately simulated, then important coupling relationships would fall out of the model. In this model, cracks grow due to mechanical or thermal loading. Also, the chemistry of fluid in the cracks affects crack growth through subcritical crack growth. A primary result of crack growth involves changes in the permeability of the rock. However, Leem admitted that the complicate THCM coupling effects of rock are not completely understood yet. This model can only simulate limited aspects of the THCM coupling such as thermal-to-mechanical, mechanical-to-hydraulic, and chemical-to-mechanical coupling processes. Thus in fact, many couplings occurred in one direction only.

Yasuhara (2005) focused on the interaction between pressure solution and the fracture evolution to reveal the coupled THCM processes. Models were developed to link processes of dissolution at the stressed interfaces of grain-to-grain contacts, diffusive transport of dissolved matter from the interface to the pore space, and the precipitation at the less-stressed surface of the grains.

Taron (2009), Taron and Elsworth (2009) studied fluid flow and deformation in fractured rock, with particular emphasis on environments under thermal and chemical stress. Thermo-mechanical driven permeability enhancement was observed in front of the advancing thermal sweep, counteracted by the re-precipitation of minerals previously dissolved into the cool injection water.

Park (2001) presented a water-rock interaction model with water-film diffusion coupled with kinetic and thermodynamic reactions between minerals and pore water in basin environments. To allow comprehensive coupling, a large set of peripheral effects, such as the ionic strength correction, calculations of molar volume of reactions, effective stress and hydrostatic equations, sediment texture evolution, were implemented.

Next, the CO_2 sequestration will be reviewed from three different perspectives: the geochemistry, the hydrogeology and geothermics. Currently, due to the limited research directly related to CO_2 sequestration from these domains, other publications were also selected if the knowledge can be applied to aid the understanding of CO_2 sequestration.

2.2. CO_2 Sequestration in Carbonate Formation – a Geochemical Perspective

Sedimentary basins are compartments of the upper crust where solid and fluid materials have accumulated over millions of years. They are long-term reactors, where

different fluids are transported, formed, modified, and consumed (Gaupp et al., 2008).

During geologic sequestration, CO_2 is mainly stored in the subsurface in one of three ways: hydrodynamic trapping, solution, or mineralization (Hitchon, 1996a). Mineralization is "permanent" sequestration of CO_2 in the sense that many carbonate phases can remain stable for geologically significant timeframes (Perkins and Gunter, 1995). All these procedures involve extensive geochemical aspects, especially when the deemed formation is formed basically by carbonate rock.

2.2.1. Some Physical and Chemical Properties of CO_2

Carbon dioxide (CO_2) plays a vital role in the Earth's environment as a necessary ingredient in the life cycle of plants and animals. It behaves as a supercritical fluid above its critical temperature (31.1°C/88.0°F) and critical pressure (72.9atm/7.39MPa/74bar), expanding to flow in its container like a gas but with a density like that of a liquid (Marini, 2007).

Figure 2.1 shows an overlap of P-T phase diagram of CO_2 and a phase diagram of the CO_2-H_2O binary at low temperature and pressure, with roughly corresponding depth data for a sedimentary basin. The different phases of CO_2-H_2O binary comprise: a solid, non-stoichiometric CO_2-clathrate-hydrate with formula close to $CO_2 \cdot 7.5H_2O$ (H in the figure); a CO_2-bearing water-rich liquid, labeled L_{aq}; a CO_2-rich liquid phase (L_{co2}); a CO_2-rich vapor phase (V).

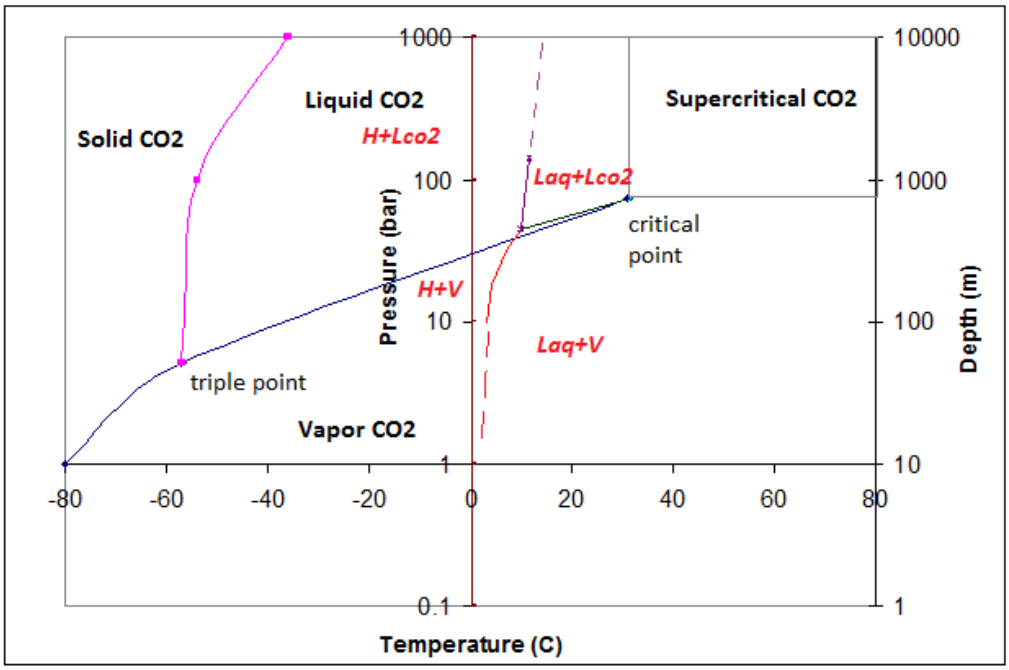

Figure 2.1. Overlap of phase diagram of CO_2 and CO_2-H_2O binary (Depth data from Oldenburg and Lewicki, 2005, P-T phase diagram of CO_2 and H_2O-CO_2 binary from Marini, 2007, dash lines are extrapolated)

The quadrupole point is at 9.77°C and 44.60 bar, at which four phases (H, L_{aq}, L_{co2}, and V) coexist. The lower critical end point of the CO_2-H_2O binary system almost coincides with the critical point of pure CO_2 (Marini, 2007).

Within a geological medium, CO_2 can be in gaseous, supercritical, or liquid conditions, depending on the depth and in-situ temperature. In continental onshore conditions, the P-T path from depth to surface passes below the critical point (Oldenburg and Unger, 2003). By such a path, CO_2 changes from supercritical to gaseous, and undergoes no large jumps in physical properties (e.g., density or viscosity) as it passes through its critical point.

Supercritical CO_2 has high density but low viscosity, which gives an added advantage of a large quantity of CO_2 contained in a reduced volume with high injection

efficiency (Shafeen et al., 2004). Heat is released or absorbed in each of the phase changes across the solid-gas, solid-liquid and liquid-gas boundaries (Freund et al., 2005).

CO_2 density increases with pressure at constant temperature (Hendricks and Blok, 1993). The density of pure CO_2 will be greatest at a given depth in a reservoir where the fluid pressure is the largest while the geothermal gradient is the least. Note that the geothermal gradient reduces CO_2 density significantly. In the absence of a geothermal gradient, CO_2 phase density exceeds water density at a depth of roughly 2750m. Thus, the CO_2 would tend to migrate downward rather than upward. With the inclusion of the geothermal gradient, CO_2 does not approach water density even at depths of 4000m (Kovscek, 2002).

A large volume of data exists on the solubility of CO_2 in water; many experimental studies have also been performed to determine the solubility of water in CO_2 (Malinin, 1959). Carbon dioxide solubility in water is best matched in a thermodynamically consistent manner when the Krichevsky-Ilinskaya equation is used (Yousef et al., 2001). Although CO_2 is soluble in water, it is not miscible with it, so that the water-driven CO_2 slug dissipates by leaving a residual phase (Metcalfe, 1982). The solubility of CO_2 is sensitive to changes in the pore water salinity, and salinity gradients are known to exist in many places.

2.2.2 Carbonate Formation Characterization

CO_2 is basic to both organic matter and carbonate, and a fundamental biological process — photosynthesis is responsible for both production of organic matter and promotion of calcification (Pomar and Hallock, 2008). Carbonate minerals crystallize

with either a trigonal or an orthorhombic crystal structure, mainly depending on the ionic radius of the cation, as shown in Table 2.2 (Appelo and Postma, 2005).

Table 2.2. Mineralogy and solubility of some carbonates (Appelo and Postma, 2005)

Trigonal	Formula	-log K	Cation radius (Å)	orthorhombic	Formula	-log K	Cation radius (Å)
Calcite	$CaCO_3$	8.48	1.12	Aragonite	$CaCO_3$	8.34	1.12
Magnesite	$MgCO_3$	8.24	0.72	Witherite	$BaCO_3$	8.56	1.42
Siderite	$FeCO_3$	10.89	0.74	Strontianite	$SrCO_3$	9.27	1.18
Dolomite	$CaMg(CO_3)_2$	17.09		Cerussite	$PbCO_3$	13.1	1.18

Limestones and dolomites tend to have much more complex pore systems than sandstones, because carbonates are usually subjected to more intricate depositional environments and post-depositional processes (Chilingar et al., 1972). Based on their porosity systems, carbonate formations can be classified into three broad types: (1) intercrystalline-intergranular, (2) fracture-matrix, and (3) vugular-solution (Langnes et al., 1972).

Based on the ratio of CaO/MgO, carbonate rocks can be classified, as shown in Table 2.3.

Table 2.3. Carbonate rocks classification (Chilingar et al., 1972)

Name	Content (%)			CaO/MgO ratio
	Dolomite	Calcite	Magnesite	
Limestone	5-0	95-100	…	>50.1
Slightly dolomitic limestone	25-5	75-95	…	9.1-50.1
Dolomitic limestone	50-25	50-75	…	4.0-9.1
Calcitic dolomite	75-50	25-50	…	2.2-4.0
Slightly calcitic dolomite	95-75	5-25	…	1.5-2.2
Dolomite	100-75	0-5	…	1.4-1.5
Very slightly magnesian dolomite	100-95	…	0-5	1.25-1.4
Slightly magnesian dolomite	95-75	…	5-25	0.80-1.25
Magnesian dolomite	75-50	…	25-50	0.44-0.80
Dolomitic magnesite	50-25	…	50-75	0.18-0.44
Slightly dolomitic magnesite	25-5	…	75-95	0.03-0.18
Magnesite	5-0	…	95-100	0.00-0.03

Based on pore size, carbonate rocks may also be classified as (1) cavernous (>2 mm), (2) very coarse (1.0-2.0 mm), (3) coarse (0.5-1.0 mm), (4) medium (0.25-0.50 mm), (5) fine (0.1-0.25 mm), (6) very fine (0.01-0.1mm), and (7) extremely fine (<0.01 mm) (Chilingar et al., 1972). Rock porosity can vary greatly (1%-37%) in a single area such as that of Mississippian carbonates (Charles) in the Williston Basin (Jodry, 1972).

Carbonate rocks are subject to changes in porosity and permeability during compaction and lithification, which may be further altered by leaching, cementation, and/or replacement. The replacement of calcite by dolomite involves an increase in porosity of about 12-13% if the reaction proceeds as follows (Chilingar and Terry, 1954):

$$2CaCO_3 + Mg^{2+} \rightarrow CaMg(CO_3)_2 + Ca^{2+} \qquad 2.2.1$$

Dolomite is less soluble than calcite as indicated that weathered limestone surfaces show deeper etching in calcite areas than in adjacent areas that have been dolomitized (Krauskopf and Bird. 1995).

2.2.3 Significance of Formation Water

Water is ubiquitous in the crust of the earth, and is in contact with most, if not all, chemical and physical reactions. Salts, hydrocarbons, and other organic matters are soluble in water. Their solubilities are influenced by the pH, the Eh, temperature and the ionic composition of formation water (Collins, 1975). Note Eh, called the oxidation-reduction potential or the redox potential, is a measure of the relative intensity of oxidizing or reducing conditions in a chemical system.

The composition of formation water can be very complicated. As an example, Table 2.4 shows water analysis results of a deep formation from a south region in the Williston Basin (Personal communication with an anonymous oil company).

Table 2.4. Analysis results of a deep formation water from a south region in the Williston Basin

Cations/Metal	Total (mg/L)	Cations/Metal	Total (mg/L)	Anions	Total (mg/L)
Boron	3.6	Aluminum	<2.7	Bromide	2.1
Calcium	330	Barium	<1.35	Chloride	830
Iron	2.6	Cadmium	<1.35	Sulfate	930
Magnesium	53	Copper	<1.35	ALK. Bicarbonate($CaCO_3$)	210
Potassium	110	Lead	<5.4	ALK. Phenolphthalein($CaCO_3$)	<10
Silica	55	Chromium	<1.35	pH	8.1
Sodium	720	Phosphorus	<2.7	Conductivity	5400μS/cm
Nickel	<1.35	Zinc	<1.35	TDS(180 °C)	3600 mg/L

Depending on the burial history, regional thermal events, water in different stratigraphic units can be very different in terms of chemical composition. The direct examination of sedimentary brines at greater depth is often limited to localities where such fluids are produced along hydrocarbons. Reliable chemical data of deep basinal formation waters are rare (Gaupp et al., 2008). On the other hand, water chemical data may also assist the identification of a specific formation (Witcher, J.C., personal communication, Dec 3, 2010, Grand Forks, ND).

The ultimate CO_2 sequestration capacity in solution of an aquifer is heavily influenced by the total amount of CO_2 that can theoretically dissolve to saturation in the formation water (Bachu and Adams, 2003). CO_2 solubility decreases with salinity. For example, at 3000 psi, 100°F, it is 68 SCF/BBL in 200,000 ppm salt water, 138 SCF/BBL in 100,000 ppm salt water, and 185 SCF/BBL in fresh water (Selley, 1976).

Table 2.5 shows the measured CO_2 solubility in a simulated pore-water from the Sleipner project, the world's first commercial-scale CO_2 storage project.

Table 2.5. Summary of CO_2 solubility experiments in synthetic Utsira porewater (after Portier and Rochelle, 2005)

Temperature (°C)	Pressure (bar)	CO_2 solubility (mol kg^{-1} H_2O) (averaged from originals)
18	100	1.312
35	100	1.020
37	80	1.006
37	90	1.020
37	100	1.051
37	120	1.132
50	80	0.920
50	100	0.956
50	120	1.095
70	80	0.681
70	90	0.690
70	100	0.719
70	110	0.862
70	120	0.852
80	100	0.779

Based on this table, the following figure can be acquired.

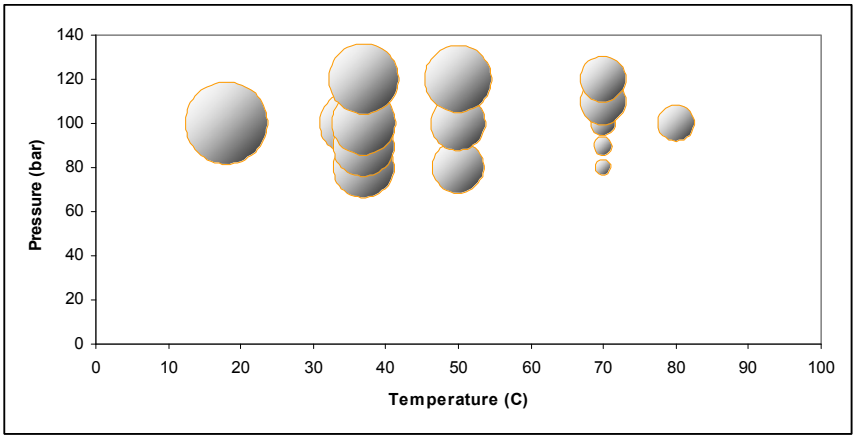

Figure 2.2. CO_2 solubility under the influence of temperature and pressure (Indicated by the bubbles, larger bubble indicates higher solubility)

The solubility of CO_2 in a saline solution can be expressed by the following equation (Portier and Rochelle, 2005):

$$m_{co_2} = \frac{\varphi_{co_2} x_{co_2} P}{\gamma_{co_2} K^H_{co_2}(T, P^{sat}_{H_2O}) \exp\left(\frac{\overline{V}^{\infty}_{co_2}}{RT}[P - P^{sat}_{H_2O}]\right)} \qquad 2.2.2$$

where T is absolute temperature (Kelvin); P is total pressure (bar); $P = P_{CO_2} + P^{sat}_{H_2O}$; x is the Mole fraction in vapour phase; R is the universal gas constant; φ is fugacity coefficient in the vapor phase; γ is the activity coefficient in the aqueous phase; K^H is Henry's constant of dissolved gas; and superscripts ∞ means infinite dilution state. The fugacity coefficient, φ, accounts for the nonlinear increase in the solubility of CO_2 with increasing P and T. Henry's Law states: the solubility of a gas in a liquid is directly proportional to the pressure of that gas above the surface of the solution.

As summarized by Zerai (2006), the aqueous solubility of CO_2 is temperature-, pressure-, and ionic strength-dependent, generally lower at elevated temperature and salinity and greater at elevated pressure. The solubility of CO_2 decreases at higher ionic strength due to a phenomenon called the "salting-out effect". The salting-out effect is that the increase in ionic strength forces the activity coefficient of CO_2 to decrease, and hence the amount of CO_2 dissolved in a solution decreases.

2.2.4. CO_2-Water-Rock Interaction

The addition of CO_2 to water initially leads to an increase of dissolved CO_2, which reacts with water to form carbonic acid. Carbonic acid dissociates to form bicarbonate ions, which can further dissociate into carbonate ions. The net effect of dissolving CO_2 in water is the removal of carbonate ions, with a lowering in pH (Fetter, 2001). This procedure can be represented by the following chemical reaction:

$$CO_2(g) + H_2O \leftrightarrow H_2CO_3 \leftrightarrow HCO_3^- + H^+ \leftrightarrow CO_3^{2-} + 2H^+ \qquad 2.2.3$$

Dissolution is rapid when formation water and CO_2 share the same pore space, but once the formation fluid is saturated with CO_2, the rate slows and is controlled by diffusion and convection rates. Dissolved carbon is distributed among three species (H_2CO_3, HCO_3^- and CO_3^{2-}) as a function of pH, pressure and temperature (Figure 2.3).

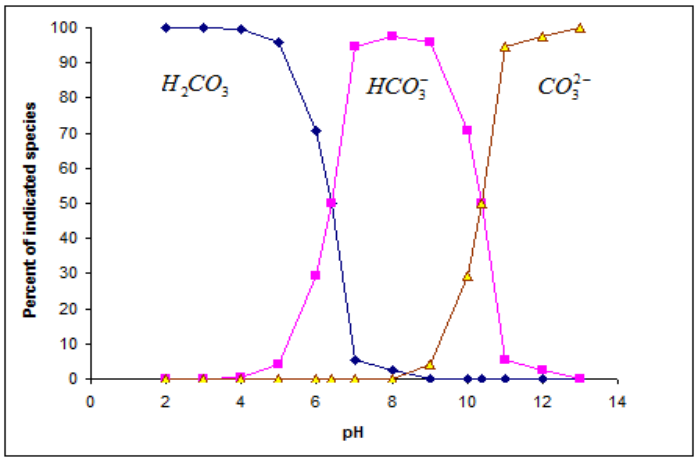

Figure 2.3. Distribution of major species of dissolved inorganic carbon at 20°C
(Data source, Table 9.5 of Fetter, 2001, p.357)

A temperature-dependent dissociation constant K for the reaction of "$H_2CO_3 \leftrightarrow H^+ + HCO_3^-$" can be defined as:

$$\log K = \frac{a_{H^+} \cdot a_{HCO_3^-}}{a_{H_2CO_3}} = \frac{\gamma_{H^+}[H^+] \cdot \gamma_{HCO_3^-}[HCO_3^-]}{\gamma_{H_2CO_3}[H_2CO_3]} \qquad 2.2.4$$

where a is activity, [ ] is concentration, and γ is an activity coefficient (Appelo and Postma, 2005).

Reaction of the dissolved CO_2 with minerals can be rapid (days) in the case of some carbonate minerals, but slow (hundreds to thousands of years) in the case of silicate minerals. Formation of carbonate minerals occurs from continued reaction of the

bicarbonate ions with calcium, magnesium and iron from silicate minerals such as clays, micas, chlorites and feldspars present in the rock matrix (Gunter et al., 1993, 1997).

The impact of pore size controlled solubility (PCS) was investigated by Emmanuel and Ague (2009). This mechanism is unlikely to affect rocks such as sandstones, but can impact carbonate and clay-bearing sediments, which typically possess high levels of submicron porosity. Thus, PCS can strongly influence the evolution of porosity in carbonate reservoirs, which has important implications for reactive transport during carbon sequestration.

The overall reactions between carbon dioxide and limestone and dolomite are:

$$CO_2 + H_2O + CaCO_3 \leftrightarrow Ca^{2+} + 2HCO_3^- \qquad 2.2.5a$$

$$2CO_2 + 2H_2O + CaMg(CO_3)_2 \leftrightarrow Ca^{2+} + Mg^{2+} + 4HCO_3^- \qquad 2.2.5b$$

These reactions are important for understanding the behavior of CO_2 trapped in carbonate formation. An increase of CO_2 results in dissolution of $CaCO_3$ and/or $CaMg(CO_3)_2$, and a decrease of CO_2 causes $CaCO_3$ and/or $CaMg(CO_3)_2$ to precipitate.

CO_2-saturated brine–limestone reactions are characterized by compositional, mineralogical, and porosity changes that are dependent on initial brine composition. The direction and magnitude of porosity changes are a function of geochemical reactions. The dissolution of calcite and dolomitization increases porosity. However, if pH is buffered by other equilibrium, such as silicate hydrolysis or reactions involving organic acids, increasing CO_2 may lead to calcite precipitation (Krauskopf and Bird, 1995).

The dissolution rates of calcite and dolomite are a function of CO_2 pressure and formation water salinity. The dissolution rates are observed to increase with increasing CO_2 pressure from 1 to 10 atm, but remain constant with further CO_2 pressure increase to

60 atm. Carbonate dissolution rates can be determined by simply taking account of the presence of CO_2 on solution pH (Gledhill and Morse, 2004; Pokrovsky et al., 2005).

Dissolution/precipitation of carbonates due to CO_2–water–rock interactions will have a significant effect on reservoir properties. Dissolution, mainly of carbonates, might increase permeability. This does not only facilitate injection but also could increase storage capacity. However, precipitation of new phases could be unfavorable for injection.

Concluding Remarks of Section 2.2

Chemical equilibrium is assumed in a formation before CO_2 sequestration. This equilibrium is disturbed by CO_2 injection. To regain a new equilibrium at a given temperature, pressure, and bulk fluid composition, the distribution of aqueous species must satisfy equilibrium relations for all possible chemical reactions in the system. The equilibrium includes electrical neutrality and mass balance.

Some chemical reactions may gradually lead to changes in porosity, and consequently, in permeability. Even if the driving forces are maintained constantly, the flow patterns evolve with the change of permeability distributions. High porosity regions attract more flow, with enhanced dissolution producing larger pores. This is a kind of geochemical self-patterning (Phillips, 2009). Overall, formations tend to be even more heterogeneous under the impact of CO_2 sequestration.

Although some mineral trapping of CO_2 has been observed, and the kinetics of these geochemical reactions seems to be rapid, only a small percentage of CO_2 is trapped in secondary carbonates. Thus, storage of CO_2 in limestone formations is more likely to be limited to ionic solubility and hydrodynamic trapping (Rosenbauer et al., 2005).

2.3. The Flooding Scenario of CO_2 – Multiphase Flow in Porous Media

Consider the scenario of CO_2 injection in a deep formation, supercritical CO_2, brine water, oil, and gas will exist simultaneously in a single formation. These fluids can be classified as incompressible, slightly compressible, or compressible, depending on how they respond to pressure and temperature.

The migration behavior of the CO_2 plume will be influenced by many factors, such as the physical structure of the target formation (heterogeneity), the chemical composition of the target formation (permeability change caused by dissolution and precipitation), the viscosities of the fluids, the densities, or more exactly the difference of densities among fluids (buoyancy effect), the flow rate of injected CO_2, hydrodynamic of in-situ fluids, heat flow regime, etc.

2.3.1. CO_2 as a Displacement Fluid

A typical large-scale CO_2 injection operation is likely to last for the lifetime of a power plant, in the order of 50~100 years (Celia and Nordbotten, 2009). While the injection proceeds, the displacement process will be CO_2 to displace the in-situ fluid (either brine or oil). After injection, the pressure perturbation will relax.

Regardless of how CO_2 is injected into the target formation, in-situ fluid displacement by CO_2 injection relies on a number of mechanisms related to the phase behavior of CO_2 and the in-situ fluid mixtures (Klins, 1984). The CO_2 plume may evolve in a relatively stabilized homogenous pattern, or grow with serious fingering, as shown in Figure 2.4. The reason of this could be very complicated, such as formation heterogeneity, viscosity and density contrast among different fluids, pressure difference between injecting well and target formation, etc.

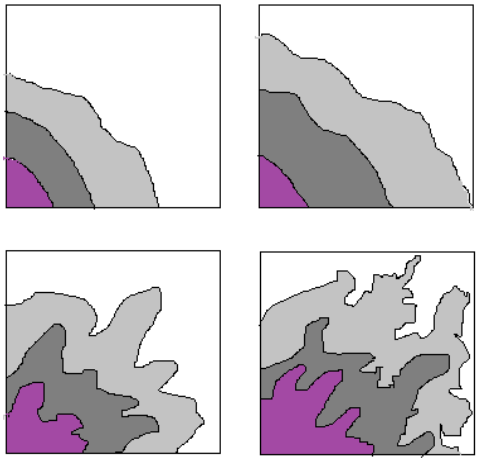

Figure 2.4. Possible areal displacement behavior of CO_2 plume (Modified after Klins, 1984)

Obviously, a homogenous pattern is more favorable because less trapped in-situ fluids in the CO_2 plumes will result in the maximization of the storage capacity. Besides, the more trapped in-situ fluids behind the CO_2 moving front, the more chemical reactions will be involved; the integrity of carbonate rock may be decreased by considering the fact that this mixture solution is likely to be more reactive with rock matrix.

Because of the density difference between CO_2 and in-situ fluid such as brine, gravity segregation effect may become more obvious with the increasing of migration path of CO_2 plume. Besides, vertical heterogeneity may also influence the flow pattern. The viscosity of CO_2 is a strong function of pressure and temperature. For a constant temperature, CO_2 viscosity increases considerably as pressure increases (Goodrich, 1980). A smaller difference of viscosity between CO_2 and in-situ fluid will favor a better displacement (Figure 2.5).

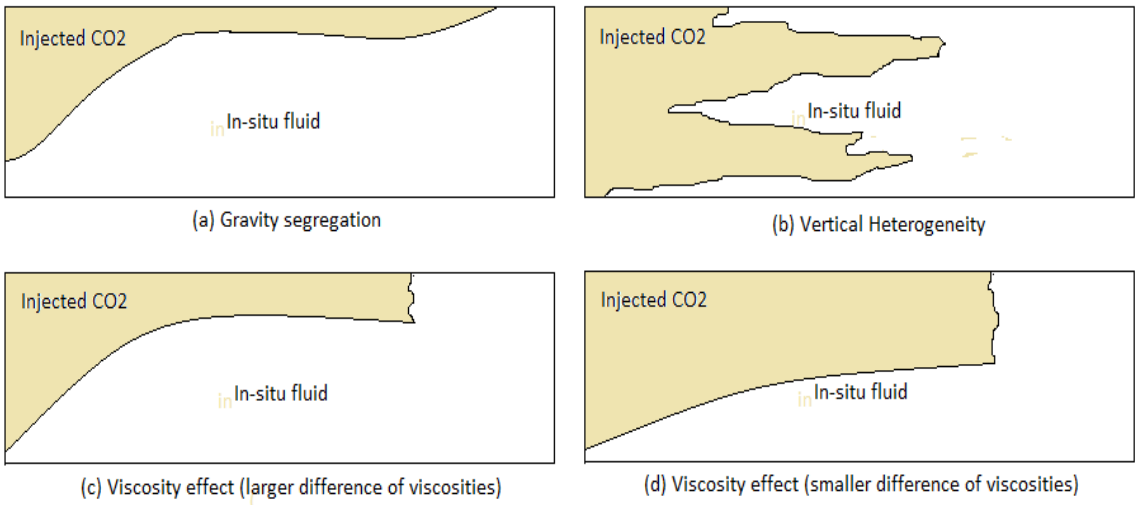

Figure 2.5. Possible vertical displacement behavior of CO_2 plume (Modified after Klins, 1984)

2.3.2. Macro Scale Mass Conservation Equation

The fact that all these phases (CO_2, water, hydrocarbon, etc) jointly fill the void space is given by the equation:

$$\sum_{i=1}^{n} S_i = 1 \qquad 2.3.1$$

where S_i is the saturation portion of each phase. Because CO_2 is injected, its mass conservation equation is:

$$\frac{\partial(\phi_{co2}\rho_{co2}S_{co2})}{\partial t} + \nabla\cdot(\rho_{co2}q_{co2}) = Q_{co2} \qquad 2.3.2$$

where, q indicates the fluid flux, and Q_{co2} is the injection rate or mass flow rate at the injection well. For other in-situ fluids, if there is no sink or source related, the mass conservation equation would be:

$$\frac{\partial(\phi_i\rho_iS_i)}{\partial t} + \nabla\cdot(\rho_iq_i) = 0 \qquad 2.3.3$$

The relationship between flow rate Q_{co2} and pressure buildup may be approximated by the Thiem equation for confined aquifer (Fetter, 2001):

$$Q_{co_2} = 2\pi(h_2 - h_1)T / \ln\left(\frac{r_2}{r_1}\right) \qquad 2.3.4$$

where T is formation transmissivity, h_1 is head at distance r_1 from the injecting well, and h_2 is head at distance r_2 from the injecting well.

The Reynolds number Re_d for CO_2 flow in rocks, is based on the average pore velocity $\bar{v}$ and an average characteristic length scale for the pores $\bar{d}$, i.e. ,

$$\mathrm{Re}_d = \frac{\rho \bar{v} \bar{d}}{\mu} \qquad 2.3.5$$

where μ is fluid viscosity. Based on this Reynolds number, four distinct flow regimes can be defined (Kaviany, 1995): Re_d >300, unsteady and chaotic flow regime; 150< Re_d <300, unsteady laminar flow regime; 1-10< Re_d <150, inertial flow regime; and Re_d <1, Darcy or creeping-flow regime.

The relationship between the average pore velocity $\bar{v}$ and the injecting rate Q_{co2} is:

$$Q_{co_2} = \frac{\Delta V}{\Delta t} = \frac{2\pi r \Delta r b \phi}{\Delta t} = 2\pi r b \phi \bar{v} \Rightarrow \bar{v} = \frac{Q_{co_2}}{2\pi r b \phi} \qquad 2.3.6$$

In the case of the constant injecting rate Q_{co_2} and formation thickness b, $\bar{v}$ will decrease with the increase of the radius r of CO_2 plume. Thus one can expect the Reynolds number will decrease from the near well region to that of far away, and the

flow regime will evolve from turbulent (chaotic) to Darcy flow at certain distance from the well.

In a three dimensional space, Darcy's law for each phase can be written in the usual form:

$$q_i = -\frac{K_i}{\mu_i}(\nabla p_i + \rho_i g \nabla l) \qquad 2.3.7$$

where q is the flow rate. This is an explicit form in terms of the gradient of pressure ∇p_i and elevation heads ($\rho_i g \nabla l$). K_i is the hydraulic conductivity and μ_i is the viscosity of phase i.

Finally, the phase pressures are related by capillary pressures (Chen, 2007). In compressible flow, the addition of another unknown, ρ, requires the introduction of some other relation. Such a relation exists in the law of the conservation of energy or the first law of thermodynamics (Schreier, 1982). For a deep formation, under high pressure, it is assumed that the flow phases, including brine water and supercritical CO_2, will have a relatively low compressibility.

2.3.3. Two Phase Flow: Bucklet-Leverett Equation

At the early stage of CO_2 sequestration, both dissolution and geochemical reactions may be ignored, as multi-phase flow, or more simply, two-phase flow (CO_2 and the major in-situ fluid) will be the dominant process (Celia and Nordbotten, 2009).

Recall Darcy's law with the consideration of relative permeability in horizontal strata (Honarpour et al., 1986),

$$q_w = -\frac{KK_{rw}A}{\mu_w}\frac{\partial p_w}{\partial l} \qquad 2.3.8a$$

$$q_{co2} = -\frac{KK_{rco2}A}{\mu_{co2}}\frac{\partial p_{co2}}{\partial l} \qquad 2.3.8b$$

where K is hydraulic conductivity and K_r is relative conductivity, A is cross section area and $\frac{\partial p}{\partial l}$ is pressure gradient with respect to flow path. If the capillary pressure can be neglected, one will have $P_w=P_{co2}$, the fraction of CO_2 flow f_{co2} will be:

$$f_{co2} = \frac{q_{co2}}{q_{co2}+q_w} = \frac{1}{1+\frac{q_w}{q_{co2}}} = \frac{1}{1+\frac{K_{rw}}{\mu_{rw}}\frac{\mu_{co2}}{K_{rco2}}} \qquad 2.3.9$$

This equation shows that at the beginning, $K_{rco2}=0$, thus $f_{co2}=0$, and finally, when K_{rw} is decreased to very low value, f_{co2} will increase, with a theoretical maximum of 1. In reality, because of the residual saturation, a strict one phase flow may never be acquired. In addition, the shape of the curve will also be influenced by the viscosity ratio between the two fluids. Typical plots of relative permeabilities and the corresponding fractional flow curve are:

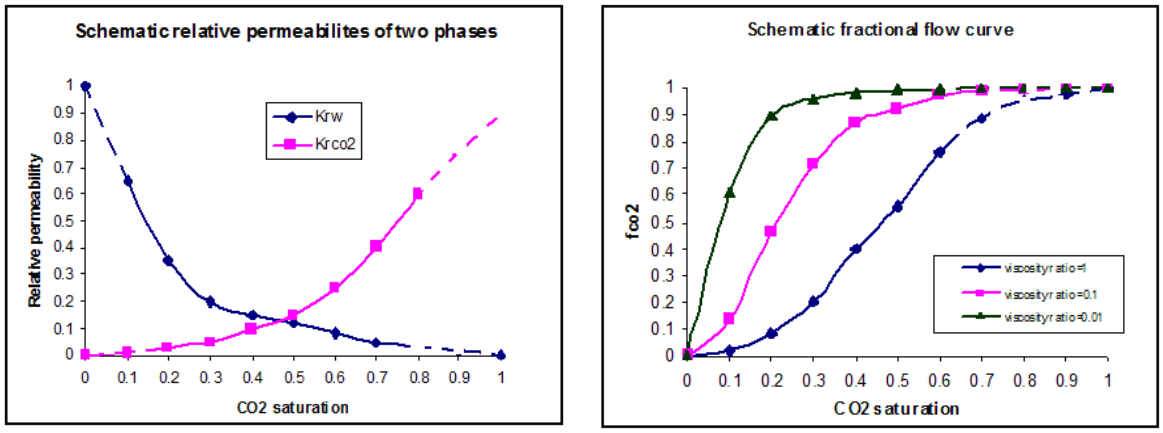

Figure 2.6. Schematic relative permeabilities and corresponding frontal flow curve

"One approach to modeling two fluid phase makes use of some simplifying assumptions that lead to what is known as the Buckley-Leverett equation. Arguably, the Buckley-Leverett approach is the best known analytical approach to investigation of this topic" (Pinder and Gray, 2008, p.155). Note the key attribute of this approach is that the problem is formulated in terms of the wetting phase; therefore, this may pose some sort of uncertainty when one tries to use it on the CO_2 displacement of brine water, in which case CO_2 may not be the wetting phase. However, it is still useful to present the derivation of this equation here as it may aid a further understanding of some fundamental concepts.

For CO_2 flow through a control volume of length Δl and cross section area of A for a time period of Δt, its mass balance equation is:

$$[(q_{co2}\rho_{co2})_l - (q_{co2}\rho_{co2})_{l+\Delta l}]\Delta t = A\Delta l\phi[(S_{co2}\rho_{co2})^{t+\Delta t} - (S_{co2}\rho_{co2})^t] \qquad 2.3.10$$

which, when $\Delta l \rightarrow 0$ and $\Delta t \rightarrow 0$, reduces to the continuity equation:

$$-\frac{\partial(q_{co2}\rho_{co2})}{\partial l} = A\phi\frac{\partial(S_{co2}\rho_{co2})}{\partial t} \qquad 2.3.11$$

If the fluid compressibility could be neglected, ρ_{co2}=constant, and $q_{co2} = f_{co2}q$, then

$$-\frac{\partial f_{co2}}{\partial l} = \frac{A\phi}{q}\frac{\partial S_{co2}}{\partial t} \qquad 2.3.12$$

Since f_{co2} is a function of only S_{co2}, by using chain rule, there is:

$$\frac{df_{co2}}{dS_{co2}}\frac{\partial S_{co2}}{\partial l} + \frac{A\phi}{q}\frac{\partial S_{co2}}{\partial t} = 0 \qquad 2.3.13$$

The equation above is the Buckley-Leverett equation. Based on some hypothesis such as the homogeneous horizontal strata and that the viscosity contrast between the

fluids is far greater than the density contrast, Nordbotten (2004) gave an analytical approximation of CO_2 plume on a finite circular domain with injection in the center of the domain as:

$$\frac{b(r,t)}{B} = \frac{1}{\lambda_{co2} - \lambda_w}\left(\sqrt{\frac{\lambda_{co2}\lambda_w A(t)}{\pi r^2}} - \lambda_w\right) \qquad 2.3.14$$

In which, b(r,t) is CO_2 depth below overburden, B is the formation thickness, λ_i of the fluid i is defined as the residual relative permeability over viscosity. A is an areal factor defined by $AB = Q_{CO_2} t / \phi$.

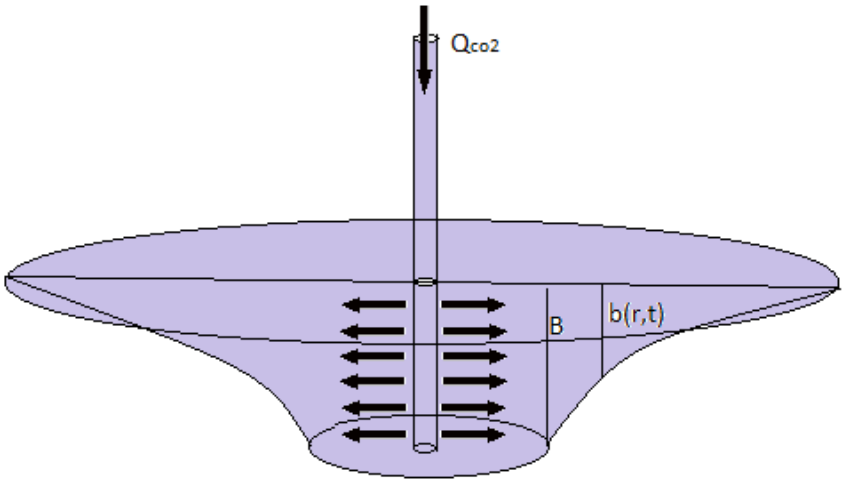

Figure 2.7. A cartoon showing the CO_2 plume in brine saturated formation (Modified after Nordbotten, 2004)

Numerical methods were also used to reveal the CO_2 flow behavior. For example, Pruess and Spycher (2007) tried to use numerical simulator to model advective and diffusive flow and transport in a multidimensional heterogeneous system containing H_2O-NaCl-CO_2 mixtures.

2.3.4. Preferential Flow Path and Gas Override Phenomenon

Because the depths of the carbonate formations under consideration are usually greater than 1000 m due to the requirement of a supercritical state of CO_2, the high overburden stress and long depositional history more likely have introduced high heterogeneity, leading to a much higher uncertainty to predict the migration behavior of the CO_2 plume.

Carbonate rocks are easily fractured, and flow in fractured aquifers depends, to a large degree, on the interconnectedness of the fracture network (Muldoon et al., 2001). Besides, the chemical reactions between rock and CO_2 may create high porosity region and these porosities may form new preferential flow paths which may evolve with time. It was found that connected hydrofacies having high hydraulic conductivity act as preferential flow paths through which particles (as surrogates for contaminants) are funneled (Anderson et al., 1999). Similar mechanism may occur when CO_2 is injected in deep formations.

Deep buried sedimentary rocks also experienced high degree of diagenetic alteration. Understanding and predicting permeability change as well as understanding the spatial distribution of pore-filling cements is a very important component in characterizing aquifer heterogeneity (Anderson, 1989). Cementation is highly variable spatially and is poorly correlated with lithofacies (Davis et al., 2006). When there is no clear positive correlation between descriptive sedimentary facies and permeability, the permeability patterns might be controlled primarily by diagenetic alterations, or cementations.

While the lithology and distribution of sedimentary units are certainly important to the description of a sedimentary formation, the connection among units of high hydraulic conductivity (channeling) has special importance in multiphase flow investigation. Monitoring the pressure draw-down behavior in a well through a specific formation may clarify if the flow is radial, in the case of a large homogeneous domain, or linear, in the case of a fractured domain with preferential flow path.

For example, during the calibration process for a formation in Denver Basin, it was found that the infinite reservoir model was unsatisfactory with the observed data; while an infinite strip model provided the best fit (Hsieh and Bredehoeft, 1981). The existence of preferential flow path due to fractures was also justified by the series earthquakes along this fracture zone during fluid injection (Healy et al., 1968). Even though it is difficult to handle this problem in a real project at least initially, it is helpful to realize the significance of preferential flow paths.

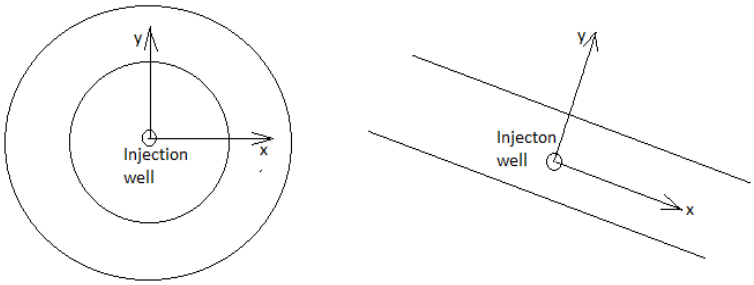

Figure 2.8. An infinite, isotropic formation model vs. a narrow, fracture zone model

For vertically averaged buildup of hydraulic head in a narrow, fracture zone model, the governing equation is (Bear, 1979):

$$T\left(\frac{\partial^2 h}{\partial x^2}+\frac{\partial^2 h}{\partial y^2}\right)=S\frac{\partial h}{\partial t}-Q(t)\delta(x)\delta(y) \qquad 2.3.15$$

where h is the vertically averaged buildup of hydraulic head above the initial head, T is the transmissivity, S is storage coefficient, and Q(t) is the variable injection rate.

For a step-varying injection rate the solution for a well located at the center of the infinite strip is (Hsieh and Bredehoeft, 1981):

$$h(x,y,t)=\frac{1}{4\pi T}\sum_{i=1}^{n}(Q_i-Q_{i-1})\sum_{m=-\infty}^{m=\infty}w\left\{\frac{\left[x^2+(y+mw)^2\right]S}{4T(t-t_{i-1})}\right\} \qquad 2.3.16$$

where w is the width of the strip.

For a semi-infinite strip reservoir, with the distance l from the injection point to the impermeable end, the analytical solution is (Hsieh and Bredehoeft, 1981):

$$h(x,y,t)=\frac{1}{4\pi T}\sum_{i=1}^{n}(Q_i-Q_{i-1})\sum_{m=-\infty}^{m=\infty}\left(\begin{array}{l} w\left\{\dfrac{\left[x^2+(y+mw)^2\right]S}{4T(t-t_{i-1})}\right\} \\ +w\left\{\dfrac{\left[(x+2l)^2+(y+mw)^2\right]S}{4T(t-t_{i-1})}\right\}\end{array}\right) \qquad 2.3.17$$

At last, because the viscosity and density contrast between CO_2 and in-situ fluids, there is a tendency for the CO_2 plume's advancing front to become tilted so that it runs over the top of the in-situ fluids. This bears some likeness to the steam override in the case of thermal recovery of oil (Butler, 1991). Obviously, whether the CO_2 plume evolves into a relatively thick ellipsoid or a thin layer extending to a much larger area under the cap rock formation will have very different implications to the storage capacity, heat transfer, and storage safety, etc.

Concluding Remarks of Section 2.3

The migration and evolution of CO_2 plume in carbonate formation can be very complicated. As a multiphase flow in porous media, a number of factors can affect the frontal stability: the viscosities of the fluids, the direction of displacement relative to

gravity, velocity, and preferential flow path caused by formation heterogeneity, gas override, etc.

Due to the density difference between CO_2 plume and in-situ fluids, the migration behavior of CO_2 plume is more likely to be a buoyancy-driven flow. Unlike those of pure Darcy-Laplace flows, buoyancy-driven flows are almost always rotational (Phillips, 2009), which makes the mathematical modeling even more difficult.

To investigate the CO_2 plume migration, a combination of sedimentological and stochastic approaches may be needed. Using time-lapse seismic data to monitor the injected CO_2 at Sleipner (Arts et al., 2004), it was found that CO_2 rising buoyantly and accumulates with high saturations which follow the structural relief. Beneath the CO_2 plume, a "velocity push-down effect" can be observed. Overall, the CO_2 plume's shape can be very complicated (Figure 2.9).

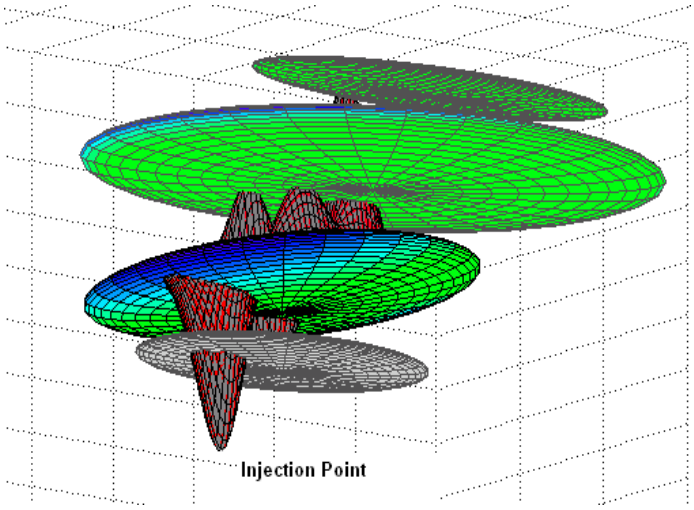

Figure 2.9. CO_2 plume based on seismic survey (Modified after Figure 5, Arts et al., 2004)

2.4. Geothermal Aspects of CO_2 Sequestration

Old sedimentary basins are usually in a state of thermal equilibrium, if there are no nearby active tectonics (Littke et al., 2008). For a sedimentary basin in a stable state,

formation fluids and formation rock matrix have a similar temperature, and this temperature generally increases with the depth. The injection of CO_2 could disturb this stable state because of the (large) temperature difference between injected CO_2 and the target formation, and the temperature difference will cause heat transfer to occur. In many cases, the scenario of CO_2 sequestration in deep formation can be treated as a relatively cold plume spreading in an (infinite) large hot zone.

For CO_2 sequestration in deep formations, the temperature of injected CO_2 (10~40°C) could be significantly lower than the target formation temperature (80~120°C). Heat transfer will occur by two major mechanisms: thermal conduction through relatively stationary materials (rock matrix), and convective transport by moving fluids (CO_2 and brine). When CO_2 plume extends over large area, its heat gain from the host formation could become large. On the other hand, the heat loss can also be an issue to the target formation as well as its overburden and underburden, especially when the target formation is thin. All these processes will be governed by the classical thermodynamic laws.

2.4.1. Temperature in Sedimentary Basin

The temperature field of sedimentary basin is one of the decisive factors governing CO_2 plume migration and CO_2-brine reaction. Temperature distribution depends basically on three processes: conduction, convection and radiation of geothermal high. Temperature is closely coupled to crustal heat flow, radiogenic heat production, convection of pore fluids, and to the depth of sedimentary rocks (Gaupp et al., 2008). Temperature is also a scalar function that characterizes the internal energy of the system (Naterer, 2003).

Geothermal temperature gradients measured could theoretically contain significant errors caused by climate change and recent glaciations, etc. However, the influence of surface temperature to the geothermal gradient will be attenuated with depth. As the surface of the earth (especially, sedimentary basin) forms a roughly horizontal, constant temperature boundary to minimize lateral temperature variation at depth, a thermal gradient may be reduced to one dimension in the vertical direction as (Beardsmore and Cull, 2001):

$$\nabla T = (\partial T / \partial z) \times k \qquad 2.4.1$$

where k is thermal conductivity and $\partial T / \partial z$ is temperature gradient over depth z. Temperature rises about 1°C for every twenty one meters downwards at the shallow depths; however, in a thick clastic sedimentary section, it will have a convex curvature due to the increase in thermal conductivity with depth caused by compaction (Gosnold and LeFever, 2009). Otherwise, the extrapolated temperature at very deep formation would be too high, significantly deviated from the actual values.

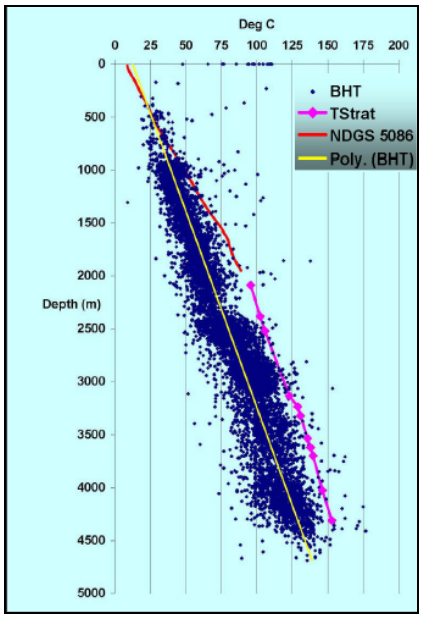

Figure 2.10. Temperature profile in the Williston Basin
(After Gosnold and LeFever, 2009; use with permission)

For CO_2 to be stored in its supercritical state there is a minimum requirement in terms of temperature: 31.1°C. In the case of Williston basin, this will be at the depth of 1000 m. However, at this depth, the rock formations are clayey rocks, which can not be taken as storage formation, then the injection point will need to be moved even further down until Permian carbonates. The depth of this formation could be up to 2300 m in the central part of this basin, while temperature at such a depth is expect to be in the range of 100°C, which would be significantly higher than the temperature of injected CO_2 from the surface of the earth.

2.4.2 Thermodynamic Laws for CO_2 Sequestration in Deep Formation

The most powerful aspects of thermodynamics is its "black box" balance approach to system analysis (Balmer, 1990). Obviously, if a system of concern only covers sedimentary formations but excludes the power plant (source of CO_2), such a scenario of CO_2 sequestration is not an isolated system in which both mass and energy

are all conserved. During the injection stage, this cannot be treated as a closed system, in which neither mass nor energy is conserved. After shutting down the injection well, for the enclosed region that is sufficiently large without fluids passing through the boundary, it becomes a closed system in case no serious leaking through cap rock occurs. Here, a closed system indicates that mass is conserved but not energy (Figure 2.11).

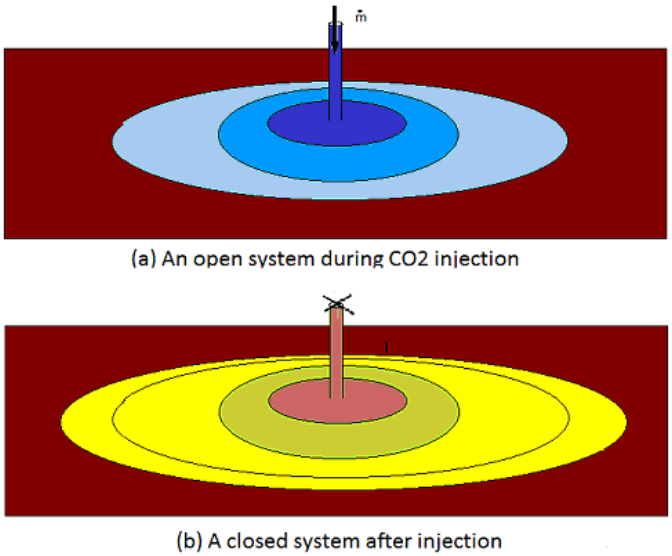

Figure 2.11. Open vs. closed system during and after CO_2 injection

The first law of thermodynamics indicates that the total energy is a conserved quantity, which requires (Bejan, 1988):

$$\underset{\substack{\text{Heat}\\\text{transfer}}}{Q_{1-2}} - \underset{\substack{\text{Work}\\\text{transfer}}}{W_{1-2}} = \underset{\substack{\text{Energy}\\\text{change}}}{E_2 - E_1} \qquad 2.4.2$$

And the most general statement of the first law of thermodynamics for an open system (Figure 2.11(a)) under CO_2 injection is:

$$\frac{dE}{dt} = \dot{Q} - \dot{W} + \sum_{in} \dot{m}(e + Pv) - \sum_{out} \dot{m}(e + Pv) \qquad 2.4.3$$

where P is the port pressure, v is volume, e is the specific energy. All these are properties of the intensive state of the fluid that crosses the boundary at time t; $\dot{m}$ is the mass flow

rate. Mass flow and energy transport occur whenever mass crosses the system boundary. The total energy includes that associated with the flow stream mass itself and the energy required to push the flow-stream mass across the system boundary (flow work).

The second law of thermodynamics states that: (1) the entropy of a system is a measure of the amount of molecular disorder within the system; (2) a system can only produce, not destroy entropy; and (3) the entropy of a system can be increased or decreased by energy transports across the system boundary (Balmer, 1990). The second law of thermodynamics assumes the following forms for open and closed systems, respectively (Bejan, 1996):

$$\underbrace{\sum_{in} \dot{m} s - \sum_{out} \dot{m} s}_{\substack{entropy \\ transfer}} + \frac{\dot{Q}}{T_0} \leq \underbrace{\frac{\partial S}{\partial t}}_{\substack{entropy \\ change}} \quad \text{: open system during injection} \qquad 2.4.4$$

$$\frac{\dot{Q}}{T} \leq \underbrace{\frac{\partial S}{\partial t}}_{\substack{entropy \\ change}} \quad \text{: closed system after injection} \qquad 2.4.5$$

In terms of the instantaneous rate of entropy generation, the above equations state:

$$\dot{S}_{gen} = \frac{\partial S}{\partial t} - \sum_{in} \dot{m} s + \sum_{out} \dot{m} s - \frac{\dot{Q}}{T} \geq 0 \quad \text{: open system during injection} \qquad 2.4.6$$

$$\dot{S}_{gen} = \frac{\partial S}{\partial t} - \frac{\dot{Q}}{T} \geq 0 \quad \text{: closed system after injection} \qquad 2.4.7$$

The issue of thermodynamic stability has its origins in the first law and the second law, or, more precisely, in the “entropy maximum” and “energy minimum” principles (Balmer, 1990). Of all the states that have the same pressure and entropy, the unconstrained equilibrium state is the one with the lowest enthalpy, which is a

thermodynamic function of a system, equivalent to the sum of the internal energy of the system plus the product of its volume multiplied by the pressure exerted on it by its surroundings (Balmer, 1990).

2.4.3 Entropy Generation in Fluid Flow and Heat Transfer

There are two main sources for internal mass flow entropy generation, one is viscous dissipation and another is diffusion of dissimilar chemical species (Balmer, 1990). When two systems with different temperatures, T_H, T_L, contact each other, there will exist a third system which is referred to as "the temperature gap" sandwiched between them. The heat transfer, Q, enters and leaves this system undiminished. By applying the second law of thermodynamics, the entropy generated in this space is (Bejan, 1996):

$$S_{gen} = \frac{Q}{T_L} - \frac{Q}{T_H} = \frac{Q(T_H - T_L)}{T_H T_L} \qquad 2.4.8$$

The entropy generation is positive as long as there is a temperature difference. The generated entropy will increase with the temperature difference if the heat transfer Q is a constant. Mechanical power must be supplied to pump CO_2 into the deep formation. The entropy generation rate and the loss of mechanical power are ultimately attributable to the viscous shearing effect present in the fluid (Bejan, 1996).

For a laminar flow such as the plane Hagen-Poiseuille flow, with the velocity profile described in Figure 2.12, the definitions of v, D, y are indicated in the figure.

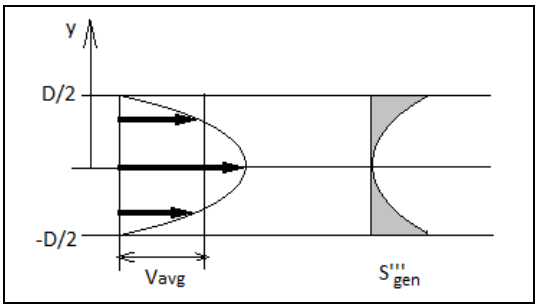

Figure 2.12. Velocity and entropy generation profiles in laminar flow (Modified after Bejan, 1996)

Its velocity equation is:

$$v = \frac{3}{2} v_{avg} \left[1 - \left(\frac{y}{D/2} \right)^2 \right] \qquad 2.4.9$$

Its entropy generation rate, per unit time and volume, is (Bejan, 1996):

$$S'''_{gen} = \frac{\mu}{T} \left(\frac{\partial v}{\partial y} \right)^2 = 36 \frac{\mu}{T} \left(\frac{v_{avg}}{D} \right)^2 \left(\frac{y}{D/2} \right)^2 \qquad 2.4.10$$

Thus in laminar flows, the generation of entropy takes place throughout the flow field, or the entire field participates in the production of entropy. However, in the turbulent regime, the generation of entropy is concentrated only in thin layers adjacent to the boundaries. Thus, laminar flow is a very energy efficient type of flow; turbulent flow is much more dissipative and consequently is a much less energy efficient flow (Balmer, 1990).

A general equation for heat transfer rate Q between two surfaces with temperatures T_1 and T_2 is:

$$Q = \bar{h} A (T_1 - T_2) \qquad 2.4.11$$

where $\bar{h}$ is heat transfer coefficient.

The local rate of entropy generation in convective heat transfer will be:

$$S'''_{gen} = \frac{1}{T}\nabla \cdot \vec{q} - \frac{1}{T^2}\vec{q} \cdot \nabla T + \rho \frac{Ds}{Dt} \qquad 2.4.12$$

In which the first term accounts for the entropy transfer associated with heat transfer, the second term represents the entropy convected into and out of the system, and the last term represents the time rate of entropy accumulation in the control volume (Bejan, 1996).

Because in general, a thermodynamic process is accompanied by entropy generation, it is considered irreversible if $S_{gen} > 0$, and it makes sense to describe Path A as being "more irreversible" than Path B whenever $(S_{gen})_A > (S_{gen})_B$. For example, a process involving larger quantities of CO_2 will be more "irreversible" than another one involving less CO_2 and at a injection temperature closer to that of formation.

2.4.4. Heat Transfer between CO_2 Plume and Target Formation by Conduction

Heat transfer can be broken into three modes: (1) conduction; (2) convection, and (3) radiation. Conduction and radiation are pure heat transports of energy, but convection is really a mass flow energy transport mode (Balmer, 1990).

The basic equation of conduction heat transfer is Fourier's law. For one-dimensional flow of heat by conduction, the heat flow is given by the following equation.

$$Q = -KA\frac{\partial T}{\partial x} \qquad 2.4.13$$

where Q is the heat flow, A is the cross-sectional area for flow, T is the temperature, x is the distance, and K is thermal conductivity. Table 2.6 shows K values for some materials.

Table 2.6. Thermal conductivity of some materials

Material	Thermal conductivity at Room temperature (W/m°C)	Source
Quartz	7.69	Butler, 1991; Beardsmore and Cull, 2001
Calcite	3.57; 3.59	Butler, 1991; Beardsmore and Cull, 2001
Dolomite	5.50; 5.51	Butler, 1991; Beardsmore and Cull, 2001
Limestone	1.7 (dry); 3.5 (wet)	Butler, 1991
	1.9; 2.21~3.1	Naterer, 2003; Beardsmore and Cull, 2001
Shale	1.0 (dry); 1.7 (wet)	Butler, 1991
Water	0.60 (liquid)	Butler, 1991
Nitrogen	0.024 (Gas, 1 atm)	Butler, 1991
CO_2	0.017 (27°C); 0.020 (77°C)	Naterer, 2003

From the above table, one can see that overall, solid materials (rocks) have much higher conductivity than that of fluids (CO_2 or water), and wet solids (limestone, shale) have higher conductivity than that of dry ones.

Fourier's equation for heat conduction in three dimension coordinate system is:

$$\left(\frac{\partial^2 T}{\partial x^2}\right)+\left(\frac{\partial^2 T}{\partial y^2}\right)+\left(\frac{\partial^2 T}{\partial z^2}\right)=\frac{1}{\alpha}\left(\frac{\partial T}{\partial t}\right) \qquad 2.4.14$$

where α is the thermal diffusivity with dimension of L^2T^{-1}.

Now consider a condition at which CO_2 is in contact with a rock particle, there is a temperature difference between these two entities, as shown in Figure 2.13. Assuming the temperature on the interface is constant when a constant flow persists.

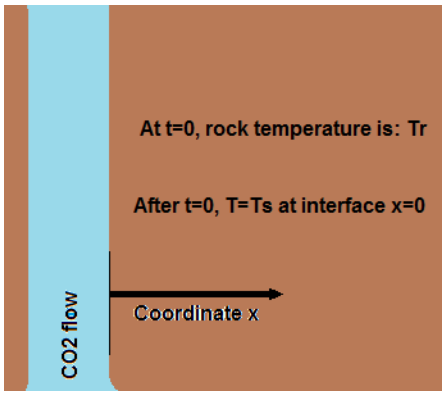

Figure 2.13 One dimensional conductive heat transfers between CO_2 and solid rock

The governing equation for this problem is Fourier's equation in one dimension, and the initial and boundary conditions are:

$$T(x,o) = T_r \qquad \text{2.4.15a}$$

$$T(\infty,t) = T_r \qquad \text{2.4.15b}$$

$$T(0,t) = T_s \qquad \text{2.4.15c}$$

By using Laplace transform, the solution is given by (Butler, 1991; Appendix A):

$$T(x,t) = T_r + (T_s - T_r) \cdot erfc\left(\frac{x}{2\sqrt{\alpha t}}\right) \qquad \text{2.4.16}$$

The heat flux from the rock solid to CO_2 plume is:

$$\frac{Q}{A} = -K\left(\frac{\partial T}{\partial x}\right)_{x=0} = \frac{K(T_r - T_s)}{\sqrt{\pi \alpha t}} \qquad \text{2.4.17}$$

This result also shows that the heat flux decreases with time as heat conducts further into the solid.

Next, imagine an isolated rock block of volume V and porosity ϕ, filled with CO_2 (Figure 2.14), the initial temperatures of rock and CO_2 are Tr and Tc, respectively.

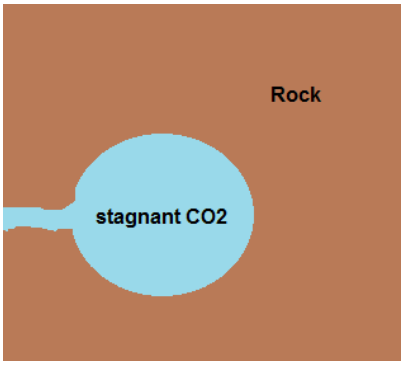

Figure 2.14. Stagnant CO_2 in rock

Due to the fact that the heat given by rock must be absorbed by CO_2 based on energy conservation, the final temperature Ts could be estimated by the following equation:

$$\dot{Q}_{rock} = \dot{Q}_{co2} \quad \Rightarrow \quad \rho_{rock} C_{rock} V(1-\phi)(Tr - Ts) = \rho_{CO2} C_{CO2} V\phi(Tc - Ts) \qquad 2.4.18$$

Using ρ_{rock} = 2680 kg/m^3, C_{rock} = 0.908 kJ/kgK, ϕ = 0.1, Tr = 110 °C, Tc = 32 °C, ρ_{co2} = 470 kg/m^3, and C_{co2} = 0.898 kJ/kgK, then Ts = 107 °C.

As a conclusion, in case CO_2 constantly flows through a rock surface, the adjacent rock temperature could drop significantly to that close to the temperature of CO_2; however, if the flow is stopped, in a stagnant situation, the final mixture temperature would be more likely close to that of rock because of its high density and quantity.

2.4.5. Heat Transfer between CO_2 Plume and Target Formation by Convection

As the CO_2 plume passes through the formation, it will absorb heat from the hotter surroundings. Thus, heat will be transferred from the formation by fluid convection. Convection heat transfer refers to the combination of molecular diffusion and bulk fluid motion (Naterer, 2003).

The basic equation of convection heat transfer is Newton's law of cooling, based on which the heat transfer rate can be computed by:

$$q = hA(T_s - T_\infty) \qquad 2.4.19$$

where, h is convection coefficient, W/m^{2}K, A is cross section area.

Consider the scenario of Figure 2.13 under the convection condition, the initial and boundary conditions are given by:

$$T(x,0) = T_i \qquad \text{2.4.20a}$$

$$T(\infty,t) = T_i \qquad \text{2.4.20b}$$

$$-K\left.\frac{\partial T}{\partial x}\right|_0 = h[T_\infty - T(0,t)] \qquad \text{2.4.20c}$$

Then the analytic solution is given by (Appendix A):

$$T(x,t) = T_i + (T_\infty - T_i)\cdot\left\{1 - erf\left(\frac{x}{2\sqrt{\alpha t}}\right) - \left[\exp\left(\frac{hx}{K} + \frac{h^2\alpha t}{K^2}\right)\right]\times\left[1 - erf\left(\frac{x}{2\sqrt{\alpha t}} + \frac{h\sqrt{\alpha t}}{K}\right)\right]\right\} \qquad \text{2.4.21}$$

In the early stage of injection, convection might be a major mechanism for the disturbance of thermal stability caused by relatively rapid CO_2 flows.

Besides the heat transfer between CO_2 and rock matrix, heat will also be transferred between CO_2 and in-situ fluids. In the case of saline aquifer, CO_2 will form a CO_2 cap above brine due to buoyancy driven by the density difference. The brine contacted with CO_2 will get cold thus descending and the lower part of "hot" brine will ascend, together with the diffusion of CO_2 into underlying brine that increases its density, a convective flow field may be formed (Hassanzadeh et al., 2005). This mechanism will accelerate the heat transfer process and the dissolution rate of CO_2.

At last, the scenario of CO_2 plume expanding in the target formation can be simplified as a sharp temperature front if neglecting thermal conduction. I.e., inside the front, the temperature is that of the injected CO_2, while outside it is he original formation temperature. The position of the front for a radial symmetric injection pattern can be estimated by energy balance using the following methodology given by Fjaer et al. (2008).

$$\frac{R_{cool}}{R_{CO2}} = \sqrt{\frac{\phi_{co2}\rho_{co2}C_{co2}}{(1-\phi_{co2}-\phi_{Brine})\rho_{rock}C_{rock}+\phi_{Brine}\rho_{Brine}C_{Brine}+\phi_{co2}\rho_{co2}C_{co2}}} \qquad 2.4.22$$

where R_{cool} is the radius of the cooled zone, and R_{co2} is the radius of the CO_2 flooded zone, ρ represents density and C represents specific heat capacity. Roughly, one can get an idea that the thermal front will lag behind the fluid migration front, and this tardiness will significantly be influenced by the porosity and specific heat capacities of different materials.

2.4.6. Chemical Thermodynamics and Special Concerns at Critical-Point Region

Hess' law states that the total amount of heat liberated or absorbed during a chemical reaction is independent of the thermodynamic path followed by the reaction. Exothermic reaction is a reaction that gives off heat, and endothermic reaction is a reaction that absorbs heat (Balmer, 1990). In general, the effect of temperature on equilibrium can be qualitatively predicted by a simple rule that endothermic reactions are favored by a rise in temperature, exothermic reactions by a fall in temperature.

The dissolution of carbonate by adding CO_2 to water is an endothermic reaction (Krauskopf and Bird, 1995). Thus, the higher the temperature of the injected CO_2, the higher dissolution of carbonate will be resulted in.

$$CaCO_3 + H_2O + CO_2 \rightarrow C_a^{2+} + 2HCO_3^- \qquad 2.4.23$$
$$\Delta G^o = +33.1 kJ/mol \quad (Gibbs \quad energy)$$
$$\Delta H^0 = -40.6 kJ/mol \quad (Enthalpy)$$

However, the above reaction is not spontaneous as its Gibbs free energy is greater than zero. Koschel et al. (2006) conducted a series of experiments to measure the enthalpy of CO_2 in water and NaCl solutions at conditions of interest for geological

sequestration, and found that the enthalpy of mixing increases linearly with the gas molar fraction in the region of total gas dissolution.

A geothermal gradient of 30°C /km in a sedimentary basin will cause reaction rates to increase 10-fold for every km of burial. Clay minerals are possible catalysts for some chemical reactions (Beardsmore and Cull, 2001). On the other hand, clay minerals can also be the by-products of carbonation reactions, such as (Marini, 2007):

$$\underset{anorthite}{CaAl_2Si_2O_8} + 2H_2O + CO_{2(g)} \Rightarrow \underset{calcite}{CaCO_3} + \underset{kaolinite}{Al_2Si_2O_5(OH)_4} \qquad 2.4.24$$

When CO_2 passes through its critical point due to upward migration or other mechanisms, special problems may occur. In thermodynamics, the critical point distinguishes itself as the terminus of the vapor-pressure curve, as a transition point in the system's number of degrees of freedom, or as a means of standardizing van der Waals' equation of state. The compressibility of fluids is very large near the critical point, as indicated by the isotherm slopes, thus the density fluctuation become exceedingly large in the critical-point region. The fluid behavior near the critical point becomes increasingly unrelated to the nature of the substance (Bejan, 1988).

It was also observed that there exists an unambiguous enhancement of thermal conductivity near the critical point (Guildner, 1958). However, despite the enhancement of the thermal conductivity, the thermal diffusivity decreases when approaching the critical point. At or near critical points, the mixing directions may change due to properties change (Chen, 2007).

Concluding Remarks of Section 2.4

The injection of CO_2 to deep formation is an entropy increasing process to the underground system, and is irreversible. The higher the temperature difference between

injected CO_2 and the formation, the higher the entropy generation, indicating the higher level of the chaos.

The heat transfer between CO_2 and formation will be conducted by conduction and convection. The rock close to the active flow path will have a much more obvious temperature drop than those in stagnant zone. Brine contacted with CO_2 will also have a decrease of temperature, together with its density increase due to CO_2 diffusion; a convective flow regime may be initiated to accelerate the heat transfer process. The abnormal behavior of CO_2 at its critical point region is also a concern when estimating the risk of sequestration.

The temperature change of formation rock will induce thermal stress, which will be an issue of rock integrity (Goodarzi et al., 2010). The influence of thermal induced stress due to CO_2 sequestration will be incorporated into the next chapter.

CHAPTER III

GEOMECHANICAL ANALYSIS OF CO2 SEQUESTRATION: THEORETICAL BACKGROUND

> *"Some may regard the model as less 'real' than the prototype. However from the logical point of view the prototype is in fact a realization in which the valid sentences of the mathematical model are to some degree satisfied. One could say that the prototype is a model of equations and the two enjoy the happy reciprocality of Menander and life. " (Aris,1978).*

From the previous sections, one can see that with the injection of CO_2, the stability of the underground system could all be disturbed in terms of its chemical, thermal and hydraulic regimes. However, if the rock matrix's stability could be ensured, then all those problems may not pose a serious safety concern. In this chapter, rock mechanics related with CO_2 geological sequestration will be studied.

The concept of representative elementary volume (REV) was implicitly used by Darcy and Terzaghi (Terzaghi and Peck, 1967); it was later formalized and precisely defined by Bear (1972). In hydrogeology, the REV is the smallest volume over which a measurement can be made that will yield a value representative of the whole. Smaller than the REV, the parameter is not representatively defined, and the material can not be treated as a continuum. The concept of a REV is implicitly adopted in the remainder of this dissertation. Thus when a certain property at a point is stated, this property is the volumetric average of the REV surrounding that point.

The models presented here are mostly linear; and the linear theories for poro-thermo-elasticity generally presume constant material properties. So the applications of these models are limited to relatively small changes of strain and temperature. Though simplified; analytical solutions to simple boundary value problems do allow one to explore easily and quickly the effects of various properties (McTigue, 1986). Besides, analytical results allow one to investigate phenomena that are consequences of boundary conditions and those as consequences of the material responses.

It is also important to distinguish the increment of an entity and the entity itself, thus the symbol "Δ" is used to make this distinction whenever needed.

3.1.Elasticity of General Geo-Materials

Even the stress-strain behavior of rock is quite complex, most rocks will behave approximately like a linear elastic material if the stresses they are subjected to are considerably lower than their ultimate strengths. Thus, the linear elasticity theory is the first step to capture rock behaviors.

The basic elastic constants include Young's modulus (E), Poisson's ratio (ν), shear modulus (G), bulk modulus (K), and Lame constant (λ), etc. According to the generalized Hooke's law, the complete set of relations between strain and stress components can be described as a double dot product between the stress and strain tensors, i.e., $\sigma = C \bullet\bullet \varepsilon$, where σ is the stress tensor, C is the tensor of elastic constants and ε is the strain tensor (Lebedev and Cloud, 2003). The matrix form is (Hudson and Harrison, 1997):

$$\begin{bmatrix} \varepsilon_{xx} \\ \varepsilon_{yy} \\ \varepsilon_{zz} \\ \varepsilon_{xy} \\ \varepsilon_{yz} \\ \varepsilon_{zx} \end{bmatrix} = \begin{bmatrix} S_{11} & S_{12} & S_{13} & S_{14} & S_{15} & S_{16} \\ S_{21} & S_{22} & S_{23} & S_{24} & S_{25} & S_{26} \\ S_{31} & S_{32} & S_{33} & S_{34} & S_{35} & S_{36} \\ S_{41} & S_{42} & S_{43} & S_{44} & S_{45} & S_{46} \\ S_{51} & S_{52} & S_{53} & S_{54} & S_{55} & S_{56} \\ S_{61} & S_{62} & S_{63} & S_{64} & S_{65} & S_{66} \end{bmatrix} \begin{bmatrix} \sigma_{xx} \\ \sigma_{yy} \\ \sigma_{zz} \\ \tau_{xy} \\ \tau_{yz} \\ \tau_{zx} \end{bmatrix} \quad 3.1$$

The [S] matrix shown above is known as the compliance matrix, which is a 6x6 matrix containing 36 elements. However, through considerations of conservation of energy, the matrix can be shown to be symmetrical, thus 21 independent elastic constants are needed to completely characterize a rock material at its elastic domain.

A material with 21 independent elastic constants is said to possess the most general form of elastic anisotropy (Crouch and Starfield, 1983). Two simplest forms of anisotropy are orthotropy and transverse isotropy, which can be imagined as a lattice of three mutually perpendicular cuboids with different sizes and all aligned along the principal axes. Isotropy can be viewed as a specific case of transversely isotropy.

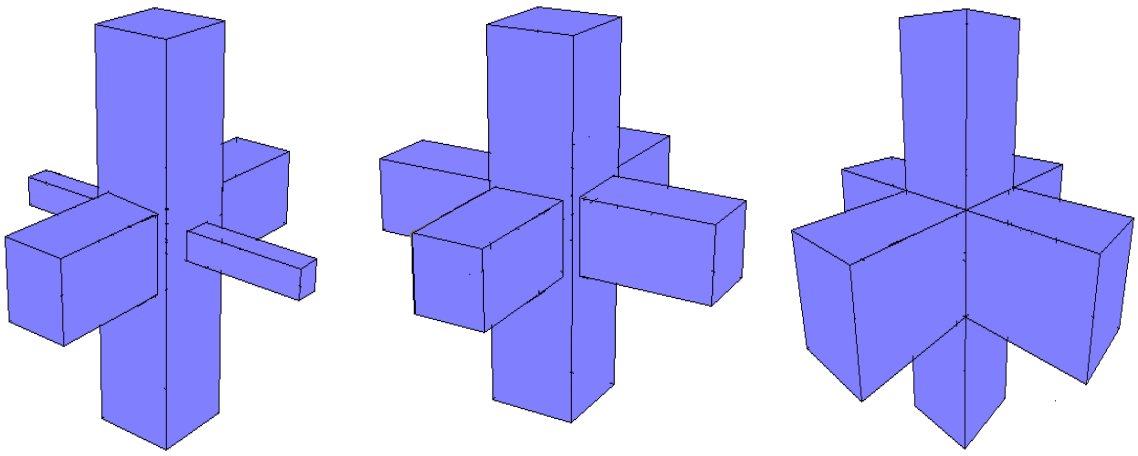

Figure 3.1. Orthotropic body (left), Transversely isotropic body (middle), and Isotropic body (right)

For orthotropic material, the compliance matrix can be represented with nine independent elastic constants as follows (Boresi and Schmidt, 2003):

$$\begin{bmatrix} \varepsilon_{xx} \\ \varepsilon_{yy} \\ \varepsilon_{zz} \\ \varepsilon_{xy} \\ \varepsilon_{yz} \\ \varepsilon_{zx} \end{bmatrix} = \begin{bmatrix} \frac{1}{E_x} & -\frac{\nu_{yx}}{E_y} & -\frac{\nu_{zx}}{E_z} & 0 & 0 & 0 \\ -\frac{\nu_{xy}}{E_x} & \frac{1}{E_y} & -\frac{\nu_{zy}}{E_z} & 0 & 0 & 0 \\ -\frac{\nu_{xz}}{E_x} & -\frac{\nu_{yz}}{E_y} & \frac{1}{E_z} & 0 & 0 & 0 \\ 0 & 0 & 0 & \frac{1}{G_{xy}} & 0 & 0 \\ 0 & 0 & 0 & 0 & \frac{1}{G_{yz}} & 0 \\ 0 & 0 & 0 & 0 & 0 & \frac{1}{G_{zx}} \end{bmatrix} \begin{bmatrix} \sigma_{xx} \\ \sigma_{yy} \\ \sigma_{zz} \\ \tau_{xy} \\ \tau_{yz} \\ \tau_{zx} \end{bmatrix} \quad 3.2$$

where E_x, E_y, E_z denote the orthotropic Young's moduli and G_{xy}, G_{yz}, G_{zx} denote the orthotropic shear moduli for shear deformation in the x-y, y-z, and z-x planes, respectively. The term ν_{xy} is a Poisson ratio that characterizes the strain in the y direction produced by the stress in the x direction, with similar interpretations for the rest.

The compliance matrix of a transversely isotropic material can be simplified to five elastic constants, instead of the nine constants needed for an orthotropic material. These constants include two Young's moduli, two Poisson's ratios and one shear modulus.

For isotropic materials, a further reduction of complexity can be made and the following equation holds (Davis and Selvadurai, 1996):

$$\begin{bmatrix} \varepsilon_{xx} \\ \varepsilon_{yy} \\ \varepsilon_{zz} \\ \varepsilon_{xy} \\ \varepsilon_{yz} \\ \varepsilon_{zx} \end{bmatrix} = \begin{bmatrix} \frac{1}{E} & -\frac{\nu}{E} & -\frac{\nu}{E} & 0 & 0 & 0 \\ -\frac{\nu}{E} & \frac{1}{E} & -\frac{\nu}{E} & 0 & 0 & 0 \\ -\frac{\nu}{E} & -\frac{\nu}{E} & \frac{1}{E} & 0 & 0 & 0 \\ 0 & 0 & 0 & \frac{1}{G} & 0 & 0 \\ 0 & 0 & 0 & 0 & \frac{1}{G} & 0 \\ 0 & 0 & 0 & 0 & 0 & \frac{1}{G} \end{bmatrix} \begin{bmatrix} \sigma_{xx} \\ \sigma_{yy} \\ \sigma_{zz} \\ \tau_{xy} \\ \tau_{yz} \\ \tau_{zx} \end{bmatrix} \quad 3.3$$

Because $G = \frac{E}{2(1+\nu)}$, one can see that only two independent elastic constants are needed for an isotropic material: Young's modulus E and Poisson's ratio ν. Besides, other elasticity parameters can also be derived from E, ν : $K = \frac{E}{3(1-2\nu)}$ and $\lambda = \frac{\nu E}{(1+\nu)(1-2\nu)}$. Note isotropic materials are materials whose response is independent of the orientation of the applied stress.

In many rock mechanics tests, the tested specimen is assumed to be isotropic. This may not be the case for some rocks. For sedimentary rocks, due to the depositional feature, an orthotropic model may be much more reasonable. However, because of the difficulty of sample acquisition / preparation and testing, an isotropic model is actually widely used. Therefore, it is vital to realize that the relationships among these elastic constants only apply for isotropic conditions. Errors (sometimes very serious ones) can be introduced upon a simple isotropic assumption. A statistical approach is used to overcome this problem by testing multiple specimens from representative locations for the same parameter or property.

3.2.Principal Stress, Principal Strain and In-situ Stress

For any general state of stress at any point in a solid body, there exist three planes at that point on which the shear stresses become zero. The remaining normal stress components on these three planes are called principal stresses (Boresi and Schmidt, 2003). The principal stresses can be found by solving σ for the following equation:

$$\begin{vmatrix} \sigma_{xx} & \tau_{xy} & \tau_{xz} \\ \tau_{xy} & \sigma_{yy} & \tau_{yz} \\ \tau_{xz} & \tau_{yz} & \sigma_{zz} \end{vmatrix} - \sigma I = A - \sigma I = 0 \qquad 3.4$$

After finding the matrix T whose columns are eigenvectors of A, the matrix $T^{-1}AT$ assumes the canonical form, in which eigenvalues represent the principal stresses in three dimensions, as shown in the following equation:

$$T^{-1}AT = T^{-1}\begin{vmatrix} \sigma_{xx} & \tau_{xy} & \tau_{xz} \\ \tau_{xy} & \sigma_{yy} & \tau_{yz} \\ \tau_{xz} & \tau_{yz} & \sigma_{zz} \end{vmatrix} T = \begin{vmatrix} \sigma_1 & 0 & 0 \\ 0 & \sigma_2 & 0 \\ 0 & 0 & \sigma_3 \end{vmatrix} \qquad 3.5$$

where σ_1, σ_2, σ_3 are principal stresses along three mutually perpendicular directions. The symmetric feature of matrix A guarantees the existence of the real solution (Uhlig, 2002).

Similarly, there are principal strains at a point, where only normal strains are present with shear strains disappeared. For isotropic materials the principal axes of stress and the principal axes of strain always coincide (Fjaer et al., 2008). On the other hand, for anisotropy materials, the base spaces of principal stress and principal strain are more likely to be different.

The motivation to find in-situ stress is to have a basic knowledge of the stress state underground and to apply the boundary conditions for stress analyses. The in-situ stress state generally is described by the three mutually orthogonal principal stresses.

Determination of the orientations of these principal stresses could be very complicated; however, for a stable sedimentary basin far away from tectonic activity (such as the Williston Basin), it is reasonable to assume the vertical stress caused by overburden is one of the principal stresses. Thus, if the rock were isotropic, there is:

$$\begin{bmatrix} \varepsilon_1 \\ \varepsilon_2 \\ \varepsilon_3 \end{bmatrix} = \begin{bmatrix} \frac{1}{E} & -\frac{\nu}{E} & -\frac{\nu}{E} \\ -\frac{\nu}{E} & \frac{1}{E} & -\frac{\nu}{E} \\ -\frac{\nu}{E} & -\frac{\nu}{E} & \frac{1}{E} \end{bmatrix} \begin{bmatrix} \sigma_1 \\ \sigma_2 \\ \sigma_3 \end{bmatrix} \quad 3.6$$

Giving the boundary condition of that the horizontal strains are zero due to the extensive flat area with the limitations on the horizontal expanding, there is $\sigma_1 = \sigma_2 = \frac{\nu}{1-\nu}\sigma_3$. This means the horizontal stresses are both equal and they are one third of the overburden if the Poisson ratio of the rock is 0.25. In fact, this usually is not the case as many other factors will influence the other principal stresses, such as the heterogeneity of the rock formations, the dispositional history, pore pressure, etc (Zoback, 2007). More discussions will be presented in the oncoming chapters as the knowledge on in-situ stresses is essential for the safe sequestration of CO_2.

3.3. Effective Stress at Elastic Domain, Plastic Domain and Failure

Rock, especially the carbonate rock, is in general porous, thus the existence of the pore fluids will also play an important role to its behavior. The concept of effective stress takes both the in-situ stress and pore pressure into account. This concept is important as it will be used for the constitutive equations, to rock properties and failure criterion (Bouteca and Gueguen, 1999). The effective stress is the stress that is applied onto the rock matrix. It controls the stress-strain, volume change, and strength behavior of a given

porous medium, independent of the magnitude of the pore pressure (Lade and De Boer, 1997).

The law of effective stress was enunciated by Terzaghi (Terzaghi and Peck, 1967) and the idea is that rock behaves under the control of the summation of stress and pore pressure (Gueguen and Bouteca, 2004), i.e.:

$$\sigma_{ij}^{eff} = \sigma_{ij} - p\delta_{ij} \qquad 3.7$$

The Kronecker delta δ_{ij} is defined by the following equation, and the reason to introduce it is that pore pressure has no effect on the shear stress.

$$\delta_{ij} = \begin{cases} 1 & if \quad i = j \\ 0 & if \quad i \neq j \end{cases} \qquad 3.8$$

Terzaghi's effective stress has been hold for soils and other unconsolidated materials for most practical purposes, but deviated from that measured for porous media such as concrete and rock. In fact, a porous medium can be either viewed as granular materials with contact points or solid materials with interconnected pores or somewhere in between, as shown in Figure 3.2.

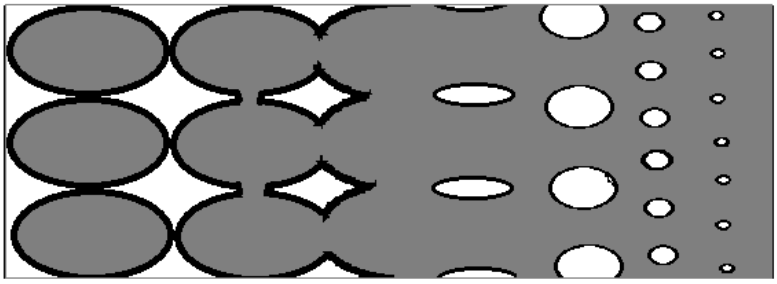

Figure 3.2. Porous medium structures: from separate grains with contact points to solid with interconnected pores (Modified after Lade and Boer, 1997)

For well cemented rock at its elastic domain, Biot's effective stress is more applicable:

$$\sigma_{ij}^{eff} = \sigma_{ij} - bp\delta_{ij} \qquad 3.9$$

where b is Biot's coefficient, and $\phi < b \leq 1$. Its definition is given by (Geertsma, 1966):

$$b = \left(\frac{\partial \sigma}{\partial p}\right)_{\Delta \varepsilon_v = 0} = 1 - \frac{K}{K_s} \qquad 3.10$$

where K is drained bulk modulus and K_s is solid skeleton's bulk modulus of rock. For Indiana limestone, this number b is about 0.7 (Hart, 2000). Many sedimentary rocks (sandstone and carbonate) have a "b" value in the range of 0.65~0.85, with clayey rock giving a higher number about 0.95 (Wang, 2000).

Similarly, in the plastic domain, the effective stress can be expressed as (Coussy, 2004):

$$\sigma_{ij}^{eff} = \sigma_{ij} - b^{Plas} p\delta_{ij} \qquad 3.11$$

Also, at failure, the effective stress can be expressed in the same style:

$$\sigma_{ij}^{eff} = \sigma_{ij} - b^{Fail} p\delta_{ij} \qquad 3.12$$

In porous rock, the plasticity and failure all imply the initiation and growth of micro-cracks and subsequent coalescence of these cracks. From theoretical derivation and laboratory test, it was found that both b^{Plas} and b^{Fail} will approach unity (Lade and Boer, 1997). In short, the Biot's effective stress will approach Terzaghi's effective stress as rock experiences from its elastic domain to plastic domain or failure, or Terzaghi's effective stress can be treated as a specific form of Biot's effective stress.

3.4.Poroelasticity and Elastic Storage Capacity

Because CO_2 will be stored in the pores of the rock, the elasticity approach has its limitation in mechanical analysis as it treats rock as solid material. In fact, rock consists

of a solid framework and a pore fluid which can not be treated independently and the way rock behaves depends, to a large extent, on the fluids filled in its pores (Fjaer et al., 2008).

The storage of CO_2 will result in an increase of pore pressure, decreasing the effective stress and thereby causing the rock to expand. Formation expanding may then cause uplift of the ground surface, or induce fractures (Rutqvist et al., 2007; 2008; 2010). However, if this increase of pore pressure will not move the material out of its poroelasticity domain, it would be considered as safe. Thus, poroelasticity setup the most conservative baseline from the standpoint of geomechanics for CO_2 sequestration.

Due to the presence of an injection source, the fluid content will be increased, and this increment can be expressed as (Biot and Willis, 1957; Berryman, 1992):

$$\Delta\zeta = -\phi\vec{\nabla}\cdot(\vec{U}_f - \vec{U}_s) = \frac{\Delta V_p - \Delta V_f}{V} \qquad 3.13$$

where $\vec{U}_f$ and $\vec{U}_s$ are the average displacements of the fluid and solid, respectively; and V_p is the pore volume, V_f is the fluid volume, and V is the reference volume. A poroelastic problem consists of four basic variables – stress change ($\Delta\sigma$), strain change ($\Delta\varepsilon$), pore pressure change (Δp) and fluid content change ($\Delta\zeta$).

Recall Equation 3.9. ($\sigma_{ij}^{eff} = \sigma_{ij} - bp\delta_{ij}$), as volumetric strain is only controlled by effective stress, there is:

$$\Delta\varepsilon = \frac{\Delta V}{V} = \frac{\Delta\sigma^{eff}}{K} = \frac{\Delta\sigma - b\Delta p}{K} = \frac{1}{K}\Delta\sigma - \frac{b}{K}\Delta p \qquad 3.14$$

where K is drained bulk modulus. The above equation shows that the volumetric strain can either be induced by the change of total stress or pore pressure, and their effects are opposite; i.e., increasing total stress will compress the rock, while increasing pore

pressure will expand the rock. Another important equation is about the relationship between a variation of fluid volume and the total stress and pore pressure. Assuming it has the following form:

$$\Delta\zeta = x\Delta\sigma + y\Delta p \qquad 3.15a$$

y is the specific storage coefficient " S_σ " at constant stress (Wang, 2000).

$$y = S_\sigma = \left.\frac{\partial\zeta}{\partial p}\right|_{\Delta\sigma=0} \qquad 3.15b$$

And x is equal to -b/K based on the potential energy conservative theory by following the same methodology of Biot (1941), thus the following matrix form stands:

$$\begin{pmatrix}\Delta\varepsilon\\ \Delta\zeta\end{pmatrix} = \begin{pmatrix}\frac{1}{K} & -\frac{b}{K}\\ -\frac{b}{K} & S_\sigma\end{pmatrix}\begin{pmatrix}\Delta\sigma\\ \Delta p\end{pmatrix} \qquad 3.16$$

Comparing with Equations 15a and 15b of Detournay and Cheng (1993), this equation is unique in terms of the three poroelastic coefficients (K, b, S_σ) that were selected. It best suits the requirements of the CO_2 sequestration problems, while avoiding the introduction of some other poroelastic coefficients as in the Equations 1.10-1.12 of Wang (2000).

These three coefficients: K, the drained bulk modulus, b, the Biot's coefficient, and S_σ, the specific storage coefficient, completely characterize the poroelastic response for an isotropic material.

Here, take a close look at S_σ. The elastic storage coefficient or the specific storage coefficient is the amount of fluid per unit volume of a saturated formation that is

stored from storage due to compressibility of the rock matrix and the pore fluid per unit change in pore pressure (head) (Fetter, 2001). This specific storage is (Wang, 2000):

$$S_\sigma = \left.\frac{\partial \zeta}{\partial p}\right|_{\Delta\sigma=0} = \left(\frac{1}{K} - \frac{1}{K_s^{'}}\right) + \phi\left(\frac{1}{K_f} - \frac{1}{K_\phi}\right) \qquad 3.15c$$

where $K_s^{'}$, K_f, K_ϕ are the bulk moduli of solid grains, pore fluid and pore spaces, respectively. If the solid grains and pores are incompressible, this will be reduced to:

$$S_\sigma = \frac{1}{K} + \phi\frac{1}{K_f} \qquad 3.15d$$

Because in hydro-geologic applications, head rather than pressure is used, thus its hydro-geologic equivalent is:

$$S_s = \rho_f g S_\sigma = \rho_f g\left(\frac{1}{K} + \phi\frac{1}{K_f}\right) \qquad 3.17$$

This actually is the same equation as that shown in Fetter (2009, Equation 3.32, p.101). Generally, it is desired that the target formation is confined, thus the storativity "S" is:

$$S = hS_s \qquad 3.18$$

where h is the formation thickness.

By incorporating the pore pressure and fluid increment and along with principal coordinates to remove shear stress and shear strain components, also assuming the principal coordinates are in the vertical and horizontal directions for a large flat lying basin, the previous linear elasticity Equation 3.6 becomes:

$$\begin{bmatrix} \Delta\varepsilon_{xx} \\ \Delta\varepsilon_{yy} \\ \Delta\varepsilon_{zz} \\ \Delta\zeta \end{bmatrix} = \begin{bmatrix} \frac{1}{E} & -\frac{\nu}{E} & -\frac{\nu}{E} & -\frac{b}{3K} \\ -\frac{\nu}{E} & \frac{1}{E} & -\frac{\nu}{E} & -\frac{b}{3K} \\ -\frac{\nu}{E} & -\frac{\nu}{E} & \frac{1}{E} & -\frac{b}{3K} \\ -\frac{b}{3K} & -\frac{b}{3K} & -\frac{b}{3K} & S_\sigma \end{bmatrix} \begin{bmatrix} \Delta\sigma_{xx} \\ \Delta\sigma_{yy} \\ \Delta\sigma_{zz} \\ \Delta p \end{bmatrix} \quad 3.19$$

In an actual situation, there is $\Delta\sigma_{zz} = 0$, i.e., the stress caused by overburden is generally constant, and $\Delta\varepsilon_{xx} = \Delta\varepsilon_{yy} = 0$, i.e., the expansion of rock formation in horizontal directions are constrained due to the flat lying. Inserting these constrains in Equation 3.19, there is:

$$\begin{bmatrix} 0 \\ 0 \\ \Delta\varepsilon_{zz} \\ \Delta\zeta \end{bmatrix} = \begin{bmatrix} \frac{1}{E} & -\frac{\nu}{E} & -\frac{\nu}{E} & -\frac{b}{3K} \\ -\frac{\nu}{E} & \frac{1}{E} & -\frac{\nu}{E} & -\frac{b}{3K} \\ -\frac{\nu}{E} & -\frac{\nu}{E} & \frac{1}{E} & -\frac{b}{3K} \\ -\frac{b}{3K} & -\frac{b}{3K} & -\frac{b}{3K} & S_\sigma \end{bmatrix} \begin{bmatrix} \Delta\sigma_{xx} \\ \Delta\sigma_{yy} \\ 0 \\ \Delta p \end{bmatrix} \quad 3.20$$

Solve this equation based on pore pressure increment Δp, there are:

$$\Delta\sigma_{xx} = \Delta\sigma_{yy} = \frac{bE}{3(1-\nu)K}\Delta p = \frac{bE}{3(1-\nu)\frac{E}{3(1-2\nu)}}\Delta p = \frac{b(1-2\nu)}{1-\nu}\Delta p \quad 3.21a$$

$$\Delta\varepsilon_{zz} = \frac{b\nu - 2\nu - b}{3(1-\nu)K}\Delta p \quad 3.21b$$

$$\Delta\zeta = -\frac{2(1-2\nu)b^2}{3(1-\nu)K}\Delta p + S_\sigma\Delta p < S_\sigma\Delta p \quad 3.21c$$

For limestone, take b=0.7, ν=0.26, ϕ=0.12 then, there are:

$$\Delta\sigma_{xx} = \Delta\sigma_{yy} = 0.45\Delta p \tag{3.22a}$$

$$\Delta\varepsilon_{zz} = -\frac{0.47}{K}\Delta p \tag{3.22b}$$

$$\Delta\zeta = -\frac{0.21}{K}\Delta p + S_\sigma \Delta p \cong -\frac{0.21}{K}\Delta p + \left(\frac{1}{K} + \frac{\phi}{K_f}\right)\Delta p$$
$$= \left(\frac{0.79}{K} + \frac{0.12}{K_f}\right)\Delta p < S_\sigma \Delta p \tag{3.22c}$$

The above Equations (3.21and 3.22) indicate the following:

1. The increment of fluid will result in the increase of pore pressure. This increase is linear under the poro-elasticity condition with rigid particles. Besides, the storage capacity under such boundary conditions is smaller than the elastic specific storage capacity which is defined under the constant stress condition.
2. The injection of the pore fluid will result in the increase of in-situ stress in the horizontal plane, and this increase is not direction-related under the isotropic assumption. The reason that horizontal stress is increased is that increased pore pressure causes the rock to expand, but this expansion is confined in the horizontal direction, thus causing the intensifying of stress. The deviatoric stress could be either increased or decreased depending on the initial differences among those principal stresses. This will set up a constraint to the CO_2 sequestration capacity.
3. The increment of strain in the vertical direction is also proportional to the increase of pore pressure; this will set up another constraint to the maximum pore pressure that could be reached. The negative sign implies the strain is in the direction of expansion, field uplift could be expected.

3.5. Pore Pressure Buildup Profile Under the Injection of Fluid Mass

Equations 3.21a-b set up the simplified relationships between stress and strain changes with respect to the pore pressure change. However, these changes can not be obtained simultaneously and universally in the field as pore pressure can not be built up simultaneously and universally in the field. CO_2 needs to be pumped through a well (a point source or a line source) to the field, thus the pore pressure will be built up following the fluid's flow, and consequently, the stress and strain will be changed step by step, here and there, leading to a rather complicated scenario even upon the simplest assumption of isotropic formation.

Consider the injection of CO_2 from a cylindrical well which has negligible dimensions in comparison with those of the target formation, so the latter can be treated as a porous continuum of infinite extent. This problem can be solved by following the same methodology as that in "continuous line source" (Wang, 2000; p.123) or "line injection of fluid mass" (Coussy, 2004; p. 120).

Based on the cylindrical symmetry, a cylindrical coordinate (r, θ, z) is adopted. There is only fluid supply from the vertical well and the fluid flow reduces to zero infinitely far from the well. First the fluid mass balance requires that:

$$Q = \int_0^\infty \dot{\zeta}\, 2\pi r dr \qquad 3.23$$

where Q is the constant flow rate and $\dot{\zeta}$ is the time derivative of ζ, which is the influx of CO_2 per unit area.

The basic diffusion equation relates the rate of change in time domain with the rate of change in space domain (Farlow, 1993). Therefore there is:

$$\frac{\partial \dot{\zeta}}{\partial t} = c\nabla^2 \dot{\zeta} \Rightarrow \frac{\partial \dot{\zeta}}{\partial t} = c \cdot \frac{1}{r} \cdot \frac{\partial}{\partial r}\left(r \frac{\partial \dot{\zeta}}{\partial r} \right) \tag{3.24}$$

where c is the fluid diffusivity coefficient.

The solution of this partial differential equation is given by (Coussy, 2004):

$$\dot{\zeta}(r,t) = \frac{Q}{4\pi ct} \exp(-\frac{r^2}{4ct}) \tag{3.25}$$

Integration of Equation 3.25 with respect to time, upon the initial condition $\zeta(r, t=0) = 0$, gives:

$$\zeta = \frac{Q}{4\pi ct} E_1(\frac{r^2}{4ct}) \tag{3.26}$$

where the exponential integral is "Well Function" in hydrogeology, given by:

$$E_1(z) = \int_z^{\infty} \frac{\exp(-\xi)}{\xi} d\xi \tag{3.27}$$

The pore pressure is obtained as (Wang, 2000):

$$p(r,t) = \frac{Q}{4\pi(k/\mu)} E_1(\frac{r^2}{4ct}) \tag{3.28}$$

where k is the permeability and μ is the viscosity of fluid.

This is actually the Theis equation in a completely confined aquifer (Fetter, 2001. p.154). Therefore, the classic Theis solution is also a poroelastic solution for radial flow condition. Overall, the increase of pore pressure decreases with the increased distance from the well, and the pore pressure in the whole field increases with time, as shown in Figure 3.3.

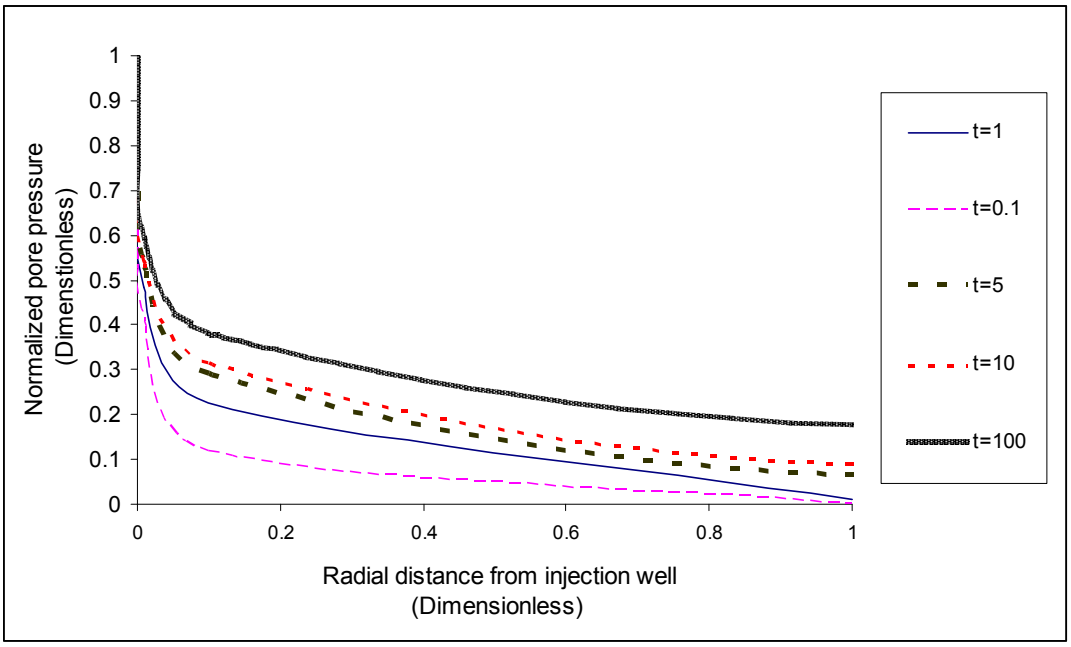

Figure 3.3. Pore pressure vs. distance from the injection well at different dimensionless time

3.6. Thermoelasticity, Thermally Induced Stress and Thermoporoelasticity

As described in the previous chapter, CO_2 sequestration will disturb the thermal regime underground, geothermal effects should also be taken into account. The theory of thermoelasticity accounts for the effect of changes in temperature on the stresses and displacements in a body (Jaeger et al., 2007). Similar to pore pressure, a change in temperature in a homogeneous and isotropic body will give rise to normal strains in three orthogonal directions and no shear strains (Boresi and Schmidt, 2003), i.e:

$$\varepsilon'_{xx} = \varepsilon'_{yy} = \varepsilon'_{zz} = -\beta\Delta T; \quad \varepsilon'_{xy} = \varepsilon'_{xz} = \varepsilon'_{zy} = 0 \qquad 3.29$$

where β denotes the coefficient of thermal expansion of the materials, which is derived from a symmetric second-order tensor upon the assumption of isotropy. Note the negative sign in equation 3.29, which is different from that of Boresi and Schmidt (2003), as in rock mechanics, it is the convention to assume compression as positive.

By incorporating the temperature change and thermal strain, along with principal coordinates to remove shear stress and strain components, the previous linear elasticity equation can be written as:

$$\begin{bmatrix} \Delta\varepsilon_{xx} \\ \Delta\varepsilon_{yy} \\ \Delta\varepsilon_{zz} \end{bmatrix} = \begin{bmatrix} \frac{1}{E} & -\frac{\nu}{E} & -\frac{\nu}{E} & -\beta \\ -\frac{\nu}{E} & \frac{1}{E} & -\frac{\nu}{E} & -\beta \\ -\frac{\nu}{E} & -\frac{\nu}{E} & \frac{1}{E} & -\beta \end{bmatrix} \begin{bmatrix} \Delta\sigma_{xx} \\ \Delta\sigma_{yy} \\ \Delta\sigma_{zz} \\ \Delta T \end{bmatrix} \tag{3.30}$$

Rock will expand when the temperature is increased, or shrink if the temperature is decreased, thus one can see that, as the temperature of injected CO_2 is generally different from that of the target formation, thermal stress will be introduced.

Given a typical boundary condition of underneath, $\Delta\varepsilon_{xx} = \Delta\varepsilon_{yy} = 0; \quad \Delta\sigma_{zz} = 0$, there is:

$$\begin{bmatrix} 0 \\ 0 \\ \Delta\varepsilon_{zz} \end{bmatrix} = \begin{bmatrix} \frac{1}{E} & -\frac{\nu}{E} & -\frac{\nu}{E} & -\beta \\ -\frac{\nu}{E} & \frac{1}{E} & -\frac{\nu}{E} & -\beta \\ -\frac{\nu}{E} & -\frac{\nu}{E} & \frac{1}{E} & -\beta \end{bmatrix} \begin{bmatrix} \Delta\sigma_{xx} \\ \Delta\sigma_{yy} \\ 0 \\ \Delta T \end{bmatrix} \tag{3.31}$$

Solve the above equation based on ΔT, one can have:

$$\Delta\sigma_{xx} = \Delta\sigma_{yy} = \frac{E\beta}{1-\nu}\Delta T \tag{3.32}$$

$$\Delta\varepsilon_{zz} = -\frac{1+\nu}{1-\nu}\beta\Delta T$$

For typical limestone, $\beta = 10^{-5}/^{\circ}K, \quad \nu = 0.25, \quad E = 25GPa$, this becomes:

$$\frac{\Delta\sigma_{xx}}{\Delta T} = \frac{\Delta\sigma_{yy}}{\Delta T} = \frac{E\beta}{1-\nu} \approx 0.3MPa/^{\circ}K \tag{3.33}$$

This indicates that thermal stresses may become quite significant if the temperature change can not be ignored. The decrease of the temperature will result in the shrinking of rock, tensile cracks may be expected.

Poroelasticity can also be extended in order to include thermal effects. This extension is achieved by considering an underlying thermo-elastic skeleton (Coussy, 2004). The constitutive equation for linear thermo-poro-elasticity upon isotropy assumption is the following equation by combining Equations 3.18 and 3.30:

$$\begin{bmatrix} \Delta\varepsilon_{xx} \\ \Delta\varepsilon_{yy} \\ \Delta\varepsilon_{zz} \\ \Delta\zeta \end{bmatrix} = \begin{bmatrix} \frac{1}{E} & -\frac{\nu}{E} & -\frac{\nu}{E} & -\frac{b}{3K} & -\beta \\ -\frac{\nu}{E} & \frac{1}{E} & -\frac{\nu}{E} & -\frac{b}{3K} & -\beta \\ -\frac{\nu}{E} & -\frac{\nu}{E} & \frac{1}{E} & -\frac{b}{3K} & -\beta \\ -\frac{b}{3K} & -\frac{b}{3K} & -\frac{b}{3K} & S_\sigma & -\beta_f \end{bmatrix} \begin{bmatrix} \Delta\sigma_{xx} \\ \Delta\sigma_{yy} \\ \Delta\sigma_{zz} \\ \Delta p \\ \Delta T \end{bmatrix} \qquad 3.34$$

where β_f is the volumetric thermal expansion of fluid. The negative sign in front of β_f indicates that increasing temperature will result in the decrease of stored fluid. This equation gives a full coupling among hydro, thermo and mechanics under small strain conditions. Now, again consider the typical sequestration boundary conditions at depth, i.e., $\Lambda\varepsilon_{xx} = \Delta\varepsilon_{yy} = 0;\quad \Delta\sigma_{zz} = 0$, there is:

$$\begin{bmatrix} 0 \\ 0 \\ \Delta\varepsilon_{zz} \\ \Delta\zeta \end{bmatrix} = \begin{bmatrix} \frac{1}{E} & -\frac{\nu}{E} & -\frac{\nu}{E} & -\frac{b}{3K} & -\beta \\ -\frac{\nu}{E} & \frac{1}{E} & -\frac{\nu}{E} & -\frac{b}{3K} & -\beta \\ -\frac{\nu}{E} & -\frac{\nu}{E} & \frac{1}{E} & -\frac{b}{3K} & -\beta \\ -\frac{b}{3K} & -\frac{b}{3K} & -\frac{b}{3K} & S_\sigma & -\beta_f \end{bmatrix} \begin{bmatrix} \Delta\sigma_{xx} \\ \Delta\sigma_{yy} \\ 0 \\ \Delta p \\ \Delta T \end{bmatrix} \qquad 3.35$$

Solve the equation based on Δp and ΔT, the results are:

$$\Delta\sigma_{xx} = \Delta\sigma_{yy} = \frac{E}{1-\nu}\left(\frac{b}{3K}\Delta p + \beta\Delta T\right) \quad 3.36a$$

$$\Delta\varepsilon_{zz} = -\left(\frac{1+\nu}{1-\nu}\right)\left(\frac{b}{3K}\Delta p + \beta\Delta T\right) \quad 3.36b$$

$$\Delta\zeta = \left(S_\sigma - \frac{2b^2E}{9K^2(1-\nu)}\right)\Delta p - \left(\frac{2bE}{3K(1-\nu)}\beta + \beta_f\right)\Delta T \quad 3.36c$$

One can see that decreasing temperature will lessen the stress increase and strain increase (in the sense of uplift); it will also benefit the storage capacity. On the other hand, after some time, with the temperature increasing due to the heat transfer, the originally stable condition might be destroyed if fluid flow is impeded by permeability reduction, i.e., an over-pressured region might be present in a low permeable formation.

Another concern is that if the temperature difference is too high, thermal stress (as indicated by Equation 3.33) may fracture the formation, thus an analysis of thermo-poro-elasticity based on intact rock condition could not be continued, whereas a new fractured model needs to be introduced.

Thermal effect generally lags off in comparison with the effect of pore pressure. This will make the analysis even more difficult. The study of many over-pressured formations implies that afterwards-heating may be a cause of abnormal high formation pressures (Chilingar et al., 2002).

3.7. Yield Criterion for Tensile Failure, Compaction Failure and Shear Failure

If the stresses that rocks are subjected to are high enough, some of the deformation will be permanent in the sense that it cannot be recovered even upon the removal of the applied stresses. This deformation is known as plastic deformation and the condition that defines the limit of elasticity and the beginning of plasticity is known as

the yield condition. A general form of yield criterion can be expressed in terms of either the stress tensor or the three stress invariants as follows (Yu, 2006):

$$f(\sigma_{ij}) = f(I_1, I_2, I_3) = 0 \quad or \quad f(\sigma_1, \sigma_2, \sigma_3) = 0 \tag{3.37}$$

Here the three stress invariants are given by:

$$I_1 = \sigma_{xx} + \sigma_{yy} + \sigma_{zz} \tag{3.38}$$

$$I_2 = \begin{vmatrix} \sigma_{xx} & \tau_{xy} \\ \tau_{xy} & \sigma_{yy} \end{vmatrix} + \begin{vmatrix} \sigma_{xx} & \tau_{xz} \\ \tau_{xz} & \sigma_{zz} \end{vmatrix} + \begin{vmatrix} \sigma_{yy} & \tau_{yz} \\ \tau_{yz} & \sigma_{zz} \end{vmatrix}$$

$$I_3 = \begin{vmatrix} \sigma_{xx} & \tau_{xy} & \tau_{xz} \\ \tau_{xy} & \sigma_{yy} & \tau_{yz} \\ \tau_{xz} & \tau_{yz} & \sigma_{zz} \end{vmatrix}$$

Tensile failure, shear failure and compaction failure can be shown in the following figure:

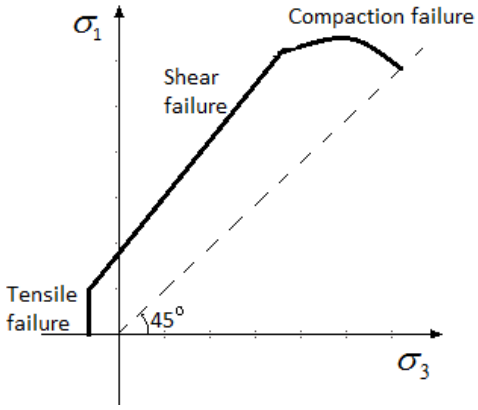

Figure 3.4. Location of the various failure modes in principal stress space (modified after Fjaer et al., 2008)

Tensile failure occurs when the effective tensile stress exceeds the tensile strength T_0. For isotropic rocks, the conditions for tensile failure will be fulfilled first for the lowest principal stress, thus the tensile failure criterion is (Fjaer et al., 2008):

$$\sigma_3 = -T_0 \tag{3.39}$$

Compaction failure is a failure mode of pore collapse, which may occur under pure hydrostatic loading or non-hydrostatic stress conditions at high confining pressure. The latter is also referred to as shear-enhanced compaction (Fjaer et al., 2008). An acceptable approximation for many rocks is given by (Bouteca et al., 2000):

$$\left(\frac{\bar{\sigma}}{p^*}\right)^2 + \left(\frac{\Delta\sigma}{p^*}\right)^2 = 1 \qquad 3.40$$

where p* is critical effective pressure for the onset of grain crushing under hydrostatic loading, $\bar{\sigma}$ is effective mean stress and $\Delta\sigma$ is deviatoric stress.

The most common failure mode is shear failure, which occurs when the shear stress along some plane is sufficiently high. Many empirical criteria have been developed to describe the onset of shear failure (or yielding), among which the Mohr-Coulomb failure criterion remains the most popular one, because it clearly captures both frictional and cohesive strength factors in shear failure; and it is easy to apply and is relatively reliable (Han, 2003).

The Mohr-Coulomb criterion which assumes a linear envelope can be expressed as (Fjaer et al, 1992):

$$|\tau| = C_0 + \mu_{fric}\sigma \qquad 3.41$$

where C_0 is the inherent shear strength or cohesion of the material, μ_{fric} is the coefficient of internal friction, τ is the shear strength and σ is the normal stress on the shear plane. This criterion can also be expressed in terms of principal stresses as:

$$\sigma_1 = 2C_0\frac{\cos\phi}{1-\sin\phi} + \sigma_3\frac{1+\sin\phi}{1-\sin\phi} \qquad 3.42$$

where σ_1 is the maximum principal stress, σ_3 is the minimum principal stress and ϕ is the friction angle.

Another commonly used empirical criterion is the Hoek and Brown criterion (Jaeger et al, 2007):

$$\sigma_1 = \sigma_3 + (m\sigma_c\sigma_3 + \sigma_c^2)^{1/2} \qquad 3.43$$

where m and σ_c are two fitting parameters. Setting σ_3=0 shows that σ_c is in fact equal to the uniaxial compressive strength. For carbonate rocks with well-developed crystal cleavage such as limestone, m is about 7 (Jaeger et al, 2007).

When porous rock is saturated with fluid, its behavior will be governed by the effective stresses. Recall Equation 3.9, and write in an integral and matrix form, this will be:

$$\begin{vmatrix} \sigma_{xx}^{eff} & \tau_{xy} & \tau_{xz} \\ \tau_{yx} & \sigma_{yy}^{eff} & \tau_{yz} \\ \tau_{zx} & \tau_{zy} & \sigma_{zz}^{eff} \end{vmatrix} = \begin{vmatrix} \sigma_{xx} & \tau_{xy} & \tau_{xz} \\ \tau_{yx} & \sigma_{yy} & \tau_{yz} \\ \tau_{zx} & \tau_{zy} & \sigma_{zz} \end{vmatrix} - b \begin{vmatrix} p & 0 & 0 \\ 0 & p & 0 \\ 0 & 0 & p \end{vmatrix} \qquad 3.44$$

Then the failure criteria for a rock with a fluid pressure are obtained by introducing the effective stress into the "dry" form of the failure criteria. In such cases, the Mohr-Coulomb criterion will be (Fjaer et al, 1992):

$$|\tau| = C_0 + \mu_{fric}(\sigma - p) \text{ or} \qquad 3.45$$

$$\sigma_1 - b_0 p = 2C_0 \frac{\cos\phi}{1-\sin\phi} + (\sigma_3 - b_0 p)\frac{1+\sin\phi}{1-\sin\phi} \qquad 3.46$$

where, b_0 is referred to as the effective stress coefficient for failure processes. Its connection to the Biot poroelastic coefficient, b, is not clear yet (Jaeger et al., 2007).

The concept of effective stress lays the foundation for rock stability investigation in CO_2 sequestration since it is effective stresses that eventually act on the rock particles to stabilize or mobilize them. By intuition, decreasing porosity means the fluid's effect is decreasing, thus its role in effective stress is decreasing.

It is also important to point out that failure criteria are based on laboratory tests and observations; they are not derived purely mathematically. For a rock, one may measure some of its properties such as permeability, porosity, Young's modulus, Poisson's ratio, etc, however, one cannot know whether it will fail until it fails, even if it is possible to make an estimation based on other rocks. For the same reason, the international science society agreed on that earthquakes are unpredictable; even though they may be monitored (Oncescu, L., personal communication, April 9, 2010, Grand Forks, ND).

3.8. Post Yielding Behavior and Plasticity, Poroplasticity

The total strain increment associated with a stress increment is assumed to consist of an elastic part and a plastic part (Fjaer et al., 2008):

$$d\varepsilon_{ij} = d\varepsilon_{ij}^{e} + d\varepsilon_{ij}^{p} \qquad 3.47$$

$d\varepsilon_{ij}^{e}$ is the elastic strain and will vanish upon the release of applied stress, and $d\varepsilon_{ij}^{p}$ is a permanent deformation, or plastic strain.

After yielding, an elastoplastic material will experience either strain hardening, strain softening, or perfect plasticity if the loading continues. Strain hardening means the stress increases with increasing strain, thus $\Delta\sigma_{ij}\Delta\varepsilon_{ij}^{p} > 0$, while strain softening means

the strain increases with decreasing stress, thus $\Delta\sigma_{ij}\Delta\varepsilon_{ij}^{p} < 0$; and perfect plasticity is the bifurcation between these two scenarios, with $\Delta\sigma_{ij}\Delta\varepsilon_{ij}^{p} = 0$ (Casey and Naghdi, 1981).

The post yielding behavior is very important to rock stability analysis. Imagining a pillar in an underground mine, if the pillar was cut too thin, it may yield and finally collapse, then the overburden will be redistributed to its neighboring pillars, and further collapse may occur in an even larger region. If this scenario occurs unintentionally, it would be a disaster to the mining operation. This indicates that strain softening is unstable, and the rock behavior under strain softening is hard to predict.

On the other hand, strain hardening is stable in the sense that one can expect the rock to sustain at least a certain burden after yielding. For example, with the increasing deposition of sediments, the increased overburden may cause some rock in a deep depth to yield. However, as there is no room for this rock to move, even if lots of micro cracks may be initialized in this rock, and this rock goes into its plasticity domain, it still "must" hold its overburden. Actually, the rock is evolving under its plasticity state, from a weaker rock to a stronger rock by rearranging its particles and possibly taking some sort of chemical reactions with pore fluids. Rock in strain-hardening plasticity is unstable considering its mineralogy stability, but it could be considered as stable regarding the geomechanical stability.

From the stand point of mathematics, perfect plasticity is the bifurcation between a chaos system (strain softening) and a stable system (strain hardening) by considering the geomechanical stability. While yielding point is another bifurcation between a chaos system (plasticity) and a stable system (elasticity) regarding the stability of mineralogy, as shown in the following Figure 3.5.

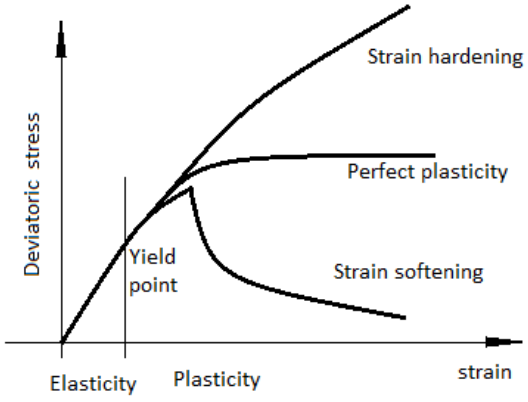

Figure 3.5. Typical failure curves for rock at different confining stress under triaxial test

In contrast to poroelasticity, poroplasticity is irreversible; its evolution can be viewed as a succession of thermodynamic equilibrium states and depends only on the loading chronology (Coussy, 2004). At the poroelastic domain, permeability is relatively stable as the rock matrix is intact; however, at the poro-plastic domain, permeability will be changed, and the evolution of permeability with respect to poroplasticity will be tested in the following chapters.

3.9. Failure by Cracks and Fracture Mechanics

The field of fracture mechanics is focused on the brittle fracture and, as a scientific discipline in its own right, is less than 40 years old. "Since hydrostatic stress states do not favor plastic flow, the material has the opportunity to seek an alternative mechanism of failure, namely cleavage fracture" (Sanford, 2003, p.59). Brittle fracture and plastic flow are competing mechanisms for failure.

Natural rock can hardly exist without non-perfection or discontinuities (cracks), especially sedimentary rocks, which have undergone million years' geological events.

There are three ways in which a fracture can be formed: one by pulling apart and two by shearing (Hudson and Harrison, 1997), as shown in Figure 3.6.

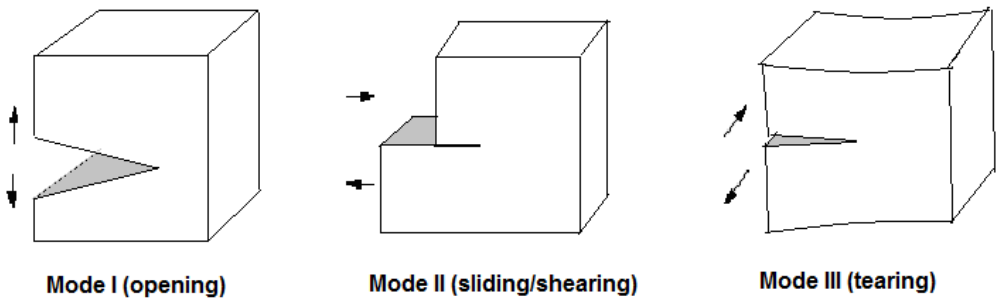

Figure 3.6. Three fracture modes (Modified after Boresi and Schmidt, 2003)

Changes in the stress state of a rock may cause cracks to initiate, grow, or close, depending on the fracture orientations with respect to the principal stresses (Fjaer et al., 2008).

Stress intensity factor is the parameter to describe the elastic stress field surrounding the crack tip. Three stress intensity factors, K_I, K_{II} and K_{III}, are employed to characterize the stress fields for these three modes. The dimensions of stress intensity factor $K_{I,(II,III)}$ are [stress]x[length]$^{1/2}$ (Boresi and Schmidt, 2003).

Since the stress intensity factor represents the strength of the singularity, i.e., the rate at which the stresses approach infinity, it is defined as (Sanford, 2003):

$$K_{I,(II,III)} = \lim_{\delta^+ \to 0} \sigma_y \Big|_{\theta=0} \cdot \sqrt{2\pi\delta} \qquad 3.48$$

where δ is the distance measured from the crack tip, and the limit is taken from the material (+) side.

In general, the stress intensity factor is in the form of:

$$K_{I,(II,III)} = \sigma\sqrt{\pi a}\cdot Y\left(\frac{a}{W}\right) \qquad 3.49$$

where $Y\left(\frac{a}{W}\right)$ is a dimensionless shape factor that embodies the effects of all of the geometric parameters and W is any characteristic in-plane dimension (such as the width of the body).

For a penny-shaped crack with radius "r" in an infinite medium, the stress intensity factor is (Fjaer et al., 2008):

$$K_I = \sigma\sqrt{\pi r}\cdot Y\left(\frac{r}{W}\right) = \sigma\sqrt{\pi r}\cdot\frac{2}{\pi} \qquad 3.50$$

If K_I exceeds a critical limit K_c, called the fracture toughness, the crack will start to grow. Thus, fracture toughness is the resistance offered by an initially fractured material against crack propagation; it is an important material property which describes the critical states of stresses or energy near the crack tip required for the propagation of brittle fracture (Krishnan et al., 1998). As a material property, K_c can only be determined by experiment.

At the instant of fracture (Sanford, 2003),

$$\sigma_{xx}\Big|_{critical} = \frac{K_c}{\sqrt{2\pi r}} f_x(\theta) + \sigma_{ox} \qquad 3.51$$

$$\sigma_{yy}\Big|_{critical} = \frac{K_c}{\sqrt{2\pi r}} f_y(\theta)$$

$$\tau_{xy}\Big|_{critical} = \frac{K_c}{\sqrt{2\pi r}} f_{xy}(\theta)$$

where f_x, f_y, f_{xy} are known functions of θ, while r and θ are the conventional crack tip co-ordinates.

Three methods are suggested by the International Society for Rock Mechanics (ISRM) to evaluate the stress toughness under mode-I conditions: (1) Chevron rod; (2) Chevron bend and (3) Chevron notched Brazilian disk test (Ouchterlony, 1988). Chevron notched Brazilian disk test will be used to determine the fracture toughness of Indiana limestone and Pierre shale in this dissertation, and more detailed laboratory approach will be explained in the corresponding chapters.

If the pore pressure within the rock exceeds the minimum principal stress plus the tensile strength of the rock, crack will be initialized.

$$p_f > T_0 + \sigma_{\min} \qquad 3.52$$

This is also referred to as hydraulic fracturing, if created with intension.

During CO_2 sequestration, the increased pore pressure, and correspondingly changed effective stress, may satisfy this failure criterion, thus tensile fractures might be introduced. Also note that if the injected CO_2 has much lower temperature than the target formation, thermally induced fracturing (TIF) is also expected, and thermal stresses will decrease the fracturing pressure (Detienne et al., 1998).

3.10.Formation Stress Path: a Site Specific Feature

Target formation for CO_2 sequestration is a dynamic system in the sense that the three-dimensional in-situ stress field will be changed with the fluctuation of pore pressure. Optimized formation loading path for fluid injection and/or production is governed by many factors, including in-situ stress, mechanical properties of rock lithology and pore pressure evolution behavior, etc. Because each basin is different in terms of these factors, formation stress path would be a unique feature and requires specific attention.

The similar increases of pore pressure may induce ground surface uplift in one place, but may introduce faulting in another place, and the faulting may even be differentiated as normal or strike-slip or thrust, etc, depending on different stress regimes (Healy et al., 1968; Goulty, 2003; Rutqvist et al., 2010).

Here follows are a series of case studies on fluid-injection/extraction-triggered earthquakes. Their implications to CO_2 sequestration are important.

The fact that a change of pore pressure underground could trigger earthquake (or faulting in the language of geomechanics) poses serious concern to the geomechanical stability analysis for CO_2 sequestration.

Disposal of waste fluids by injection into a deep well has triggered earthquakes near Denver, Colorado (Healy et al., 1968). In 1961, a deep disposal well was drilled through 3,638 meters of nearly flat-lying sedimentary rocks in Denver basin for the U.S. Army at the Rocky Mountain Arsenal, northeast of Denver, Colorado. Soon after the operation of injection, earthquakes were recorded within 8 kilometer of the disposal well.

The coincidence in time between the beginning of injection and the start of the earthquake sequence, and the increased earthquake activity during periods of high fluid injection provided evidence that fluid injection was the cause. It was found that these earthquakes were controlled by preexisting fracture patterns, and they were in a zone of maximum fracture porosity (Healy et al., 1970). It was also found that there was a net migration of epicenters away from the well consistent with the advance of a pore pressure front during the period of fluid injection; and earthquake activity continued at least 6 years and produced a third $M \geq 5$ earthquake 21 months after the end of injection (Healy et al., 1968).

Injected fluid in stable continental region can also trigger earthquake, such as a persistent earthquake sequence in Ashtabula, northwest Ohio (Seeber et al., 2004). This earthquake sequence lasted at least 16 years since 1987 and all originated from a small area close to a waste fluid injection well, which had pumped about $3\times10^5 m^3$ waste fluid in the basal Paleozoic formation with a wellhead pressure of 100 bars from 1986 to 1994. The pattern of accurate hypocenters is consistent with the high pore-pressure anomaly spreading from the injection site. The earthquakes are interpreted as reactivated pre-existing faults. The spreading pore-pressure anomaly can remain significant to large distances and for long times, as stress changes as small as 0.1 bar (1.45 psi) are sufficient to trigger or inhibit earthquakes (Reasenberg and Simpson, 1992).

The third example is what occurred at Paradox Valley, located in the eastern portion of the Paradox Basin, Colorado. Since 1991, more than $4x10^6 m^3$ brine was pumped into deep Paleozoic and Precambrian strata to migrate the shallow saline aquifer's pollution to the Colorado River. This injection has induced over 4,000 surface-recorded, seismic events (Ake et al., 2005). The target formation is the Mississippian-age Leadville Limestone, a locally vuggy, highly-fractured, very-tight dolomitic limestone at a depth of 4.3 km. A temporal correlation between injection and event hiatuses, and a correlation between event rate and injection intensity were observed. The faulting are consistent with shear failures, while no tensile or Mode I fractures were recognized. It was also suggested that the huge injected volume might be sufficient to alter the in-situ stress on favorably-orientated slip planes; and the stresses on these planes might be reduced by the occurrence of previous events.

On the other hand, fluid extraction could also trigger earthquakes (faulting), as reported by Segall (1989). Earthquakes were felt near the Goose Creek oil field in south Texas, where oil production caused the field to subside by as much as 1 m between 1917 and 1925 (Pratt and Johnson, 1926); earthquakes accompanied oil production from the Wilmington oil field in Long Beach, California, where subsidence between 1936 and 1966 reached 9 m (Kovach, 1974); active reverse faulting has been recognized within the Buena Vista Hills oil field, California, where a 2.6-km-long fault slipped at a rate of 2cm/yr between 1932 and 1967 (Nason et al., 1968); the rate of earthquakes increased dramatically when the average reservoir pressure dropped by 25 MPa at the Rocky Mountain House, Alberta, Canada, where all these faulting events were located below the reservoir formation (Wetmiller, 1986). Both normal and thrust faulting may accompany fluid extraction (Segall, 1989).

Thus, pore pressure fluctuation, either increase or decrease, may all trigger faulting. The injection of CO_2 will most likely increase the pore pressure, and then it is reasonable to pay attention to the occurrence of faulting (earthquakes). Unlike other fluid waste, the buoyancy effect during CO_2 sequestration may be much larger thus these faulting may enhance upward migration of CO_2, which poses a serious safety concern. The threshold pressure change (buildup or dropdown) is critical to trigger faulting. In the case of the Rocky Mountain Arsenal, this critical pore pressure buildup is only 32 bars by comparing earthquake epicenters with distribution of pressure buildup (Hsieh and Bredehoeft, 1981). One may assume that this area was already very close to failure prior to injection.

Concluding remarks

The geomechanical stability analysis for CO_2 sequestration is challenged by many factors. Firstly, the field experience is very limited so far and many that may be available are related with enhanced oil recovery (EOR). In the case of EOR, the pore pressure in an oil field has already been dropped, thus the injection of CO_2 more likely would recover this pore pressure instead of resulting in abnormally high pressure, and the over pressure may also be migrated by production of oil in the case of an oil field. All these would be different for a sequestration operation with respect to a saline aquifer.

Secondly, the mathematical analysis has an intrinsic limitation upon the simple assumption, such as isotropy or, homogeneity, etc., thus, it could only approximate the reality in a very rough sense; even though it may provide very valuable guidelines.

Pore-pressure-change induced earthquakes by themselves may already be disasters; if not, the enhanced vertical permeability of CO_2 may be an issue, unlike the injection of other fluids with densities comparable with that of the in-situ fluids. Formation stress path is the core for stability study and it is a site specific feature requiring a large amount of local information.

The oncoming chapters will describe the methodology to handle this problem both from laboratory tests and numerical simulations.

CHAPTER IV

LABORATORY TESTING ON INDIANA LIMESTONE FOR CO2 SEQUESTRATON IN CARBONATE FORMATION

CO_2 sequestration can be divided into two stages. The first stage is to inject CO_2 into the target formation; and the second stage is to store CO_2 in such a formation for a designated period of time. At the first stage, the key question is how the strength, porosity and permeability of the host rock will evolve during CO_2 injection, as a result of coupled dissolution, transportation and precipitation phenomena (Gaus et al, 2002). At the second stage the concerns are: Will rock matrix dissolution result in reservoir compaction by pore collapse or other deformation mechanisms? Will these changes be large enough to break the caprock or ruin the trapping mechanism (Zoback and Zinke, 2002; Rutqvist et al, 2007)?

Sequestration of CO_2 is proposed to be conducted in depleted oil reservoir and saline aquifers in the Williston Basin, a 500,000 square kilometers structural basin (Nelms and Burke, 2004). More detailed discussion with respect to this basin's geology features will be present in Chapter VII. Reservoirs in the Williston Basin are generally classified as carbonate type (Downey et al., 2001). For example, the Mississippian Mission Canyon Formation is a prolific oil producer in the Williston Basin. The Mission Canyon Formation is a shallowing-upward regressive sequence ranging from basinal deep-water carbonates to evaporate-dominated coastal sabkhas and evaporative lagoons.

A stratigraphic cross section across the North Dakota portion of the Williston Basin illustrates the lateral facies change from evaporates on the northeast margin of the basin to carbonates towards the basin center (Moore, 2001).

Dissolution of the injected CO_2 in pore water can result in low pH and may change the geomechanical properties of the host rock, especially when the host formation is carbonate rock (Renard et al, 2005; Le Guen et al, 2007). As chemical reaction may occur and continue in a geologic time, the initial stress condition is critical, which could form a baseline for further evaluations. Carbonate rocks saturated with supercritical CO_2 at great depth have very different states of stresses, pressures and temperatures in comparison with surface conditions. The flow of non-wetting phase into a geological formation is controlled by its capillary displacement pressure and effective permeability. Both of these properties are fluid dependent. Storage of CO_2 has brought attention to the influence of CO_2 as a flowing phase into these properties (Jimenez, 2006).

Indiana limestone was chosen as the specimen to represent the carbonate reservoir rock due to its availability. Indiana limestone is chemically pure, averaging 97% plus calcium carbonate, and 1.2% calcium-magnesium carbonate, thus qualifying the material as a chemical stone (Hill, 2003). The absolute values of such parameters as the permeability, porosity, compressive strength, etc, may not apply to other carbonate reservoirs directly, however, the trend of their changes during CO_2 flooding may give hints to what might be expected in the reservoir conditions.

4.1. Experimental Methods

A triaxial testing system has been developed to investigate the rock behavior at great depth (Zeng et al., 2008). The rock sample is put in a core holder made of steel. The

core holder is connected with three pumps (Figure 4.1), which can control the radial pressure, axial pressure and pore pressure, respectively. The pressure change and the fluid volume change in the pumps can all be controlled and recorded accurately by an electronic system. Data acquisition frequency is 1/6 Hertz. The core holder is enclosed in an air bath which allows the temperature to be controlled precisely.

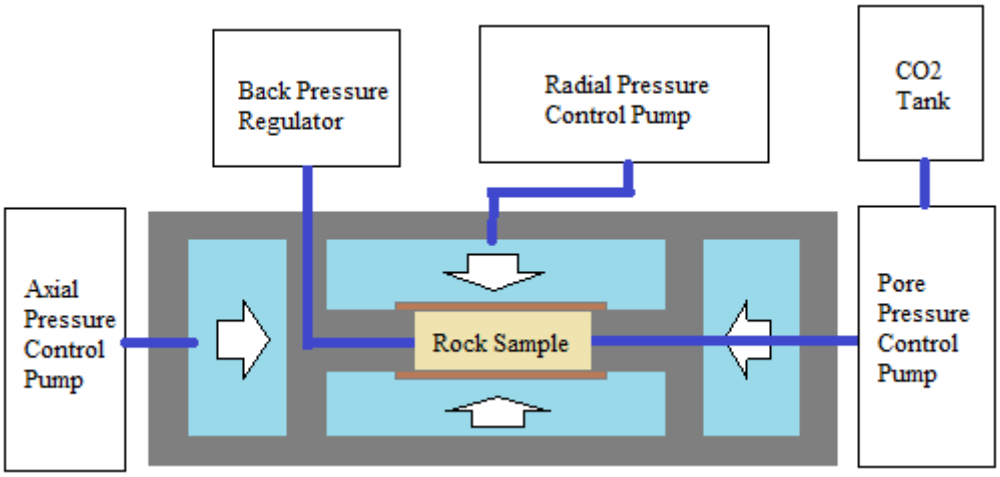

Figure 4.1. Schematic experimental setup

Flooding tests and permeability tests can also be conducted using this facility. In case of flooding test, the pore pressure control pump will take supercritical CO_2 from a CO_2 tank and inject it at a pre-set flow-rate and pressure through the rock sample. CO_2 will be released after passing the back pressure regulator, which ensures that the CO_2 through the sample is in its supercritical state.

Water is used in this system to transfer the pressures. The compressibility of water is a function of the environmental pressure and temperature. The isothermal compressibility (c_w) is expressed as

$$c_w = -\frac{1}{V_1}\left(\frac{dV}{dp}\right)_T = \left(1-\frac{V_2}{V_1}\right)\frac{1}{p_2 - p_1} \qquad 4.1$$

where V_1 and V_2 are the volumes at pressures p_1 and p_2. The ratio V_2/V_1 is equivalent to the amount of water expansion as the pressure drops from p_2 to p_1. For the experiments in this dissertation, the temperature is from room temperature to 220 ºF (100 ºC), and the pressure variation is generally in the range of 10 psi and 5,000 psi. The estimated compressibility of water is about $3\text{x}10^{-6}$ psi^{-1} (Tiab and Donaldson, 2004), then: $V_2/V_1 = 1-(3\times10^{-6})\times5000 = 1-0.015 = 0.985$. Thus the volume change is 1.5% after the pressure change over 5,000 psi. This error is considered minor and the influence of water compressibility in this system can be ignored for the required accuracy.

Due to the specific geometry of the triaxial cell, there is a fixed relationship among axial pressure, radial pressure, and the true stress applied on the sample based on force equilibrium (Figure 4.2).

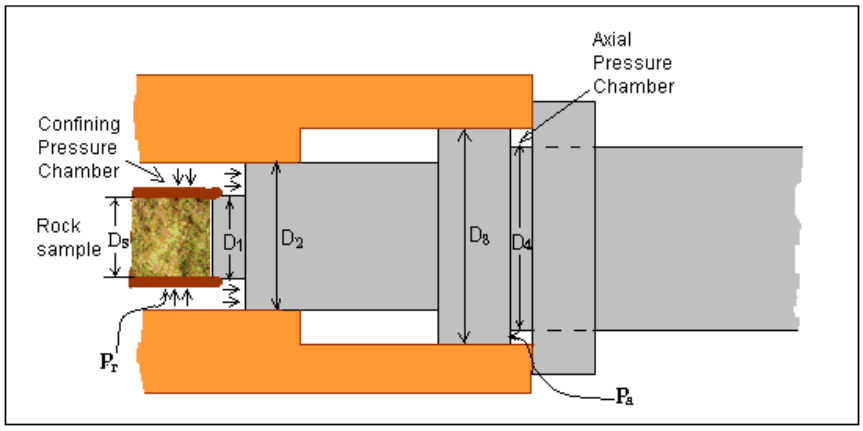

Figure 4.2. Triaxial core holder lay out

$$\sigma_s \bullet A_s + P_r \bullet A_r = P_a \bullet A_a \qquad 4.2$$

where $A_s = \frac{1}{4}\pi D_s^2$, $A_r = \frac{1}{4}\pi(D_2^2 - D_1^2)$, $A_a = \frac{1}{4}\pi(D_3^2 - D_4^2)$, and D_s is sample diameter, D_1 is piston diameter, D_2 is diameter of radial pressure chamber, D_3 is outer diameter of the axial pressure chamber, D_4 is inner diameter of the axial pressure chamber.

4.2. Petrophysical Tests

Petrophysical tests will give some basic properties of rock, such as density, porosity, permeability, etc. Effort was also made to estimate relative permeability.

4.2.1. Density and Porosity

The dimension of the specimen is trimmed into cylindrical pieces of 5.08 cm (2 in) in length and 2.54 cm (1 in) in diameter. The porosity of the specimens is 15% with very low standard deviation (Table 4.1), indicating the homogeneity of the rock.

Table 4.1. Density and porosity of specimens

Specimen	Bulk density (g/cm^3)	Saturated density (g/cm^3)	Dry density (g/cm^3)	Porosity
ILA0807	2.61	2.37	2.22	0.15
ILA0407	2.62	2.37	2.21	0.16
ILA1107	2.61	2.37	2.22	0.15
ILA1007	2.61	2.39	2.25	0.14
ILA0207	2.62	2.40	2.26	0.14
ILA0607	2.61	2.37	2.22	0.15
ILA0107	2.59	2.36	2.22	0.14
ILA0307	2.61	2.37	2.22	0.15
ILA0707	2.58	2.35	2.20	0.15
ILA1207	2.64	2.41	2.27	0.14
Average	2.61	2.38	2.23	0.15
Std. dev.	0.02	0.02	0.02	0.01

4.2.2. Permeability

Permeability is part of the proportionality constant in Darcy's law which relates discharge (flow rate) and fluid physical properties (e.g. viscosity), to a pressure gradient applied to the porous media. Permeability is a property of the porous media only, not the fluid. In naturally occurred materials, it ranges over many orders of magnitude (Fetter,

2001). Permeability of petroleum reservoir rocks may range from 0.1 to 1,000 mD or more (Tiab and Donaldson, 2004). The quality of a reservoir as determined by permeability, in mD, may be judged as: poor if k<1, fair if 1<k<10, moderate if 10<k<50, good if 50<k<250 and very good if k>250. There is not a specifically defined relation between permeability and porosity values.

Recall Equation 2.3.7, Darcy's law; also note the sample is level in core holder, after rearrangement with respect to permeability k, there is:

$$k = \frac{q\mu L}{A\Delta p} \qquad 4.3$$

where μ is the fluid viscosity, Δp is the pressure drop across the sample, L is the length of the sample, q is the flow rate, and A is the cross section area.

Steady-state method was employed to measure permeability. For example, for sample 08IL96 (length 2.06 in (5.24 cm), radius 0.480 in (1.22 cm)) under a hydrostatic confining pressure of 300 psi, the outlet pump pressure was kept at 100 psi constant. The inlet pump pressure was increased from 100 psi to 170 psi stepwise, while the flow rate was recorded, from which one can get Figure 4.3. Alternatively, the flow rate can be increased stepwise, while the pressure difference between inlet and outlet pump to be recorded correspondingly.

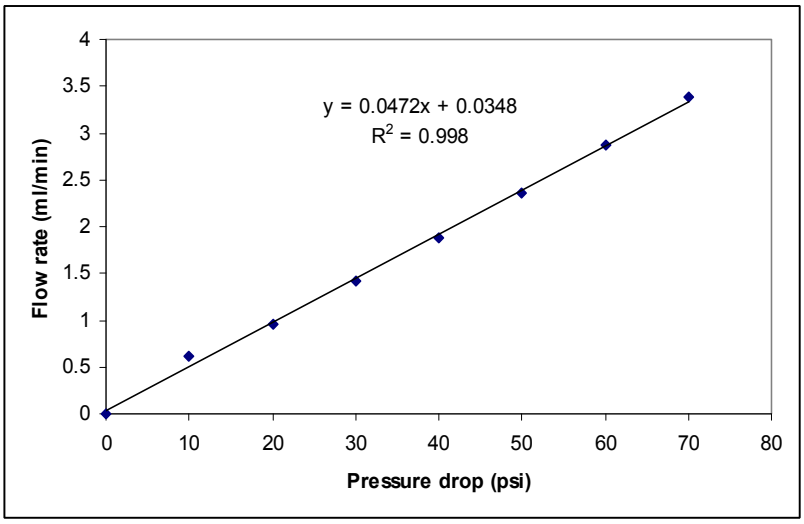

Figure 4.3. Relationship between flow rate and pressure drop
(Sample 08IL96, Length 52.42mm, Diameter 24.38mm)

Thus the permeability is calculated as:

$$k = \frac{q\mu L}{A\Delta p} = \frac{0.0472cm^3/60\sec \times 1.00\times10^{-3}Pa\cdot\sec\times 5.242cm}{\pi\times 1.219^2 cm^2\times 1psi\times 6894.7Pa/psi}$$

$$= 1.281\times10^{-10}cm^2\times\frac{1Darcy}{9.87\times10^{-9}cm^2} = 12.98mD$$

Similarly, the permeability can be obtained for other samples as well. Table 4.2 shows the test result.

Table 4.2. Permeability test results

Specimen ID	Pressure drop over flow rate (psi/(ml/min))	Intrinsic permeability (mD)
08IL07	19.710	12.286
08IL08	14.413	16.801
08IL09	29.221	8.287
08IL96	21.358	12.975
Average		12.587
Standard Deviation		3.488

The permeability of the specimen averages 12.59 mD with a relatively higher standard deviation, as this property is more site-dependent. In a reservoir condition,

repair of permeability damage can be difficult and expensive. The in-situ permeability variation can be big due to migration and deposition of fines (Tiab and Donaldson, 2004; Lyons et al., 2005). Thus, laboratory test results should be applied to the actual conditions with caution.

The feature of a flow (laminar or turbulent) depends on the flow rate and viscosity of the fluid. From the standpoint of hydrogeology, high flow rate and low flow rate have very different impacts on the petro-physical behavior of porous medium. Flow path may not be homogeneous. Sometimes a favorable flow path may form.

4.2.3. Relative Permeability Estimation of Supercritical CO_2 with respect to Water

Relative permeability is a concept used to relate the absolute permeability of a porous system to the effective permeability of a particular fluid in the system when that fluid only occupies a fraction of the total pore volume (Archer and Wall, 1986). Recall equation 2.3.8b, and rearrange it with respect to the relative permeability, there is:

$$k_{rco2} = \frac{k_{effective}}{k_{absolute}} = \frac{1}{\frac{q_{co2} \cdot \mu_{co2} \cdot L}{A \cdot \Delta p_{co2}}} \cdot \frac{q_{r-co2} \cdot \mu_{co2} \cdot L}{A \cdot \Delta p_{co2}} = \frac{q_{r-co2}}{q_{co2}} \qquad 4.4$$

where q_{co2} is the flow rate at 100% saturation of CO_2, and q_{r-co2} is the flow rate at a certain level of saturation. I.e., the relative permeability CO_2 with respect to water can be estimated by comparing the flow rate of CO_2 at a certain water saturation level to that at the complete dry condition.

In this test, one pump was used to unify the axial and radial pressure to ensure the sample in a hydrostatic state, 2,000 psi; two other pumps were all full of CO_2 and their pressures were 1,230 psi and 1,200 psi, as an upstream pump and a downstream pump

respectively. At the same time, the oven temperature was kept at 150 °F. These conditions would ensure CO_2 in its supercritical state.

First, the sample was completely dried in oven and vacuumed in order to obtain a full saturation of CO_2; consequently, the flow rate at such a condition defined the absolute permeability. As CO_2 was in its supercritical state, the flow rates of upstream and downstream pumps were almost the same due to the negligible compressibility of CO_2. Then, the sample was taken out and saturated with water, and put back to the core holder for CO_2 flooding. The immediate CO_2 flow rate indicated a permeability right after the CO_2 breakthrough, and the saturation level of water was assumed to be high at such point. After several hours, the sample was taken out, its water saturation level was measured and the CO_2 flow rate immediately before removal was assumed to correspond to such a water saturation level. Then, the sample was put back into the core holder again, after 24 hours, the sample was taken out again, its water saturation level was measured and the CO_2 flow rate immediately before removal was assumed to correspond to such a saturation level, and so on.

The water saturation level and the corresponding relative permeability together defined the CO_2 flow behavior, as shown in Figure 4.4. The dash line indicates a condition not acquired by test, but by extrapolation.

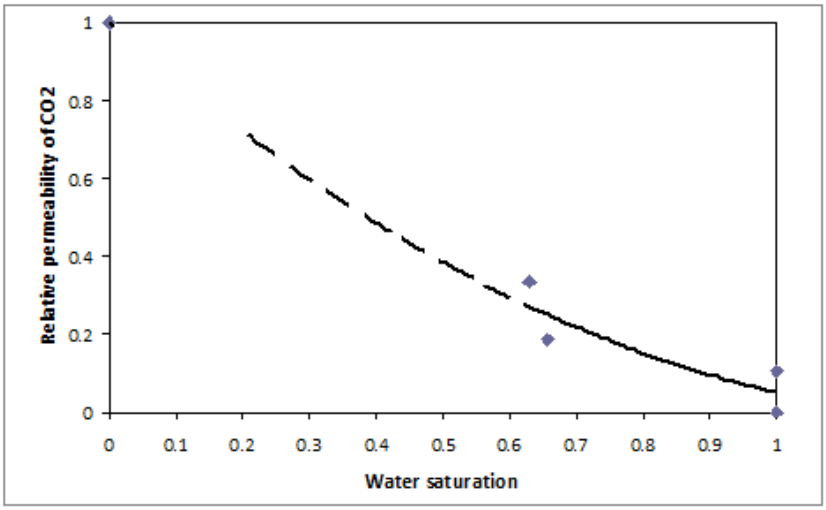

Figure 4.4. Relative permeability of CO_2 with respect to water (150 °F (65.6 °C), 1,200 psi (8.27 MPa))

It was found that CO_2 breakthrough was instant after the upstream and downstream pumps' pressures were differentiated; however, the water saturation level seems to persist at a certain level even after a long time of CO_2 flooding. It is possible that CO_2 may never be able to replace all the water in the rock under such a temperature and pressure condition. The reasonable explanations include that some pore throats are so small that capillary pressure may prevent CO_2's intake, and some pores were bypassed by CO_2 flow (Figure 4.5).

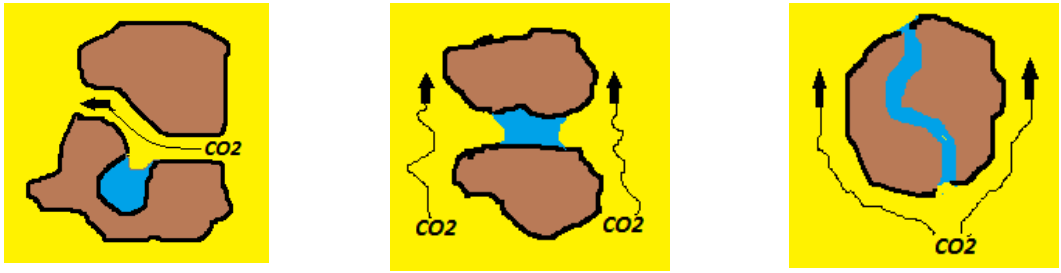

(a) water trapped in dead pores

(b)water bypassed due to minor pressure gradient

(c) capillary effect due to small opening of pores

Figure 4.5. Possible mechanisms for trapped water that cannot be displaced

To verify this mechanism, a test was conducted on a rock sample (Sample 08IL130) that was initially saturated with water (saturated weight 59.5g). After 510 hours

of dry CO_2 flooding (150 °F, 1,200 psi), when the sample was taken out, it was not completely dry (the weight was 56.8 g versus dry weight 55.4 g). It seems the residual water trapped in the pores was immovable. The retention S_r against CO_2 can be calculated as:

$$S_r = n - S_y = \frac{(59.5g - 55.4g)/1g/cm^3}{\pi \times 5.15cm \times (2.48cm)^2/4} - \frac{(59.5g - 56.8g)/1g/cm^3}{\pi \times 5.15cm \times (2.48cm)^2/4} \quad 4.5$$
$$= (16.4 - 10.8)\% = 5.6\%$$

where n is porosity and S_y is the yield due to CO_2 flooding. Therefore, it is reasonable to assume that a residual saturation of water does exist, and is temperature and pressure dependent. This is similar to that in the petroleum reservoirs where residual water is always kept in the pores (Chakma et al., 1991).

4.3. Basic Mechanical Properties of Indiana Limestone before CO_2 Flooding

4.3.1. Young's Modulus, Poisson's Ratio, Shear Modulus and Bulk Modulus

As Indiana limestone's Young's modulus is close to aluminum, an aluminum standard is used to calibrate the results after the triaxial strength tests. The tests' results by calibration using this in-house developed facility were in good agreement with those conducted on a MTS 816 Rock Test System (Liu, H., personal communication, Oct 6, 2010, Grand Forks, ND).

After triaxial test, a plot of axial stress vs. axial and radial strains can be developed (Figure 4.6), from which Young's modulus, Poisson's ratio, and ultimate compressive strength can be obtained. Based on the test of dry rock, Indiana limestone's Poisson's ratio is 0.26 and Young's modulus is 3.96×10^6 psi (27.3 GPa).

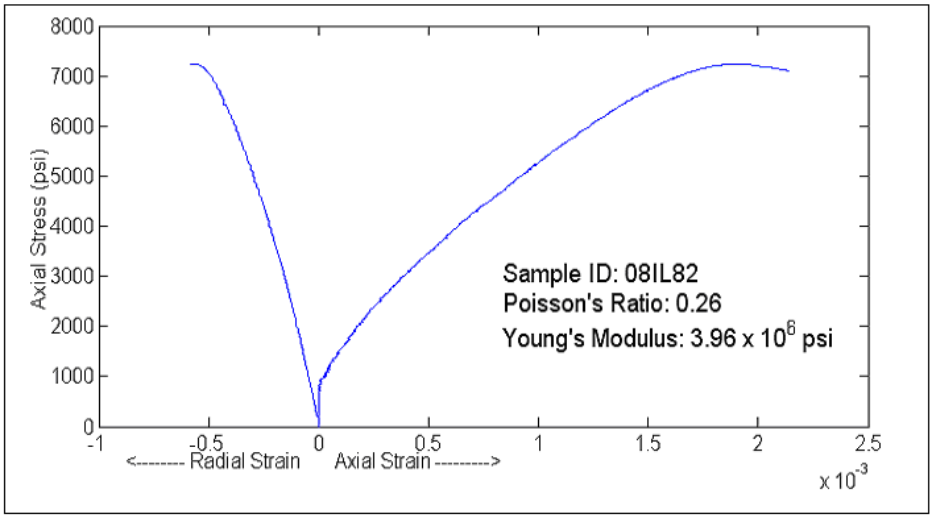

Figure 4.6. Axial and radial strains as functions of axial stress

Table 4.3 shows the triaxial test results for dry rocks. Mohr's circles and failure envelop in the τ-σ plane based on the data from this table are shown in Figure 4.7.

Table 4.3. Triaxial tests of dry Indiana limestone at room temperature

Specimen ID	Confining Pressure		Ultimate Compressive Strength	
	(psi)	(MPa)	(psi)	(MPa)
08IL66	0	0	4338	29.91
08IL33	500	3.45	7275	50.16
08IL46	1000	6.89	9080	62.60
08IL54	1500	10.34	11183	77.10
08IL02	2000	13.79	14522	100.13

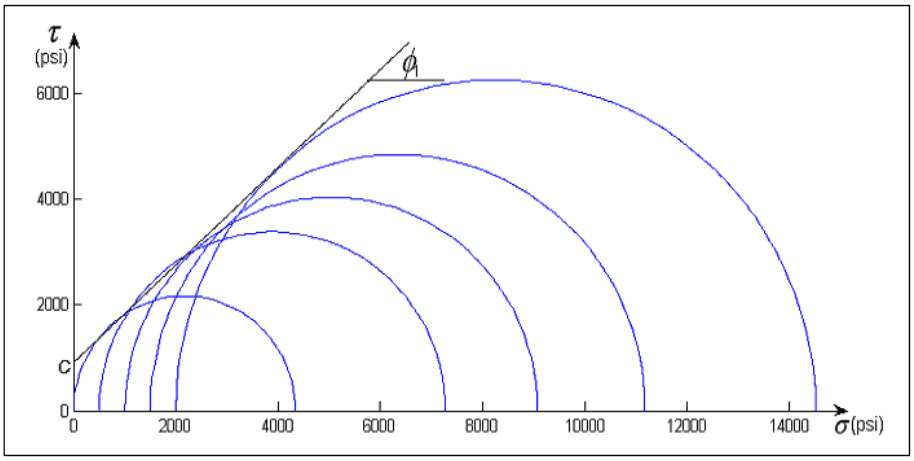

Figure 4.7. Mohr-Coulomb envelope of Indiana limestone (dry rock at room temperature)

From Figure 4.7, the Mohr-Coulomb failure criterion can be expressed as:

$$\tau = \sigma \tan(\phi) + C_0 = \sigma \tan(42^\circ) + 960\,psi \qquad 4.6$$

where C_0 is cohesion and ϕ is friction angle. This sets up a baseline for further evaluation.

After yielding, Indiana limestone shows strain-softening behavior at low confining pressures, and minor strain-hardening behavior at high confining pressures. Besides, the correlated failure behaviors evolve from brittle fractures (shear band) to plastic flow, as shown in the following Figure 4.8.

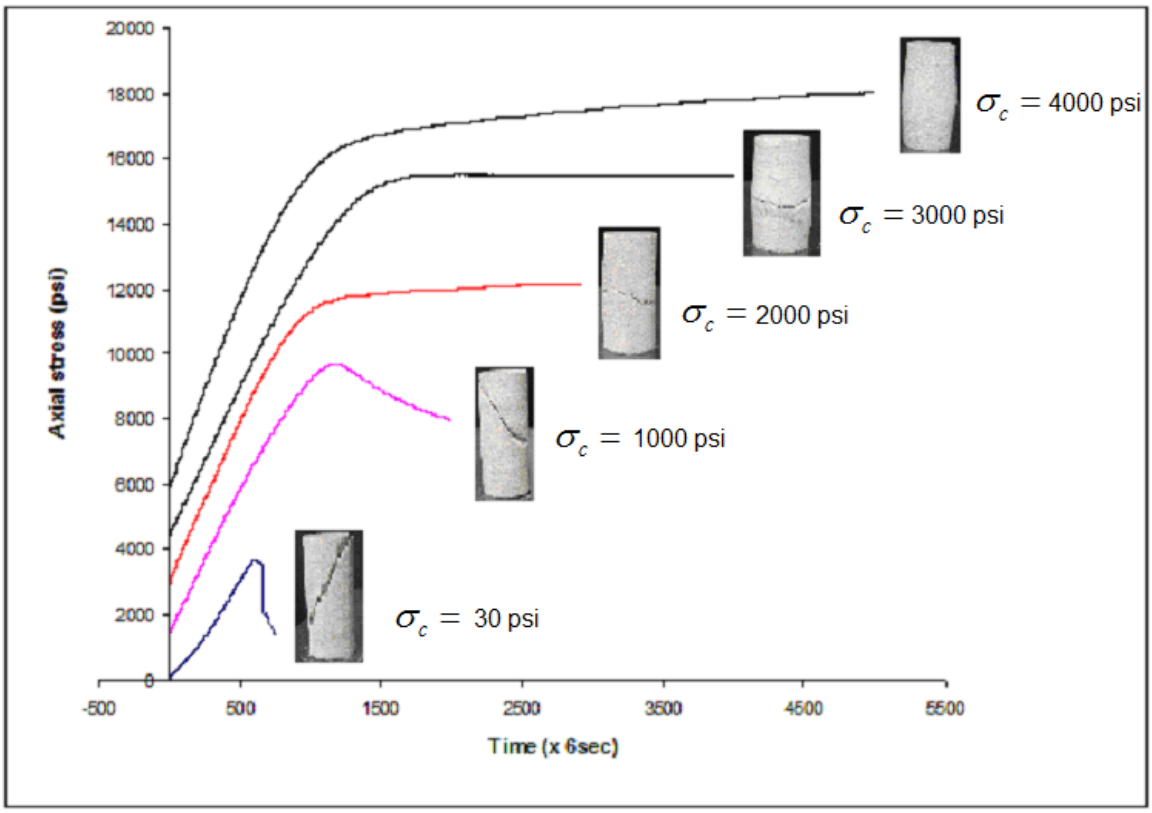

Figure 4.8. Indiana limestone shows different post yielding behaviors with different failure features at different confining pressures

Shear modulus and bulk modulus were measured using a NER Autolab 1500 system, which were about 1.9×10^6 psi (13GPa) and 3.0×10^6 psi (21GPa), respectively.

These values indicate that Indiana limestone could be approximated by an isotropic model.

4.3.2. Tensile Strength

Tensile strength of rock is one of the most important parameters influencing stability. Brazilian test is one of the commonly-used indirect methods for determining the tensile strength of rock (Claesson and Bohloli, 2002). Tensile strength is calculated in this test by using an equation, which assumes isotropic material properties. As Indiana limestone is very close to an isotropic material, this method is used to find its tensile strength.

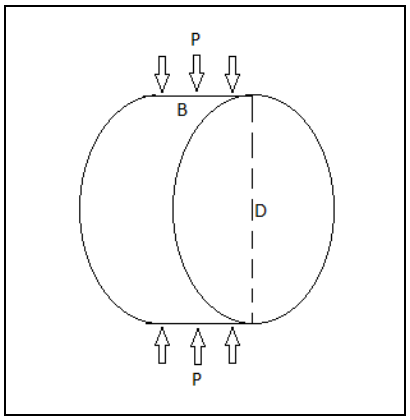

Figure 4.9. Brazilian test for tensile strength

In the Brazilian test, a disc of material is subjected to two opposing normal strip loads at the disc periphery. The applied load is P. The thin disc has a diameter D and thickness B. The tensile strength is given by (ISRM, 1978):

$$T_0 = \frac{2P}{\pi DB} \qquad 4.7$$

After a test, a typical failure behavior of rock sample and the curve of loading force versus piston displacement are shown in Figure 4.10:

Sample T10LA2
D:50.32mm;B:16.82mm

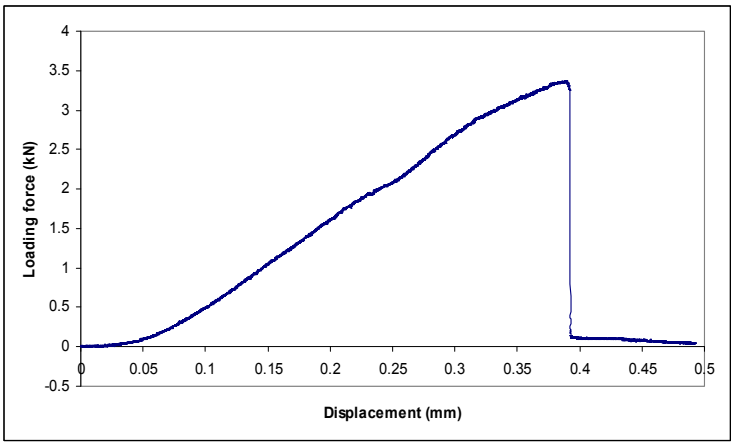

Figure 4.10. Brazilian test result of an Indiana limestone specimen
(sample T10LA2, displacement speed: 3mm/min)

The results of Brazilian tests conducted using MTS 816 Rock Test System are shown in Table 4.4.

Table 4.4. Tensile strength of dry Indiana limestone at room temperature

Specimen ID	P	D	B	T_0	
	N	mm	mm	(MPa)	(psi)
T10L02	1527	24.83	13.30	2.94	427
T10LA1	2612	50.30	15.64	2.11	306
T10LA2	3373	50.32	16.82	2.54	368
T10LA3	3022	50.46	16.81	2.27	329
T10LA4	3117	50.28	16.82	2.35	340
T10LA5	3708	50.26	15.78	2.98	432
T10LA6	1645	24.82	12.77	3.30	479
T11LB5	8266	50.33	40.58	2.58	374
T11LB6	5002	50.22	24.72	2.57	372
T11LB7	6496	50.29	32.62	2.52	366
T11LB9	6604	50.41	32.93	2.53	367
Average				2.61	378
Standard Deviation				0.34	50

From Table 4.4, the average uniaxial tensile strength of Indiana limestone is 378 psi (2.61 MPa) with a standard deviation of 50 psi (0.34 MPa).

4.3.3. Skempton's Coefficient and Biot's Coefficient

Skempton's coefficient *B* is defined as the ratio of the induced pore pressure to the change in applied stress for undrained condition (Skempton, 1954), and Biot's

coefficient b is the ratio between confining pressure and pore pressure upon constant strain.

$$0 = \Delta\zeta = -\frac{b\Delta\sigma}{K} + S_\sigma \Delta p \Rightarrow B = \frac{b}{KS_\sigma} = \left.\frac{\delta p}{\delta\sigma}\right|_{\Delta\zeta=0} \quad \text{4.8a}$$

$$0 = \Delta\varepsilon = \frac{\Delta\sigma}{K} - \frac{b\Delta p}{K} \Rightarrow b = \left.\frac{\delta\sigma}{\delta p}\right|_{\Delta\varepsilon=0} \quad \text{4.8b}$$

where $\Delta\zeta$ is pore fluid increment, K is drained bulk modulus, S_σ is specific storage coefficient, p is pore pressure and σ is confining stress.

One can see that there is an intrinsic correlation between Biot's coefficient b and Skempton's coefficient B. Biot coefficient can also be estimated by $b = 1 - K / K_s$ (Eqn. 3.10), where K_s is solid skeleton's bulk modulus of rock. $b \leq 1$ as $K \leq K_s$. It was suggested that b may not be constant if K/K_s is not constant. Poor agreement was found between experimental and theoretical b values (Chen et al, 1995). There may be a trend of decreasing b with decreasing permeability and porosity of carbonate rocks (chalks and limestone).

The test result for Skempton's coefficient is shown in Table 4.5 and Figure 4.11. Note the sample is relatively large and a new facility was developed for this test. The method is to change the confining pressure of the sample stepwise, while recording its pore pressure.

Table 4.5 Skempton's coefficient of Indiana limestone

Confining pressure (psi)	Pore pressure (psi)	Section slope
600	282	0.675
1000	552	0.672
1500	888	0.660
2000	1218	0.578
2500	1507	0.502
3000	1758	0.470
3500	1993	0.466
4000	2226	0.278
3500	2087	0.384
3000	1895	0.482
2500	1654	0.544
2000	1382	0.678
1500	1043	0.728
1000	679	0.808
600	356	
Average		0.566
Standard deviation		0.146

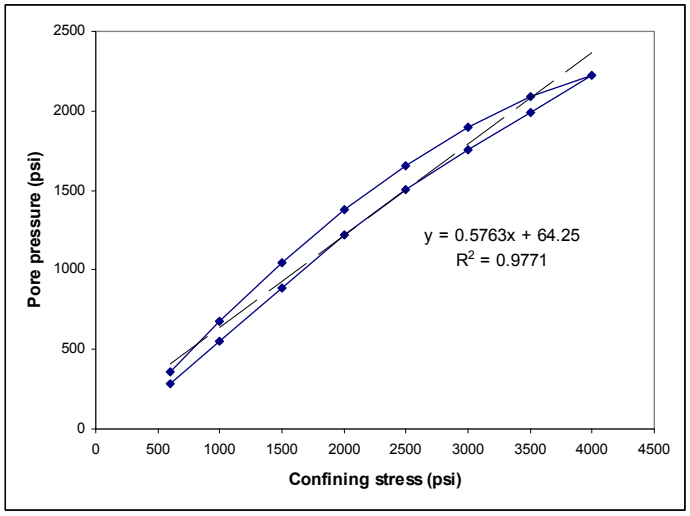

Figure 4.11. Induced pore pressure by changing confining pressure
(Sample 09ILB2, Length 105.35mm, Diameter 50.42mm)

From Figure 4.11, one can see that Skempton's coefficient is close to a constant (0.58) but not strictly, and it has a trend of decreasing with increasing confining pressure.

This agrees with the intuition that with the increased overburden, the rock matrix will be compressed and thus become stiffer, sharing more overburden pressure.

Table 4.6 and Figure 4.12 show the test result of Biot's coefficient for Indiana limestone using NER Autolab 1500. The method is to adjust confining pressure and pore pressure at different stages to keep a constant strain by closely monitoring the strain change.

Table 4.6 Biot's coefficient of Indiana limestone

Confining pressure		Pore pressure	
MPa	psi	MPa	psi
50.1	7266	20.4	2958
50.1	7266	20.5	2973
45.1	6541	13.9	2016
45.0	6527	13.8	2001
40.2	5830	7.6	1102
40.2	5830	7.5	1088
35.1	5090	1.1	160

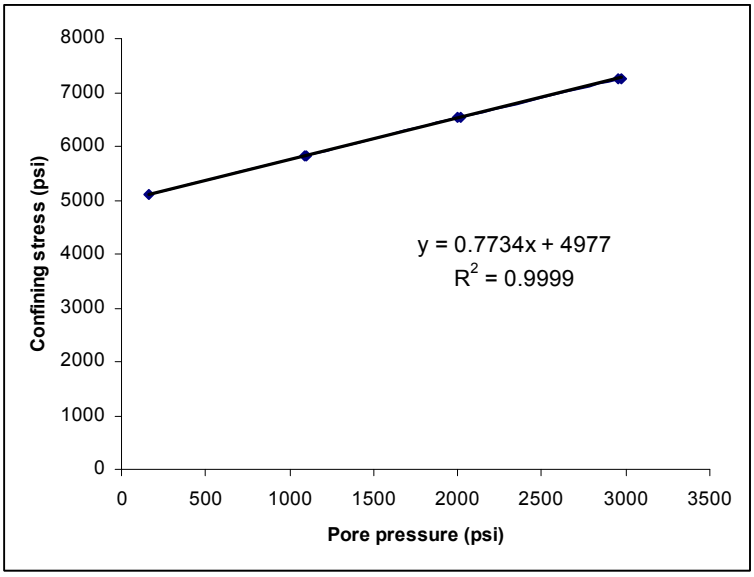

Figure 4.12. The correlation between pore pressure and confining pressure upon constant strain (Sample 01262011BI2)

From the above figure, one can read that Biot's coefficient *b* for Indiana limestone is about 0.77.

4.4. Geochemical Tests: CO_2 Flooding through Rock Cores

The major interest in this series of tests is to study the chemical reaction between the rock and the injected fluid (CO_2 and/or water) during different flooding schemes, including pure and brine water, pure CO_2, and water-alternating-gas (WAG) injection. The purpose of these geochemical tests is to detect the sensitivity or chemical stability of the carbonaceous rock to different flooding schemes. CO_2 was kept in its supercritical status at all these tests. After CO_2 flooding, rock's mechanical properties will be changed (most likely deteriorated); and how to detect these changes will be presented in the oncoming section.

In these tests, similar cylindrical Indiana limestone specimens were used. All specimens have been cleaned in water to remove dust. All specimens have no obvious transfiguration after being dried in the oven or immersed in the water. The limestone specimens show relatively stable chemical property, which means that its total dissolved solids are relatively minor after a lengthy flooding.

4.4.1 De-ionized Water Flooding

The first type of test is by injecting only de-ionized (DI) water. Initially, the total dissolved solid (TDS) increased abruptly; however, this trend was transient and didn't show a continued increase over time. The pH value was consistent. This indicates that the chemical reaction was not active in this case. The initial increase of TDS is probably due to the loose fines that were flushed by water.

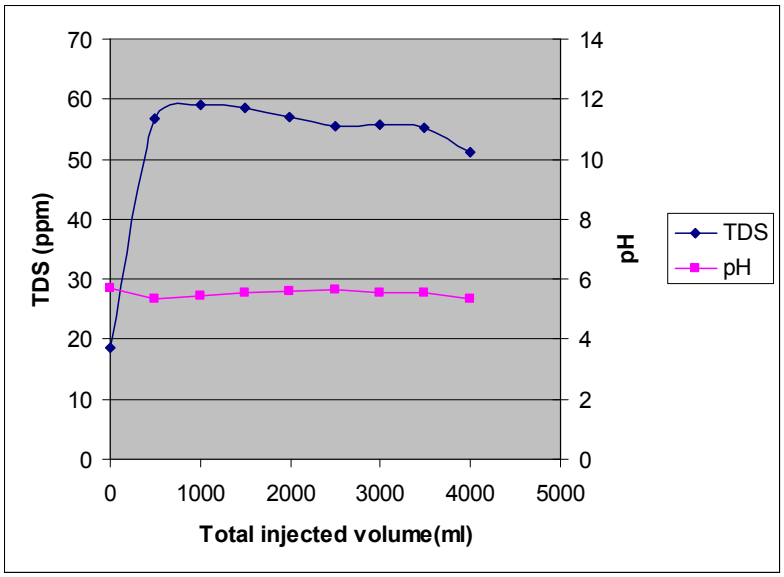

Figure 4.13. Flooding with DI water only (Sample 08IL17)

4.4.2 Pure Supercritical CO_2 Flooding

This test is by injecting only supercritical CO_2. Both the TDS and the pH value were consistent. This indicates that the chemical reaction was not active in this case. Unlike the case of DI water, there was not an obvious initial increase of TDS, which may indicate that due to the low viscosity, the shear stress offered by CO_2 was too small to carry those loose fines that were flushed by water. The readings were fluctuated or even missed for some time, and this was caused by the strong bubbling of CO_2 after passing through back pressure regulator.

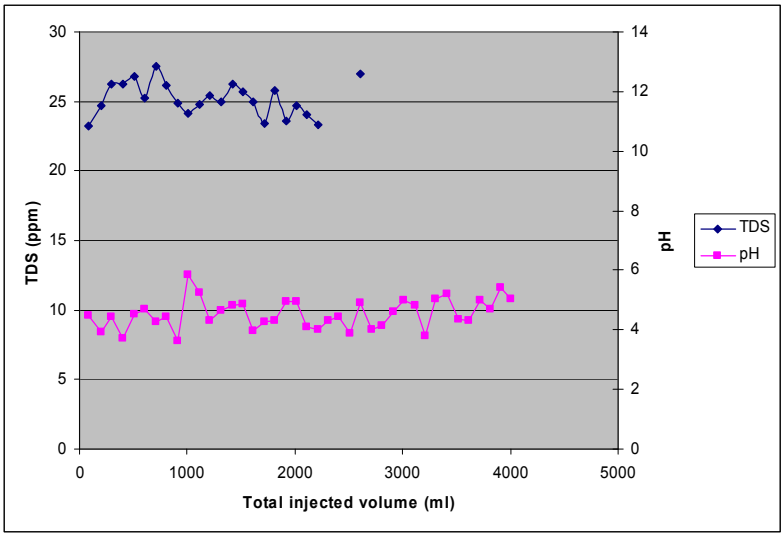

Figure 4.14. Flooding with supercritical CO_2 only (Sample 08IL23)
(Note: due to the strong turbulence caused by CO_2 bubbling, some TDS readings were missing)

4.4.3. Water-Alternating-Gas (CO_2) (WAG) Flooding

WAG flooding showed different features by comparing with the previous two types of tests. It is obvious that the TDS increased linearly with the injected volume by flooding the sequence of DI water and CO_2, and the test results seemed not to be sensitive to the mixture scheme (the ratio between water and CO_2) (Figures 4.15, 4.16, 4.17). Besides, the residential time adjusted by the flow rate could influence the total dissolved solids to some degree. At last, in all these tests, pH was not as sensitive as TDS was. In fact, all the reactions occurred in a weak acidic regime.

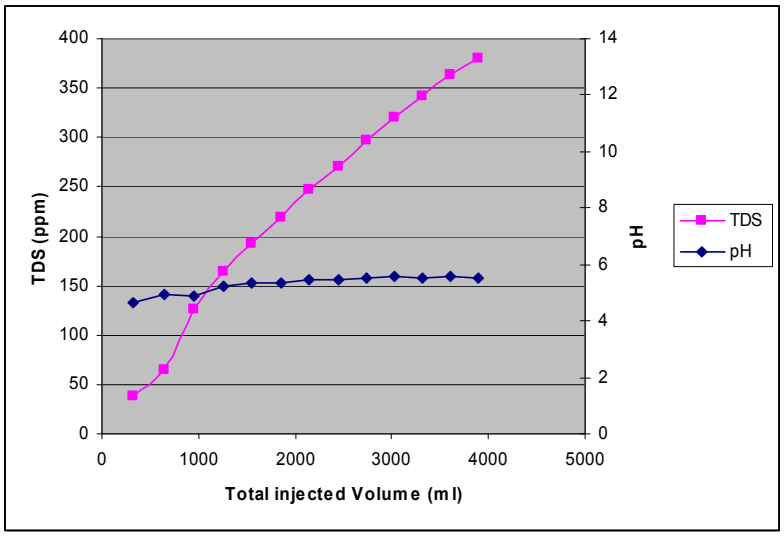

Figure 4.15. DI water alternating CO_2 flooding (V_{CO2}:V_{H2O}=2:1) (Sample 08IL38)

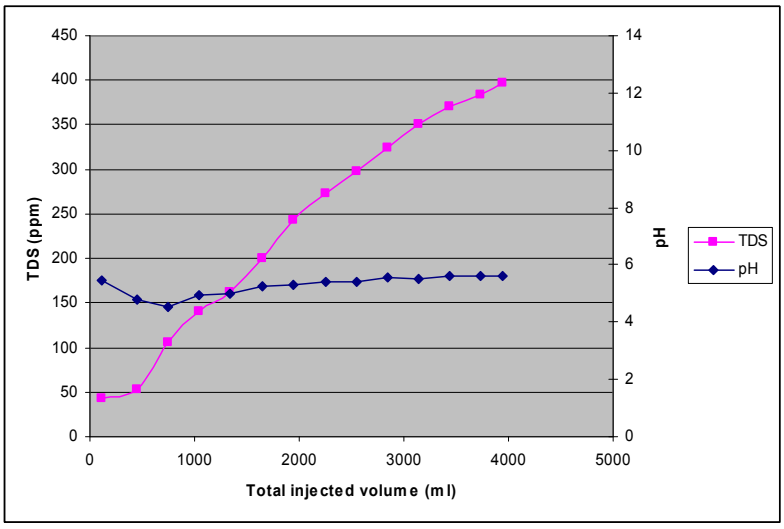

Figure 4.16. DI water alternating CO_2 flooding (V_{CO2}:V_{H2O}=1:2) (Sample 08IL22)

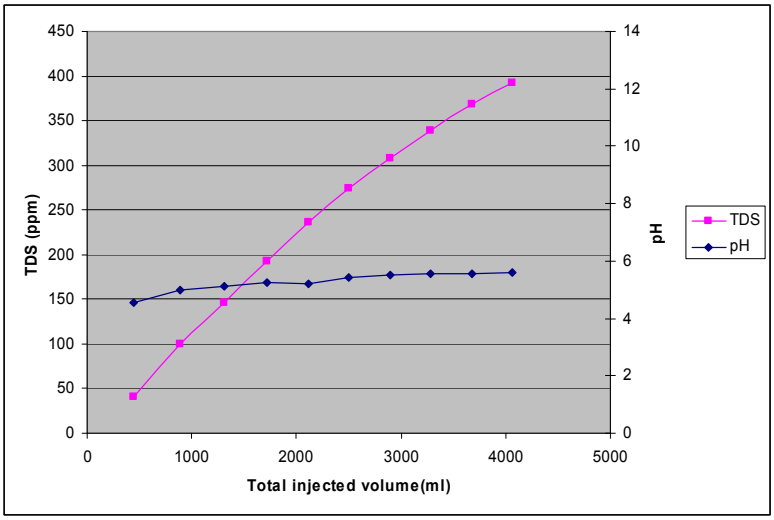

Figure 4.17. DI water alternating CO_2 flooding (V_{CO2}:V_{H2O}=1:1) (Sample 08IL26)

Figure 4.18 compares the flooded with un-flooded specimen. Scale bars are in centimeters. From this figure, one can see that there are slightly damaged portions for the specimens after flooding. The most obvious damages occurred in the center as holes, as well as on the edges. As the rock samples are generally short, migration of fines can be observed in most of the tests, while deposition phenomenon can hardly be justified.

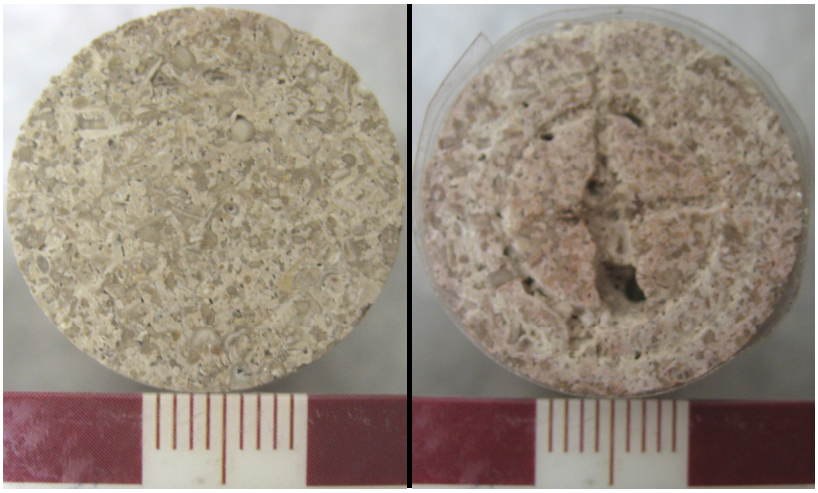

Figure 4.18. Specimen before and after CO_2 flooding

4.4.4. Sensitivity Analysis on Flow Rate

The second group of tests is a sensitivity analysis on flow rate. These tests were conducted at temperature of 136 °F and flow rate in the range of 0.1 to 1.0 ml/min, and in all the tests, CO_2 was ensured in its supercritical condition. The total flooded volume of each case and the ratio (1:1) between CO_2 and water were all kept the same, the difference was only the flow rate.

Initially, TDS followed the same trend, but after several (3-4) cycles, the data diverged, and the highest TDS occurred in the lowest flow rate; and the lowest TDS occurred in the highest flow rate (Figure 4.19). In all these tests, pH was not as sensitive as TDS was. Further, all the tests were in a weak acidic regime, similar to the previous tests.

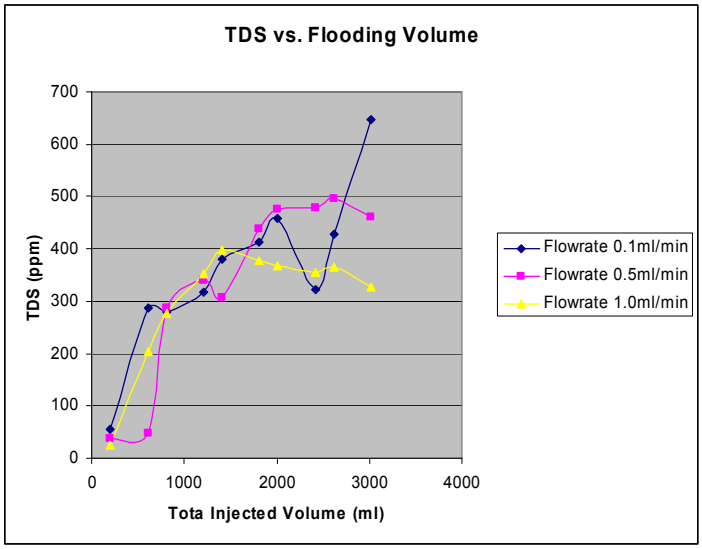

Figure 4.19. A comparison for TDS under different flow rates

For all these tests, the absolute TDS at the end of flooding was acquired by drying the overflow collection beakers in oven. One can see that even under the similar total flooding volumes, the total dissolved solids can be quite different due to the different

flow rate. For a lower flow rate, the TDS was higher, which was probably caused by the much longer residential time, as shown in Table 4.7. Here, Residential Time = Total Flooding Volume/Flow Rate.

Table 4.7. TDS results for specimens under different flow rates

Specimen ID	Flow Rate (ml/min)	Residential Time (hour)	Total Flooding Volume (ml)	TDS (g)
08IL47	1.0	50	3022	1.3853
08IL61	0.5	100	3010	1.4189
08IL74	0.1	500	3005	2.0025

4.5. Geomechanical Properties of Rock after CO_2 Flooding

The effect of chemical reactions between calcareous material, formation fluid and flooding fluid (supercritical CO_2) on rock properties can be significant. Chemical reactions may dissolve rock cementation, collapse rock skeleton, and thus the pore structures may be changed and rock quality may be deteriorated.

4.5.1. Rock Strength Deterioration due to CO_2 Flooding

Table 4.8 shows the triaxial test results for a rock sample after flooding CO_2 and water of total volume of 6,000 ml (V_{H2O}: V_{CO2}=2:1) at 0.5 ml/min flow rate. The Mohr circles in the τ-σ plane based on the data from this table are shown in Figure 4.20. A continuous failure state triaxial test was conducted to define the Mohr-Coulomb failure envelope.

Table 4.8. Triaxial strength tests of Indiana limestone after flooding with CO_2 and water at 136 ºF

Specimen ID	Confining Pressure	Ultimate Compressive Strength
	(psi)	(psi)
08IL49	500	4650
08IL49	1000	6206
08IL49	1500	7435
08IL49	2000	8437
08IL49	2500	9490

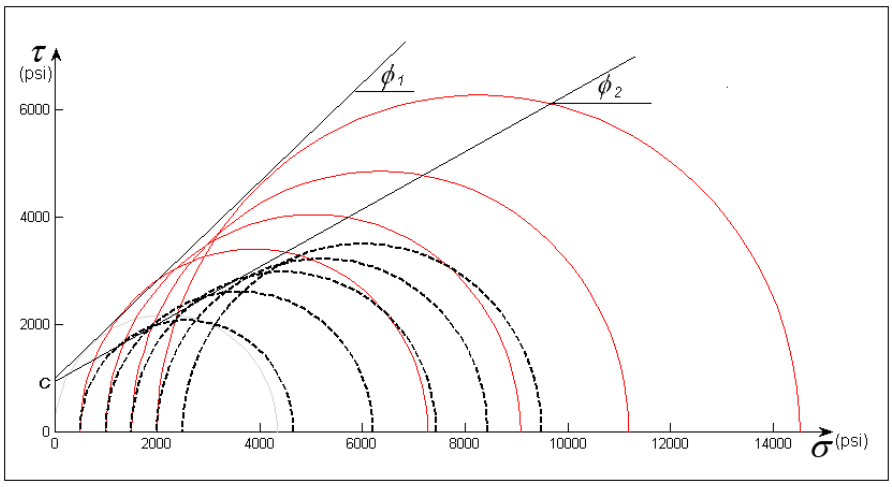

Figure 4.20. Mohr-Coulomb envelope of drained Indiana limestone after flooding 6,000 ml fluid at 136 ºF

From Figure 4.20, the friction angle is obtained as $\phi_2 = 26°$, where ϕ_1 represents the intact rock. One can see that after flooding of supercritical CO_2, rock strength was decreased significantly. The friction angle decreased from ϕ_1 (42°, without flooding) (Figure 4.7) to ϕ_2 (26°, after flooding).

Many factors come into play during the procedure of water alternated gas (CO_2) flooding, such as the fluid volume, flow rate, salinity of solution, temperature, etc. Depending on the distance from the injection well, the flow rate can be high or low. The salinity of different formations can also be different. Table 4.9 shows the differences in terms of Young's modulus and Poisson's ratio for eight specimens under different scenarios. Here, the Poisson's ratios were tested under a confining pressure of 500 psi for all the samples. In the case of flooding, the volume ratio between water solution and CO_2 was all kept at 2:1. Temperature was kept at 136 ºF for all the tests. For saline water simulation, NaCl was used as the solute.

Figure 4.21 are the strength test results corresponding to the samples in Table 4.9.

Table 4.9. Results of drained triaxial tests for rock samples after different flooding scenarios

Specimen ID	Flooding Volume and Flow Rate	Poisson's Ratio	Young's Modulus ($x10^6$ psi)
08IL82	No flooding	0.26	3.96
08IL114	3000 ml WAG* 100,000 ppm (0.5 ml/min)	0.27	4.21
08IL106	3000 ml WAG* 10,000 ppm (0.5 ml/min)	0.13	2.38
08IL53	3000 ml WAG** (0.75 ml/min)	0.16	1.51
08IL61	3000 ml WAG** (0.01 ml/min)	0.12	2.18
08IL74	3000 ml WAG** (0.1 ml/m)	0.15	1.58
08IL47	3000 ml WAG** (1 ml/min)	0.05	2.25
08IL117	Weak acid *** Saturated 96 hours	0.18	1.18

- WAG: water alternated gas (CO_2); salinity of solution is in ppm.
- ** WAG: water alternated gas (CO_2); water is de-ionized.
- *** Weak acid: white vinegar, pH = 3.5

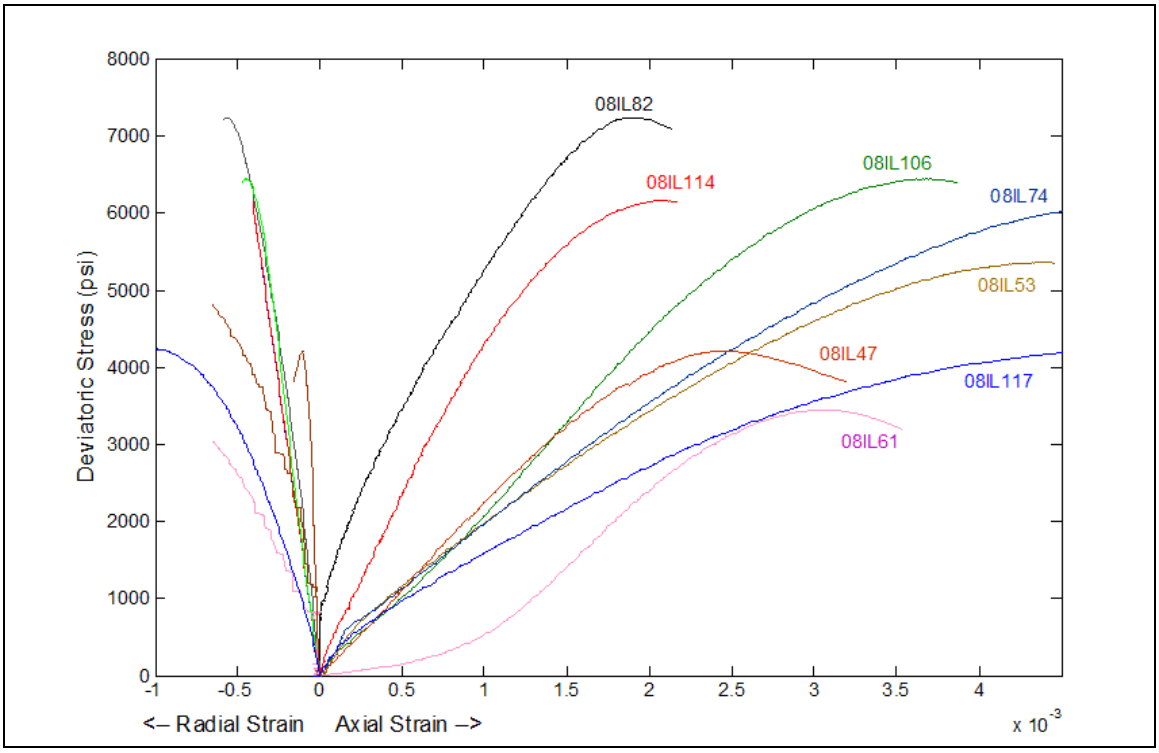

Figure 4.21. Triaxial test results for different samples

Overall, after flooding, Young's modulus and the ratios between lateral strain and axial strain of the rock samples all decreased. The levels of decrease are different, and may be related to the different flooding schemes. Basically, the condition of dry rock without flooding (Sample 08IL82) and that of the rock eroded in weak acid (Sample 08Il117) set up the upper and lower boundaries for all the rocks that were flooded.

However, one exception exists: the specimen that was flooded with the lowest flow rate (Sample 08IL61). The curve of sample 08IL61 may indicate an initial period of pore collapse. The reason may be that the pore fluid residential time in this sample was extremely long due to a very low flow rate (0.01ml/min) compared with others. Thus the porosity of this sample was increased significantly due to dissolution.

For Sample 08IL114, even its ultimate compressive strength is lower than that of 08IL82 (dry rock without flooding) as expected, its Young's modulus did not decrease as others. Note this sample has been flooded with the highest salinity solution of 100,000 ppm. In such a case, precipitation and deposition of fines may overrun the dissolution of fines, thus the porosity of this sample may not increase, rendering it more competent. Whether this competence can persist is questionable if the flooding volume is increased. Also note the porosity involved with salt is hard to measure by traditional water saturation method.

4.5.2. Long Term Storage Effect

The understanding of long term effects of CO_2 storage in carbonate reservoirs is challenged by many uncertainties, including geochemical effects of CO_2 on carbonates, the coupled chemical–mechanical effects, etc.(Gledhill and Morse, 2004). These effects

are time-dependent, thus extreme caution should be exercised in using lab results which are generally acquired within a relatively short period.

Here is the methodology: first to plot the failure envelope of dry rock in principal stress space, which can be treated as a baseline, and then plot the failure envelope of water saturated rock, pure supercritical CO_2 saturated rock, and water-CO_2 mixture saturated rock, etc. In case of the mixture of two phase fluids, initially the rock was saturated with water and then a minor flooding of CO_2 was conducted. Thereafter, the pore pressure was controlled by the pump full of CO_2, in such a condition, a mixture of CO_2 and water was expected in the core sample. Test results are shown in Table 4.10 and Figure 4.22.

Table 4.10. Results of triaxial tests on rock samples with or without pore fluids

Sample ID	Minimum principal stress (psi) $\sigma_2 = \sigma_3$	Maximum principal stress (psi) σ_1	Pore pressure (psi) p	Pore fluid	Temperature (°F)
Tension	-378		0	N/A	Room temp.
08IL66	0	4338	0	N/A	Room temp.
08IL33	500	7275	0	N/A	Room temp.
08IL46	1000	9080	0	N/A	Room temp.
08IL54	1500	11183	0	N/A	Room temp.
08IL02	2000	14522	0	N/A	Room temp.
10IL05	30	3778	0	N/A	150
10IL51	1000	9288	0	N/A	150
10IL48	2000	12364	0	N/A	150
10IL53	3000	15123	0	N/A	150
10IL67	4000	16656	0	N/A	150
10IL64	2000	10213	1200	water	150
10IL68	3000	12107	1200	water	150
10IL59	4000	15045	1200	water	150
10IL65	2000	10770	1200	CO_2	150
10IL58	3000	13650	1200	CO_2	150
10IL59	4000	16198	1200	CO_2	150
10IL46	2000	8917	1200	water and CO_2	150
10IL63	3000	12144	1200	water and CO_2	150
10IL69	4000	14763	1200	water and CO_2	150

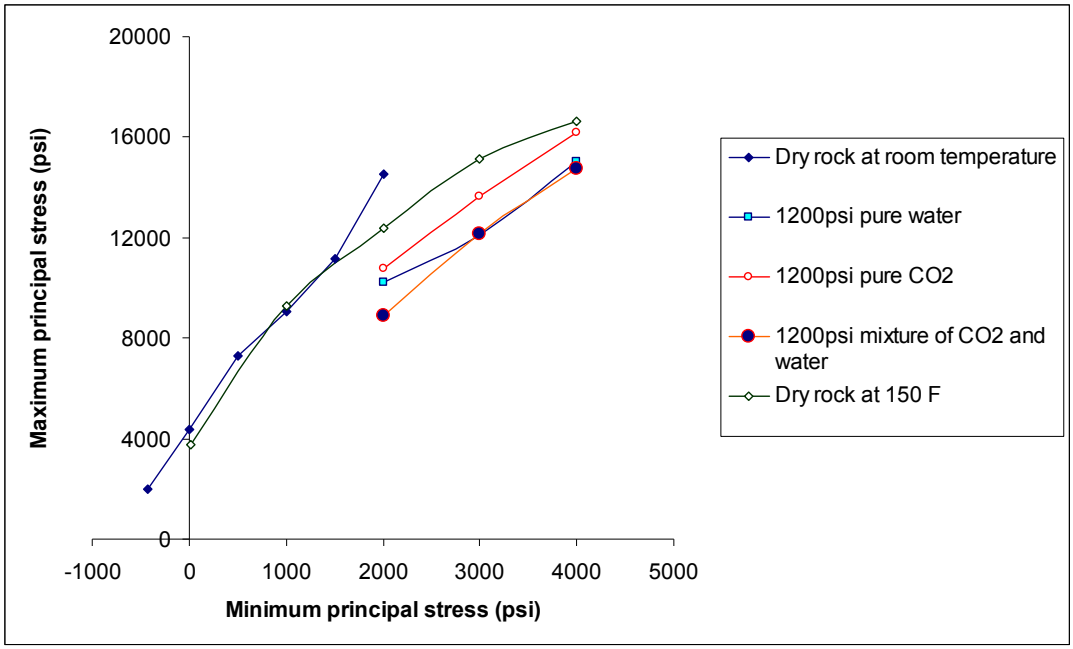

Figure 4.22. Location of the various failure envelopes in principal stress space

Overall, the data from the tests on dry rock define the highest strength envelope. Compare the situations between CO_2 saturated rock and water saturated rock or water and CO_2 mixture saturated rock, one can see that the CO_2 saturated condition tends to be higher, as justified by the fact that all the corresponding ultimate compressive strengths are greater in the cases of CO_2 saturated rock samples. From the standpoint of geo-mechanics, this is hard to explain as all the pore pressures were kept the same. The reason may be that as the wettability and /or compressibility of CO_2 and water are different, the micro-crack developing mechanisms probably are different regarding the tests on these different groups.

4.5.3. Stress-dependent Permeability and its Implication to CO_2 Sequestration

Permeability controls the rate of fluid flow in porous media. Even though it represents an original geometric property of the porous system, it changes with the

variation of stress (Bai et al., 1997). These variations will influence the flow pattern, and consequently, further change on the pore pressure buildup pattern can be expected.

This group of experiments was performed under the following conditions: the confining pressure was constant and the pore pressure on the upstream pump was 10 to 30 psi higher than the down stream pump. In the case of triaxial test, the downstream pump was shifted to apply axial pressure, and then the pore pressure on the lower end was directed to the atmosphere. Of course, the confining pressure was always much higher than the pore pressure to avoid leakage. The flow rate of upstream pump and pressure drop across sample were used to define permeability.

First, a series of tests on permeability reduction due to increase of hydrostatic pressure was conducted, and their results are shown in the following figure.

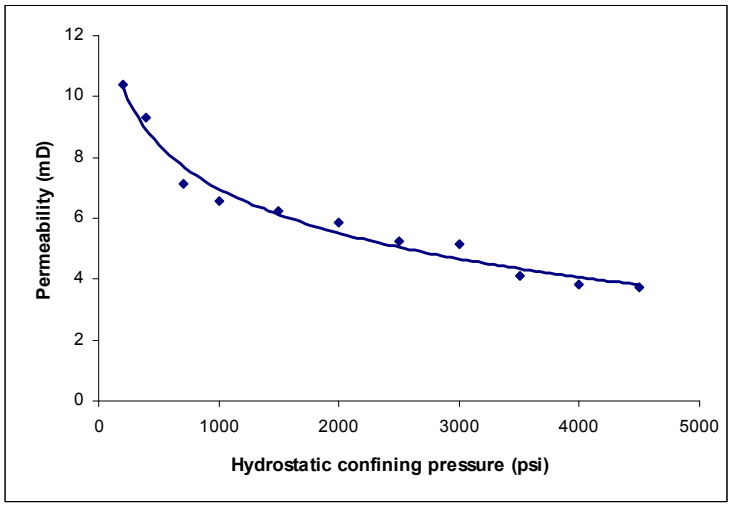

Figure 4.23. Permeability reduction due to confining pressure increase
(Sample 10IL29, Length 52.57mm, Diameter 24.80 mm)

The correlation between permeability and hydrostatic confining pressure can be approximated by the following formula:

$$k = 21.452 - 2.0963 \ln \sigma; \quad R^2 = 0.97 \qquad 4.9$$

where k is permeability in mD, σ is confining pressure in psi.

Permeabilities were also monitored while conducting triaxial tests on rock samples. The following figure shows that at low radial confining pressure (100 psi), permeability increased significantly after the shear failure stage. That is, the flow was transformed from a relatively stable flow through rock matrix to a flow mainly through shear fractures.

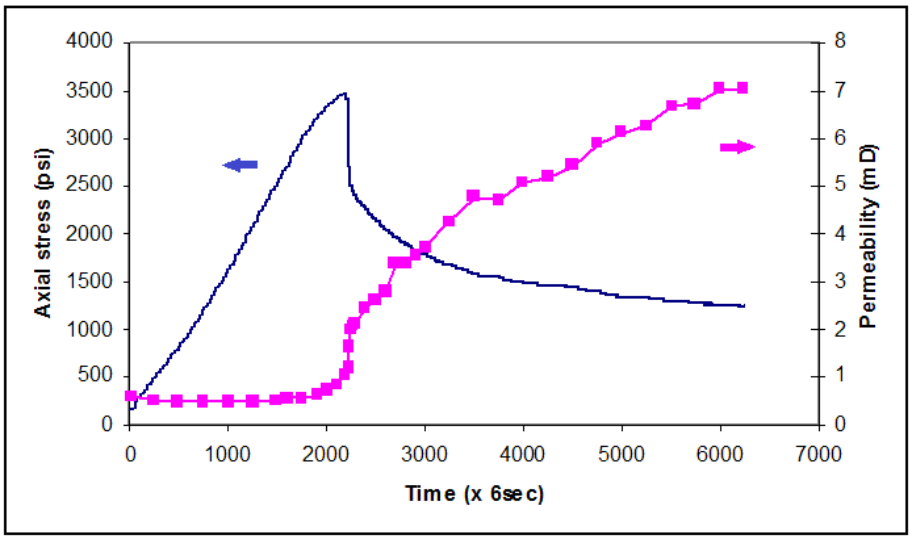

Figure 4.24. Permeability variation with respect to stress under triaxial compression (Sample 10IL08, Length 50.16 mm, Diameter 24.82 mm, Confining Pressure 100 psi)

The following figure basically shows a similar permeability enhancement as that of the previous example, but giving a more complicated variation, indicating that fluid permeability in a complete stress-strain process under triaxial compression is closely related to the evolution of the microstructure in the rock (Wang and Park, 2002).

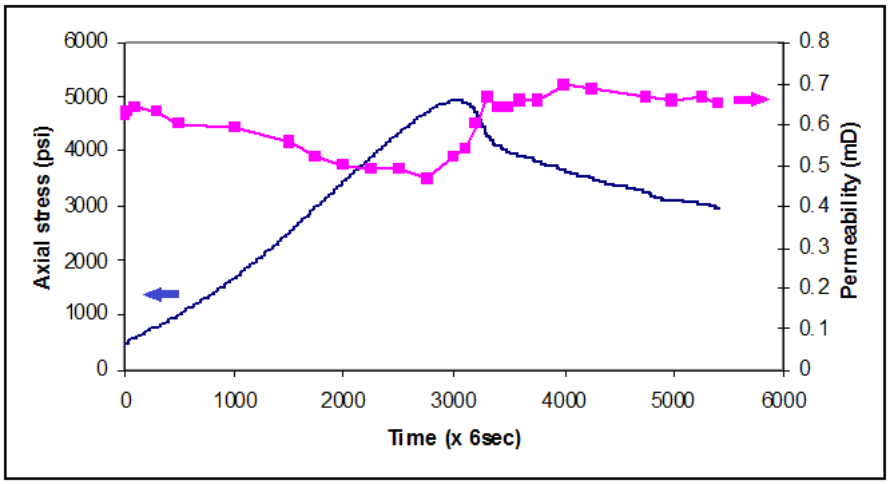

Figure 4.25. Permeability variation with respect to stress under triaxial compression (Sample 09Il06, Length 50.40 mm, Diameter 24.81 mm, Confining Pressure 300 psi)

From the above figure, one can see that in the initial compression stage, permeability decreased as some pores and micro cracks were closed due to compression. However, permeability started to increase at the yielding point, where dilation and coalescence of micro cracks enhanced the communication among flow channels. The largest permeability jump corresponded to the occurrence of brittle fracture. At the strain softening stage, permeability was kept at a relatively high level even with some sort of fluctuation. Different samples may have slightly different features, but the overall trends were the same, i.e., the permeability increased for a strain softening model. However, for either a strain hardening or an elastic-perfect-plastic model, permeability decreased in all cases, as shown in Figure 4.26.

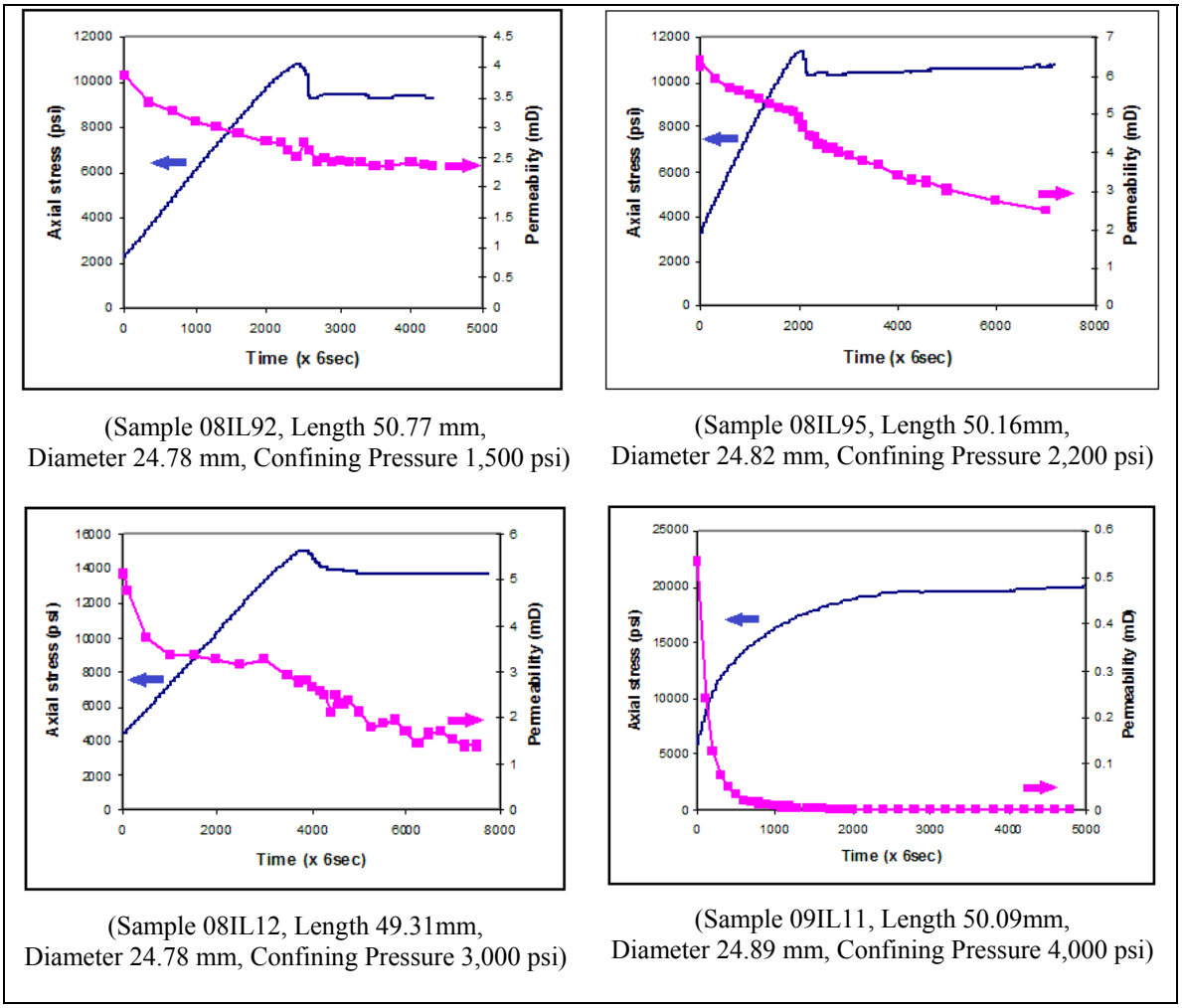

(Sample 08IL92, Length 50.77 mm, Diameter 24.78 mm, Confining Pressure 1,500 psi)

(Sample 08IL95, Length 50.16mm, Diameter 24.82 mm, Confining Pressure 2,200 psi)

(Sample 08IL12, Length 49.31mm, Diameter 24.78 mm, Confining Pressure 3,000 psi)

(Sample 09IL11, Length 50.09mm, Diameter 24.89 mm, Confining Pressure 4,000 psi)

Figure 4.26. Permeability variation with respect to stress under triaxial compression

Permeability variation in carbonates is a strong function of the relative contributions of compaction and micro cracking, in which pore collapse decreasing permeability and micro-cracking enhancing permeability (Yale and Crawford, 1998). Therefore, permeability may either decrease or increase after the collapse of rock matrix. It is more likely that post yielding behavior of permeability is governed by the minimum principal stress or confining pressure in these tests, i.e., whether the fractures formed after yielding are available for flow is dependent on the in-situ stress. These fractures may be open to allow an even faster flow in the case of low confining pressure, or they

may be closed due to high confining pressure, and permeability could potentially be reduced by unavailability of the previous channels connected by pores or present fractures closed by high confining stress or both.

Because the pore pressure buildup is also a function of permeability; it is inversely proportional to the permeability (Eqn. 3.28). Thus, a reduced permeability will result in a much higher level of pore pressure, and an abnormal high pore pressure may introduce further fracturing of formation. Rock at deep depth behaves differently than that at shallow depth. Rock failure at deep depth more likely will reduce its apparent permeability rather than enhance the permeability. From the stand point of geo-mechanics, moving rock out of its elastic domain will pose uncertainty with respect to the stability concern. Permeability reduction under plasticity at great depth may cause further fracturing due to pore pressure buildup. Then, the challenge is to predict the orientation and fate of these fractures, whether they will grow vertically into the caprock formations to endanger the integrity or horizontally to enhance the storability, etc.

4.6. Fracture Toughness Measurement

Fracture toughness is the resistance offered by a material against preexisting crack's propagation. It is an important material property which describes the critical states of stresses or energy near the crack tip required for the propagation of fracturing (Krishnan et al., 1997; Ayatollahi and Aliha, 2008).

Cracked chevron notched Brazilian disc (CCNBD) method, an International Society for Rock Mechanics (ISRM) suggested method (ISRM, 1995), was used to measure fracture toughness of Indiana limestone. This method uses a specimen with a chevron shaped notch cut along the core diameter, as shown in the following figure.

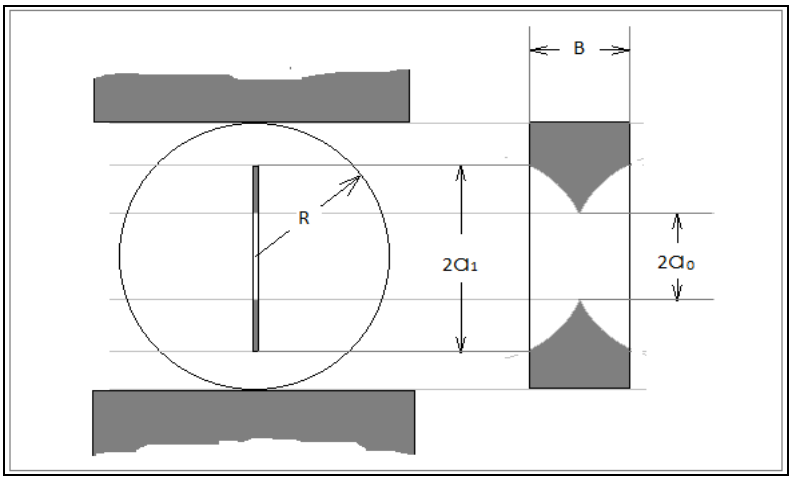

Figure 4.27. The cracked chevron notched Brazilian disc specimen (modified after ISRM, 1995)

The chevron notch causes crack propagation to start at the tip of the V alignment and to proceed outwards in a stable fashion. All the dimensions of the geometry should be converted into dimensionless parameters with respect to the specimen radius R as follows:

$$\alpha_0 = a_0/R; \quad \alpha_1 = a_1/R; \quad \alpha_B = B/R \tag{4.10}$$

And the selected dimensions should satisfy the following restrictions:

$$\alpha_1 \geq 0.4; \quad \alpha_1 \geq \alpha_B/2; \tag{4.11}$$
$$\alpha_B \leq 1.04; \quad \alpha_B \geq 1.1729 \cdot \alpha_1^{1.6666}; \quad \alpha_B \geq 0.44$$

With the help from the Technology Department of UND, a circular diamond saw mounted on a computer controlled lathe was used to cut the required notch, in which the flanks of the chevron notch were straight by a linear cutting motion. As programmed, the chevron notches were ensured to be exactly in the center of the disc and the geometrical dimensions conformed to the given tolerances, as shown in Figure 4.28.

Figure 4.28. CCNBD specimen preparation

After finishing the sample preparation, the MTS rock tester was used to compress the sample to develop a failure surface for further measurements, and at the same time, the force versus displacement curve was recorded, as shown in Figure 4.29 and 4.30.

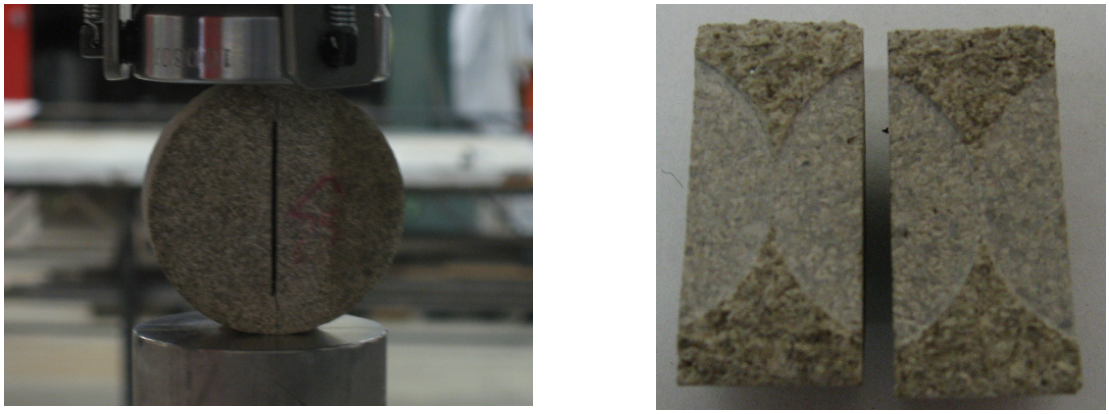

Figure 4.29. Sample compressed by MTS rock tester and the fracture surface after failure

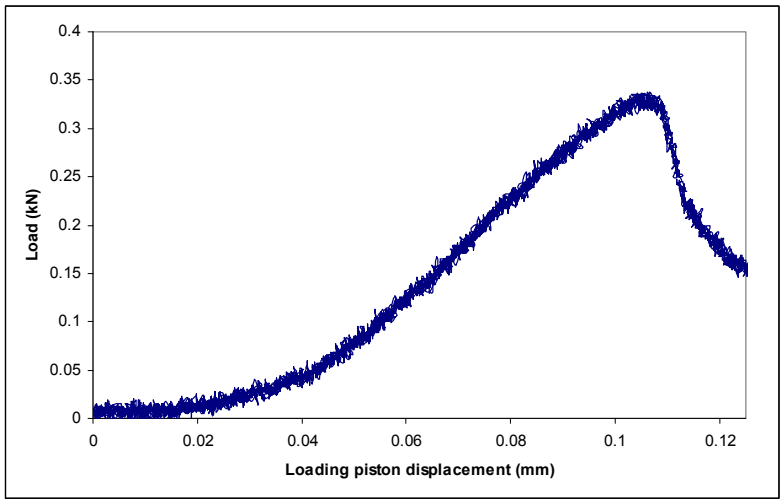

Figure 4.30. Load versus displacement of loading piston (Sample T10L06)

The fracture toughness of the specimen was calculated by the following formula (ISRM, 1995).

$$K_{IC} = \frac{P_{\max}}{B \cdot \sqrt{D}} \cdot Y^*_{\min} \text{; where } Y^*_{\min} = u \cdot e^{v \cdot \alpha_1} \qquad 4.12$$

where $P_{\max}$ is the maximum load that breaks the sample, and $Y^*_{\min}$ is called the critical dimensionless stress intensity value, which is determined by the specimen geometry, and u and v are constants interpolated by α_0 and α_B from Table 2 of ISRM (1995) (Appendix B).

It was noted that some minor modifications to this formula and the "u", "v" values were suggested during the past few years (Zeng and Roegiers, 2000; Wang et al., 2004; Wang, 2010). However, before a formal standard is published by the ISRM, Eqn. 4.12 was followed to keep the test results consistent. The test results are shown in Table 4.11.

Table 4.11. Fracture toughness tests on Indiana limestone

Sample ID	Diameter	Thickness	$2a_1$	$2a_0$	Y^*_{min}	Pmax	K_{IC}
	D (mm)	B (mm)	(mm)	(mm)		(kN)	$MPa\sqrt{m}$
10F03	50.35	20.38	33.90	17.12	0.930878	1.463	0.298
10F04	50.18	16.81	30.06	9.08	0.772534	1.455	0.299
10F11	50.34	17.82	31.07	9.46	0.831154	0.942	0.196
10F07	50.48	19.56	36.69	19.48	1.019895	0.962	0.223
Average							0.261
Standard deviation							0.052
T10L03	24.73	11.82	17.60	0.00	0.890603	0.626	0.300
T10L04	24.45	11.26	17.89	2.43	0.900698	0.588	0.301
T10L05	24.78	11.70	18.29	4.27	0.930112	0.485	0.245
T10L06	24.80	12.14	17.97	2.78	0.889921	0.338	0.157
T10L07	24.78	11.38	18.41	3.83	0.936906	0.574	0.300
T10L08	24.52	12.02	17.28	2.76	0.860530	0.668	0.305
T10L09	24.50	11.28	18.09	4.36	0.935208	0.546	0.289
Average							0.271
Standard deviation							0.054

From the tests results, one can see that these results are insensitive to the sample sizes as fracture toughness is an intrinsic mechanical property of materials. However, the diameter of the sample should be related to the size of the largest grain in the rock by a ratio of at least 10:1 (ISRM, 1995); obviously, this criterion is believed to be sufficiently satisfied by considering the fine grain nature of limestone. All the tested samples were in the valid geometrical range as shown in the following figure.

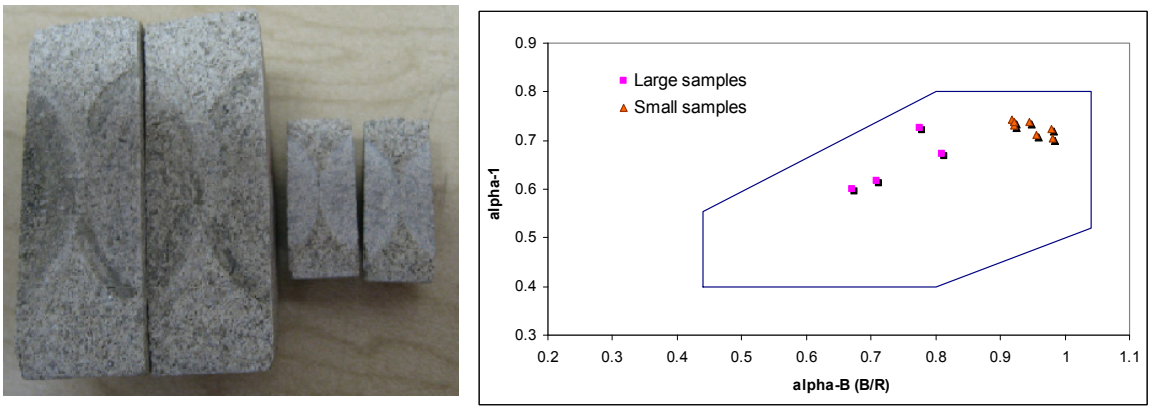

Figure 4.31. Both large and small samples (left) are in the valid geometrical range (right)

Some experimental studies support the assumption that fractures, once initiated, will propagate as long as the stress intensity at the crack tip exceeds the fracture toughness of the material (Warpinski et al., 1979).

Concluding Remarks

CO_2 flooding tests are usually very time consuming and labor intensive, ranging from several days to several weeks. Generally, the total dissolved fine particles (TDS) show a trend of increase with the increasing of mixed flooding fluids (CO_2 and water); however, TDS does not show an increased trend with either pure water flooding or pure CO_2 flooding.

Overall, after CO_2 flooding, the rock's mechanical strength was deteriorated and this deterioration is case dependent, thus complicated. When CO_2 is under the static sequestration, the pure CO_2 saturated rocks even tend to be more competent than the rock saturated with pure water or mixture of water and CO_2. This may reveal the different micro-cracking mechanisms caused by different molecule level properties such as wettability, etc. The high level saturation of CO_2 might be expected in a deep formation where water is in its gaseous state.

As important poroelastic properties, Skempton's coefficient and Biot's coefficient were measured. Skempton's coefficient shows a minor discrepancy from a perfect linear behavior at high pressure regimes. In the earth's crust, there is always a component of compressive stress field. For that reason, the linear elastic mechanics framework may be not sufficient to deal with porous rocks in situ (Gueguen and Bouteca, 2004), but can only give an approximation at best.

Permeability is a tensor that closely relates to stress tensor. It can either be enhanced or destroyed with different loading paths. In short, when rock matrix is relatively stable, permeability will also be relatively stable. However, after the collapse of rock matrix, whether the permeability will be increased or decreased will more likely to be dependent on the openness of fractures or shear band. A decreased permeability may cause abnormal high pore pressure and thus induce further fracturing of the rock formations.

Fracture toughness is an intrinsic rock property that indicates how easy or difficult a crack can propagate in a rock formation. Fracture can never be avoided as the occurrence of flaws is an intrinsic nature of any type of rock. Even a small pore pressure perturbation in porous rock could trigger micro cracking in a critically stressed earth crust (Muller, 2006). Fracture development could either be favorable as to facilitate the flow and increase storage capacity or unfavorable as to endanger the trapping mechanism.

CHAPTER V

LABORATORY TESTING ON PIERRE SHALE FOR CO2 SEQUESTRATION UNDER CLAYEY CAPROCK

In order to proceed with a large-scale carbon storage project, a risk assessment is likely to be required, with leakage estimation at its core (Celia and Nordbotten, 2009). Leakage through caprocks may occur as (1) rapid ("catastrophic") leakage due to seal-breaching or damage of well casing (corrosion of pipes and cements); (2) slow leakage governed by capillary sealing efficiency and relative permeability (after capillary break-through pressure is exceeded); (3) diffusive loss of dissolved gas through saline water or hydrocarbon-saturated pore space (Krooss et al., 1988; Zoback and Zinke, 2002; Shafeen et al., 2004; Al-Basali et al., 2005; Chiquet et al., 2005; Rutqvist et al., 2007; Busch et al, 2008). Problems related to borehole leaking are specific, and more artificial factors involved, thus will not be covered.

Clayey rocks (clays, claystones, shales, mudrocks, siltstones) represent a major constituent of sedimentary basin fill and act as potential flow barriers and seals for subsurface fluid transport (Hildenbrand and Krooss, 2003). Thus, very often, the caprocks are composed by the clayey rocks, and the investigation of geomechanical stability upon CO_2 sequestration will be directed to an understanding of shale, a type of representative clayey rock.

5.1. Caprock Integrity and Potential Leakage Problems

Long-term caprock integrity represents the single most important constraint on the long-term isolation performance of natural and engineered CO_2 storage sites. CO_2 influx from natural accumulation or injection for EOR/storage or saline-aquifer disposal all lead to geochemical alteration and geomechanical deformation of the caprock, enhancing or degrading its seal integrity, depending on the relative effectiveness of these interdependent processes (Johnson et al., 2004).

Ideally, a sealing rock unit should be regional in nature and uniform in lithology, especially at its base. If there are lateral changes in the basal units of a seal rock, the chance of migration out of the primary reservoir into higher intervals increases. However, if the seal rock is uniform, regionally extensive and thick, then the main concerns will be the physical rock strength and any natural or artificial penetrations (faults, fractures and wells) (Smith et al., 2009).

Field-scale measurement methods of the permeability of caprock for formation gas storage projects were theoretically developed in the 1950s and 1960s (Hantush, 1960). These water-pumping tests measure the rate of leakage across the caprock (Miller et al., 1966). A related type of test, pressure 'leak-off' test, can be used to measure caprock permeability and in-situ stress (Zoback, 2007). The capacity of a seal rock to hold back fluids can also be estimated from core samples by mercury injection capillary pressure (MICP) analysis, a method widely used in the oil industry (Vavra et al., 1992). The resulting data of MICP analysis can be used to derive the height of a column of reservoir rock saturated by a particular fluid (e.g. CO_2) that the sealing strata would be capable of holding back.

During geological CO_2 sequestration, dissolved CO_2 will diffuse slowly into the lower section of the caprock where, depending on the caprock mineralogy, it might trigger geochemical reactions affecting crucial parameters such as porosity and, therefore, possibly the sealing capacity and integrity (Gaus et al., 2002 & 2005). Another concern is that the desiccation of clays could lead to caprock failure. Theoretically, desiccation can occur as a consequence of dissolution of water in supercritical CO_2 or due to the geochemical reactions (Bennion et al., 2000).

Influx-triggered mineral reactions within typical shale rocks will generally reduce micro-fracture apertures. Geomechanical integrity degradation is highly dependent on reservoir properties and initial geomechanical degradation has been shown inversely proportional to reservoir permeability and lateral continuity and proportional to influx rate. The currently secure caprock of a given natural CO_2 site might be incapable of providing an effective seal for an engineered injection, as the pressure increase associated with CO_2 accumulation may result in net aperture widening of cap-rock micro-fractures (Johnson et al., 2004).

Local deformations of caprock may activate latent discontinuities and deformation rates may be sub-critical with respect to cataclastic behavior of the rock mass. The transition from non-cataclastic to cataclastic behavior is also of importance (Mutschler et al., 2009).

A combination of diffusion experiments and conventional gas sorption tests on the Muderong Shale from Western Australia has provided evidence for significant CO_2 storage capacity in clayey sequences (Busch et al., 2008). However, limited by the poor accessibility due to low permeability, this retention capacity can only be considered as an

additional beneficial feature of the clayey caprocks overlying potential CO_2 storage sites.

Overall, the understanding of the clayey caprocks' behavior under the influence of CO_2 tends to be a key element for the site characterization and leakage estimation. However, in the petroleum industry, as clayey rocks (shales) are generally not the primary target, cores from deep boreholes (>1000m) are very scarce. In addition, clayey rocks from deep formations have certain characteristics which make them difficult to handle correctly under laboratory conditions; these include the low permeability and high sensitivity to contacting fluids (Horsrud et al., 1998).

The difficulty to acquire cores from deep formations led to the investigation on the outcrops. However, with increasing depth, effects of compaction and diagenesis cause the clayey rocks to deviate more and more from typical properties and behaviors of clay. Clay minerals also alter with the buried depth, which complicates the laboratory work (Garcia-Romero et al., 2005).

Pierre shale from the Pembina Gorge of North Dakota was used as a medium to perceive the caprock behavior. Because real caprock formations are not directly accessible, an outcrop composed of a similar or close lithology as the caprock is considered as an analogue of the caprock, which is parallel to the concept of "aquifer/outcrop analogue" that is widely used in the hydrogeology research (Miall and Tyler, 1991; Anderson, 1997; Heinz and Aigner, 2003).

5.2. Sample Collection and Preparation

The main clay mineral groups are the kandite group, such as kaolinite, dickite, nacrite; the illite group, such as illite, hydro-micas, phengite, glauconite; the smectite group, such as montmorillonite, beidellite, saponite, etc (Deer et al., 1966). The

constituents of shale include: frame silicates (quartz, feldspar and zeolites), clay minerals (kaolinite, smectite-illite-muscovite, chlorite), carbonates and organic matters. The major clayey layers in the Williston Basin are shown in Figure 5.1, which generally correspond to the seals for oil and gas reservoirs or saline aquifers. One can see that the Pierre shale is one of the thickest shale formations in this basin; and the basin can be described in a very rough sense as carbonate formations covered by shale.

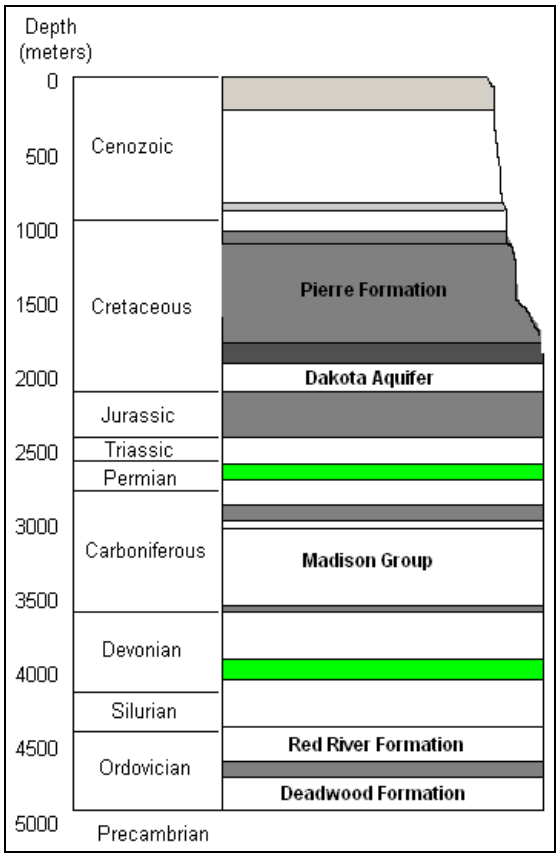

Figure 5.1. Typical rock column in central Williston Basin, major clayey rock layers in gray and salt layers in green (after Bluemle et al., 1999, and Murphy, 2009)

The normal Devonian marine shales of the Williston Basin contain up to 70% chlorite, but typical values are 10 to 20% (Weaver, 1989). The Upper Cretaceous Pierre shale was deposited in a regressive-transgressive-regressive sequence. Near western Montana, the Pierre equivalent rocks consist of continental sandstone and shale deposits,

some with volcanic debris. These facies degrade seaward into marine sandstones, and farther east into shales and marlstones.

The Paleozoic shales have more illite and less montmorillonite than the Cenozoic shales. The quartz in the Pierre shale is extremely fine with the primary mode in the range of 1.4 to 2.7 μm. The fine size suggests much of the quartz, along with volcanic ash, was wind transported (Weaver, 1989).

Figure 5.2 shows the uppermost named member of the Pierre shale, the Odanah Member, which is exposed in this gravel pit close to Walhalla, North Dakota. It was deposited in a shallow-water marine environment during the Cretaceous about 80 million years ago. The Odanah Member is hard, siliceous, light-gray shale. Because of its hardness, it forms conspicuous cliffs and is quarried for road surfacing material. Fossils are scarce in the Odanah, although oyster fossils have been recovered (Hoganson et al., 2004).

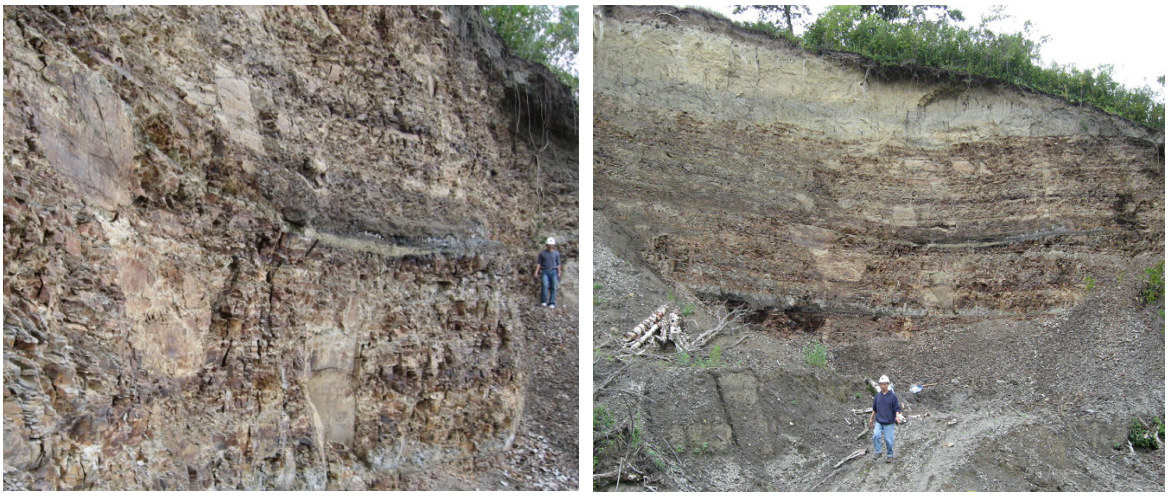

Figure 5.2. Outcrop of Pierre shale sampling site, view to the northeast (left) and to the northwest (right) (May 25, 2009)

The overall strikes of the collected samples are in the North-South direction

(N10E), with very gentle dip angles (1~3˚ or even less) due to the west. This observation is coincided with the description of Bertog (2002, p. 134): "During times of tectonic quiescence, sedimentation patterns reflected a retroarc foreland basin with north-south trending parallel facies belts, however during times of tectonic activity in Wyoming and Utah, the axial basin and the Williston Basin in the northern part of the basin subsided, resulting in a north to south dichotomy in sedimentation patterns."

Extreme difficulties were encountered when preparing these samples due to their very weak features. Initially, one ton of raw rock may only yield several pieces of intact samples. However, with the improvement of the machinery and lab skills, unexpected cracks during coring were greatly minimized. In these samples, the total amount of clay is about 60% and quartz is about 20% of the overall components. Porosity is estimated as about 37%. At room condition, these shales can be easily disintegrated into thin layers upon contact with fresh water (Figure 5.3).

Figure 5.3. Changes of Pierre shale samples after contact with different fluids
(crumbled in water (right), darkened in mineral oil but still intact (left), unchanged in air (middle))

The chemical formula of montmorillonite is $(OH)_4Al_4Si_8O_{20}.nH_2O$. The water is present as a layer of water that penetrates the lattice, between the silica layer of one three

layer, silica-alumina-silica unit and the silica layer of the adjacent one. The addition of water can cause the lattice to expand and the clay to swell (Butler, 1991). However, the swelling effect can be observed but is not very significant. Thus non expansive clay (illite) is possibly more dominant than expansive clay (montmorillonite). This is also in agreement with Peter Gale, a geologist from New England Research, Inc (Gale, P., personal communication, March 18, 2010, White River Junction, VT).

In fact, there is good evidence that smectite clays in sediments change slowly over the temperature range of 70 and 150°C to mixed-layer smectite-illites and ultimately to illite. Illite is the most common clay ion in older shale. In Cenozoic sediments and sedimentary rocks recovered from boreholes, illite commonly becomes more abundant with depth, indicating that in the warmer parts of diagenetic environments other clay minerals alter slowly to illite (Weaver, 1989).

5.3. Permeability Tests for Low Permeable Rock Samples

Permeability is important for the understanding of a caprock, because it can give indications about sealing efficiency of the caprocks. Permeability variations also indicate mechanical, hydraulic and structural changes of the material. Both steady-state flow method and transient method were used to detect the permeability of Pierre shale.

5.3.1. Steady-State Flow Method

In these tests, a short shale sample is sandwiched in two short pieces of Indiana limestone. The overall permeability (perpendicular to layering of this composite sample) is given by (Fetter, 2001):

$$k = \frac{L}{\frac{l_1}{k_1} + \frac{l_2}{k_2} + \frac{l_3}{k_3}} \qquad 5.1$$

where L is the thickness of the composite sample, and l_1, l_2, l_3 for each pieces, with $L = l_1+l_2+l_3$. k, k_1, k_2, k_3 are the permeabilities of the composite sample and each pieces, correspondingly. Because the permeability of Indiana limestone is much higher than that of shale, i.e., k_1 , $k_3 >> k_2$, one can deduce that k is mainly determined by k_2 (shale), e.g. $\frac{k}{L} = \frac{k_2}{l_2}$. Another advantage of using limestone is that a homogeneous flow front can be expected on the surface of shale.

As gas flow in nano-pores cannot be described simply by the Darcy equation, processes such as Knudsen diffusion and slippage flow in the solid matrix separate gas flow behavior from Darcy-type behavior. But if the pressure is increased, Knudsen diffusion can be reduced, and the ratio of apparent permeability will approach Darcy permeability (Zeng et al., 2004; Javadpour, 2009).

For compressible fluid flow, usually characterized by gas flow, Darcy's Law can be modified as:

$$k = \frac{q_o \mu L}{A \Delta p} \frac{p_o}{p_m} \qquad 5.2$$

For shale, this becomes:

$$k_2 = \frac{l_2}{L} k = \frac{l_2}{L} \frac{q_o \mu L}{A \Delta p} \frac{p_o}{p_m} = \frac{q_o \mu l_2}{A \Delta p} \frac{p_o}{p_m} \qquad 5.3$$

where A is cross sectional area of rock sample, μ is fluid viscosity (for nitrogen, this is $1.76 \times 10^{-5}\, Pa.\sec$ at room temperature), Δp is pressure drop across sample, l_2 is the shale

sample length, p_m is the average of inlet and outlet pump pressures, p_o is outlet pump pressure, and q_o is flow rate at outlet pump (Note: p_o and q_o can also be replaced by inlet pump data p_i and q_i).

Under confining pressure 1,200 psi, inlet pump pressure 500 psi, and outlet pump pressure 30 psi, the inlet and outlet pump volume changes are shown in the following figure.

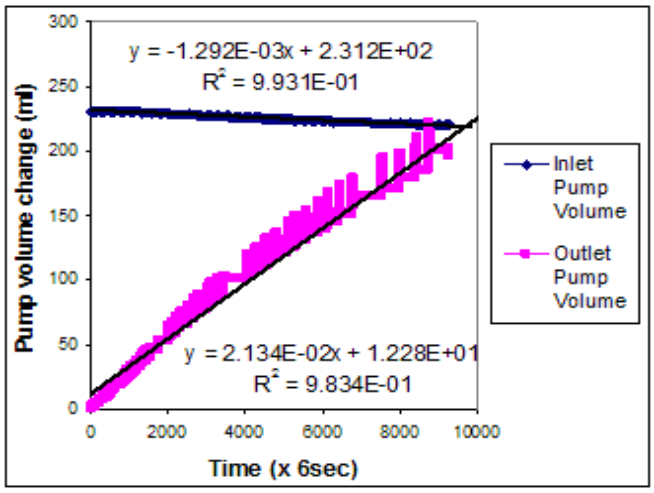

Figure 5.4. Inlet and outlet pump volume changes (Sample 09C008)

Based on outlet pump's flow rate and pressure drop, the permeability is calculated as follows:

$$k_2 = \frac{q\mu l_2}{A\Delta p}\frac{p_o}{p_m} = \frac{(2.134\times10^{-2}\,cm^3/6\,\text{sec})\times(0.995cm)\times1.76\times10^{-5}\,Pa.\text{sec}}{(3.14\times1.26^2\,cm^2)\times(470\,psi)\times\frac{265\,psi}{30\,psi}\times6894.7\,pa/psi}$$

$$= 4.3626\times10^{-16}\,cm^2\times\frac{1Darcy}{9.87\times10^{-9}\,cm^2} = 44.2nD$$

If using the inlet flow rate and pressure drop, the permeability is:

$$k_2 = \frac{q\mu l_2}{A\Delta p}\frac{p_i}{p_m} = \frac{(1.292\times10^{-3}\,cm^3/6\,\text{sec})\times(0.995cm)\times1.76\times10^{-5}\,Pa.\text{sec}}{(3.14\times1.26^2\,cm^2)\times(470\,psi)\times\frac{265\,psi}{500\,psi}\times6894.7\,pa/psi}$$

$$= 4.4022\times10^{-16}\,cm^2\times\frac{1Darcy}{9.87\times10^{-9}\,cm^2} = 44.6nD$$

Ideally, the permeability calculated based on the inlet pump data and the outlet pump data should be the same. However, because the gas (nitrogen) collected by the outlet pump is less than the gas released by the inlet pump, possibly due to gas diffusion through the viton sleeve to the radial confining pump and maybe minor gas sorption in the sample, the permeability calculated based on the outlet flow is smaller than that calculated based on the inlet flow; and this difference can indicate if the gas diffusion and/or sorption effects are serious.

5.3.2. Transient Method

For low permeable rock, another technique called pulse decay can be used. This is a transient method, and it is implemented under unsteady-state conditions.

The method of transient pulse decay was first proposed by Brace and Martin (1968). In this test, a sample is connected to two reservoirs at a constant and equilibrant pressure at the beginning of the test. Then, a sudden pressure pulse is applied in the upstream reservoir and the successive pressure evolutions in both reservoirs are recorded.

Figure 5.5. Upstream and downstream reservoirs across the sample

The equation governing one-dimensional compressible fluid transportation in a sample is (Marsala et al., 1998):

$$\frac{\partial^2 p}{\partial x^2} = \frac{\mu C_f}{k}\left[\phi_c + \frac{C_s - (1+\phi_c)C_M}{C_f}\right]\frac{\partial p}{\partial t} \qquad 5.4$$

where p is the pore pressure inside the sample, x is the distance along the sample axis,

C_f is the compressibility of the pore fluid, C_s is the bulk compressibility of the sample, C_M is the rock matrix compressibility of the sample, μ is fluid viscosity, ϕ_c is sample effective porosity, k is permeability, and t is time. It is demonstrated by the experiments that the pressure gradient decays exponentially to zero. The permeability can be computed by the following formula (Marsala et al., 1998):

$$k = \frac{\mu C_f L}{At\left(\frac{1}{V_U} + \frac{1}{V_D}\right)} \bullet \ln\left[\frac{\Delta p\left(\frac{V_D}{V_U + V_D}\right)}{p_{U(t)} - p_f}\right] \qquad 5.5$$

where V_U is upstream reservoir volume, V_D is downstream reservoir volume, P_f is final pressure at equilibrium, and Δp is initial pressure difference.

The upstream and downstream reservoirs are actually formed by narrow pipes and the pores of limestone. Their volumes cannot be measured directly but can be derived by the tests based on the ideal gas law (note nitrogen is very close to ideal gas at room temperature, thus is used to derive the required volume value):

$$p_1(V_{pump}^{time-1} + V_{\mathrm{Re}servoir)} = p_2(V_{pump}^{time-2} + V_{\mathrm{Re}servoir}) \qquad 5.6$$

After a series of tests, it was found that V_U = 9.22 ml, and V_D = 6.35 ml for the test on sample 09C008. The upstream and downstream reservoir pressure changes are shown in the following figure.

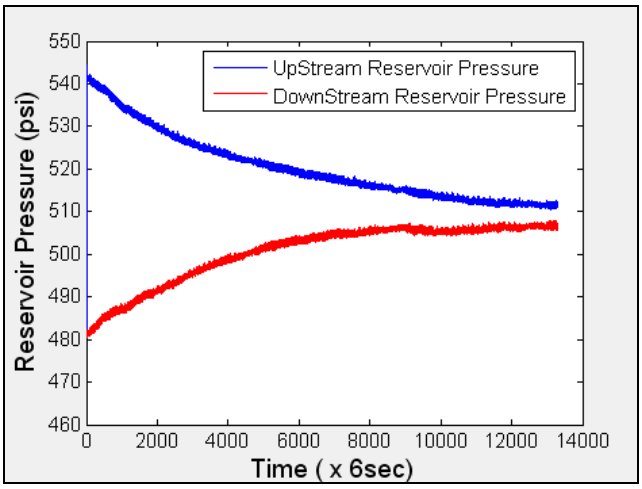

Figure 5.6. Upstream and downstream reservoir pressure changes (Sample 09C008)

Then, the permeability can be calculated by reading a point in the curves. For example, for a point at 8,000 (×6 sec) and 515 (psi) on the upstream reservoir pressure curve in the above figure, the permeability can be calculated as:

$$k = \frac{1.76\times10^{-5}\,Pa.\sec\times 1/(500\times 6894.7Pa)\times 0.995cm}{(3.14\times 1.26^2\,cm^2)\times 48000\sec\times\left(1/9.22cm^3+1/6.35cm^3\right)}$$
$$\times\ln\left[\frac{60\,psi(6.35/(9.22+6.35))}{515\,psi-510\,psi}\right]\times\frac{1Darcy}{9.87\times10^{-9}\,cm^2}=12.84nD$$

In comparison to the results from the previous section, one can see that the results acquired by these two different methods (steady-state and transient) are in the same order, especially when regarding the low permeability at the nD range. As transient method introduces more parameters such as upstream and downstream reservoir volumes, for small size of sample, the result may not be better than that obtained by steady-state method. Thus, for the following tests, steady-state method was employed to ensure a common base for data comparison.

5.3.3. Factors Influencing Permeability

After the previous tests on Sample 09C008 at 1,200 psi confining pressure, the

temperature was increased from room temperature to 136 °F, and the confining pressure was increased to 4,000 psi. The viscosity of nitrogen changed and can be acquired from Sutherland's equation (Crowe et al., 2005):

$$\mu = \mu_0 \left(\frac{T}{T_0}\right)^{\frac{3}{2}} \frac{T_0 + S}{T + S} = 1.76 \times 10^{-5}\, Pa \cdot \sec \times \left(\frac{331}{273}\right)^{\frac{3}{2}} \frac{273 + 107}{331 + 107} = 2.038 \times 10^{-5}\, Pa \cdot \sec$$

The flow history was recorded as shown in the following figure.

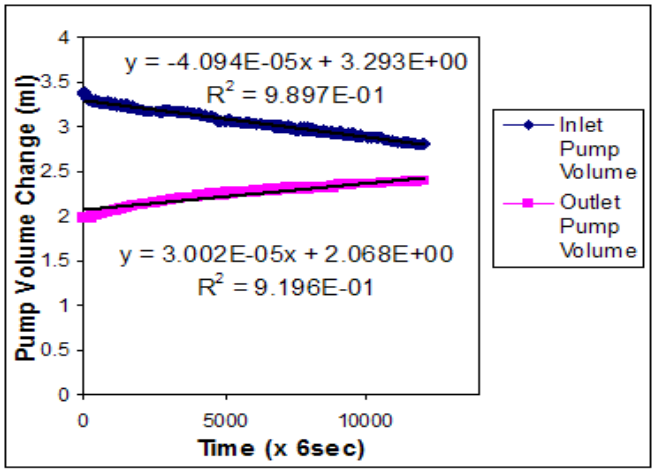

Figure 5.7. Inlet and outlet pump volume changes with time
(Sample 09C008, confining pressure 4,000 psi, temperature 136 °F)

Based on the inlet pump readings, the permeability can be calculated as follows:

$$k_2 = \frac{q\mu l_2}{A\Delta P}\frac{p_i}{p_m} = \frac{(4.09442 \times 10^{-5}\, cm^3/6\sec) \times (0.995cm) \times 2.038 \times 10^{-5}\, Pa.\sec}{(3.14 \times 1.26^2\, cm^2) \times (300psi) \times \frac{1350psi}{1500psi} \times 6894.7\, pa/psi} = 1.51nD$$

Similarly, using the outlet pump data, $k_2 = 0.886nD$

The deviation in this case is much higher, due to the higher diffusion effect at higher confining pressure and higher temperature regime. One can also find that permeability is greatly reduced with the increase of confining pressure and temperature.

The increase of the confining pressure may also destroy the pore structure in a

sample, causing a permanent loss of permeability. The following figure shows a sample's permeability change in response to confining pressure. The numbers (1 through 7) indicate the test sequence. One can see that the permeability decreased with the increase of confining pressure (1 through 4); and even after the confining pressure was reduced (4 through 7), the permeability cannot be recovered. Table 5.1 shows the detailed permeability calculated using data from upstream and down stream pumps.

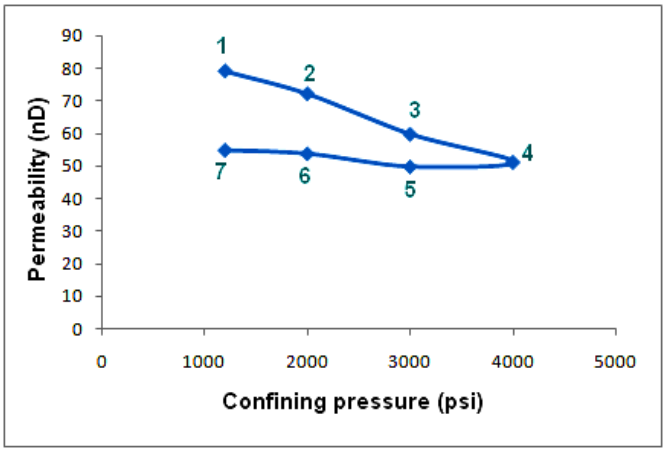

Figure 5.8. Permeability changes with confining pressure (Sample 100117)

Table 5.1. Permeability changes with confining pressure

Confining pressure	Permeability (inlet)	Permeability (outlet)	Permeability (average)
(psi)	(nD)	(nD)	(nD)
1200	81.2	76.7	79.0
2000	74.0	69.9	72.0
3000	59.7	59.4	59.6
4000	52.0	50.1	51.0
3000	51.7	47.5	49.6
2000	54.1	53.1	53.6
1200	57.0	52.4	54.7

For low permeable rock, fracture can also significantly influence the permeability. During the experiments, one of the tested samples' permeability was found to be one order higher than that of the rest. After a careful examination, an intrinsic fracture was found (Figure 5.9). Table 5.2 shows the permeability changes with respect to the

confining pressure. At the last stage (4,000 psi), after the permeability test, the flow was stopped for 3 hours and then was resumed. However, the permeability did not reach the previous level. Thus, an isolated point "7" is present in Figure 5.10. Obviously, flow history is also a factor to influence the permeability.

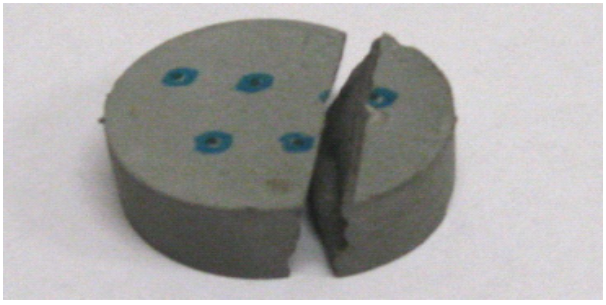

Figure 5.9. A hidden fracture was found after test (Sample 100122)

Table 5.2. Permeability changes with confining pressure

Confining pressure	Permeability (inlet)	Permeability (outlet)	Permeability (Average)
(psi)	nD	nD	nD
1200	488	467	477
2000	456	432	444
2500	435	399	417
3000	413	389	401
3500	371	361	366
4000	212	196	204
Flow was stopped for 3 hours and then resumed			
4000	126	120	123

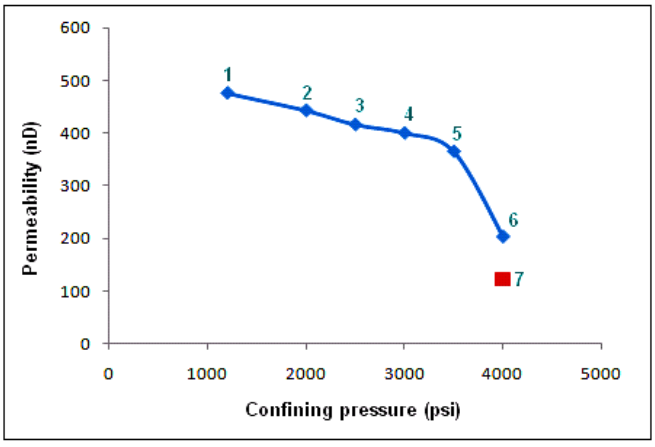

Figure 5.10. Permeability changes with confining pressure, and flow history (Sample 100122, 3-hour interruption between 6 and 7)

Under high confining pressure, water can also be used as working flow. The samples were all intact after these tests. This may indicate that shale deterioration under water, which is commonly observed at the surface conditions either in the lab or in the field, may not be extrapolated to a deep condition (high temperature and high pressure regime). For the water to flow through dry shale, a typical curve is shown in Figure 5.11.

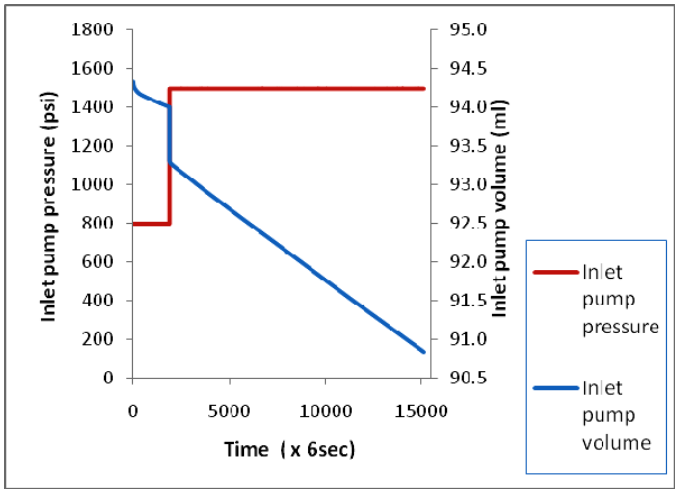

Figure 5.11. Water flow through a dry shale
(Sample 100201, Confining Pressure 2,000 psi, Length 9.82 mm, Diameter 24.92 mm)

The confining pressure was 2,000 psi. The inlet pump flow rate increased from $1.077\times10^{-4}ml/6sec$ to $1.844\times10^{-4}ml/6sec$ when the pressure drop increased from 800 psi to 1,500 psi (the outlet was directed to the atmosphere). Figure 5.12 shows a more detailed water flow history at the early stage. One can see that a diffusion curve is followed by a straight line, which indicates a stable flow condition was established after saturation by diffusion.

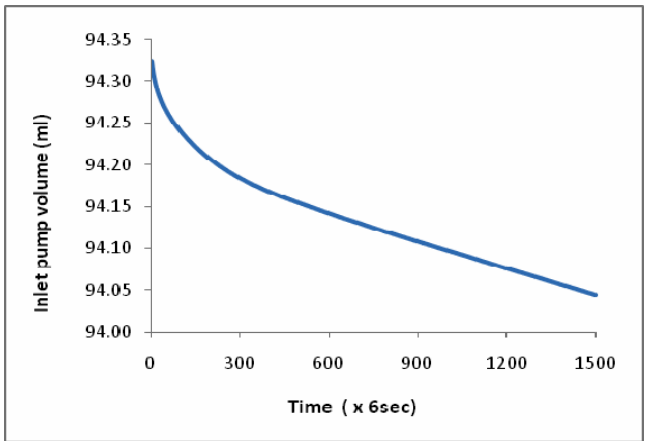

Figure 5.12. A diffusion curve at the beginning of water flow though shale (Sample 100201)

The permeability of the sample shown in Figures 5.11 and 5.12 is calculated as 66.8 nD, which is very close to the permeability of those samples tested using gas flow.

Permeability may also be influenced by some physical and/or chemical reactions. It may increase due to dissolution or decrease due to precipitation. In lab conditions, due to the short length of the sample, dissolution is more likely to be observed than precipitation.

Figure 5.13 shows the dissolution effect as indicated by the increased permeability with flow time. The sample was held under the confining pressure of 4,000 psi and 136 °F for 25 days. Water was used as the working fluid. Inlet pump pressure was increased from 1,200 psi to 3,200 psi, and then decreased to 1,200 psi again (test sequence is labeled by the numbers 1 through 6), while the outlet was directed to the atmosphere. The sample was intact after the test.

The relatively flat trend line may indicate that, even though permeability increases with the pressure gradients, this relationship may be weak. It also allows an apparent permeability to be averaged as 10.5 nD under the confining pressure of 4,000 psi.

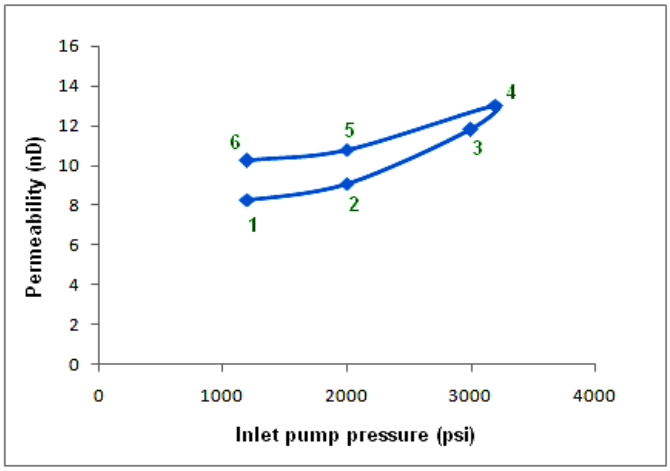

Figure 5.13. Permeability increases due to dissolution
(Sample 09C003: Diameter 24.1 mm, Length 12.4 mm)

5.4. CO_2 and Rock Interaction

The following table shows the permeability test results when CO_2 was used as the working fluid. In comparison to those results tested with nitrogen, the permeability tested with CO_2 seems more sensitive to the confining pressure. The higher deviation between the inlet and outlet pump data at a higher confining pressure may also indicate a higher gas diffusion and/or sorption effect.

Table 5.3. Permeability by using CO_2 as a working flow

Confining pressure	Permeability		Permeability (Average)	Standard deviation
	(inlet)	(outlet)		
(psi)	nD	nD	nD	nD
1200	363	357	360	4.2
3000	69.6	27.3	48. 5	29.9

Dry samples which had undergone single phase flow, either water, nitrogen or CO_2, all preserved their integrity after permeability tests. However, for a sample first under water flow and then under CO_2 flow, serious disintegration was found as shown in Figure 5.14. On the other hand, for CO_2 flow through an oil-wetted sample, the integrity is well preserved, as shown in Figure 5.15.

Figure 5.14. Rock deterioration after water flow followed by CO_2 flow

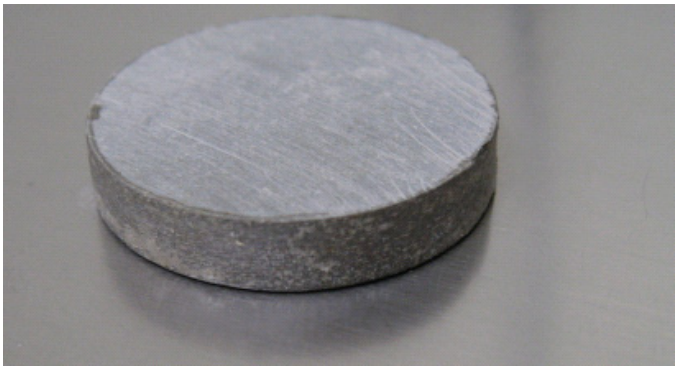

Figure 5.15. Oil saturated rock was intact after CO_2 flow (note the sample turned to its original color)

Under room conditions, the disintegration of shale caused by water generally shows a swelling feature, and the fractures tend to develop in a multi-layered pattern (Figure 5.3). However, the sample in Figure 5.14 shows a different failure feature: the disintegration proceeded into fines and the swelling effect was absent or minor. The orientation of fractures developed randomly.

A possible explanation is that, as CO_2 reacted with water to release large quantities of H^+, in which the initial ionic balance of the rock was destroyed, leading to its extensive deterioration (Lyklema, 1995). A study also found that the reaction of shale and arkose materials in CO_2-brine systems at 200 °C and 200 bar for 80 days resulted in the precipitation of magnesite, analcite ($NaAlSi_2O_6.H_2O$), and clays (Kaszuba et al., 2003).

5.5.Triaxial Compression Test

After some preliminary tests on the shale samples, as well as on aluminum standard, lead standard and polycarbonate standard, it was found that the Young's modulus and Poisson's ratio of polycarbonate is the closest to these shale samples. Thus, it was chosen as the primary standard, while aluminum standard was also kept as a reference. Figure 5.16 shows Sample 09PA05 after a triaxial test; one can see that the shear failures are well-defined.

Figure 5.16. Rock sample after triaxial test (Sample 09PA05)

Based on the stress-strain curve as shown in Figure 5.17, the Young's modulus and Poisson's ratio can also be derived; they are 2.0×10^5 psi (1.4 GPa) and 0.36, respectively. Compared to previous chapter, it is found that the Young's modulus of Pierre shale is one order less than that of Indiana limestone.

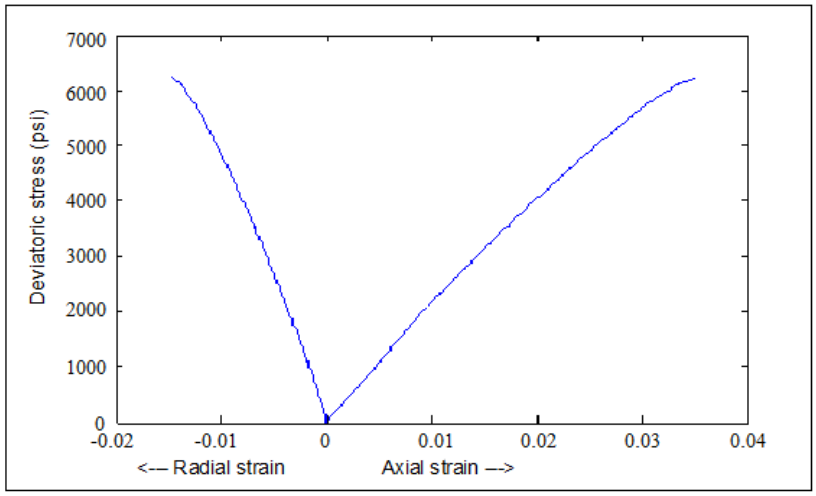

Figure 5.17. Stress-strain curve (Sample 09PA05)

Table 5.4. Triaxial test results of shale samples

Sample ID	Confining Pressure	Ultimate Compressive strength	Residual Strength	Young's Modulus	
	(psi)	(psi)	(psi)	($x10^5$ psi)	(GPa)
09PA01	100	5250	3940	2.3	1.6
09PA02	100	4930	2270	2.0	1.4
09PA07	500	7190	4395	2.3	1.6
09PA06	500	3650	4580	2.3	1.6
09PA05	1000	7940	6128	2.0	1.4
09PA08	2000	11830	10046	2.4	1.7

Figure 5.18 shows the triaxial compression test results of some samples at different confining pressures. Sample 09PA06 shows different features compared to other samples (red line). It does not have a peak axial strength that stands out; however, its residual strength is comparable with sample 09PA07, which is also under the same radial confining pressure (500psi). By checking the sample's history during preparation, it was found that this sample had been submerged in mineral oil for 45 days; even its surface appeared dry when conducting the tests. Note that other samples were all dry rocks.

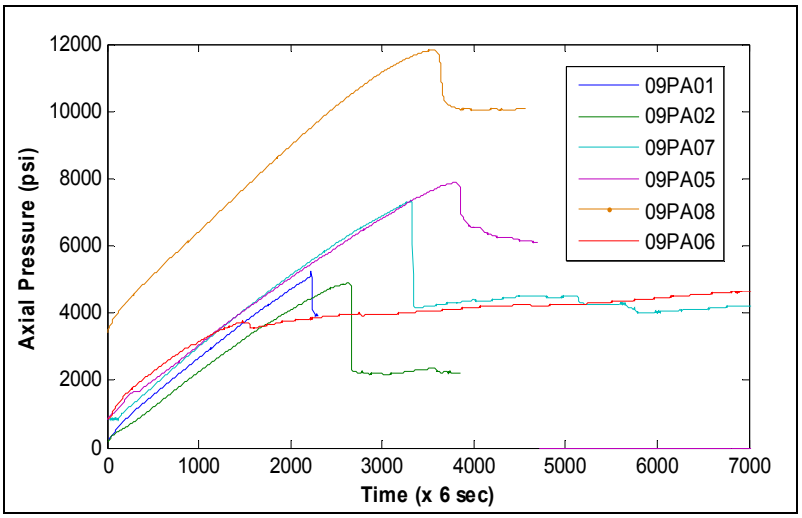

Figure 5.18. Plot of axial stress versus time

Because shale has low permeability, the inner moisture may not be always expressed on its surface. This may indicate that for shale, due to the uncertainty of its saturation (wetness), sometimes residual strength may be more reliable for constructing the Mohr-Coulomb failure envelope (Figure 5.19). Note the abnormally small red circle formed by 09PA06.

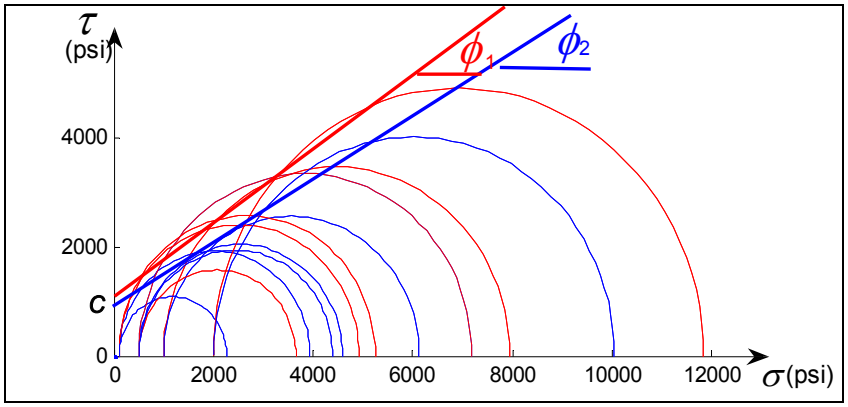

Figure 5.19. Mohr-Coulomb failure envelope of Pierre shale
(Red lines: based on ultimate compressive strength; Blue lines: based on residual strength)

The Mohr-Coulomb criterion based on the ultimate compressive strength (UCS) of only dry rocks can be expressed as:

$\tau = \sigma \tan(34°) + 1100$ psi 5.7a

where $C_{01} = 1{,}100$ psi, and $\phi_1 = 34°$.

The Mohr-Coulomb criterion based on the residual strengths of rocks, regardless of saturation (wetness), can be expressed as:

$\tau = \sigma \tan(31°) + 950$ psi 5.7b

where $C_{02} = 950$ psi, and $\phi_2 = 31°$.

Eq 5.7b is more conservative than Eq 5.7a, but has a better consistency with those related circles.

5.6.UCS and UTS Measurement by Point Load Test

The point load test (PLT) is an attractive alternative to acquire the UCS because it can provide similar data at a lower cost. The PLT has been used in geotechnical analysis for over forty years (ISRM, 1985).

The relationship between UCS and the point load strength could be expressed as:

$$UCS = Y_c I_{s(50)} \quad 5.8$$

where $I_{s(50)} = P A_e / D_e^2$, in which $D_e^2 = 4DB/\pi$, and D is specimen diameter, B is specimen thickness, P is gauge pressure at failure, A_e is effective area of the jack piston (1.76 in^2 for this lab), and Y_c is a conversion factor.

Because the cores tested were close to 50mm in diameter, the correction from I_s to $I_{s(50)}$ is unnecessary (Rusnak and Mark, 1999). The PLT's accuracy in predicting the UCS depends on the ratio "Y_c" between UCS and the point load strength, which is actually a tensile strength (Fjaer et al., 1992). Das (1985) and Vallejo et al. (1989) all suggested the number 12.6 for the conversion factor for shale. It was found "12" is a

reasonable choice for Pierre shale, since this agrees with the previous triaxial test results very well.

Based on some literature reviews (ISRM, 1985), the following formula was used to determine the uniaxial tensile strength (UTS):

$$UTS = 1.25 I_{s(50)} \qquad 5.9$$

To detect the influence of CO_2 on the rock strength, relatively large samples (2.4 inches in diameter and 1 in thickness) were prepared. These samples were put into a container full of CO_2 at atmosphere pressure, while a reference group was kept in another container full of air. After three months, these samples were subjected to the point load tests (Figure 5.20), and the results are shown in Table 5.5.

From the point load test results (Table 5.5), it seems that the CO_2–processed group tends to be weaker than the reference group, though very small so far.

Table 5.5 Point load test results

Sample ID	D (in)	B (in)	P (psi)	UCS (psi)	UTS (psi)
Samples stored in a container full of CO_2					
09PL01	2.41	1.05	800	5244	546
09PL02	2.41	1.17	920	5412	564
09PL03	2.41	1.02	750	5061	527
09PL04*	2.41	1.16	500	2967	309
Average				5239	546
Samples stored in a container full of air as a reference group					
09PL05	2.41	1.08	950	6054	631
09PL07	2.42	1.14	930	5592	582
09PL08	2.41	1.23	900	5036	525
09PL09	2.41	0.87	600	4747	494
Average				5357	558

* Sample 09PL04 was not taken into the average due to its unqualified failure feature. Note the surface failure on sample 09PL04 in Figure 5.20.

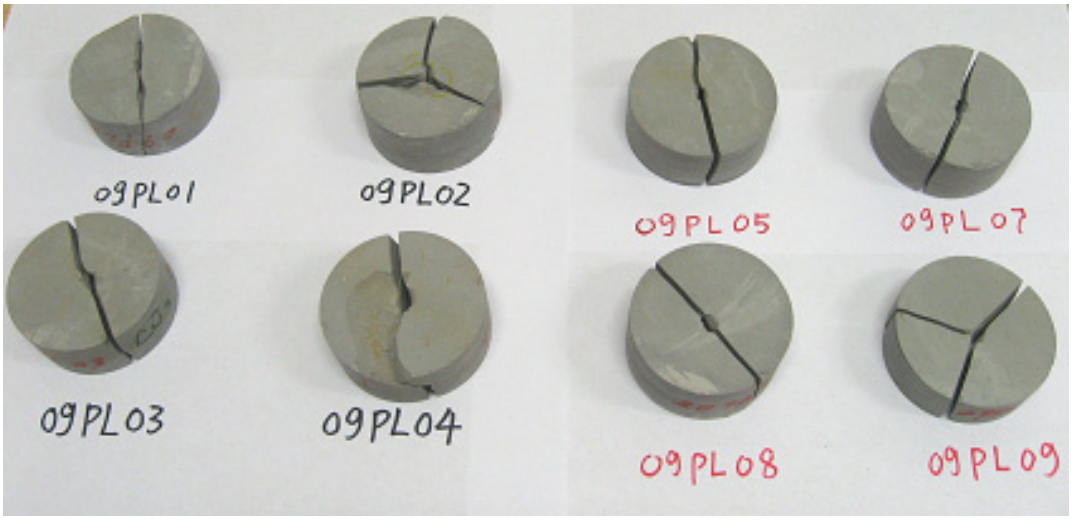

Figure 5.20. Pierre shale samples after point load tests

Brazilian tests were also conducted on Pierre shale using a MTS rock tester and the anisotropy of Pierre shale is demonstrated by Figure 5.21. As the Brazilian test is only valid if primary fracture initiates from the center of the specimen and spreads along the loaded diameter, most of the test results shown in Figure 5.21 can not be used to derive the tensile strength of Pierre shale.

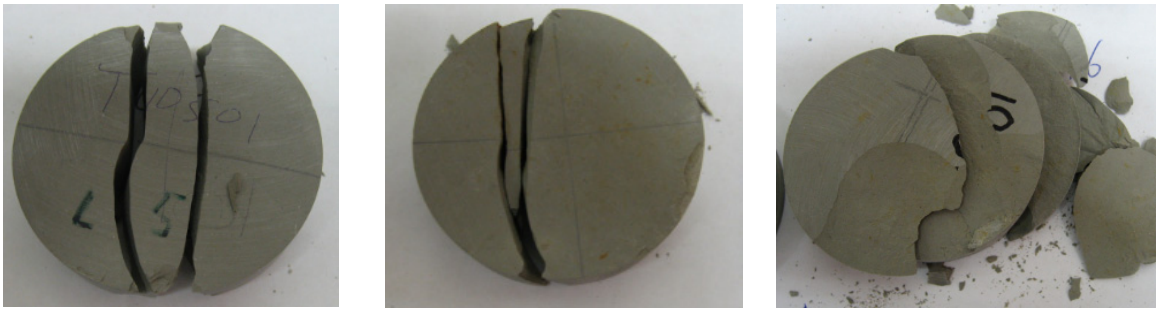

T10SA1 T10SA2 T10SA3

Figure 5.21. Brazilian test is not suitable for Pierre shale due to its anisotropy feature

5.7. Fracture Toughness Measurement

The Cracked Chevron Notched Brazilian Disc (CCNBD) specimens were used to determine Mode I fracture toughness as suggested by ISRM (ISRM, 1995), which is the

similar method that is used to measure the fracture toughness of Indiana limestone. A typical load versus displacement curve based on loading piston is shown in the following figure.

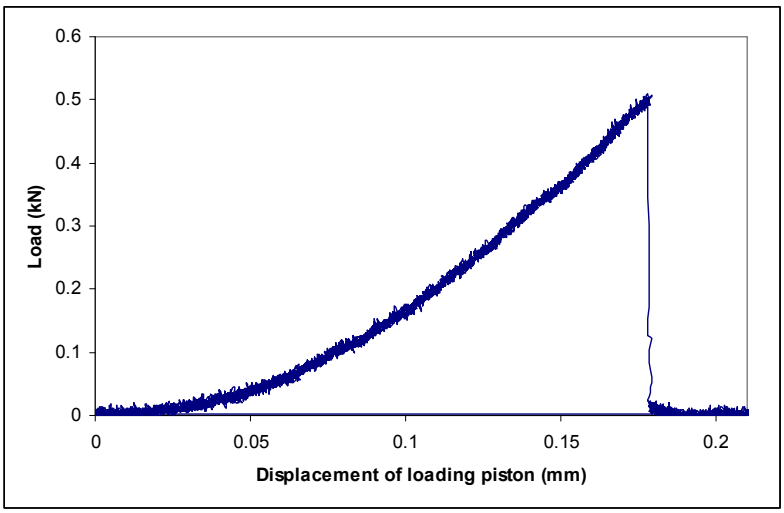

Figure 5.22. Load versus displacement of loading piston (sample T10S01)

Similar to tests on limestone, both large and small samples were tested; and it was found that the fracture surfaces were all very well developed (Figure 5.23). Thus, the anisotropy of shale seems to be overcome by the pre-cut fractures.

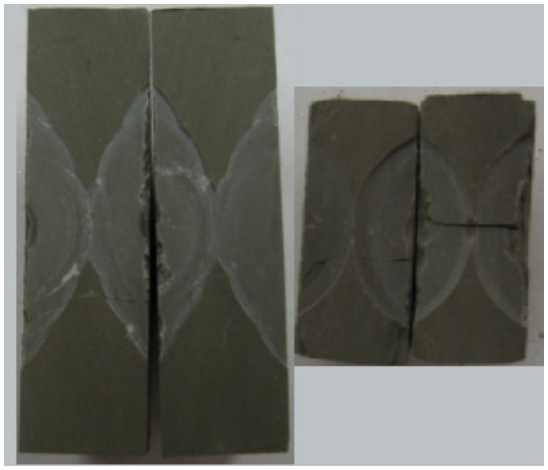

Figure 5.23. Both large and small samples show well defined fracture surfaces

Also note all the samples tested were in the valid geometrical range as shown in

the following figure.

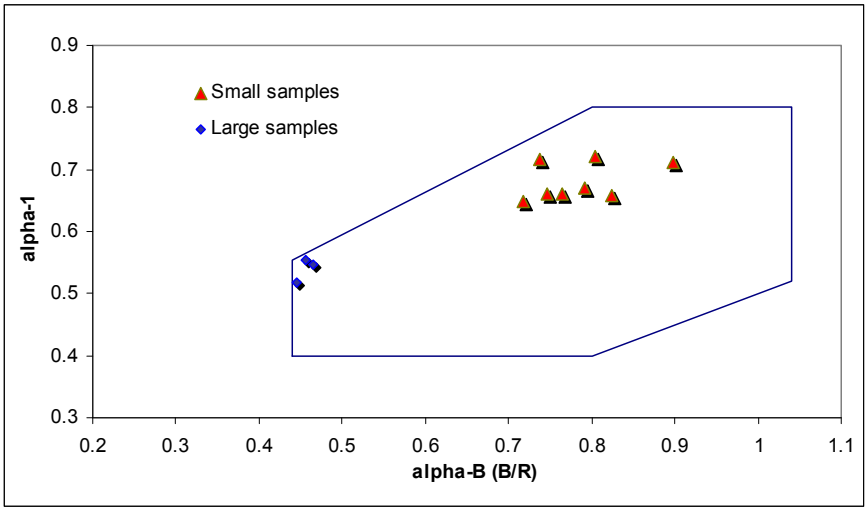

Figure 5.24. Only samples in the valid geometrical range were used for calculation

The test results are shown in the following table.

Table 5.6. Fracture toughness tests on Pierre shale

Sample ID	Diameter	Thickness	2a1	2a0	Y*min	Pmax	KIC
	D (mm)	B (mm)	(mm)	(mm)		(kN)	$MPa\sqrt{m}$
T10S01	25.84	9.65	17.05	2.42	0.826497	0.510	0.272
T10S02	25.59	9.78	16.92	0.00	0.812046	0.436	0.226
T10S03	25.02	11.24	17.80	1.75	0.875578	0.421	0.207
T10S04	25.92	9.30	16.80	0.00	0.808306	0.487	0.263
T10S05	25.00	9.22	17.88	6.30	0.945540	0.395	0.256
T10S06	26.20	10.38	17.53	5.52	0.854318	0.555	0.282
T10S07	24.88	10.00	17.92	7.12	0.956106	0.428	0.259
T10S08	25.02	10.32	16.45	0.00	0.787968	0.487	0.235
Average							0.250
Standard deviation							0.025
T10SB1	51.21	11.69	28.37	3.65	0.733445	0.868	0.241
T10SB2	51.20	11.93	27.97	9.63	0.737625	0.701	0.191
T10SB4	50.77	11.30	26.30	6.38	0.693323	1.305	0.355
Average							0.262
Standard deviation							0.084

Compared to previous chapter, one can see that the fracture toughness of Pierre shale is smaller than that of Indiana limestone. And for both rocks, large samples have higher standard deviation, which may be attributed to the fact that the larger a sample, the

more defects in a sample. So the concern would be if the fracture toughness of caprock is even smaller than that of the target formation, then the fractures created in target formation may be easily extended to the caprock formation.

5.8. Non-destructive Method to Measure the Mechanical Properties of Weak Rock

Using traditional compression method, either uniaxial compression test or triaxial compression test, to measure the mechanical properties of rock may cause permanent damage to the rock, especially when the rock is a sort of weak sedimentary rock, such as shale. Therefore, a non-destructive method based on the measurements of elastic waves is another approach that is desired. It is also attractive if obtaining rock samples is expensive because of it being in a deep formation.

For the bulk modulus, Young's modulus and Poisson's ratio, the formulas based on P-wave velocity v_p, and S-wave velocity v_s for an isotropic material are (Fjaer et al., 2008):

$$K = \rho v_p^2 - \frac{4}{3}\rho v_s^2 \tag{5.9a}$$

$$E = \rho v_s^2 \frac{3v_p^2 - 4v_s^2}{v_p^2 - v_s^2} \tag{5.9b}$$

$$\nu = \frac{v_p^2 - 2v_s^2}{2(v_p^2 - v_s^2)} \tag{5.9c}$$

For a shale sample 08PA18 (length 53.34 mm, diameter 25.40 mm, density 1.52g/cm^3), the test results conducted by NER Autolab 1500 are shown in the following table.

Table 5.7. Elastic properties derived by elastic waves' measurements

Event	Confining pressure	Differential pressure	V_p	V_{s1}	V_{s2}	Average V_s	Bulk modulus	Young's modulus	Poisson's Ratio
	(MPa)	(MPa)	(m/s)	(m/s)	(m/s)	(m/s)	K (GPa)	E (GPa)	ν
1	5.1	0.4	2266	1217	1222	1219.5	4.79	5.86	0.296
2	5.2	0.5	2272	1218	1222	1220.0	4.83	5.87	0.297
3	5.2	0.4	2272	1224	1222	1223.0	4.81	5.89	0.296
4	10.2	0.6	2311	1227	1228	1227.5	5.06	5.97	0.303
5	10.2	0.5	2268	1222	1227	1224.5	4.78	5.90	0.294
6	15.1	0.3	2312	1233	1233	1233.0	5.04	6.01	0.301
7	20.1	0.4	2331	1231	1242	1236.5	5.16	6.06	0.304
8	20.3	0.4	2318	1240	1234	1237.0	5.07	6.05	0.301

The results are close to those conducted using destructive method. In addition, the results should only be applied as a rough estimation because shale is not an isotropic material. In fact, the method to derive the mechanical properties for anisotropic materials by measuring compressive and shear wave velocities is much more complicated (Lo et al., 1986), with specific sample preparation required.

At last, it was also noticed that there was a trend that Young's modulus increases with the increase of confining stress, even this trend was relatively minor, as shown in the following Figure 5.25.

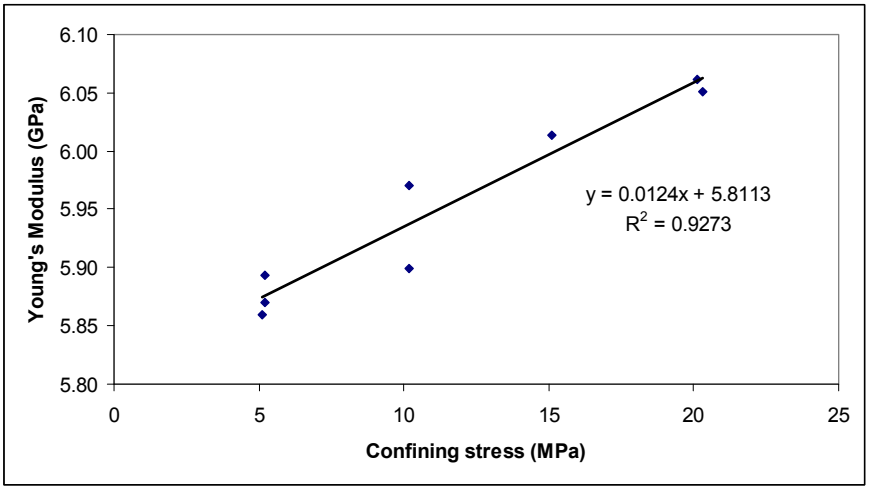

Figure 5.25. The Increase of Young's modulus with respect to confining stress

Concluding remarks

Outcrop Pierre shale can be easily weathered. Only the intact pieces were taken for lab tests; and only those that could preserve their integrity after sample preparation were tested. Thus, the laboratory test results probably define the upper boundary rather than the average of their mechanical strength.

Pierre shale samples have much lower Young's modulus and friction angles compared with many other types of rock such as limestones and/or dolostones. In a basin scale, one may imagine that the clayey layer will bear much more deformation than its neighboring formations under the same tectonic activity.

Dry Pierre shale shows much higher peak uniaxial strength than oil-wetted ones; however, their residual strengths are comparable, which may indicate that for Pierre shale, the Mohr-Coulomb failure envelope constructed based on the residual strength may be even more reliable. Shale strength may also be decreased by exposure to CO_2.

Dry shale is relatively stable under a single phase flow, even with water, provided the confining pressure is high. However, serious deterioration was observed on the sample under CO_2 flow after water flow. The mechanisms of shale deterioration at surface due to exposure to water and at depth due to multiphase flow (CO_2 and water) are different (Ma and Eggleton, 1999).

Many factors can influence the permeability of clayey rock, including confining pressure, flooding history, fractures, etc. In the field, permeability (as demonstrated by the dispersivity of tracer) is generally orders of magnitude greater than values obtained from laboratory experiments, and it appears to increase as the size of the high concentrated plume increases (Gillham and Cherry, 1982). This phenomena associated

with natural hydro-geologic environments have been attributed to the effects of geologic heterogeneity.

The clayey caprock can either be water wetted (above the oil reservoir) or hydrocarbon wetted (above the saline aquifer) or intermediate. The original host formation pressure is often taken as the primary criterion, which is based on the assumption that the sealing capacity of the caprock that retained the fluid in the first place should be adequate to prevent the injected CO_2 from escaping through the caprock (Bachu and Adams, 2003). However, the interfacial tension of the new system may differ from that of the original system greatly, and this change might result in a lower capillary sealing pressure of the caprock (Li et al., 2006). The fluid phase change may potentially result in a serious deterioration of the caprock.

Argillaceous sediments at sufficient depths (>1000m) may have mean pore-sizes of a few nano-meter or smaller, thus the fixed charges associated with clay surfaces are responsible for a component of 'bound' water differing considerably from bulk water in both structure and dynamics (Hall, 1994). How to correlate laboratory test results to actual field condition remains a challenge.

The fracture toughness of caprock in comparison with that of the target formation is a key parameter to address the question whether a facture developed underneath could be extended easily upwards.

CHAPTER VI

GEOMECHANICAL STABILITY STUDY BY NUMERICAL MODELING

With the development of computer science, numerical modeling has found its ever important role in geosciences. In fact, major parts of current research either in the natural or social sciences can no longer be imagined without numerical simulations. The main motives to run simulations are: (1) to investigate the detailed dynamics of a system, (2) to perform numerical experiments and support laboratory experiments, and (3) to develop hypotheses and models or even new theories (Hartmann, 1996).

In geosciences, laboratory tests can provide a reliable understanding of rock materials but are constrained to small scales. Field observations can provide large scale information, but how to interpret these information may be an issue. In addition, a consistent field record over many years may be needed in order to obtain a meaningful derivation, let alone the financial and labor problems related. All these limitations direct to the application of numerical modeling, which can apply laboratory results to a field problem during a short time frame. In fact, it may be advantageous if laboratory tests, field observations, and numerical modeling could be incorporated (Figure 6.1), with different emphasis on different areas for different projects.

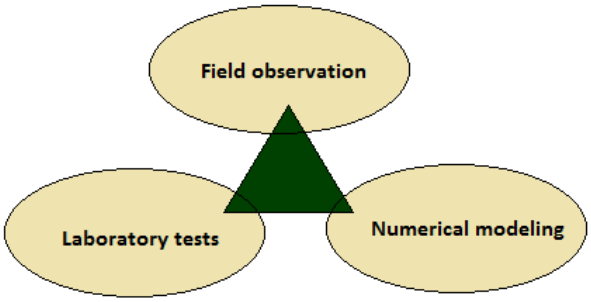

Figure 6.1. A triangle for geosciences research

A program (FLAC) based on finite difference method is used in this numerical study. For many practical applications the continuum approach is valid, provided the properties are applied as an average and the length scale is large compared to the size of the heterogeneities (Fjaer et al., 2008). However, a major difficulty of using this kind of software is how to simulate a fault (or fracture), which is a discontinuity within a continuous domain, and this will be one of the key issues that need to be solved in this chapter.

6.1. Finite Difference Method (FDM)

The finite difference method is a numerical method to approximate differential equations by using finite difference equations to approximate partial derivatives (Ames, 1977). Finite difference method is based on the Taylor series (Dahlquist and Bjorck, 1974), as shown in Equation 6.1.

$$\frac{y(x_{n+1})-y(x_n)}{h} = y'(x_n)+\frac{h}{2}y''(x_n)+\frac{h^2}{3!}y'''(x_n)+\frac{h^3}{4!}y^{iv}(x_n)+\cdots \qquad 6.1$$

By the Lax equivalence theorem, a consistent, two-level difference scheme for a well-posed linear initial value problem is stable if, and only if, it is convergent.

FLAC3D is an explicit finite difference program to study, numerically, the mechanical behavior of a continuous three-dimensional medium as it reaches equilibrium

or steady plastic flow (Itasca, 2006a). In FLAC3D, the laws of motion for the continuum are transformed into discrete forms of Newton's law at the nodes, and the resulting system of ordinary differential equations is then solved numerically using an explicit finite difference approach in time. In explicit finite difference scheme, the entity at time n+1 depends explicitly on the entity at time n. This scheme has the advantages that are relatively simple and computationally fast.

6.2. Numerical Rock Mechanical Properties Validation

The measured mechanical properties of rocks can be directly used as the input of numerical rock models. To verify these numerical rock models, a series of numerical tests needs to be conducted to allow a comparison between laboratory test results and the numerical test results. Of course, a strict similarity can hardly, if not impossible, ever be obtained as rock is never a perfectly homogenous material and numerical space is a vacuum space where energy is strictly conserved, different from the real world, where heat dissipation occurs everywhere and all the time (Zhou, 2007). However, a general similarity, such as the overall failure behavior and the trend of stress-strain curve, etc., will allow a judgment whether the numerical model is reasonably close to the reality and the numerical tests make sense.

6.2.1. A Strain-Hardening/Softening Mohr-Coulomb Model for Indiana Limestone

From the laboratory tests section, one can see that Mohr-Coulomb criterion applies to the failure behavior of Indiana limestone very well, and the after-yielding behavior of this type of rock can either be strain-softening, perfect plasticity or strain-hardening, depending on the confining pressure. Thus, a strain-hardening/softening Mohr-Coulomb model is chosen from the many models available in the FLAC3D to

describe Indiana limestone.

The strain-hardening/softening Mohr-Coulomb model in FLAC3D is based on Mohr-Coulomb model with non-associated shear and associated tension flow rules. In this model, the cohesion, friction, dilation and tensile strength may harden or soften after the onset of plastic yield; while in a pure Mohr-Coulomb model, those properties are assumed to remain constant.

Consider a stress-strain curve of a typical uniaxial or triaxial test at low confining pressure for a limestone, which softens upon yield and attains some residual strength as in the following Figure 6.2.

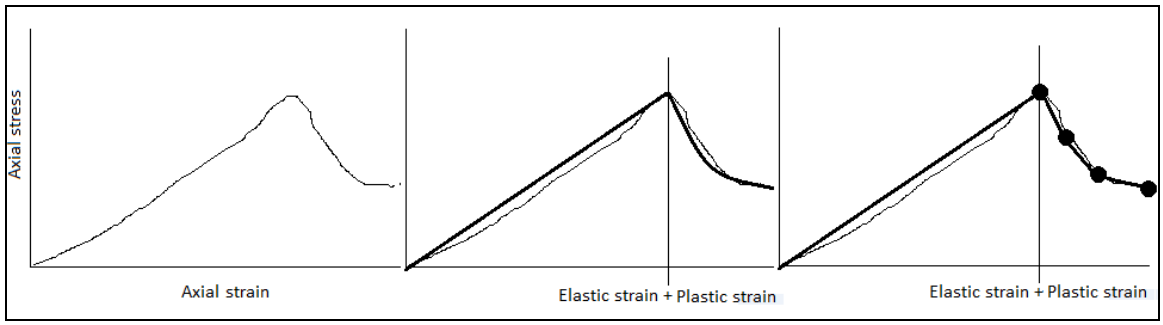

Figure 6.2. Plastic strain is approximated by linear segments

The curve can be firstly approximated by a straight line to the point of yield; in that range, the strain is assumed to be elastic only. After yield, the total strain is composed of elastic and plastic parts. In the softening/hardening model, the cohesion, friction, dilation and tensile strength can be defined piece wisely as a function of the plastic portion of the total strain.

The failure envelope for this model corresponds to a Mohr-Coulomb criterion (shear yield function) with tension cutoff. To implement this model, an elastic guess is firstly computed by adding to the stress components, increments calculated by application

of Hooke's law to the total strain increments. Principal stresses and corresponding directions are then calculated. If the stresses violate the yield criterion, then either shear failure takes place or tensile failure occurs. Otherwise, no plastic flow takes place, and new increment of stresses is used for the next step (Itasca, 2006a).

At low pressure and temperature regime, Indiana limestone can be described by the shear softening model in FLAC3D. The strain-softening model assumes both a brittle softening due to reduction in cohesion, and a gradual softening due to a reduction in friction angle.

It is important to validate the mechanical properties of rock sample by conducting numerical tests, in comparison with the actual tests.

6.2.2. Numerical Tests: Uniaxial Test, Brazilian Disc Test and Triaxial Test

Numerical uniaxial test is the first test to verify the numerical behavior of Indiana limestone. Table 6.1 shows the parameters for this rock model.

Table 6.1 Input parameters for Indiana limestone under the numerical uniaxial test

Basic mechanical property	
Density (kg/m^3)	2400
Bulk modulus (Pa)	2.12×10^{10}
Shear modulus (Pa)	1.21×10^{10}
Cohesion (Pa)	6.00×10^{6}
Friction angle	42°
Tensile strength (Pa)	2.00×10^{6}
Dilation angle	10°
Loading rate	3×10^{-7} (m/s) both upper and lower piston

Note the basic mechanical properties assigned were based on the actual laboratory tests described in Chapter IV, and strain-softening behavior was calibrated based on the observation of these laboratory tests. The focus of these calibrations was on the shear band or shear fracture development. The well-defined shear band indicates the shear

fracture developed after failure (Figure 6.3) and the corresponding strain-stress curves are shown in Figure 6.4. One may make a comparison with Figure 4.8, the rock sample at low confining pressures.

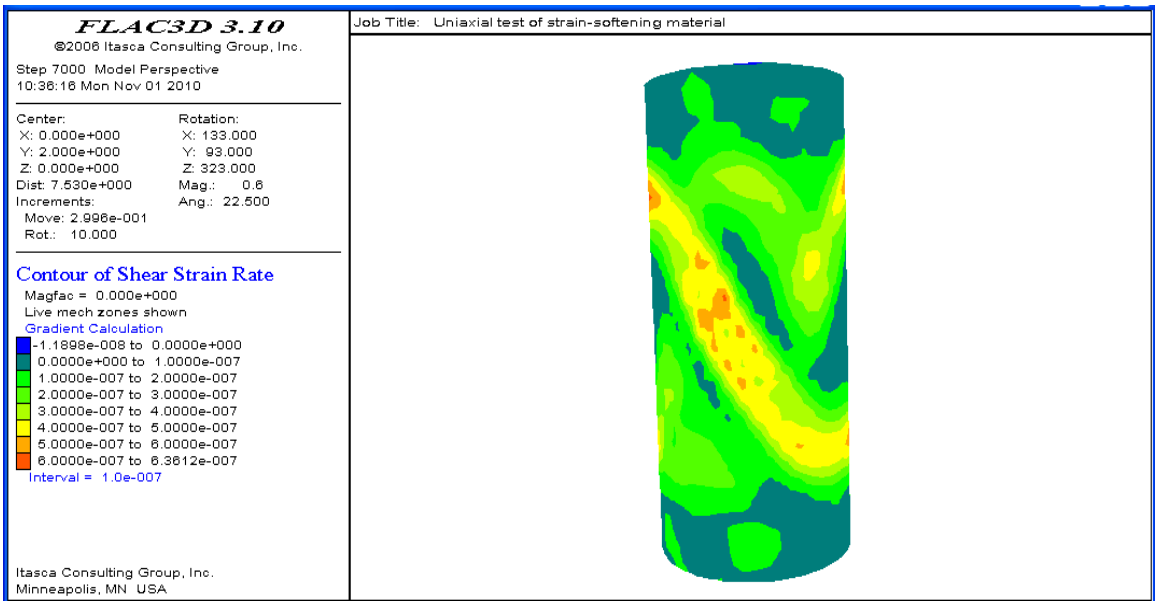

Figure 6.3.Contours of shear-strain rate indicating shear bands after failure of rock

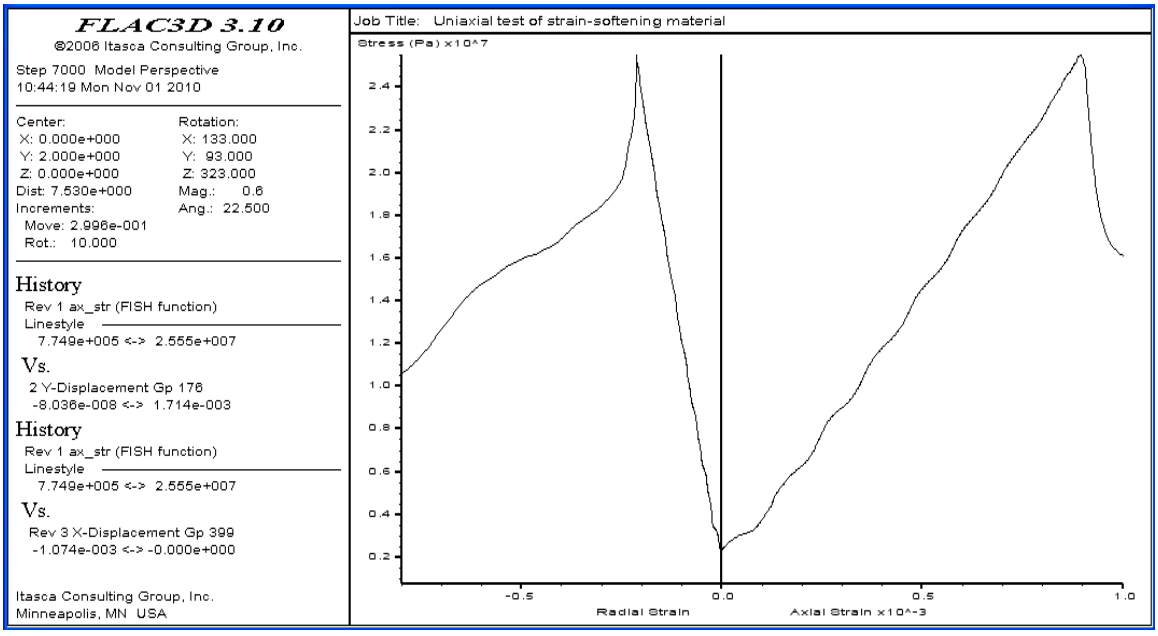

Figure 6.4. Axial strain, radial strain as a function of axial stress

Next, numerical Brazilian disc tensile test was conducted on this rock model and

the results are shown in the following Figures 6.5 and 6.6. By comparing with Figure 4.10, one can see that a good agreement presents. The abnormal displacements as indicated by the red and green dots in Figure 6.5 imply the potential failure regions; in reality, these are demonstrated by the larger opening of the fracture at both tips (Figure 4.10, left). Here the fracture is clearly indicated by the displacement contour.

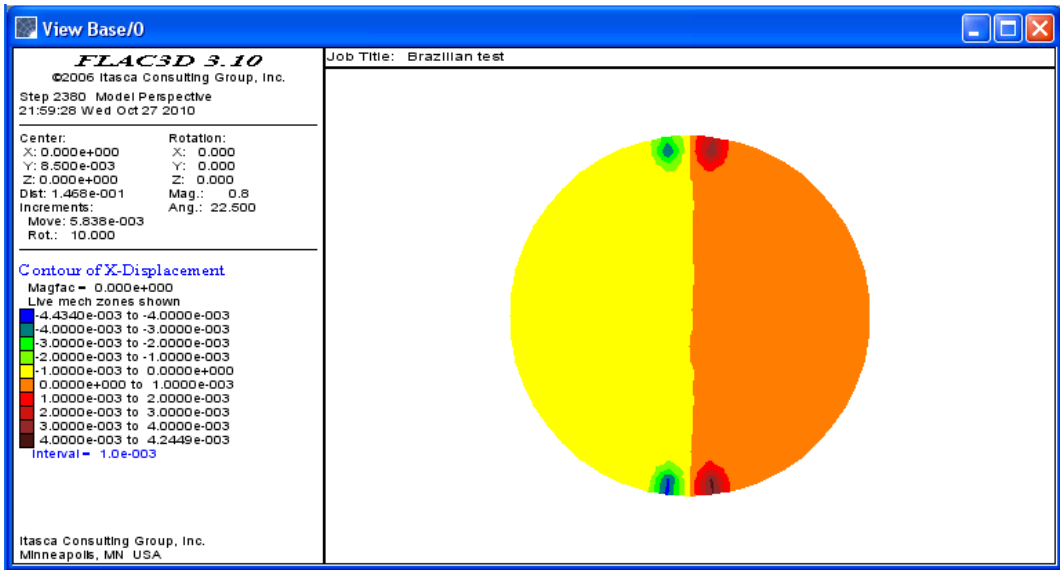

Figure 6.5. The dissection of a rock sample under the Brazilian test

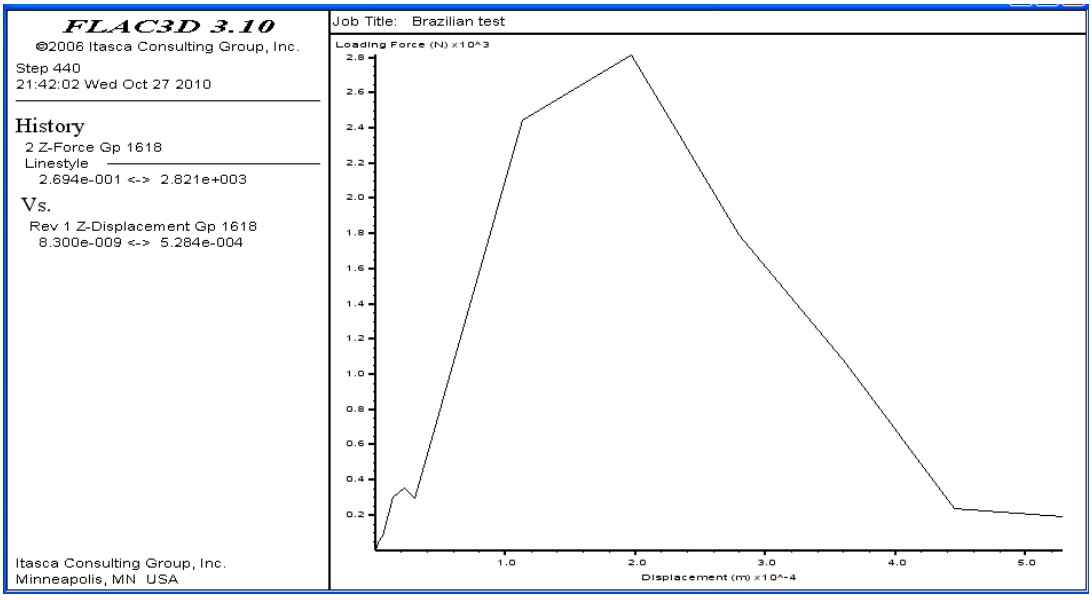

Figure 6.6. The curve of load versus displacement of the numerical Brazilian test

In the numerical triaxial test, besides the strain-softening model, strain-hardening model and elastic-perfect-plastic model (pure Mohr-Coulomb model) were also considered, as shown in the following Figure 6.7, 6.8, and 6.9. Note rock model in Figure 6.7 is strain-softening; it is elastic-perfectly-plastic in Figure 6.8, and is strain-hardening in Figure 6.9.

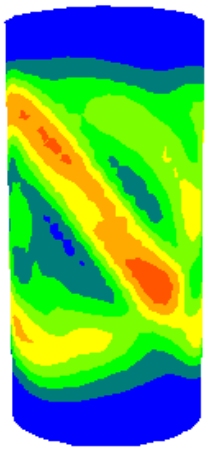

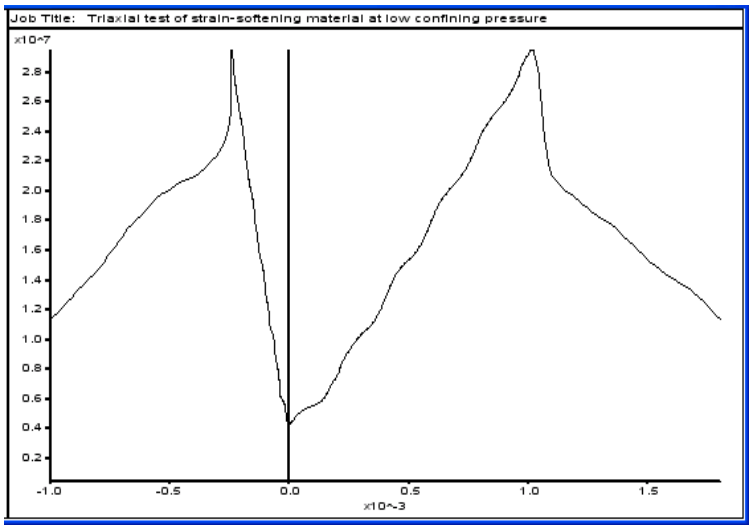

Sample image after test Axial stress versus axial strain and radial strain curves

Figure 6.7. Numerical triaxial test on rock sample at low confining pressure (30 psi)

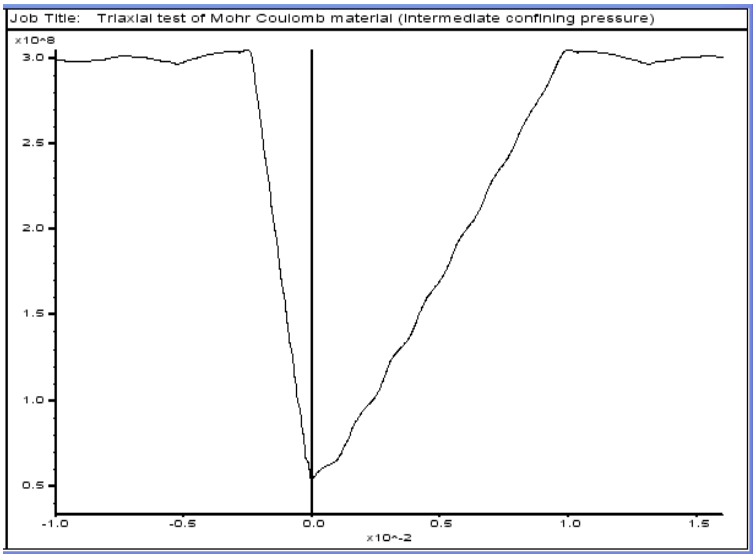

Sample image after test Axial stress versus axial strain and radial strain curves

Figure 6.8. Numerical triaxial test on rock sample at intermediate confining pressure (2,000psi)

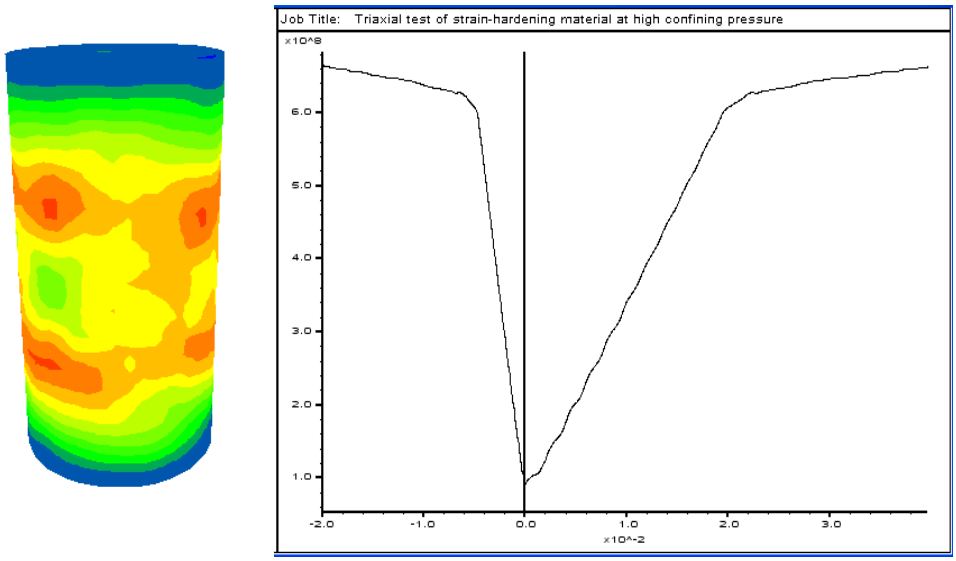

Sample image after test Axial stress versus axial strain and radial strain curves

Figure 6.9. Numerical triaxial test on rock sample at high confining pressure (4,000psi)

One can see that a well defined fracture can only be developed by using strain-softening model, and this agrees with the actual laboratory tests (Figure 4.8). Note rock samples do not present well defined fractures under strain-hardening or perfect plastic flow. Here, which model should be used will be determined by the confining stress, or more exactly, the minimum effective principal stress.

Rocks at low confining stress (such as those near the ground surface) tend to behave brittle (strain-softening) and at high confining stress tend to be ductile (strain-hardening or perfect plastic). However, rock at deep formations with high confining stress can still fail in a brittle manner; the reason is that the increased pore pressure reduces the minimum effective principal stress. From the standpoint of numerical simulation, the logic is that rock changes from a strain-hardening model to a strain-softening model if the increased pore pressure (or decreased minimum effective principal stress) crosses over a certain threshold.

6.3. Faulting Simulation

Fracture in small rock samples induced in laboratory tests could be extrapolated to the occurrence of faulting on the fields. Geomechanical modeling of fault stability is an integral part to ensure the safe storage of carbon dioxide in subsurface formations. Faulting of rock is the response to tension, compression or shearing stress. Fault planes are usually permeable zones along which fluids can penetrate and even deposit valuable ores (Levin, 1981). Joint is the fracture that presents little or no relative displacements between the two separated blocks, which can be treated as a special case of fault.

The underground stress state can be described using three mutually orthogonal principal stresses and the pore pressure (Fjaer et al., 1992). Differentiating principal stresses could introduce faulting in the rock formations, and the type of fault (normal, reverse (thrust), or strike-slip fault) and its angle is dependent on both the effective principal stresses and the mechanical properties of rock formations.

The correlation between faulting and in-situ stress regime was first recognized by Anderson (1951), as shown in the following Figure 6.10. For horizontally bedded sedimentary basin, it is common to assume that the vertical stress is a principal stress, i.e., σ_v. With such assumption, the other two principal stresses on the horizontal plane would be σ_h and σ_H , and there is always $\sigma_H \geq \sigma_h$.

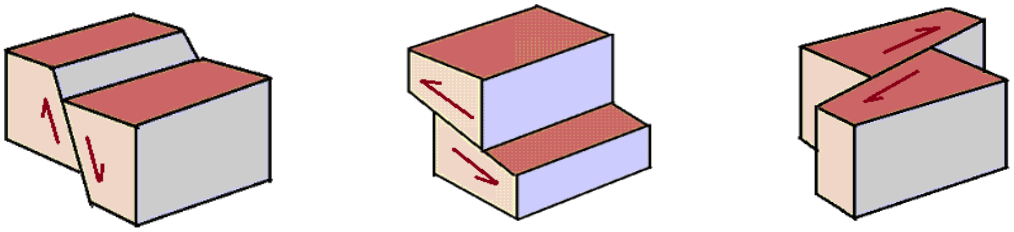

(a) Normal fault $\sigma_v > \sigma_H > \sigma_h$

(b) Reverse (Thrust) fault $\sigma_H > \sigma_h > \sigma_v$

(c) Strike-slip fault $\sigma_H > \sigma_v > \sigma_h$

Figure 6.10. Fault types and the corresponding principal stress regimes

There is an intrinsic correlation between macro-scale faulting (Figure 6.10) and micro-scale rock fracture (Figure 3.6). Mode I fracture is an opening mode, and this mode may correspond to normal faulting, the joints created by rock cooling, or tension failure due to high pore pressure; Mode II fracture is due to sliding or shearing, which may correspond to the other two types of faulting; and Mode III fracture may be considered as a combination of different faulting behaviors in the field.

In the numerical space, differentiating three principal stresses will result in faulting in a rock block. The following Figure 6.11 shows the numerical testing results with different faulting types, and these in-situ stress induced faults are indicated by strain concentrations. The in-situ stresses listed below are the threshold data in which faulting was just initialized.

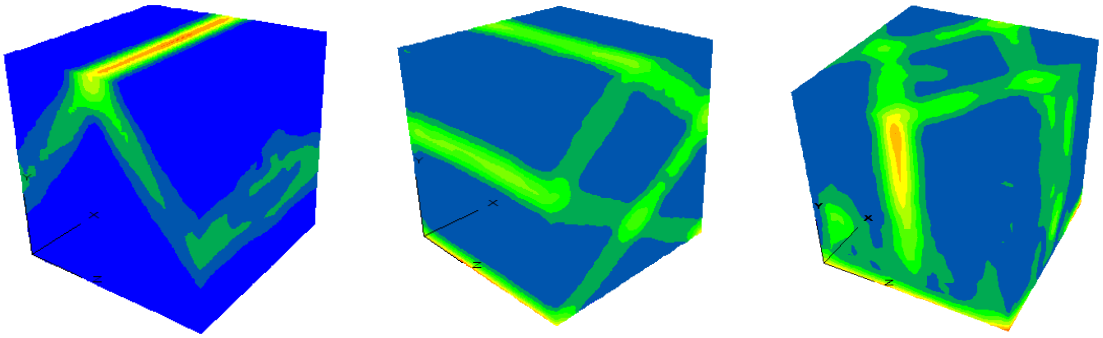

(a) Normal fault
$\sigma_v = 1.40\times10^8\,Pa(20{,}300\,psi)$
$\sigma_H = 3.50\times10^7\,Pa(5{,}070\,psi)$
$\sigma_h = 2.50\times10^7\,Pa(3{,}630\,psi)$

(b) Reverse fault
$\sigma_H = 1.04\times10^8\,Pa(15{,}100\,psi)$
$\sigma_h = 3.50\times10^7\,Pa(5{,}070\,psi)$
$\sigma_v = 2.00\times10^7\,Pa(2{,}900\,psi)$

(c) Lateral (Strike-slip) fault
$\sigma_H = 1.06\times10^8\,Pa(15{,}400\,psi)$
$\sigma_v = 4.50\times10^7\,Pa(6{,}530\,psi)$
$\sigma_h = 1.50\times10^7\,Pa(2{,}180\,psi)$

Figure 6.11. Fault types and the corresponding principal stresses in numerical space

Once a fault is initialized, generally it will be a weak plane; even though the opposite may also be present. And then this fault will be simulated by the interface model or weak zone in FLAC3D. It is well noticed that to initialize a fault and to reactivate a pre-existing fault will need different threshold of stresses.

A weak zone can be generated by defining weaker mechanical properties in comparison with its neighbors, and a few weak zones can be grouped into a specific geometry shape to represent a fault. On the other hand, interface model in FLAC3D is characterized by Coulomb sliding and/or tensile and shear bonding, which has the properties of friction, cohesion, dilation, normal and shear stiffness, and tensile and shear bond strength. Both approaches can be used to simulate faulting, as shown in the following Figure 6.12.

However, usually it is much more difficult to acquire the parameters that are required for the construction of an interface model, especially for a field without data support from actual laboratory test. On the other hand, a weak zone approach is more reasonable as it approximates the reality in an even more "natural" sense, i.e., the weak properties of materials can be either measured in laboratory or estimated based on the adjacent intact rock specimens. Therefore using weak zone to simulate faulting is recommended (Han, Y.H., personal communication, Nov, 2010; Han is a senior research staff of Itasca group, Minneapolis, MN).

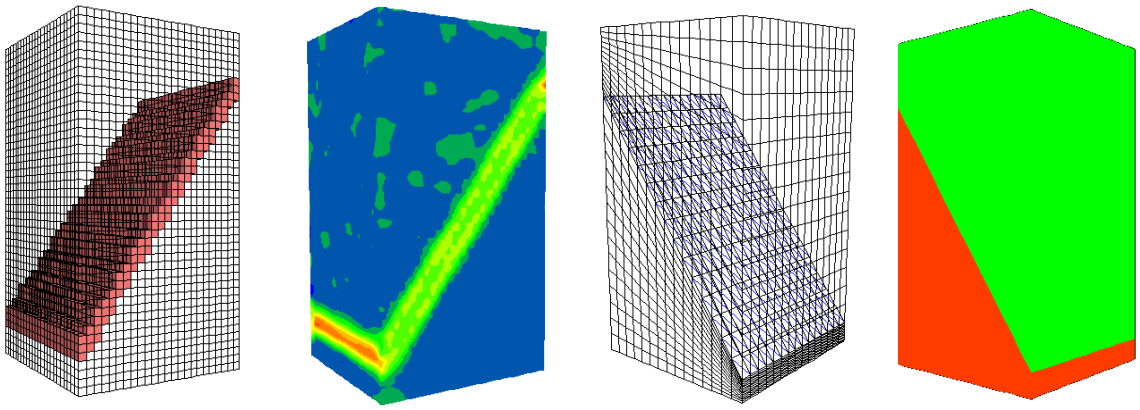

(a) Fault simulated by weak zones (b) Fault simulated by interface model

Figure 6.12. Fault simulation by different approaches

6.4. CO_2 Plume Simulation

Three fundamental processes can bring about permanent rock deformation, including cataclasis such as faulting, intra-crystalline plasticity and flow by diffusive mass transfer of matter through grains (Rutter, 1983). Besides in-situ stresses and intrinsic rock properties, pore fluid also plays an important role in the stability of rock formations.

FLAC3D models the flow of fluid through a permeable solid. The flow modeling may be done in parallel with the mechanical modeling in order to capture the effects of fluid and solid interaction (Itasca, 2006b). The variables involved in the description of fluid flow through porous media are the pore pressure, saturation and permeability. These variables are related through the fluid mass balance equation, Darcy's law for fluid transport, a constitutive equation specifying the fluid response to changes in pore pressure, saturation, volumetric strains, etc.

Different permeabilities can be assigned to different blocks to define the fluid flow behavior. For example, the CO_2 plume may either be expanding in a circular motion or directed by a preferential flow path, as shown in the following Figure 6.13. The CO_2 plume migrated from a vertical injection well is identified by the pore pressure contour. One may also make a comparison with Figures 2.7 and 2.8.

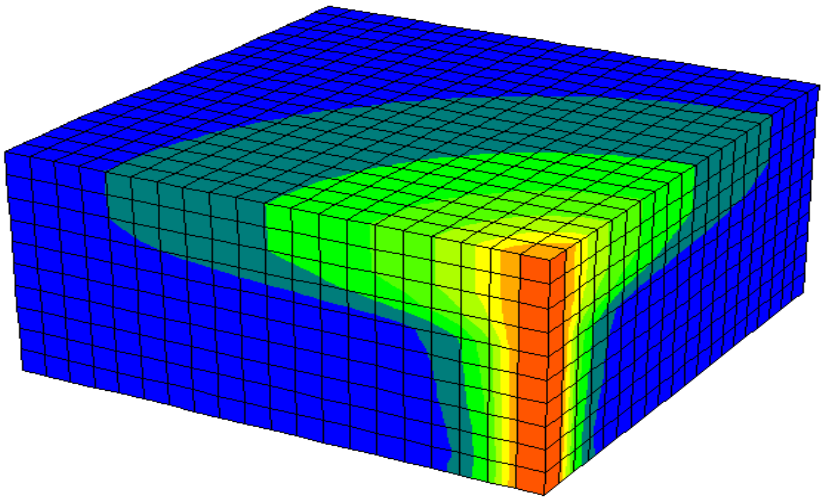

(a) CO_2 plume expands in a homogenous formation

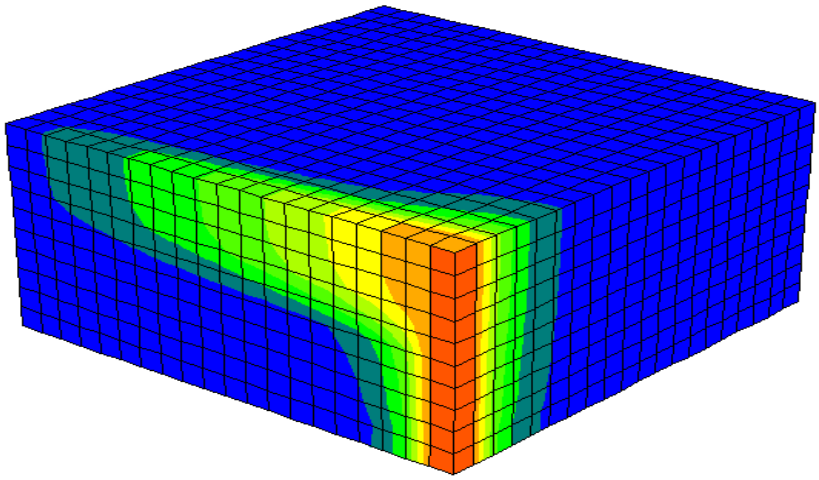

(a) CO_2 plume directed by preferential flow path

Figure 6.13. CO_2 plume migration simulation

6.5. Formation Stress Path Simulation

Formation stress path refers to the changes in the in-situ stresses that accompany changes in pore pressure during injection or production (Goulty, 2003), as pore pressure changes cause deformation processes due to the coupling between pore pressure and stresses. Formation stress path is essential for fracture initiation or fault reactivation and other geomechanical issues, such as sand production, drilling mud losses, hydraulic

fracturing, etc (Altmann et al., 2010).

The behavior of a rock block under the influence of pore pressure buildup was simulated. At first, a rock sample was installed with initial pore pressure and in-situ stresses (in this case, the depth is about 5,000ft (or 1,520 m)), and then the pore pressure was increased stepwise.

The results are summarized as in the following Table 6.2.

Table 6.2. Formation stress path simulation results

Numerical sample ID	Initial in-situ stress conditions	Pore pressure (psi)		
		Initial state: Pore pressure at 2,600psi	Pore pressure increased to 3,500psi	Pore pressure increased to 4,800psi
N_L_0	σ_H= 6,500 psi σ_h = 5,000 psi σ_v = 5,000 psi	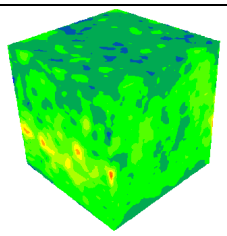	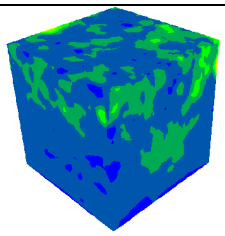	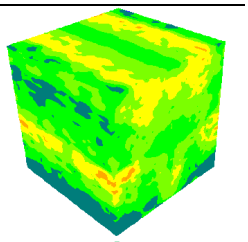
N_L_300	σ_H= 11,600 psi σ_h = 5,000 psi σ_v = 5,000 psi	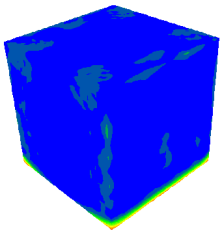	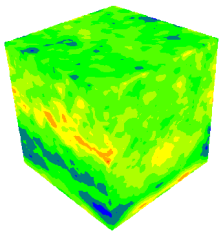	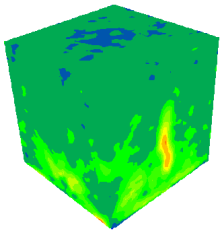
N_L_1000	σ_H= 18,800 psi σ_h = 5,000 psi σ_v = 5,000 psi	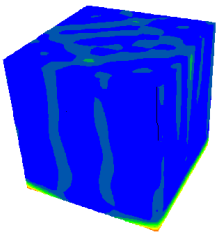	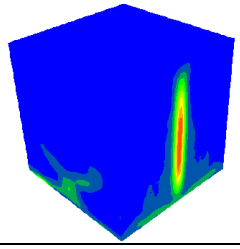	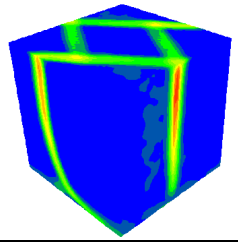

Here, for sample N_L_0, the initial state was very safe, and the increases of pore pressure did not cause strain concentration at both steps; for sample N_L_300, the initial state was not very close to failure either, the increase of pore pressure at the first step didn't cause strain concentration but raised minor concentration at the second stage; for

sample N_L_1000, which was already very close to failure at the beginning, the increase of pore pressure caused strain concentration at both stages: the higher the increase of pore pressure, the worse the scenario. This can also be justified by the Mohr-Coulomb failure envelope approach, as shown in the following Figure 6.14.

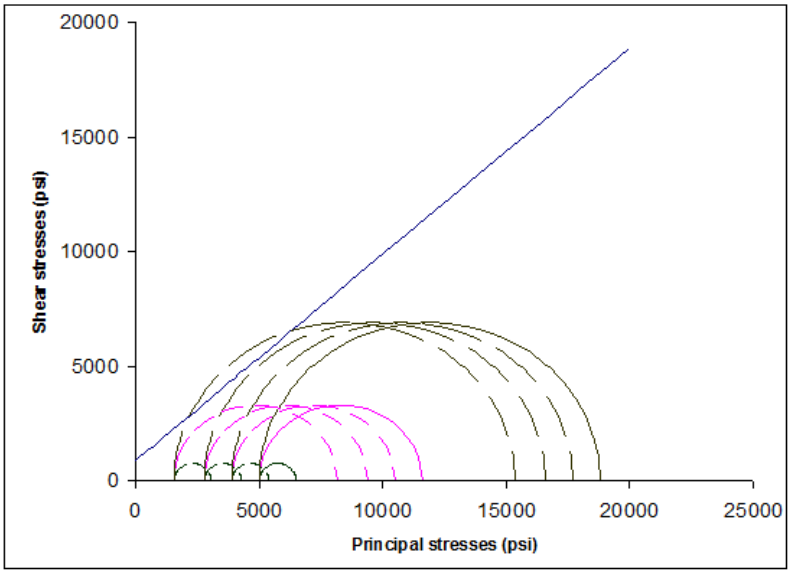

Figure 6.14. Pore pressure increase induced failure by drawing Mohr Coulomb envelope

Concluding Remarks

By injecting CO_2 into the reservoir, pore pressure builds up, resulting in a decrease of effective stress, often heterogeneously. This increased pore pressure will shift the Mohr's Circle to the left, and may approach the frictional failure envelope (Jaeger et al, 2007). Once the envelope is reached, faults may either be initialized or be reactivated abruptly. Early CO_2 breakthrough may be triggered. The potential for this to occur should be evaluated on a site-specific basis as part of baseline study.

Numerical modeling is a powerful tool to predict or verify the failure behavior of rock formation under different conditions. Whether the increase of pore pressure due to fluid injection may initialize (or reactivate) faults or not depends on the conditions of

initial in-situ stresses, the geomechanical properties of rock formations, and the level of pore pressure fluctuation.

However, it is important to recognize that a challenge to simulate a real situation lays in "up-scaling" laboratory scale strength parameters so that they may be applied to much larger scales of design. Rock mass properties are intrinsically difficult to determine (Pine and Harrison, 2003). It is generally accepted that there is a significant reduction in strength with increasing sample size of concern, as the larger a region, the more imperfections involved. Failure is most likely to be determined by the weakest part. The overall properties of rock mass generally must be determined from fields where stress or strain is obtained from solutions to boundary value problems (Pariseau, 1988).

The Mohr-Coulomb envelope for rock mass may greatly be reduced in comparison with intact rock, thus the difference between principal stresses will also be much more constrained and further, the room to allow pore pressure fluctuation would be much smaller.

Due to this "up-scaling" difficulty, and the constrain on energy conservative issue in numerical space, as mentioned before, the results from numerical simulations should only be taken as a guide for an overall understanding of this problem.

With the development of computer software and more reliable field tests to be conducted, some difficulties may be overcome, but some may not be, at least in the foreseeable future. Thus it is important to recognize the limitation of the numerical approach.

CHAPTER VII

GEOMECHANICAL STABILITY ANALYSIS FOR CO2 SEQUESTRATION IN THE WILLISTON BASIN

The evaluation of suitable regions for large scale CO_2 injection and storage is a multidisciplinary subject that must consider many different factors. From the standpoint of geomechanics, the premier concerns are the assessment of in-situ stress, fault initiation, and fault reactivation mechanisms (such as those due to pore pressure change and/or rock quality deterioration because of chemical reactions with injected fluids).

Sedimentary basins are the logical choice of geological sequestration of CO_2 because they possess the right type of porous and permeable rocks. However, convergent basins subject to volcanism, faulting and earthquakes, like those in California, may pose safety and environmental risks. Divergent basins are located in much more stable areas that are not prone to volcanism and earthquakes. Thus, geological sequestration of CO_2 in divergent basins is much safer than in convergent basins because of the tectonic stability and general lack of significant hazardous events (Bachu, 2000).

As a large intra-cratonic basin, the Williston Basin is considered by many a favorable region for CO_2 sequestration due to its tectonic setting. In fact, the Weyburn CO_2 sequestration project at this basin can be considered as a pioneer in the global carbon sequestration effort (White et al., 2011).

7.1. Regional Geology of the Williston Basin

The Williston Basin is a 500,000 square kilometer (or 190,000 square miles)

structural basin, not bounded by topography, in eastern Montana, western North Dakota, western South Dakota, southern Saskatchewan and southwestern Manitoba. It is a large elliptical downwarp with the deepest point (about 4,800 m or 16,000 ft) near Watford City, North Dakota (Fisher et al., 2005). This basin is entirely situated within the North America Craton, which has remained relatively stable since the Precambrian. The earliest extensive deposition of sedimentary rock in this basin began in the late Cambrian (Bluemele, 2000).

The entire stratigraphic succession in this basin ranges from Middle Cambrian and Early Ordovician sandstones that directly overlie the Precambrian basement to Quaternary rocks at surface. Two categories of rocks are resulted from the depositional history: Paleozoic rocks that are mainly carbonate, evaporate and minor shale; Mesozoic rocks that are dominated by shale, siltstone and sandstone (Laird, 1964; Murphy et al., 2009).

Due to the thickness of the sediment package in the basin, the nature of the Precambrian basement surface is not very clear. A common belief is that this basin is mostly underlain by the Trans-Hudson Orogen or Western Dakota Mobile Belt with two cratons (Superior Craton and Wyoming Craton) on the east and west edges (Green et al., 1985). The mountains on the Trans-Hudson Orogen were entirely eroded long before the early Cambrian, when the basin started to form. However, the roots of these mountains remain and some may have significant relief. These mountain roots most likely have an overall north-south trend parallel to the Precambrian Orogenic activities (Bluemele, 2000).

Rocks deposited during all periods of Phanerozoic time are present in the basin.

Carbonates dominate the Paleozoic rocks, while Mesozoic and Cenozoic rock sequences are mainly clastic (Gerhard et al., 1982). Sloss's (1988) sequence concept is well defined by the rocks in this basin. Over the history of the basin shallow tropical or subtropical seas transgressed several times, which resulted in the accumulation of thick sedimentary package. The basin also experienced periods of erosion as the seas regressed, indicated by the many unconformities found between many rock formations.

The impacts of recent Quaternary glacial events are constrained to shallow depths and have a limited influence on the geologic structure in this basin. Nevertheless, by removing a certain portion of overburden, a higher horizontal stress may be "locked" in place to make the stress estimation at shallow depths more complicated (Lyons and Plisga, 2005).

The left lateral shearing motion along the Colorado-Wyoming and Fromberg zones during pre-Phanerozoic time is thought to have created enough tension to develop sag for this basin (Fisher et al., 2005). The basement is dissected into blocks by a series of tectonic features referred as lineaments, which are believed to be responsible for the origin of structures and depositional patterns within this basin. The major geological structures in this basin include the Nesson anticline, Billings Anticline, Cedar Creek Anticline and Poplar Dome (Figure 7.1).

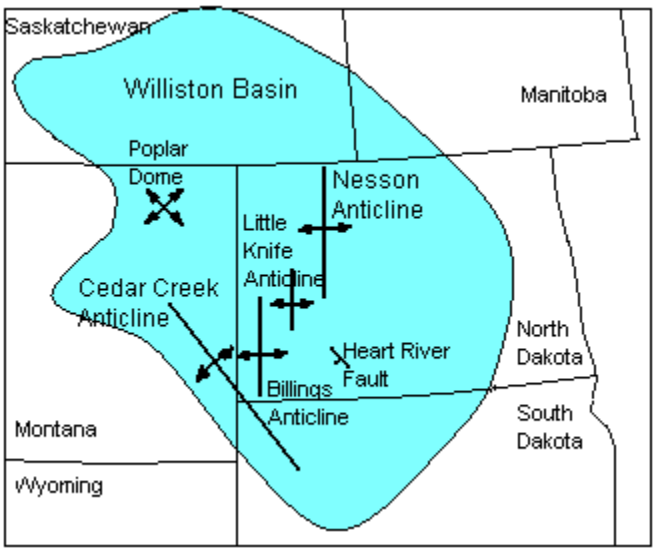

Figure 7.1. Major geological structures in the Williston Basin (modified after Gerhard et al., 1982)

Since the Williston Basin is located relatively far inside the North America Craton, the Cordilleran Orogenic activity may have little disturbance to this basin's stability (Downey et al., 2001). However, it may induce some strike-slip faulting movements found in the west flank of this basin (LeFever et al., 1987).

7.2. Hydrological, Geothermal and Geochemical Facts

The geological framework of the Williston Basin is well documented; however, fluid movement within that framework is not (Bachu and Hitchon, 1996). Aquifers are predominantly clastic or carbonate in composition and aquitards include shale, evaporites and filled breccias. Both aquifers and aquitards are locally and laterally discontinuous (Leonard et al., 1983; Iampen and Rostron, 2000).

Five major aquifers (Downey, 1984) are recognized in the northern Great Plains region, which includes the Williston Basin. These aquifers are separated by four major confining units. The current gravity-driven flow model of the basin involves recharge at the uplifts (the Black Hills, Pryor Mountains, Bighorn Mountains, Beartooth Mountains

and Little Rocky Mountains), lateral flow across the basin toward the north–east and discharge along the eastern margins (Downey and Dinwiddie, 1988). Altitude differences between the recharge and discharge areas of more than 1,000 m provide the driving force for regional fluid flow pattern.

However, this basin-scale model is very simplified, and researchers found that recharging groundwater from the southwest do not pervasively penetrate all formations across the basin. Instead, they appear to preferentially move into the basin as fingers or "tongues" of light water. There is also a slow flow to stagnant zone of brines in the deepest central part of the basin (Rostron and Holmden, 2003).

Shallow aquifers can become contaminated if deeper saline aquifers discharge the water by upward leakage. In northeastern North Dakota, for example, aquifers in rocks of Cretaceous and Paleozoic age on the eastern flank of the Williston Basin contain highly mineralized water that is under artesian pressure. These types of salty water are common in surface waters in Pembina, Walsh, and Grand Forks Counties, where only salt-tolerant plants and aquatic life can servive (Whitehead, 2009). The slightly higher head on the east side of the Red River and north side of the Assiniboine River may provide an effective pressure barrier that prevents north-eastward migration of saline water from the basin (Grasby and Betcher, 2003).

The $\delta^{18}O$ values of formation waters in Paleozoic strata on the northeast flank of the Williston Basin suggest fresh waters intruded deep into the basin and mixed with basin brines. The regional scale flow systems of sedimentary basins may be highly dynamic, and the present-day flow system of this basin is likely reestablishing the new boundary conditions set upon the removal of the ice sheet (Grasby and Betcher, 2000).

On a regional basis the three basic factors controlling the thermal regime are the regional heat flow, thermal conductivity and heat transfer by ground-water movement. The geothermal gradient in the Williston Basin is about 2 degrees Fahrenheit per 100 feet of depth (or 35 °C/km) (Morgan and Gosnold, 1989).

Ground-water flow is clearly responsible for much of the lateral variation of heat flow in the Great Plains. Regional groundwater flow over structures in the Williston Basin's North Dakota portion generates local heat-flow anomalies in the order of 10 to 20 mWm^{-2} (Gosnold, 1988 & 1999). Aquifers in the Williston Basin shows a temperature-distribution pattern with the lowest temperature near the margins of the basin and the highest near the center of the basin (Whitehead, 2009). Thus, depending on the locations, temperature varies along a single formation.

Water temperatures in the upper Cretaceous aquifers are around 32 °C (90 °F) as measured in Fox Hills Sandstone. The underlying lower Cretaceous aquifers are 88 °C (190 °F) in part of the Williston Basin as measured in Dakota Sandstone. The upper Paleozoic aquifers are greater than 100 °C (212 °F) in some areas of the Williston Basin. The lower Paleozoic aquifers (mostly Cambrian sandstones and Ordovician limestones) are approaching over 150 °C (302 °F) in the deep parts of the basin (Gosnold, 1999).

The temperature field of sedimentary basins is one of the decisive factors governing petroleum generation and coal evolution as well as many other diagenetic reactions. Warm water tends to migrate upwards while cold water tends to descend. Combining this local circulation with the basin wide ground water flow pattern, a proposed geothermal and hydrological flow regime can be drawn as the following Figure 7.2.

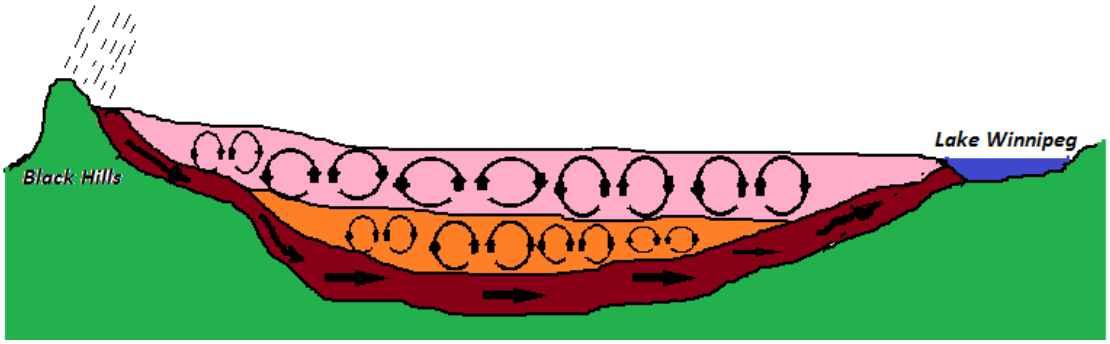

Figure 7.2. A proposed flow regime cartoon of the Williston Basin

Geochemically, three main types of water are present in the basin: (1) a "fresher" water of dominantly Ca-SO_4 type with total dissolved solids (TDS) less than seawater (35 g/l), (2) a "brine" of dominantly Na-Cl type with TDS>100 g/l, and (3) a "brine" of Na-Ca-C1 composition with TDS>200 g/1. Water composition across the basin varies aerially and vertically with a general pattern of increasing TDS with depth. Fresh waters are from meteoric recharge into the basin, and the brines are mixtures of waters from dissolution of evaporates and salty in-situ saline waters (Iampen and Rostron, 2000). It is generally accepted that halite dissolution is the source of the high salinities in the pre-Mississippian section of the basin (Chipley and Kyser, 1991).

Density (and hence buoyancy) can affect flow; and changes in water composition can assist in determining the relative strength of aquitards, especially in cases where there are open hydrodynamic systems. Over the deeper, central part of the basin salinity differences greater than 100,000 mg/1 are found. This suggests that in this region the aquitard (Bakken) is very tight (Hitchon, 1996b).

7.3. Faulting/Folding Mechanisms and Principal Stress Assessment

Two types of forces are responsible for the state of stress in the upper, elastic part of the Earth's lithosphere (Zoback at al., 1989). One is tectonic stress and the second is

overburden-derived stresses with impacts from local effects, such as topography, anisotropy of elastic properties, etc. Based on extensive literature review and core sample observation, the Williston Basin is believed to be in a combined normal and strike-slip faulting regime.

In a large scale, this basin lies within the North American Mid-Plate Stress Province, which is characterized by NE-SW trending of the maximum horizontal stress orientation. The basal drag could be exerted by the lithosphere sliding southwestward across the asthenosphere (Zoback and Zoback, 1980). Historically, the left lateral shearing motion is thought to have created enough tension to develop a sag for the formation of this basin (Gerhard et al., 1982). The basement is dissected into blocks by a series of tectonic features referred as lineaments (Figure 7.3), which are believed to be responsible for the origin of structures and depositional patterns within this basin (Fisher et al., 2005).

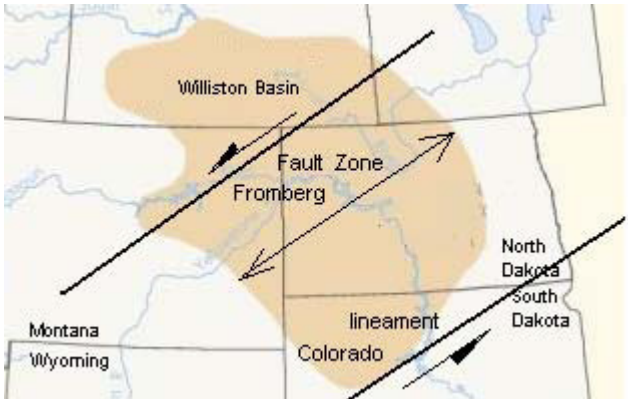

Figure 7.3. Relationship of Fromberg-Colorado-Wyoming shear zones to the Williston Basin (Modified after Gerhard et al., 1982)

Locally, normal faulting due to differential compaction may be widely distributed. For example, an anticline can be created in two different stress regimes: either in a tectonic or horizontal compressive stress regime or in an overburden, or a vertical

compressive stress regime. When the horizontal stress is the maximum principal stress, the rock layers are squeezed to form folds. This folding is commonly observed in mountain building areas where two tectonic plates converged. When the vertical stress is the maximum principal stress, the sedimentary layers are compacted by gravity over geologic time after the initial deposition as flat layers.

Since the crystalline rock basement terrain may not be flat, above the basement highs less subsidence occurs than above the basement lows. Depending on the basement terrain, an anticline may form above a ridge; and a dome may form above a hummock (Figure 7.4). Uplift of the basement may also create an anticline (LeFever et al., 1987). The maximum principal stress in this case would be in the vertical direction. This can be considered as a variation of the second case. The Nesson anticline, which is one of the largest structures in the Williston Basin, was created in an overburden compression stress regime (LeFever et al., 1987; Fisher et al., 2005).

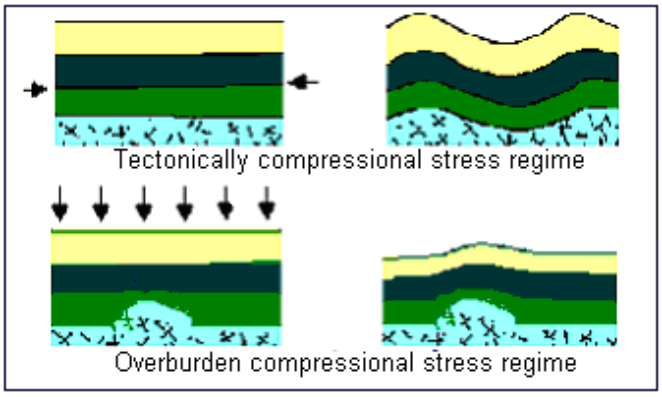

Figure 7.4. Mechanisms of anticline generation
(Upper case: Tectonic compression; Lower case: Overburden compression)

Vertical or sub-vertical fractures within deep formations, both open and cemented, were obeserved in many places in the past (Begnaud and Claiborne, 1985; Bell and Babcock, 1986). These fractures, when observed in the oriented cores, tend to be

dominated in the NE-SW direction, which implies the direction of the maximum horizontal stress. Because fluids prefer to flow along fractures that are oriented parallel to the maximum in-situ horizontal stress direction (Barton and Zoback, 1995), it is not unexpected that there is a coincidence between the basin wide flow pattern and the maximum in-situ horizontal stress directions.

The direction of the maximum principal stress dictates the stress regime (Newmark, 1984). As either normal faulting or strike-slip faulting could produce a vertical or sub-vertical fracture in the field, more information is needed for the identification of a stress regime.

During different geological times, the basement movement may transfer between active and in-active, thus a strike-slip faulting regime may be switched to a normal faulting regime, or vise versa. Currently, the Williston Basin is a seismically inactive area, with only several minor earthquakes recorded in North Dakota (Ayash et al., 2009). The magnitude of these earthquakes (occurred in 1909, 1968, 1970, 1994 and 1998) are all very low. The earthquakes may either be normal faulting, due to compaction collapses or strike-slip faulting, due to horizontal movement. However, considering the low magnitudes and frequency, the possibility of the former seems higher.

Even though the NE-SW trended maximum horizontal stress orientation (at least at the North Dakota part of the Williston Basin) is widely accepted, the anisotropy between the maximum and minimum horizontal stresses seems to be very low (Roundtree et al., 2009). Figure 7.5 shows core sample images taken from wells drilled in Nesson anticline at depths of 3,005 m (9,859 ft) and 3,478 (11,410 ft) m. The horizontal fractures in Figure 7.5(a) were created along planes of weakness by the tensile force that is

relieved after the removal of the overburden. Figure 7.5(b) shows a colonial coral as indicated by the hexagonal pattern. This fossil has not undergone deformation in the plane of the thin section, which is assumed in the horizontal plane. The stress for the rock did not exceed elastic limit since the fossil is still in the same shape as it would have grown. This supports the assumption that there is an isotopic distribution of stresses at this depth, which is a typical situation when the vertical stress is the maximum principal stress, implying a normal faulting regime.

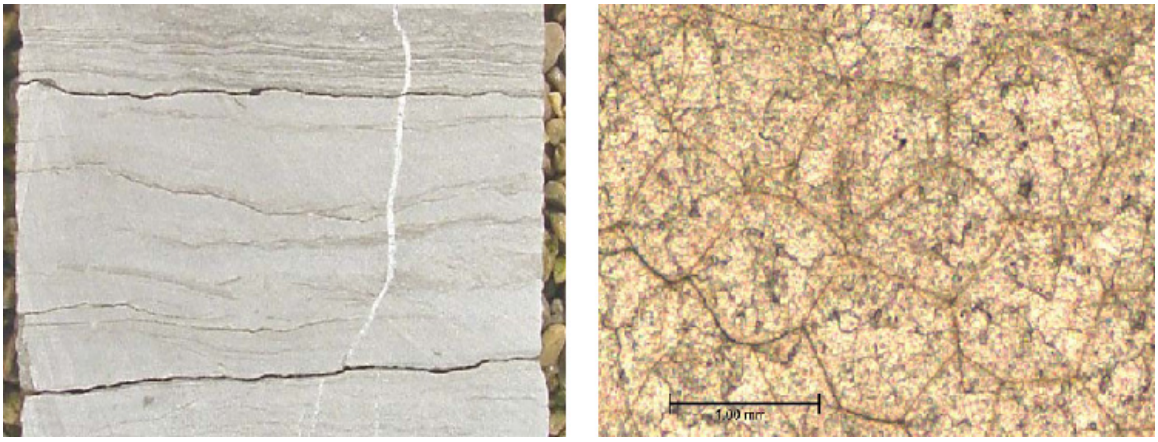

Figure 7.5. (a) Core sample cross section image (depth: 3005m, location: Latitude: 48.316263 Longitude: -103.004936) (b) Core sample plan view, thin section from NDIC well 25 (depth: 3478m, location: Latitude: 48.271398 Longitude: -102.954715) (NDIC Core Sample Library, 2007)

Overall, sedimentary rock formations in the Williston Basin are in a normal faulting regime whereas strike-slip faulting could occur in the Precambrian basement (McLennan et al., 1986). For the sedimentary layers of interests to CO_2 sequestration, the maximum principal stress is generally in a vertical direction, with a maximum horizontal stress in the NE-SW direction and a slightly smaller minimum horizontal stress in the NW-SE direction. Some grounds include:

- This basin is situated within the North America Craton, which has remained in a stable state since the beginning of basin evolution.

- The basin is so large that the curvature of the earth must be taken into account. Even though the basin is deep in its center, the overall basement slope is less than 1°, and therefore the horizontal stress could only be transferred by the friction of the bedrock. The shearing movements of bedrock within this basin today seem very weak as indicated by the quiescent seismicity. Further, the faulting may not be critically stressed.
- The energy generated by tectonic movement to the west has mostly been dissipated in the Cordilleran Orogenic Belt and East Montana Volcanic Intrusion. The west side of this basin accommodates some portion of the strike-slip movements that are not dissipated. The east side of this basin is less active than the west side.
- Large-scale lineaments may be not necessary to reflect shearing in the sedimentary layers but reflect basement structures sheared before, and may be associated with ancient subsurface fluid flow systems (Penner, 2006).
- The distribution of major structures in this basin coincides with the rugged Trans-Hudson Orogen. These structures are the deformed expression of the basement terrain.
- Evidence from wells drilled in the Nesson anticline indicates the existence of a Precambrian high underneath, supporting the assumption that vertical stress could potentially create this anticline. Minor faults related with anticlines were found to be almost vertical. These faults may have been induced by the differential subsidence caused by gravity.
- The core sample images from this basin generally demonstrate textures that were

formed in an overburden compressive stress regime.

However, as the Williston Basin extends to a great area and consists of many layers, even reverse faulting regimes could occur in some areas or depths due to burial or erosion history, shearing activities, heterogeneities or localized specific structures.

7.4. In-situ Stresses' Magnitudes Estimation

To describe the state of stress at a point in the subsurface, the magnitudes and orientations of three orthogonal principal stresses are needed. As mentioned before, one of the principal stresses will be vertical. This can also be justified as: the present-day topography across the Williston Basin is close to horizontal, thus one of the principal stresses will be close to vertical. Some minor relief effect on deflecting stresses will be minimal below depths of a few hundreds meters, so the generalization that one principal stress is vertical will hold (Bell et al., 1994).

For a subsurface point at the depth of z, the vertical stress magnitude can be estimated by integrating the bulk density log of the overlying rocks, as shown in the following equation (Fairhurst, 2003):

$$\sigma_v = \int_0^z \rho(z) g dz \qquad 7.1$$

where σ_v is the vertical stress, $\rho(z)$ is the bulk density of the overlying rock layers, and g is the gravitational acceleration. Figure 7.6 shows the estimates of in-situ stress for a rock column in the Beaver Lodge field at the Nesson anticline (Appendix C). The basic data was acquired from the North Dakota Geological Survey Circular No.210 (Eastwood, 1959); the missing layers were estimated based on the North Dakota Survey Stratigraphic Column (Bluemle et al., 1999).

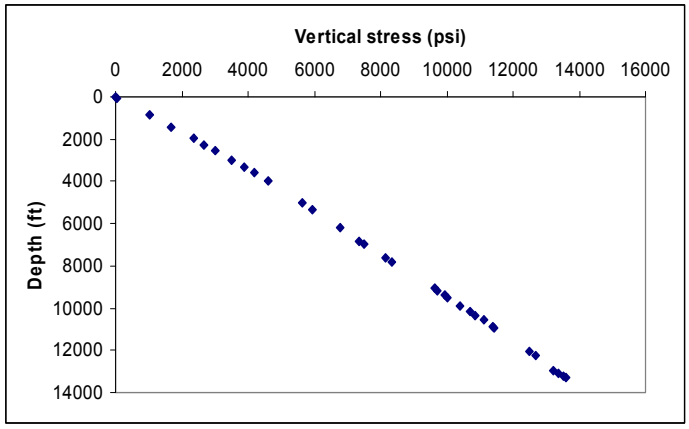

Figure 7.6. In-situ vertical stress distribution at the Beaver Lodge field in the Williston Basin

Thus, the vertical stress can be approximated as having a gradient of 1.0 psi/ft (22.62 MPa/km).

The maximum horizontal stress is generally in the NE-SW direction as discussed, and its magnitude is very close to the vertical stress. For example, the stress magnitude measured by micro-fracing at Regina shows that at a depth of 2,168 meters (7,113 ft), the vertical stress is 54.2 MPa (7,860 psi), with a maximum horizontal stress of 55.3 MPa (8,020 psi); at a depth of 2,213 meters (7,260 ft), the vertical stress is 55.3 MPa (8,020 psi), with a maximum horizontal stress of 52.8 MPa (7,660 psi) (Bell et al., 1994).

The minimum horizontal stress has a direction perpendicular to that of the maximum horizontal stress, and its magnitude is of the greatest concern because it is the combination of all three principal stresses that controls the failure of rock formations. An important hypothesis is that the crust contains critically stressed faults that limit its strength (Townend and Zoback, 2000), i.e., the difference between maximum and minimum stresses cannot be arbitrarily large. Actually, there exists a threshold and once this threshold is approached, a failure (faulting) will occur, again and again, to maintain in-situ stress state below this threshold. This threshold is closely related to pore-fluid

pressure and rock frictional coefficients, which is between 0.6 and 1.0. In a word, "faulting keeps the crust strong" (Townend and Zoback, 2000).

A critically stressed region is usually evidenced by the widespread occurrence of earthquakes, such as those in California, USA, and Japan. However, this may not be the case of the Williston Basin. From a series of reported measurements and field experiences (Begnaud and Claiborne Jr., 1985; Bell et al., 1994; Roundtree and Eberhard, 2009), the minimum horizontal stress is probably in the range of 0.65~0.95 times of the maximum principal stress, no matter the maximum principal stress is the vertical or the other horizontal stress.

7.5. Pore Pressure Estimation and Overpressure Phenomena

The hydrostatic pressure is equal to the vertical height of a column of in-situ fluid (water) extending from the surface to the depth of interest:

$$P = \int_0^z \gamma_f(z)dz \qquad 7.2$$

where γ_f(z) is the specific weight of the formation fluid. If the formation fluids are all close to water (62.4lb/ft^3 or 1,000 kg/m^3), the pressure gradient will be about 0.433 psi/ft (9.79 MPa/km). As the specific weight of water increases with its salinity, the averaged hydrostatic pressure gradient is usually higher than 0.433 psi/ft. For example, a remarkably consistent normal pressure gradient of 0.465 psi/ft (10.5 MPa/km) was found in the Gulf coast region (Ham, 1966). In the Williston Basin in North Dakota, a gradient of 0.512 psi/ft (11.6 MPa/km) was found in some localities because of the high salinity of formation fluid, which could be as high as 356,000 ppm (Finch, 1968).

If a formation pressure is much higher than that calculated using the fluid specific

weight, the formation is over-pressured. Overpressure formations are noted to be present in around 180 basins across the world (Hunt, 1990). In the Williston Basin, overpressure formations, such as Bakken and Tyler, are also present at different locations, but most likely occurred in the relatively deep, central part of the basin (Cramer, 1986 & 1992). Formation pressures below an overpressure formation could return to normal, as shown in Table 7.1 and Figure 7.7.

Table 7.1. Initial formation pressure at the Antelope Field, ND (Finch, 1968)

Reservoir	Depth	Datum	IRP	Gradient
	(ft)	(ft)	(psig)	(psi/ft)
Mississippian	9,088	-6,750	4,207	0.463
Devonian (Sanish) (over-pressured)	10,560	-8,400	7,670	0.725
Devonian (Nisku)	10,778	-8,661	5,047	0.468
Silurian	12,060	-9,500	5,527	0.458

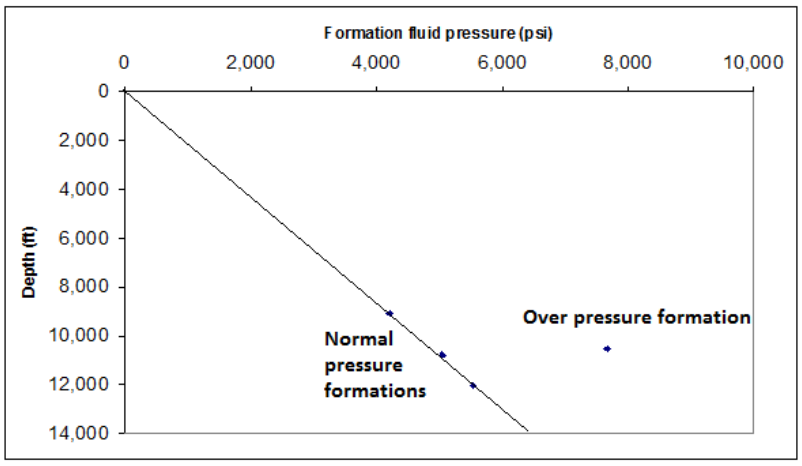

Figure 7.7. A layer of overpressure formation sandwiched by normal formations based on Table 7.1.

Overpressure can be caused by many factors, such as compaction, tectonic compression, faulting, diapirism, high geothermal sources, phase changes of minerals, hydrocarbon generation, upward migration of gases, osmosis, etc (Chilingar et al., 2002). In the case of the Williston Basin, the cause of overpressure formation is generally attributed to hydrocarbon generation (Price, 2000); even though other mechanisms, such

as faulting, may be reasons, or at least in some special cases (Cramer, 1986).

Overpressure formation is a strong flow barrier due to its high pore pressure with respect to its adjacent layers, and the permeability of an overpressure formation is presumed to be extremely low in the sense that fluids in such formation are locked in a geological time frame. The normal pressure of the formations under an overpressure formation may indicate that there are still communications between these formations and the upper normal formations. Because, unlike solid particles, the pressure transfer in fluid systems could be much more complicated. In fact, long range fluid migration within permeable strata of sedimentary basins is a well documented phenomenon. The Williston Basin is in a hydrodynamic regime (Bachu and Hitchon, 1996), and this regime varied with geological time, as evidenced by distal accumulations of petroleum from the source rocks (Khan et al., 2006).

Figure 7.8 shows that even point C is directly underneath point B; its pore pressure may correlate with A, a much distant point, rather than point B, as the over-pressure formation is a strong barrier to inhibit the communication between B and C.

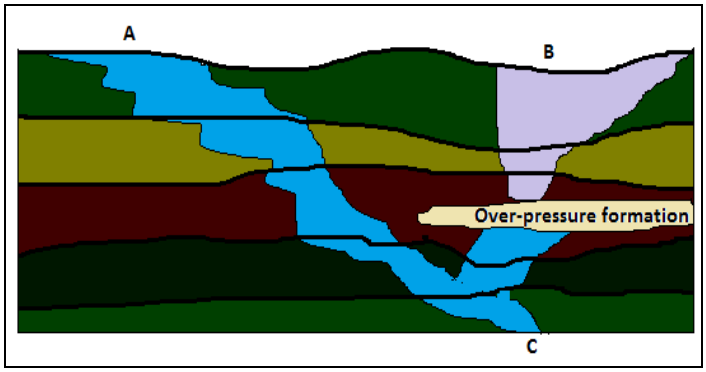

Figure 7.8. Overpressure formation is a strong barrier to inhibit fluid communication.

For an overpressure formation, faulting may act as a valve. It releases the pore fluid if the stress regime favors, and this valve would be closed once the stress regime

evolves to another state due to the increased effective stress by releasing locked pore fluid (Chilingar et al., 2002).

Thus the pressure in the overpressure formation may give an implication on the threshold about how much the pore pressure could be raised above the normal pressure trend line before introducing faulting during CO_2 sequestration. Comparing the pressure difference between normal-pressured and over-pressured formations (Table 7.1 and Figure 7.7), one can see that as the Williston Basin is not close to an incipient failure, the room for pore pressure increase is considerable large in comparison with Denver Basin, where seismicity could be triggered by small pore pressure increase of only 32 bars (Hsieh and Bredehoeft, 1981).

The materials on the interface between the over-pressured shale (or salt) and the adjacent formations are generally believed to be so weak that there can be essentially no shear stress acting on it. Thus, there will be a tendency for principal stresses to re-orient themselves to be parallel or perpendicular to these weak planes (Zoback, 2007). Therefore, the extension and dipping direction of an over-pressure formation also have implications on in-situ stress.

7.6. Compaction Failure and its Impact to Faulting

The increase of pore pressure may induce faults, especially when the regime is very close to a failure state, such as those cases mentioned before (Healy et al., 1968; Seeber et al., 2004; Ake et al., 2005). These phenomena were also verified in the previous chapter by numerical simulation.

However, based on the analysis of in-situ stress and a geological background study on the Williston Basin, the basin might be in a relatively stable state that is not very

close to a failure state; thus, the room for pore pressure fluctuation (including dissipation) might be large before this fluctuation (or increase in the case of fluid injection) could ever cause faulting. This might also be justified by the fact that there is relatively little seismic activity with the long history of oil production in this basin in comparison with many other areas (Nason et al., 1968; Kovach, 1974; Wetmiller, 1986).

However, before an optimistic conclusion could ever be drawn, another concern, compaction failure and its influence on faulting requires special attention.

Towse (1957) had investigated the petrology of Beaver Lodge Madison limestone reservoir, North Dakota. It was noticed that some small dolomite crystals formed along stylolite seams. Here, stylolites are diagenetic features that are commonly present in carbonate rocks (Park and Schot, 1968), indicating fluid migration channels (in the past). In fact, many core samples in the Wilson M. Laird Core and Sample Library, North Dakota Geological Survey, show that stylolites are ubiquitous through many carbonate formations in the Williston Basin (Figure 7.9).

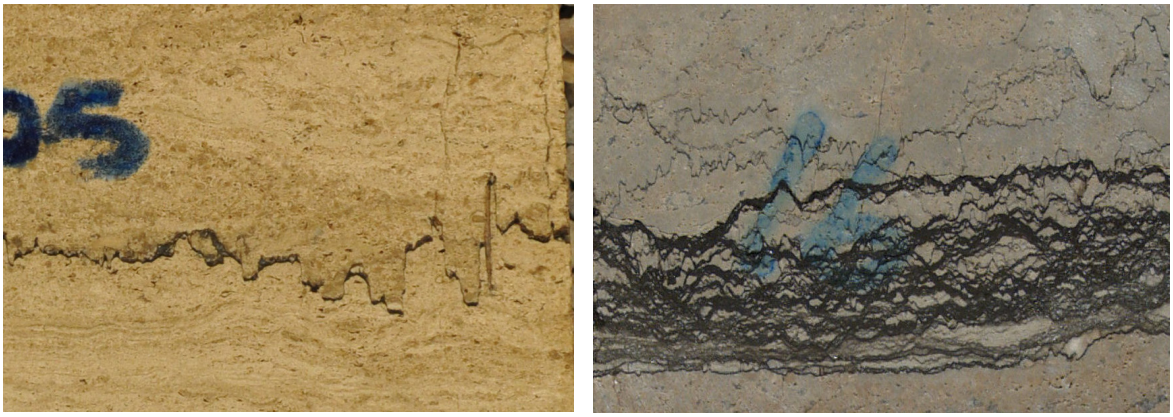

Figure 7.9. Stylolites in Madison Formation, the Williston Basin
(Left: NDIC File No: 3577, 3105 ft depth; Right: NDIC File No: 11546, 4017 ft depth)

The fluids available during the formation of stylolites are either the in situ pore fluid or the extraneous fluid supplied by the flowing groundwater, or both. Sometime, the

waters responsible for stylolite solution may be downward percolating surface waters charged with carbon dioxide in solution, and unsaturated (Dunnington, 1954). The scenario of stylolites developing can be simplified as that in Figure 7.10, in which rock quality deteriorated due to pressure solution and followed by compaction failure.

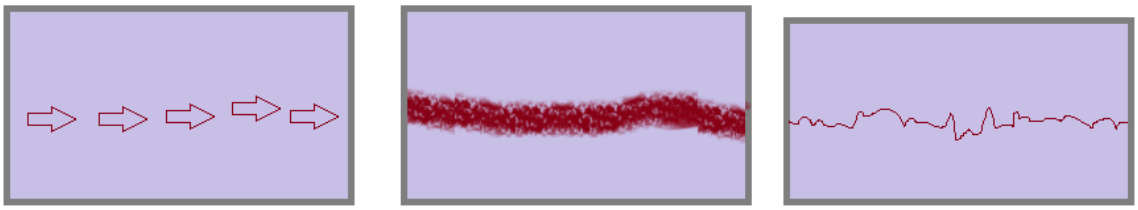

Figure 7.10. Stylolites in carbonate formation due to pressure solution

Stylolites are distinctive and pervasive structures in carbonates that result from water-assisted pressure solution; and pressure solution is one of the principal deformation mechanisms in crustal rock, which has a major influence on formation structure at depth (Galmudi, 1999). Carbonate rocks display a wide variety of pressure solution phenomenon which occurs both during diagenesis and deformation, and sliding along some faults may be accommodated by pressure solution processes (McClay, 1977).

Even the mechanisms of stylolites development and CO_2 sequestration induced heterogeneity are not identical; stylolites can be treated as an analogue in the sense that they might all be prone to chemical compaction due to porosity increase by solutions. These solutions could either be pressure solution in the case of stylolites or CO_2 enriched solution in the case of CO_2 sequestration.

Higher-than-average local porosity causes higher-than-average local solubility, because the grain-to-grain contact area is lower. This higher solubility may drive the porosity even higher (Merino, 1987). Pressure-solution kinetics is self-accentuating and hence is a progressive phenomenon (Sinha-Roy, 2002). In parallel, during CO_2

sequestration, higher porosity regions attract more CO_2 enriched flow, with enhanced dissolution to produce larger pores. This is termed as geochemical self-patterning (Phillips, 2009). Thus, both pressure solution and CO_2 enriched solution have the similar effects to dissolve rock matrix in a non-homogeneous pattern, creating more porous regions in carbonate formations; and these higher porous regions are prone to compaction failures even the boundary conditions of in-situ stresses are not changed.

The stylolite morphology indicates that the late or post-diagenetic stage is marked by many shear-related micro-structures because at the stage of stylolites formation, the rock has been compacted to such an extent that shear fractures can develop (Sinha-Roy, 2002). Tension fractures expressed as tension gashes may also be developed with stylolites if the sedimentary basin ever experienced tectonic extensions (Nelson, 1981). More information is needed to distinguish shear and tension fractures in the field, since both have vertical or sub-vertical patterns as stylolites zones generally occurred horizontally. Many stylolites-associated fractures had acted as pathways for a part of the saturated fluid to escape the stylolites zones, as indicated by the deposition of late stage calcite cements along those flow paths.

Stylolites are thought to be analogous, mechanically, to anti-cracks, similar to compaction bands in porous sandstone (Mollema and Antonellini, 1996; Antonellini et al., 2008; Benedicto and Schultz, 2010). It is a variation of Mode I fracture (Figure 3.6), or so-called anti-Mode I fracture.

Rock properties together with loading conditions determine what deformation mechanism can occur. The formed structure will affect the subsequent deformation, since its presence changes the properties of the rock and the local stress states. Geological

structures (including, but not limited to, joints, pressure solution seams, deformation bands, lineations, foliations, folds and faults) seldom occur alone but appear as zone, set, multiple sets and domains (Zhang, 2008).

In the Williston Basin, faults are hard to recognize, moment magnitudes of earthquakes for rupture events tend to be very small, and minor faults related to anticlines are almost vertical (Fisher et al., 2005). The subvertically or vertically dipping faults are commonly thought of as being caused by the differential subsidence (or compaction) of rock layers.

Another type of compaction failure may be related with the evolution of salt layers in this basin. For the formations formed by thick salt evaporites, the subsurface dissolution of these salts can initialize the development of fractures. This mechanism was considered a major structure-forming process in south-central Saskatchewan (McTavish and Vigrass, 1987). The salt formations include Piper, Opeche and Prairie (3,300 m or 10,800 ft depth at the central part of the basin). Among them, the Devonian Prairie Formation is the most extensive. Here, the effect of dissolution of salt poses special significance, because not only it has a geomechanical stability concern by itself, but also it bears a likeness to the rock quality deterioration of carbonate rock caused by pressure solution (stylolites).

7.7. Numerical Simulation of Compaction Failure due to CO_2 Sequestration

Consider a typical CO_2 flooding scenario that a portion of target rock formation is in contact with CO_2 (Figure 7.11).

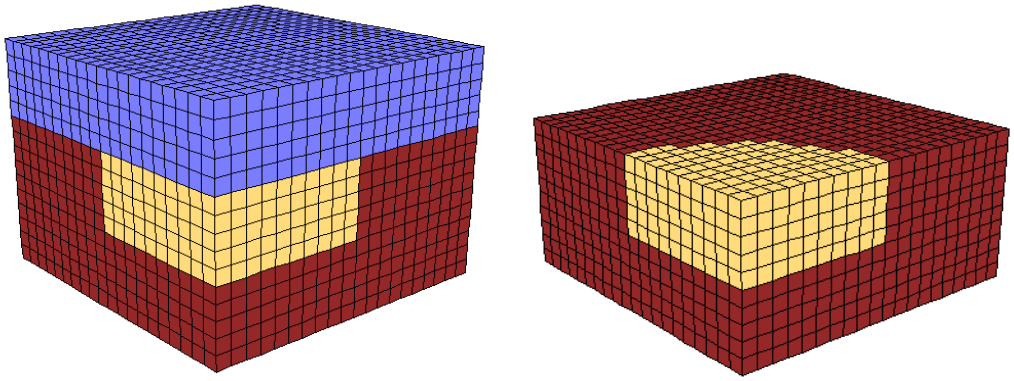

(a) (b)

Figure 7.11. Rock formation influenced by CO_2 plume with and without caprock shown

Over time, the quality of this portion of rock may be decreased due to the chemical reactions between the rock and CO_2/brine systems. Figure 7.12 shows the strain concentration related with the CO_2 plume influenced rock portion. Depending on the actual flooding path, the scenario could be very complicated. The weakening of the influenced portion with respect to the non-weakening part may induce stress heterogeneities that could penetrate through the caprock formation, endangering its trapping integrity.

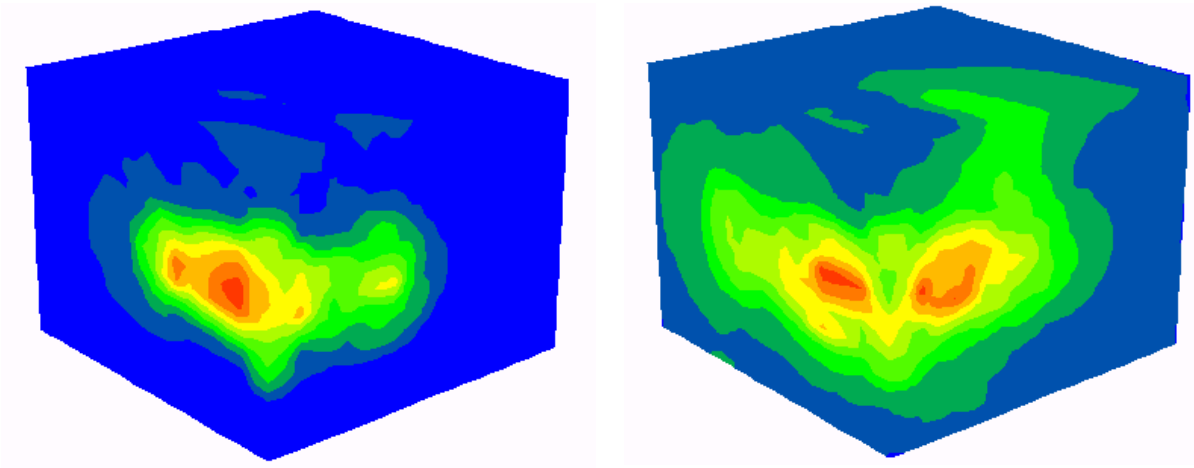

(a) Strain concentration is confined within target formation.

(b) Strain concentration extends into caprock formation.

Figure 7.12. Strain concentration related to CO_2 plume influenced rock portion

From Figure 7.12, one can see that depending on the level of rock quality deterioration in the target formation, the strain concentration may or may not extend into the caprock formation.

Concluding Remarks

As the Williston Basin is most likely in the normal faulting regime in the sedimentary formations and in the strike-slip faulting regime in the crystalline basement, the faults, once initiated tend to grow in a vertical or sub-vertical pattern, which are very unfavorable to CO_2 sequestration. A formation with a high concentration of vertical fractures poses more challenges for CO_2 sequestration (Nelms and Burke, 2004).

Because the basin may not be very close to an incipient failure, the room for pore pressure increase may be large. But this may raise another concern; i.e., the threshold for tensile failure may be reached at some stage, thus, knowing hydraulic fracturing break-down pressure is essential for safe CO_2 sequestration as well as CO_2 injection (Zeng, 2002).

The compaction failure due to rock quality deterioration may occur in a much longer time frame and be even more persistent. How to simulate this remains a challenge, especially because of the difficulty to detect the flow path that evolves over time. The flow path will be opened and enhanced by dissolution, closed by compaction, and reopened by the increased pressure potential, and so on.

A fault at shallow depth, due to the smaller horizontal stress, may extend upwards to a great distance before it is closed, or simply reaches the ground surface. For a deep fault, there is the possibility that it may be closed before extending upward to a significant distance because of the relatively isotropic distribution of stresses in the

Williston Basin. However, if a fault occurs beneath the CO_2 container layer, the tremendous buoyancy driven force of CO_2 may alter the in-situ stress condition, thus hindering the closure of the otherwise small fault (Rutqvist et al., 2008). This steeply dipping fault may form a potential pathway for CO_2 leakage.

An analogue between stylolites and CO_2 sequestration induced formation heterogeneity exists in the sense of chemical compaction. Stylolitization might be a long, drawn-out continuous process, which operates throughout the diagenetic history of its host-rock (Park and Schot, 1968). CO_2 sequestration in carbonate formation can also introduce long-term changes to the host formations by the chemical reaction between CO_2 enriched solution and rock matrix. This mechanism bears the similarity of rock matrix weakening by solutions as that in stylolites. CO_2 stored at Sleipner showed a layer by layer pattern, possibly resembling a very early stage of stylolite-type development. Therefore, a detailed study on the natural stylolites would shed light on the predication of CO_2 sequestration in deep carbonate formations in the long run.

CHAPTER VIII

CONCLUSIONS AND RECOMMENDATIONS

8.1. Conclusions

CO_2 sequestration in deep carbonate formations is a complicated geological process, raising issues upon different time scales. The presumed equivalent and stable status of underground formations would be non-reversibly transformed with respect to the geochemical, hydraulic, geothermal, and geomechanical regimes.

CO_2 sequestration poses serious concern to the existing environment because of the two intrinsic properties of CO_2: (1). It has a strong tendency to migrate upwards because of its buoyancy driving effect under most geological conditions; (2). It is chemically active, both with target formation and cap rock formation.

This dissertation presents the literature researches, laboratory tests and numerical simulations regarding this topic with emphasis on geomechanical stability analysis.

By conducting combined geochemical and geomechanical laboratory tests, the deterioration of geomechanical properties (strength, Young's modulus, Poisson's ratio) of a carbonate rock (Indiana limestone) upon CO_2 injection has been confirmed and quantified. By conducting coupled hydro-mechanical laboratory tests, the dependency of permeability to confining pressure in a carbonate rock (Indiana limestone) under hydrostatic and differential stress conditions has been experimentally quantified, and the implication of this dependency to CO_2 sequestration was investigated.

Similarly, experimental tests demonstrated that clayey caprock as represented by

Pierre shale showed a tendency to be weaker upon the contact with CO_2. The success on weak rock sample preparation allowed large quantities of tests on shale to be conducted with reliable results. It was experimentally showed that residual strength is a more repeatable index than peak strength in expressing the behavior of shale.

By developing a strain softening model based on the mechanical properties directly acquired from laboratory testing, rock failure behavior was simulated under different stress regimes. Strain localization due to pore pressure increase was numerically investigated. The numerical test results showed that the calibrated rock model's behavior is highly consistent with laboratory test results, thus giving the confidence for its large scale predication beyond laboratory testing.

Since there is no evidence that fracture toughness of target formation would be necessarily lower than that of caprock formation, the fracture developing mechanism is one of the primary concerns for the geomechanical analysis of CO_2 sequestration in deep formations. Once fractures are developed in a target formation, one may not count on an assumption that these fractures could be impeded by the caprock formation. The fact might be more likely on the opposite; i.e., a caprock formation formed by clayey rock could potentially be weaker, or at least not stronger, than the target storage formation formed by carbonate rocks in terms of their mechanical strengths.

Based on theoretical derivation, case studies, laboratory and numerical tests, it is concluded that two mechanisms are competing for the potential developments of fractures upon CO_2 sequestration: pore-pressure buildup induced faulting and compaction failure of high porosity regions created by CO_2 enriched solution, with the former possibly occurring in a relatively short time frame and the latter more persistent over a

much longer time scale.

Depending on the in-situ stress status and pore pressure buildup pattern, the increased pore pressure may reactivate preexisting faults or induce new fractures (faulting), with the orientation of these induced fractures to be determined by the in-situ stress and rock formation properties. The induced fractures may be open to CO_2 migration and this migration may cause further fracture developments to endanger the trapping mechanisms.

The chemical reactions between carbonate rocks and CO_2 – brine system may change the porosities or rock structures, and thus the permeability of rock formation; this will further change the fluid flow pattern, as well as mechanical properties of rock, incorporated with thermal effect such as thermally induced fractures. The compaction failure caused by rock quality deterioration has long been a well-observed phenomenon in carbonate formations. Compaction failure may occur over a much longer geological time scale and its influence to the geomechanical stability is even more complicated and persistent, although it may be subtle at the first appearance.

Because of the difficulty to investigate many geological problems due to the time span or location, or both, the concept of analogue between two different entities is widely used such as the outcrop/aquifer analogue in hydrogeology. This dissertation proposed that an analogue between stylolites and CO_2 sequestration induced formation heterogeneity exists, since both pressure solution and CO_2 enriched solution during CO_2 sequestration in carbonate formations may all introduce abnormal porous regions, which are prone to compaction failure. Thus the influences of stylolites to rock formations may give implications to CO_2 sequestration regarding its geological future.

Geomechanical stability analysis for CO_2 sequestration in the Williston Basin has revealed that the stress regime in the sedimentary rock layers is generally in a normal faulting regime whereas strike-slip faulting could occur in the Precambrian basement. There is a correlation of basin wide flow pattern and in-situ stress regime. For the sedimentary layers of interests to CO_2 sequestration, the maximum principal stress is generally in a vertical direction, favoring the development of vertical fractures, thus posing potential safety concern for CO_2 sequestration. The occurrences of over-pressured formations in this basin imply the room for pressure increase is considerably large. Therefore, persistent compaction failure is expected to be more pronounced rather than cataclasis due to CO_2 sequestration in the Williston Basin.

8.2. Recommendations for Future Research

A vast set of problems still exist that merit further theoretical, laboratory, field and numerical investigation, which are potential areas for future research.

- Mathematically, more complicated models may be introduced to this problem, with the consideration of anisotropy and non-linearity of material properties.
- More laboratory tests, both on carbonate rocks and clayey rocks, are always valuable for the understanding of this problem. Especially, as compaction failure generally requires a much higher pressure and temperature, with the introduction of new laboratory facilities, tests under more “difficult” conditions are expected to investigate this kind of failure behavior in more detail.
- Numerical modeling, in cooperation with more field data, can be carried to conduct a more detailed coupling research among hydro-thermal-chemo-mechanical behavior.

APPENDICES

APPENDIX A

ANALYTIC SOLUTION OF HEAT TRANSFER PROBLEMS

Consider Fourier's equation in one dimension with the following initial and boundary conditions:

$$\frac{\partial^2 T}{\partial x^2} = \frac{1}{\alpha}\left(\frac{\partial T}{\partial t}\right) \qquad 2.4.14$$

$$T(x,0) = T_r \qquad 2.4.15a$$

$$T(\infty,t) = T_r \qquad 2.4.15b$$

$$T(0,t) = T_s \qquad 2.4.15c$$

Taking the Laplace transform of 2.4.14 with the initial condition gives:

$$\frac{d^2U}{dx^2} = \frac{1}{\alpha}sU - \frac{1}{\alpha}T(x,0) = \frac{1}{\alpha}sU - \frac{1}{\alpha}T_r$$

Solving this ordinary differential equation (ODE) gives:

$$U(x,s) = c_1 e^{\sqrt{\frac{s}{\alpha}}x} + c_2 e^{-\sqrt{\frac{s}{\alpha}}x} + \frac{T_r}{s}$$

Transform the boundary condition of 2.4.15b, there are:

$$\lim_{x\to\infty} U(x,s) = \lim_{x\to\infty}(c_1 e^{\sqrt{\frac{s}{\alpha}}x} + c_2 e^{-\sqrt{\frac{s}{\alpha}}x} + \frac{T_r}{s}) = c_1 e^{\sqrt{\frac{s}{\alpha}}x} + \frac{T_r}{s}$$

$$\lim_{x\to\infty} U(x,s) = \lim_{x\to\infty} L(T(x,t)) = L(\lim_{x\to\infty} T(x,t)) = \frac{T_r}{s}$$

Thus, c_1=0.

Transform the boundary condition of 2.4.15c, there are:

$$U(0,s) = L(T(0,t)) = \frac{T_s}{s}$$

$$U(0,s) = c_2 + \frac{T_r}{s}$$

Thus, $c_2 = (T_s - T_r)/s$, and $U(x,s) = \frac{T_s - T_r}{s} e^{-\sqrt{\frac{s}{\alpha}}x} + \frac{T_r}{s}$

By inverse transformation, the solution is given as:

$$T(x,t) = T_r + (T_s - T_r) \cdot erfc\left(\frac{x}{2\sqrt{\alpha t}}\right) \qquad 2.4.16$$

The Laplace transform operations used in this solution include (Schiff, 1999):

F(s)	f(t)
$sF(s) - f(0^+)$	$f'(t)$
1/s	1
$\frac{e^{-a\sqrt{s}}}{s} \quad (a > 0)$	$erfc\left(\frac{a}{2\sqrt{t}}\right)$

If changing the boundary condition to the followings,

$$T(x,0) = T_i \qquad 2.4.20a$$

$$T(\infty,t) = T_i \qquad 2.4.20b$$

$$-K\left.\frac{\partial T}{\partial x}\right|_0 = h[T_\infty - T(0,t)] \qquad 2.4.20c$$

With the similar methodology above, one can quickly reach the following step:

$$U(x,s) = c_2 e^{-\sqrt{\frac{s}{\alpha}}x} + \frac{T_i}{s}$$

Making Laplace transform with respect to 2.4.20c, there is:

$$L(\frac{\partial T}{\partial x})\Big|_0 = \frac{h}{K}L[T(0,t)] - \frac{h}{K}L(T_\infty) \Rightarrow \frac{\partial U(x,s)}{\partial x}\Big|_0 = \frac{h}{K}U(0,s) - \frac{h}{K}\cdot\frac{T_\infty}{s}$$

As $\frac{\partial U(x,s)}{\partial x}\Big|_0 = -\sqrt{\frac{s}{\alpha}}c_2 e^{-\sqrt{\frac{s}{\alpha}}x}\Big|_0 = -\sqrt{\frac{s}{\alpha}}c_2, and \quad U(0,s) = c_2 + \frac{T_i}{s},$ thus, there is:

$-\sqrt{\frac{s}{\alpha}}c_2 = \frac{h}{K}(c_2 + \frac{T_i}{s}) - \frac{h}{K}\cdot\frac{T_\infty}{s} \Rightarrow c_2 = \frac{T_\infty - T_i}{s}\cdot\frac{1}{1+\frac{K}{h}\sqrt{\frac{s}{\alpha}}}$, then U(x,s) can be acquired as:

$$U(x,s) = c_2 e^{-\sqrt{\frac{s}{\alpha}}x} + \frac{T_i}{s} = \frac{T_\infty - T_i}{s}\cdot\frac{1}{1+\frac{K}{h}\sqrt{\frac{s}{\alpha}}}\cdot e^{-\sqrt{\frac{s}{\alpha}}x} + \frac{T_i}{s}$$

$$= (T_\infty - T_i)\cdot\left[\frac{e^{-\sqrt{\frac{s}{\alpha}}x}}{s} - \frac{e^{-\sqrt{\frac{s}{\alpha}}x}}{\sqrt{s}(\sqrt{s}+\frac{h}{K}\sqrt{\alpha})}\right] + \frac{T_i}{s}$$

Using a formula from Debnath and Bhatta (2007, Page 623) ,

F(s)	f(t)
$\frac{\exp(-b\sqrt{s})}{\sqrt{s}(\sqrt{s}+a)}, \quad a \geq 0$	$\exp[a(b+at)]erfc(a\sqrt{t}+\frac{b}{2\sqrt{t}})$

by inverse Laplace Transform, the answer is:

$T(x,t) = T_{i)} + (T_\infty - T_i)\cdot\left[erfc(\frac{x}{2\sqrt{\alpha t}}) - e^{\frac{hx}{K}+\frac{h^2}{K^2}\alpha t}\cdot erfc(\frac{h}{K}\sqrt{\alpha t}+\frac{x}{2\sqrt{\alpha t}})\right]$. Using Error

Function instead of Complementary Error Function, there is 2.4.21, as follows.

$$T(x,t) = T_i + (T_\infty - T_i)\cdot\left\{1 - erf\left(\frac{x}{2\sqrt{\alpha t}}\right) - \left[\exp\left(\frac{hx}{K}+\frac{h^2\alpha t}{K^2}\right)\right]\times\left[1 - erf\left(\frac{x}{2\sqrt{\alpha t}}+\frac{h\sqrt{\alpha t}}{K}\right)\right]\right\} \quad 2.4.21$$

APPENDIX B

REQUIRED PARAMETERS FOR FRACTURE TOUGHNESS

Table 2 of IRSM, 1995.

Table 2. Values of u and v

α_0	0.100	0.150	0.175	0.200	0.225	0.250	0.275	0.300	0.325	0.350	0.375	0.400	0.425	0.450
							u							
α_B														
0.440	0.2747	0.2774	0.2791	0.2808	0.2825	0.2844	0.2865	0.2883	0.2914	0.2943	0.2979	0.3024	0.3069	0.3120
0.480	0.2727	0.2752	0.2765	0.2782	0.2795	0.2812	0.2833	0.2856	0.2882	0.2918	0.2954	0.2994	0.3039	0.3090
0.520	0.2708	0.2727	0.2740	0.2757	0.2771	0.2788	0.2806	0.2828	0.2857	0.2887	0.2925	0.2968	0.3013	0.3060
0.560	0.2689	0.2705	0.2716	0.2733	0.2744	0.2763	0.2781	0.2805	0.2831	0.2867	0.2901	0.2943	0.2989	0.3039
0.600	0.2667	0.2684	0.2696	0.2709	0.2721	0.2739	0.2757	0.2782	0.2812	0.2844	0.2882	0.2921	0.2967	0.3015
0.640	0.2649	0.2665	0.2674	0.2685	0.2701	0.2719	0.2738	0.2764	0.2791	0.2825	0.2863	0.2905	0.2947	0.2992
0.680	0.2632	0.2646	0.2655	0.2667	0.2682	0.2704	0.2718	0.2744	0.2774	0.2807	0.2848	0.2888	0.2930	0.2971
0.720	0.2611	0.2628	0.2637	0.2650	0.2667	0.2683	0.2705	0.2727	0.2763	0.2794	0.2831	0.2871	0.2916	0.2954
0.760	0.2598	0.2612	0.2625	0.2637	0.2650	0.2668	0.2693	0.2719	0.2744	0.2781	0.2819	0.2860	0.2895	0.2934
0.800	0.2582	0.2602	0.2611	0.2625	0.2641	0.2657	0.2680	0.2706	0.2736	0.2772	0.2811	0.2845	0.2878	0.2916
0.840	0.2572	0.2586	0.2599	0.2612	0.2628	0.2649	0.2672	0.2699	0.2727	0.2763	0.2801	0.2831	0.2867	0.2891
0.880	0.2562	0.2578	0.2593	0.2602	0.2621	0.2642	0.2668	0.2691	0.2723	0.2754	0.2793	0.2816	0.2853	0.2867
0.920	0.2553	0.2572	0.2582	0.2598	0.2613	0.2634	0.2658	0.2684	0.2716	0.2747	0.2782	0.2811	0.2831	0.2856
0.960	0.2549	0.2566	0.2578	0.2593	0.2612	0.2633	0.2655	0.2685	0.2710	0.2746	0.2767	0.2799	0.2811	0.2825
1.000	0.2547	0.2564	0.2576	0.2591	0.2610	0.2630	0.2653	0.2679	0.2709	0.2738	0.2768	0.2786	0.2794	0.2794
1.040	0.2544	0.2565	0.2576	0.2593	0.2608	0.2627	0.2653	0.2678	0.2708	0.2727	0.2747	0.2769	0.2769	0.2765
							v							
0.440	1.7813	1.7820	1.7820	1.7833	1.7863	1.7893	1.7923	1.7967	1.7966	1.7977	1.7973	1.7932	1.7901	1.7850
0.480	1.7748	1.7763	1.7787	1.7800	1.7843	1.7881	1.7907	1.7934	1.7952	1.7929	1.7923	1.7901	1.7866	1.7811
0.520	1.7694	1.7734	1.7758	1.7769	1.7808	1.7845	1.7884	1.7907	1.7911	1.7920	1.7897	1.7860	1.7823	1.7784
0.560	1.7644	1.7701	1.7732	1.7748	1.7794	1.7822	1.7856	1.7877	1.7885	1.7864	1.7857	1.7820	1.7779	1.7725
0.600	1.7620	1.7668	1.7692	1.7727	1.7770	1.7792	1.7826	1.7835	1.7833	1.7831	1.7805	1.7782	1.7733	1.7689
0.640	1.7580	1.7631	1.7671	1.7707	1.7732	1.7757	1.7788	1.7794	1.7795	1.7779	1.7753	1.7716	1.7686	1.7652
0.680	1.7550	1.7602	1.7640	1.7676	1.7707	1.7711	1.7757	1.7759	1.7754	1.7741	1.7700	1.7666	1.7630	1.7612
0.720	1.7536	1.7580	1.7616	1.7647	1.7661	1.7698	1.7708	1.7722	1.7693	1.7683	1.7652	1.7617	1.7574	1.7562
0.760	1.7497	1.7553	1.7568	1.7600	1.7635	1.7656	1.7649	1.7652	1.7662	1.7624	1.7593	1.7554	1.7548	1.7528
0.800	1.7474	1.7506	1.7538	1.7557	1.7581	1.7611	1.7613	1.7603	1.7596	1.7561	1.7525	1.7512	1.7509	1.7494
0.840	1.7430	1.7487	1.7500	1.7522	1.7545	1.7547	1.7551	1.7548	1.7535	1.7499	1.7469	1.7473	1.7448	1.7497
0.880	1.7392	1.7438	1.7446	1.7487	1.7490	1.7492	1.7478	1.7487	1.7463	1.7452	1.7403	1.7434	1.7414	1.7493
0.920	1.7357	1.7390	1.7413	1.7423	1.7440	1.7446	1.7443	1.7432	1.7411	1.7389	1.7360	1.7363	1.7417	1.7448
0.960	1.7299	1.7337	1.7358	1.7370	1.7372	1.7373	1.7372	1.7346	1.7344	1.7309	1.7343	1.7331	1.7414	1.7483
1.000	1.7243	1.7279	1.7300	1.7308	1.7310	1.7307	1.7306	1.7297	1.7273	1.7270	1.7258	1.7302	1.7394	1.7525
1.040	1.7196	1.7213	1.7231	1.7232	1.7246	1.7256	1.7237	1.7231	1.7204	1.7238	1.7272	1.7293	1.7423	1.7569

APPENDIX C

DESCRIPTION OF ROCK FORMATION IN THE WILLISTON BASIN

Typical rock column and hydro facts of the Williston Basin (Edited based on Eastwood, 1959; Bluemle et al., 1999; Murphy et al., 2009; Bachu and Hitchon, 1996).

Rock Unit	B (m)	Depth (m)	Density (kg/m^3)	P (MPa)	Hydro-Facts	Lithology characteristics
OAHE	10	0	1700	0	Aquifer	clay, sand, silt, gravel, glacial till
Coleharbor Group	250	10	1900	0.2		glacial till, clay, river sediments, pebbles
Unnamed Unit	70	260	2300	4.8		gravel, sand, cobbles, river sediments
ARIKAREE	80	330	2200	6.4		sandstone, lake and river deposits
White River Group	85	410	2100	8.1		siltstone, sandstone, clay, conglomerate
GOLDEN VALLEY	90	495	2200	9.9		sandstone, mudstone, lignite, claystone
SENTINEL BUTTE	150	585	1950	11.8		coal, sand/silt/mudstone, swamp deposits
BULLION CREEK	140	735	2000	14.7		mudstone, siltstone, sandstone, coal
SLOPE-LUDLOW	180	875	2000	17.4		sand/siltstone, coal, marine/lake deposits
HELL CREEK	80	1055	2100	21.0		sand/mudstone, river/estuarine sediment
FOX HILLS	90	1135	2000	22.6		mud/siltstone, near/offshore marine deposits
PIERRE	560	1225	1800	24.4	Aquitard	shale, mudstone, offshore marine deposits
Colorado Group	290	1785	2000	34.2		shale, bentonite, offshore marine deposits
MOWRY	70	2075	2100	39.9		shale, bentonite clay, offshore marine
INYAN KARA	150	2145	2300	41.4	Aquifer	sandstone, shale, quartzose, nonmarine
Jurassic System	350	2295	2200	44.7	Aquitard	shale, sandstone, limestone, gypsum
SPEARFISH	180	2645	2400	52.3		silts/mud/sandstone, halite, shallow marine
OPECHE	120	2825	2000	56.5		shale, mudstone, salt, shallow marine
BROOM CREEK	80	2945	2300	58.9	Aquifer	sandstone, dolomite, shale, shallow marine
AMSDEN	100	3025	2350	60.7		dolostone, shale, sandstone, anhydrite
TYLER	60	3125	2100	63.0		shale, mudstone, sandstone, marine-swamp
OTTER	40	3185	2300	64.2	Aquitard	shale, carbonaceous, limestone, offshore
KIBBEY	50	3225	2200	65.1		sandstone, shale, limestone, shallow marine
CHARLES	200	3275	2400	66.2		carbonate, offshore to near shore marine

Table cont.

MISSION CANYON	200	3475	2300	70.9	Aquifer	limestone, anhydrite, shale, dolostone
LODGEPOLE	190	3675	2500	75.4		Limestone, mudstones, shale, chert
BAKKEN	40	3865	2300	80.1	Aquitard	shale, siltstone, argillaceous dolomite
THREE FORKS	60	3905	2500	81.0		dolostone, limestone, siltstone, shale
BIRDBEAR	30	3965	2300	82.4		limestone, dolostone, near shore marine
DUPEROW	120	3995	2400	83.1		limestone, dolostone, mudstone, anhydrite
SOURIS RIVER	90	4115	2100	85.9		dolostone, limestone, evaporites, shale
DAWSON BAY	50	4205	2300	87.8		dolostone, limestone, shale, (fossiliferou)
PRAIRIE	150	4255	2000	88.9		evaporites, halite, clay/siltstone, potash
WINNIPEGOSIS	50	4405	2500	91.9		dolostone, limestone, mudstone, anhydrite
ASHERN	40	4455	2400	93.1		dolostone, shallow marine deposits
INTERLAKE	260	4495	2500	94.0		dolostone, limestone, anhydrite, siltstone
STONEWALL	20	4755	2400	100.4	Aquifer	limestone, dolostone, anhydrite infilling
STONY MT	60	4775	2500	100.9		dolostone, limestone, shale,(fossiliferous)
RED RIVER	170	4835	2600	102.3		limestone, dolomitic mudstone, anhydrite
ROUGHLOCK	20	5005	2300	106.7		shale, limestone, offshore marine deposits
BLACK ISLAND	60	5025	2500	107.1		sandstone, quartz, shale, pyrite, fluvial
DEADWOOD	240	5085	2700	108.6		limestone, sandstone, shale
Precambrian	…	5325		114.9		granite, schist, amphibolites facies, gneiss

Note. The estimations of rock densities are based on rock stratigraphy description.

REFERENCES

Adler, P.M., 1992. Porous Media: Geometry and Transports. Butterworth-Heinemann, a division of Reed Publishing (USA) Inc.

Ake, J., Mahrer, K., O'Connell, D., Block, L., 2005. Deep-injection and closely monitored induced seismicity at Paradox Valley, Colorado. Bulletin of the Seismological Society of America, vol. 95, no. 2, pp. 664-683.

Al-Basali, T.M., Zhang, J., Sharma, M.M., 2005. Measurement of the sealing capacity of shale caprocks. SPE 96100. In: SPE Annual Tech. Conf. and Exhibit., Houston, Texas, Oct. 9-12.

Altmann, J.B., Muller, T.M., Muller, B.I.R., Tingay, M.R.P., Heidbach, O., 2010. Poroelastic contribution to the reservoir stress path. International Journal of Rock Mechanics & Mining Sciences 47, pp. 1104-1113.

Ames, W.F., 1977. Numerical Methods for Partial Differential Equations. 2nd edition. Academic Press, Inc.

Anderson, E. M., 1951. The Dynamics of Faulting and Dyke Formation with Applications to Britain. 2nd edition, Edinburgh, Oliver and Boyd.

Anderson, M.P., 1989. Hydrogeologic facies models to delineate large-scale spatial trends in glacial and glaciofluvial sediments, Geological Society American Bulletin, 101, pp. 501-511.

Anderson, M.P., 1997. Characterization of geological heterogeneity, in: Dagan, G., and Neuman, S.P. (Eds.), Subsurface Flow and Transport: a Stochastic Approach. Cambridge, U.K., Cambridge University Press, pp.23-43.

Anderson, M.P., Aiken, J.S., Webb E.K., Mickelson, D.M., 1999. Sedimentology and hydrogeology of two braided stream deposits. Sedimentary Geology 129, pp. 187-199.

Antonellini, M., Tondi, E., Agosta, F., Aydin, A., Cello, G., 2008. Failure modes in deep-water carbonates and their impact for fault development: Majella Mountain, central Apennines, Italy. Marine and Petroleum Geology 25, pp. 1074-1096.

Appelo, C.A.J., Postma, D., 2005. Geochemistry, Groundwater and Pollution. 2nd edition. CRC Press, Taylor & Francis Group.

Archer , J.S., Wall, C.G., 1986. Petroleum Engineering: Principles and Practice. 1st edition. Springer

Aris, R., 1978. Mathematical Modeling Techniques. University of Minnesota. Dover Publications, Inc.

Arts, R., Eiken, O., Chadwick, A., Zweigel, K., van del Meer, L., Zinszner, B., 2004. Monitoring of CO_2 injected at Sleipner using time-lapse seismic data. Energy 29, pp. 1383-1392.

Ayash, S.C., Dobroskok, A.A., Sorensen, J.A., Wolfe, S.L., Steadman, E.N., Harju, J.A., 2009. Probabilistic approach to evaluating seismicity in CO_2 storage risk assessment. Energy Procedia 1, pp. 2487-2494.

Ayatollahi, M.R., Aliha, M.R.M., 2008. On the use of Brazilian disc specimen for calculating mixed mode I-II fracture toughness of rock materials. Engineering Fracture Mechanics 75, pp. 4631-4641.

Bachu, S., Hitchon, B., 1996. Regional-scale flow of formation waters in the Williston Basin. AAPG Bulletin, vol. 80, no. 2, pp. 248–264.

Bachu, S., Gunter, W.D., 1999. Storage capacity of CO_2 in geological media in sedimentary basins, with application to the Alberta basin. In: Greenhouse Gas Control Technologies, (Eliasson, B., P.W.F. Riemer and A. Wokaun, eds.), Pergamon, Elsevier Science Ltd., Amsterdam, pp. 195-200.

Bachu, S., 2000. Sequestration of CO_2 in geological media: criteria and approach for site selection in response to climate change. Energy Conversion & Management 41, pp. 953-970.

Bachu, S., 2001. Geological sequestration of anthropogenic carbon dioxide: Applicability and current issues. In: Gerhard, L.C., Harrison, W.E., Hanson, B.M. (Eds.), Geological Perspectives of Global Climate Change, American Association Of Petroleum Geologists, pp. 285-303.

Bachu, S., Adams, J. J., 2003. Sequestration of CO_2 in geological media in response to climate change: capacity of deep saline aquifers to sequester CO_2 in solution. Energy Conversion and Management, vol. 44, iss. 20, pp. 3151-3175.

Bachu, S., Bonijoly, D., Bradshaw, J., Burruss, R., Holloway, S., Christensen, N.P., Mathiassen, O.M., 2007. CO_2 storage capacity estimation: methodology and gaps. International Journal of Greenhouse Gas Control, vol. 1, iss. 4, pp. 430-443.

Bagheri, M.A., 2006. Modeling Geo-mechanical Effects on the Flow Properties of Fractured Reservoirs. PhD dissertation. University of Calgary, Canada.

Bai, M., Meng, F., Elsworth, D., Zaman,M., Roegiers, J.-C., 1997. Numerical modeling of stress-dependent permeability. International Journal of Rock Mechanics & Mining Sciences. 34, pp. 3-4.

Balmer, R.T.,1990. Thermodynamics. West Publishing Company.

Barton, C.A., Zoback, M.D., 1995. Fluid flow along potentially active faults in crystalline rock. Geology, vol. 23, pp. 683-686.

Bear, J., 1972. Dynamics of Fluids in Porous Media. American Elsevier Publishing Company, Inc.

Bear, J., 1979. Hydraulics of Groundwater. McGraw-Hill, New York.

Beardsmore, G. R., Cull, J.P., 2001. Crustal Heat Flow: a Guide to Measurement and Modeling. Cambridge University Press.

Begnaud, W.J., Claiborne Jr., E.B., 1985. Vertical fracture growth considerations in the Mission Canyon/Ratcliffe Formations of the North Alexander area. SPE 14375. In the 60th Annual Technical Conference of the Society of Petroleum Engineering held in Las Vegas, NV Sep. 22-25.

Bejan, A., 1988. Advanced Engineering Thermodynamics. John Wiley & Sons, Inc.

Bejan, A., 1996. Entropy Generation Minimization. CRC Press LLC.

Bell, J.S., Babcock, E.A., 1986. The stress regime of the Western Canadian Basin and implications for hydrocarbon production. Bull. Can. Petrol. Geol., vol. 34, pp.364-378.

Bell, J.S., Price, P.R., McLellan, P.J., 1994. In-situ stress in the Western Canada Sedimentary basin. In Mossop, G.D. and Shetsen, I., compilers. Geological Atlas of Western Canada Sedimentary Basin: Canadian Society of Petroleum Geologists and Alberta Research Council, pp.439-446.

Benedicto, A., Schultz, R.A., 2010. Stylolites in limestone: magnitude of contractional strain accommodated and scaling relationships. Journal of Structural Geology, vol. 32, pp. 1250-1256.

Bennion, D. B., Thomas, F. B., Ma, T., Imer, D., 2000. Detailed protocol for the screening and selection of gas storage reservoirs. SPE 59738, presented at the SPE/CERI Gas Technology Symposium held in Calgary, Alberta Canada, April 3-5.

Berryman, J.G., 1992. Effective stress for transport properties of inhomogeneous porous rock. Journal of Geophysics Research, vol. 97. no. B12, pp.17409-17424.

Bertog, J.L., 2002. High Resolution Event Stratigraphic and Sequence Stratigraphic Interpretation of the Lower Pierre Shale (Campanian) with the Description of the New Walhalla and Chamberlain Members. PhD Dissertation, the University of Cincinnati.

Biot, M.A., 1941. General theory of three-dimensional consolidation. Journal of Applied Physics, 12, pp. 155-164.

Biot, M.A., Willis, D. G., 1957. The elastic coefficients of the theory of consolidation. Journal of Applied Mechanics. 24, pp. 594-601.

Bluemle, J.P., Anderson, S.B., Carlson, C.G., 1999. North Dakota Stratigraphic Column. North Dakota Geological Survey.

Bluemle, J.P., 2000. The Face of North Dakota (3rd Ed.) Education Series 26. North Dakota Geological Survey.

Boresi, A.P., Schmidt, R.J., 2003. Advanced Mechanics of Materials. John Wiley & Sons, Inc.

Bouteca, M.J., Gueguen, Y., 1999. Mechanical properties of rocks: pore pressure and scale effects. Oil & Gas Science and Technology – Rev. IFP, (Editions Technip) vol. 54, no.6, pp. 703-714.

Bouteca, M.J., Sarda, J-P., Vincke, O., 2000. Constitutive law for permeability evolution of sandstones during depletion. SPE 58717, presented at SPE International Symposium on Formation Damage, Lafayette, LA, Feb 23-24.

Brace, W.F., Martin, R.J., 1968. A test of the law of effective stress for crystalline rocks of low porosity. Int. J. Rock Mech. Mining. Sci. vol. 5, pp. 415-426.

Bradley R.A., Watts E.C., Williams E.R., 1991. Limiting net greenhouse gas emissions in the US. vol. 1, Report to the US Congress, US DOE.

Busch, A., Alles, S., Gensterblum, Y., Prinz, D., Dewhurst, D.N., Raven, M.D., Stanjek, H., Krooss, B.M., 2008. Carbon dioxide storage potential of shales. International Journal of Greenhouse Gas Control, vol. 2, iss. 3, pp. 297-308.

Butler, R. M., 1991. Thermal Recovery of Oil and Bitumen. Prentice-Hall, Inc.

Carneiro, J.F., 2009. Numerical simulations on the influence of matrix diffusion to carbon sequestration in double porosity fissured aquifers. International Journal of Greenhouse Gas Control, vol. 3, pp. 431-443.

Casey, J., Naghdi, P.M., 1981. On the characterization of strain-hardening in plasticity. J. Appl. Mech. Trans. ASME, 48(2), 285-296.

Celia, M.A., Nordbotten, J.M., 2009. Practical modeling approaches for geological storage of carbon dioxide. Ground Water, vol. 47, no. 5. pp 627-638.

Chakma, A., Islam, M.R., Berruti, F., 1991. Enhanced Oil Recovery. American Institute of Chemical Engineers.

Chen, Z.X., 2007. Reservoir Simulation: Mathematical Techniques in Oil Recovery. Society for Industrial and Applied Mathematics.

Chen, H.Y., Teufel, L.W., Lee, R.L., 1995. Coupled fluid flow and geomechanics in reservoir study-1. theory and governing equations. SPE 30752. Annual Conference. October, 22-25.

Chiaramonte, L., 2008. Geomechanical Characterization and Reservoir Simulation of a CO_2 Sequestration Project in a Mature Oil Field, Teapot Dome, WY. PhD Dissertation, Stanford University.

Chilingar, G.V., Terry, R. D., 1954. Relationship between porosity and chemical composition of carbonate rocks. Pet. Eng. vol. 26, pp. 341-342.

Chilingar, G.V., Mannon, R.W., Rieke, III, H.H., 1972. Introduction to carbonate reservoir rocks. Chapter 1 in: Chilingar, G.V., Mannon, R.W., Rieke, III, H.H. (Eds.), Oil and Gas Production from Carbonate Rocks. American Elsevier Publishing Company, Inc.

Chilingar, G.V., Serebryakov, V.A., Robertson, Jr. J.O., 2002. Origin and Prediction of Abnormal Formation Pressures. Development in Petroleum Science: 50. Elsevier Science B.V.

Chiquet, P., Broseta, D., Thibeau, S., 2005. Capillary alteration of shaly caprocks by carbon dioxide. In: SPE Europec/EAGE Annual Conf. (SPE 94183), June 13-16, Madrid, Spain.

Claesson, J., Bohloli, B., 2002. Brazilian test: stress field and tensile strength of anisotropic rocks using an analytical solution. International Journal of Rock Mechanics and Mining Sciences, vol. 39, pp. 991–1004.

Chipley, D., Kyser, T.K., 1991. Large scale fluid movement in the Western Canadian Sedimentary Basin as recorded by fluid inclusions in evaporites. In: Christopher, J.E., Haidl, F.M. (Eds.), Sixth International Williston Basin Symposium, (Saskatchewan Geological Society, Regina, Saskatchewan), pp. 265–269.

Collins, A.G., 1975. Geochemistry of Oilfield Waters. Elsevier Scientific Publishing Company, Amsterdam.

Coussy, O., 2004. Poromechanics. John Wiley & Sons, Ltd.

Cramer, D.D., 1986. Reservoir characteristics and stimulation techniques in the Bakken Formation and adjacent beds, Billings Nose area, Williston Basin. SPE 15166, presented at the Rocky Mountain regional meeting of the SPE held in Billings, MT, May 19-21.

Cramer, D.D., 1992. Treating pressure analysis in the Bakken Formation. Journal of Petroleum Technology, 44(1), pp.20-27.

Crouch, S.L., Starfield, A.M., 1983. Boundary Element Methods in Solid Mechanics with Applications in Rock Mechanics and Geological Engineering. George Allen & Unwin Publishers Ltd.

Crossley, N.G., 1998. Conversion of LPG salt caverns to natural gas storage, A Transgas experience. Journal of Canadian Petroleum Technology, vol. 37(12), pp. 37-47.

Crowe, C.T., Elfer, D.F. Roberson, J.A., 2005. Engineering Fluid Mechanics. 8th Ed. John Wiley & Sons, Inc.

Dahlquist, G., Björck, A., 1974. Numerical Methods. Translated by Ned Anderson. Prentice-Hall, Inc., Englewood Cliffs, N.J.

Das, B.M., 1985. Evaluation of the point load strength for soft rock classification. Proc. 4th int. conf. on Ground Control in Mining. Morgantown, WV. pp.220-226.

Davis, R.O., Selvadurai, A.P.S., 1996. Elasticity and Geomechanics. Cambridge University Press.

Davis, J.M., Roy, N.D., Mozley, P.S., Hall, J.S., 2006. The effect of carbonate cementation on permeability heterogeneity in fluvial aquifers: An outcrop analog study. Sedimentary Geology, vol. 184, pp. 267–280.

Davison J, Freund, P., Smith, A., 2001. Putting carbon back in the ground. Cheltenham, UK, February: IEA Greenhouse R&D Programme; 2001.

Dean., R.H., Gai, X., Stone, C.M., Minkoff, S.E., 2003. A comparison of techniques for coupling porous flow and geo-mechanics. SPE 79709, presented at the SPE reservoir Simulation Symposium held in Houston, Texas, Feb 3-5.

Debnath, L., Bhatta, D., 2007. Integral Transforms and Their Applications. 2nd edition. Taylor & Francis Group, LLC.

Deer, W.A., Howie, R.A., Zussman, J., 1966. An Introduction to the Rock-Forming Minerals. Wiley, New York.

Detienne, J-L., Creusot, M., Kessler, N., Sahuquet, B., 1998. Thermally induced fractures: a field-proven analytical model. SPE 30777, SPE reservoir evaluation & Engineering, pp. 30-35.

Detournay, E., Cheng, A., H-D., 1993. Fundamentals of poroelasticity, chapter 5 in: Fairhurst, C. (Eds), Comprehensive Rock Engineering: Principles, Practice and Projects, vol. II, Analysis and Design Method. Pergamon Press, pp. 113-171.

Downey, J.S., 1984. Geohydrology of the Madison and associated aquifers in parts of Montana, North Dakota, South Dakota, and Wyoming, U.S. Geological Survey Professional Paper 1273-G, pp. G1–G47.

Downey, J.S., Dinwiddie, G.A., 1988. The regional aquifer system underlying the northern Great Plains in parts of Montana, North Dakota, South Dakota and Wyoming—Summary. US Geol. Survey Professional Paper 1402-A, 63.

Downey, M.W., Threet, J.C., Morgan, W.A., 2001. Petroleum Provinces of the Twenty-first Century. The American Association of Petroleum Geologists, Tulsa, Oklahoma, USA.

Dunnington, H.V., 1954. Stylolite development post-dates rock induration. Journal of Sedimentary Petrology, vol. 24, no.1, pp. 27-49.

Eastwood, W.P. 1959. North Dakota Geological Survey Circular No.210, North Dakota Industrial Commission, Oil and Gas Division.

Emmanuel, S., Ague, J.J., 2009. Modeling the impact of nano-pores on mineralization in sedimentary rocks. Water Resources Research. vol. 45, W04406, doi: 10.1029/2008 WR 007170. 12 pages.

Ennis-King,J., Paterson, L., 2007. Coupling of geochemical reactions and convective mixing in the long-term geological storage of carbon dioxide. International Journal of Greenhouse Gas Control, vol. 1, pp. 86 – 93.

Fairhurst, C. 2003. Stress estimation in rock: a brief history and review. International Journal of Rock Mechanics & Mining Science, vol. 40, pp. 957-973.

Farlow, S.J., 1993. Partial Differential Equations for Scientists and Engineers. Dover Publications, Inc.

Fetter, C.W., 2001. Applied Hydrogeology. Prentice-Hall, Inc.

Finch, W.C., 1968. Abnormal pressure in the Antelope field, North Dakota. SPE. 2227, presented at the SPE 43rd annual fall meeting held in Houston, Texas, Sep. 29 - Oct. 2.

Fisher, D.W., LeFever, J.A., LeFever, R.D., Anderson, S.B., Helms, L.D., Whittaker, S., Sorenson, J.A., Smith, S.A., Peck, W.D., Steadman, E.N., Harju, J.A., 2005. Overview of Williston Basin geology as it relates to CO2 sequestration. Plains CO2 Reduction Partnership Report, University of North Dakota Energy and Environmental Research Center, Grand Forks, North Dakota, USA.

Fjaer, E., Holt, R.M., Horshrud, P., Raaen, A.M., Risnes, R., 1992. Petroleum Related Rock Mechanics. 1st Edition. Elsevier

Fjaer, E., Holt, R.M., Horshrud, P., Raaen, A.M., Risnes, R., 2008. Petroleum Related Rock Mechanics. 2nd Edition. Elsevier

Freund, P., et al., 2005. Properties of CO_2 and carbon-based fuels. IPCC Special Report on Carbon Dioxide Capture and Storage. Cambridge University Press, Cambridge, UK and New York, NY, USA, Chapter 5, pp. 385-398.

Galmudi, D., 1999. Pressure Solution, Porosity Reduction, and Transport in Rocks. PhD Dissertation, Dept. of Geophysics, Stanford University.

Gammons, C. H., Wood, S.A., Jonas, J.P., Madison, J.P., 2003. Geochemistry of the rare-earth elements and uranium in the acidic Berkeley Pit lake, Butte, Montana. Chemical Geology, vol. 198, pp. 269– 288.

Garcia-Romero, E., Vegas, J., Baldonedo, J. L., Marfil, R., 2005. Clay minerals as alteration products in basaltic volcaniclastic deposits of La Palma (Canary Islands, Spain). Sedimentary Geology, vol.174, issue 3-4, pp. 237-253.

Gaupp, R., et al., 2008. Fluids in sedimentary basins: an overview. In: Littke, R., et al. (Eds), Dynamics of Complex Intracontinental Basins – the Central European Basin System. Springer – Verlag Berlin Heidelberg.

Gaus, I., Azaroual, M., Czernichowski-Lauriol, I., 2002. Preliminary modeling of the geochemical impact of CO_2 injection on the caprock at Sleipner. BRGM Report, BRGM/RP-52081-FR, 43.

Gaus, I., Azaroual, M., Czernichowski-Lauriol, I., 2005. Reactive transport modeling of the impact of CO_2 injection on the clayey caprock at Sleipner (North Sea). Chemical Geology, vol. 217, pp.319-337.

Geertsma, J., 1966. Problems of rock mechanics in petroleum production engineering. In: Proceedings of the 1st Congress International Society or Rock Mechanics, Lisbon, vol. I, pp. 585–594.

Gerhard,L.C., Anderson,S.B., LeFever,J.A., Carlson,C.G., 1982, Geological development, origin, and energy mineral resources of the Williston Basin, North Dakota: North Dakota Geological Survey Miscellaneous Series 63,pp.31.

Ghassemi, A., Nygren, A., Cheng, A.H-D., 2008. Effect of heat extraction on fracture aperture: a poro-thermo-elastic analysis. Geothermics 37 (5), pp. 525-539.

Gillham, R.W., Cherry, J.A., 1982. Contaminant migration in saturated unconsolidated geologic deposits. Geophysical Society of America Special Paper 189, pp. 31-62.

Gledhill, D.K., Morse, J.W., 2004. Dissolution kinetics of calcite in $NaCl–CaCl_2–MgCl_2$ brines at 25 °C and 1 bar pCO_2, Aquatic Geochemistry 10 (1–2), pp. 171–190.

Goff, F., Lackner, K.S., 1998. Carbon dioxide sequestering using ultramafic rocks. Environmental Geosciences, 5(3):89-101.

Golomb, D., 1993. Ocean disposal of CO_2: Feasibility, economics and effects. Energy Conversion and Management, vol. 34, I. 9-11, pp. 967-976.

Goodarzi, S., Settari, A., Zoback, M., Keith, D.W., 2010. Thermal aspects of geo-mechanics and induced fracturing in CO_2 injection with application to CO_2 sequestration in Ohio River Valley. SPE 139706, presented at the SPE conference at New Orleans, Louisiana, Nov 10-12.

Goodrich, J.H., 1980. Review and analysis of past and ongoing carbon dioxide injection field tests. SPE/DOE 8832, 1st Joint DOE/SPE symposium on enhanced oil recovery, Tulsa, April 20-23.

Gosnold, W.D., 1988. Analysis of heat flow and groundwater flow in the South Dakota geothermal anomaly Transactions - Geothermal Resources Council, vol. 12, pp. 251-255.

Gosnold, W.D., 1999. Stratabound geothermal resources in North Dakota and South Dakota. Natural Resources Research, vol. 8, no. 3, pp.177-192.

Gosnold, W.D., LeFever, R.D., 2009. Heat flow and thermal maturity in the Williston basin. 17th Willsiton Basin petroleum conference, April 26-28, Regina, Canada.

Goulty, N.R., 2003. Reservoir stress path during depletion of Norwegian chalk oilfields. Petroleum Geosciences, vol. 9, pp. 233-241.

Grasby, S.E., Betcher, R.N., 2000. Pleistocene recharge and flow reversal in the Williston basin, central North America. Journal of Geochemical Exploration 69–70, pp. 403–407.

Grasby, S.E., Betcher, R.N., 2003. Regional hydro-geochemistry of the carbonate rock aquifer, southern Manitoba. Canadian Journal of Earth Sciences, vol. 39, pp. 1053-1063.

Green, A.G., Weber, W., Hajnal, Z., 1985, Evolution of proterozoic terranes beneath the Williston Basin. Geology, vol.13, pp.624-628.

Gueguen, Y., Bouteca, M., 2004. Mechanics of Fluid Saturated Rocks. Elsevier Academic Press.

Guildner, L.A., 1958. The thermal conductivity of carbon dioxide in the region of the critical point. Physics, vol. 44, pp.1149-1153.

Gunter, W.D., Perkins, E.H., McCann, T.J., 1993.Aquifer disposal of CO_2-rich gases: reaction design for added capacity. Energy Conversion and Management, vol. 34, pp. 941–948.

Gunter, W.D., Wiechar, B., Perkins, E.H., 1997. Aquifer disposal of CO_2-rich greenhouse gases: Extension of the time scale of experiment for CO_2-sequestering reactions by geochemical modeling. Mineralogy and Petrology, vol. 59, pp. 121–140.

Hall, P.L., 1994. Physical and chemical aspects of the development of over-pressuring in sedimentary environments. Clay Minerals, vol. 29, pp. 425-437.

Ham, H. H., 1966. A method of estimating formation pressures from Gulf Coast well logs. Gulf Coast Association of Geological Societies Transactions. vol. 16, pp. 185-197.

Han, G., 2003. Rock Stability under Different Fluid Flow Conditions. PhD Dissertation, University of Waterloo, Canada, 196 pages.

Hantush, M.S., 1960. Analysis of data from pumping tests in anisotropic aquifers. Journal of Geophysical Research, vol. 71, pp. 421-426.

Hart, D. J., 2000. Laboratory Measurements of Poro-elastic Constants and Flow Parameters and Some Associated Phenomena. PhD Dissertation, University of Wisconsin – Madison.

Hartmann, S., 1996. The world as a process: simulations in the natural and social sciences, in: Hegselmann, R., et al. (Eds.), Modelling and Simulation in the Social Sciences from the Philosophy of Science Point of View, Theory and Decision Library. Springer, 1st edition, pp. 77-100.

Hassanzadeh, H., Pooladi-Darvish, M., Keith, D.W., 2005. Modeling of convective mixing in CO_2 storage. JCPT, Oct 2005, vol. 44, no. 10.

Healy, J.H., Rubey, W.W., Griggs, D.T., Raleigh, C.B., 1968. The Denver earthquakes. Science, New Series, vol. 161, no. 3848, pp. 1301-1310.

Healy, J.H., Hamilton, R.M., Raleigh, C.B., 1970. Earthquakes induced by fluid injection and explosion. Tectonophysics, vol. 9, pp. 205-214.

Heinz, J., Aigner, T., 2003. Hierarchical dynamic stratigraphy in various quaternary gravel deposits, Rhine glacier area (SW Germany): implications for hydrostratigraphy. International Journal of Earth Science, vol. 92, pp.923-938.

Hendricks, C.A., Blok, K. 1993. Underground storage of carbon dioxide. Energy Convers. Mgmt, 34(9-11), pp. 949-957.

Herzog, H., 2001. What future for Carbon capture and sequestration? Environmental Science and Technology, 35: 7, pp. 143A-153A.

Hildenbrand, A., Krooss, B.M., 2003. CO_2 migration processes in argillaceous rocks: pressure-driven volume flow and diffusion. J. Geochem. Expl., vol. 78-79, pp.169-172.

Hill, J. R., 2003. Indiana Limestone. The Trustees of Indiana University.

Hitchon, B, (editor), 1996a. Aquifer disposal of carbon dioxide: hydrodynamic and mineral trapping—proof of concept. Geoscience Publishing Ltd. Box 79088, Sherwood Park, Alberta T8A 5S3, Canada.

Hitchon, B., 1996b. Rapid evaluation of the hydrochemistry of a sedimentary basin using only 'standard' formation water analyses: example from the Canadian portion of the Williston Basin. Applied Geochemistry, vol. 11, pp. 789-795.

Hoganson, J.W., et al., 2004. Geology and Prehistoric Life of the Rendezvous Region. North Dakota Geological Survey.

Honarpour, M., Koederitz, L., Harvey, A.H., 1986. Relative Permeability of Petroleum Reservoirs. CRC Press, Inc.

Horsrud, P., Sonstebo, E.F., Boe, R., 1998. Mechanical and petrophysical properties of North Sea Shales. International Journal of Rock Mechanics & Mining Science, vol. 35(8), pp. 1009-1020.

Hsieh, P.A., Bredehoeft, J.D., 1981. A reservoir analysis of the Denver earthquakes: a case of induced seismicity. Journal of Geophysical Research, vol. 86, no. B2, pp. 903-920.

Hudson, J.A., Stephenson, O., Anderson, J., 2005. Guidance on numerical modeling of thermo-hydro-mechanical coupled processes for performance assessment of radioactive waste repositories. International Journal of Rock Mechanics & Mining Science, vol. 42, pp. 850-870.

Hudson, J.A., Harrison, J.P., 1997. Engineering Rock Mechanics: an Introduction to the Principles. Elsevier Ltd.

Hunt, J.M., 1990. Generation and migration of petroleum from abnormally pressured compartments. AAPG Bulletin, 74: 1-12.

IEA (International Energy Agency) Information Paper, 2004. Carbon dioxide capture and storage issues – Accounting and baselines under the United Nations framework convention on climate change (UNFCCC). Prepared by Susanne Haefeli, Martina Bosi and Cedric Philibert. Paris, May.

Iampen, H.T., Rostron, B.J., 2000. Hydrochemistry of pre-Mississippian brines, Williston Basin, Canada – USA. Journal of Geochemical Exploration 69–70, pp. 29–35.

IPCC (Intergovernmental Panel on Climate Change), 2005. In: Metz, B., Davidson, O., de Coninck, H.C., Loos. M., Meyer, L.A. (Eds), Special Report on Carbon Dioxide Capture and Storage. Cambridge University Press, Cambridge, UK and New York, NY, USA, Chapter 5, pp. 195-276.

ISRM (International Society for Rock Mechanics), Commission on Standardization of Laboratory and Field Tests. 1978. Suggested methods for determining tensile strength of rock materials. International Journal of Rock Mechanics & Mining Science Geomechanic Abstract, vol. 15, pp. 99–103.

ISRM, 1985. Suggested method for determining point load strength. International Journal of Rock Mechanics & Mining Science, vol. 22, pp. 51-60.

ISRM Testing Commission (formed by R.J. Fowell, J.A. Hudson, C. Xu, J.F. Chen, and X. Zhao), 1995. Suggested method for determining mode-I fracture toughness using cracked chevron-notched Brazilian disc (CCNBD) specimens, International Journal of Rock Mechanics & Mining Science Geomechanic Abstract, 32 (1), pp. 57–64.

Itasca consulting group, Inc., 2006a. FLAC3D: Fast Lagrangian Analysis of Continua in 3 Dimensions, Theory and background. Itasca consulting group, Inc., MN.

Itasca consulting group, Inc., 2006b. FLAC3D: Fast Lagrangian Analysis of Continua in 3 Dimensions, Fluid-mechanical interaction. Itasca consulting group, Inc., MN.

Jaeger, J.C., Cook, N.G.W., Zimmerman, R.W., 2007. Fundamentals of Rock Mechanics. 4th ed. Blackwell Publishing.

Javadpour, F., 2009. Nanopores and apparent permeability of gas flow in mudrocks (shales and siltstone). J. Canadian Petrol Tech., vol. 48(8).

Jimenez Gomez, Jaime Alberto, 2006. Geomechanical Performance Assessment of CO_2-EOR Geological Storage Projects. PhD Dissertation, The University of Alberta, 295 pages.

Jodry, R.L., 1972. Pore geometry of carbonate rocks (Basic geologic concepts). Chapter 2 in: Chilingar, G.V., Mannon, R.W., Rieke, III. H.H. (Eds), Oil and Gas Production from Carbonate Rocks. American Elsevier Publishing Company, Inc.

Johnson, D.B., Hallberg, K.B., 2005. Acid mine drainage remediation options: a review. Science of the Total Environment, vol. 338, Issue. 1-2, pp. 3-14.

Johnson, J.W., Nitao, J.J., Morris, J.P., 2004. Reactive transport modeling of cap rock integrity during natural and engineered CO_2 storage. In Carbon Dioxide Capture for Storage in Deep Geologic Formations (Elsevier: ISBN0080445705).

Kaszuba, J.P., Janecky, D.R., Snow, M.G., 2003. Carbon dioxide reaction processes in a model brine aquifer at 200°C and 200bar: implications for geologic sequestration of carbon. Appl. Geochem. vol. 18, pp. 1065-1080.

Kaviany, M., 1995. Principles of Heat Transfer in Porous Media. Springer-Verlag New York, Inc.

Khan, D.K., Rostron, B.J., Margitai, Z., Carruthers, D., 2006. Hydrodynamics and petroleum migration in the upper Ordovician Red River formation of the Williston Basin. Journal of Geochemical Exploration, vol. 89, pp. 179-182.

Kling, G.W., Clark, M.A., Wagner, G.N., Compton, H.R., Humphrey, A.M., Devine, J.D., Evans, W.C., Lockwood, J.P., Tuttle, M.L., Koenigsberg, E.J., 1987. The 1986 lake Nyos gas disaster in Cameroon, West Africa. Science. Apr 10; 236 (4798):169-75.

Klins, M. A., 1984. Carbon Dioxide Flooding: Basic Mechanics and Project Design. International Human Resources Development Corporation, Boston, MA.

Koschel, D., Coxam, J-Y., Rodier, L., Majer, V., 2006. Enthalpy and solubility data of CO_2 in water and NaC(aq) at conditions of interest for geological sequestration. Fluid Phase Equilibria, vol. 247, pp. 107-120.

Kovach, R.L., 1974. Source mechanisms for Wilmington oil field, California, subsidence earthquakes. Seismological Society of America Bulletin, vol. 64, no. 3, pt. 1, pp. 699-711.

Kovscek, A.R., 2002. Screening criteria for CO_2 storage in oil reservoirs. Petroleum Science and Technology, vol. 20, no. 7 &8, pp. 841-866.

Krauskopf, K.B., Bird, D.K., 1995. Introduction to Geochemistry. McGraw-Hill, Inc.

Krevor, S. C., 2009. Mineral Carbon Dioxide Sequestration: Enhancing Process Kinetics and a Resource Base Assessment for Minerals Suitable for Use in Enhanced Carbonation Processes. PhD Dissertation, Columbia University.

Krishnan, G.R., Zhao, X.L., Zaman, M., Roegiers, J-C., 1998. Fracture toughness of a soft sandstone. International Journal of Rock Mechanics & Mining Science, vol. 35, no.6, pp. 695-710.

Krooss, B.M., Leythaeuser, D., Schaefer, R.G., 1988. Light hydrocarbon diffusion in a caprock. Chemical Geology, vol. 71, pp. 65-76.

Kumar, A., Noh, M., Pope, G.A., Sepehrnoori, K., Bryant, S., Lake, L.W., 2004. Reservoir simulation of CO_2 storage in deep saline aquifers. SPE 89343, presented at the SPE/DOE 14th Symposium on improved oil recovery held in Tulsa, Oklahoma, April 17-21.

Lackner, K.S., Wendt, C.H., Butt, D.P., Joyce, E.L., Sharp, D.H., 1995. Carbon dioxide disposal in carbonate minerals. Energy, vol. 20(11), pp. 1152-1170.

Lade, P.V., De Boer, R., 1997. The concept of effective stress for soil, concrete and rock. Geotechnique, vol. 47, no. 1, pp. 61-78.

Laird, W.M., 1964. Resume of the stratigraphy and structure of North Dakota: Third International Williston Basin Symposium, Bismarck, ND, North Dakota Geological Society, p.39-44.

Langnes, G.L., Robertson, Jr. J.O., Chilingar, G.V., 1972. Secondary recovery and carbonate reservoirs. American Elsevier Publishing Company, Inc.

Lauwerie, H.A., 1955. The transport of heat into an oil layer caused by the injection of hot fluid. Journal of Applied Science Research, Section A, vol 5, pp. 145-150.

Lebedev, L.P., Cloud, M.J., 2003. Tensor Analysis. World Scientific Publishing Co., Ltd.

Leem, J., 1999. Micromechanical Fracture Modeling on Underground Nuclear Waste Storage: Coupled Mechanical, Thermal, and Hydraulic Effects. PhD Dissertation, University of Arizona.

LeFever, J.A., LeFever, R.D., Anderson, S.B., 1987. Structural evolution of the central and southern portions of the Nesson Anticline, North Dakota. Fifth international Williston Basin symposium, Grand Forks, ND. June. pp.147-156.

Le Guen, Y., Renard, F., Hellmann, R., Brosse, E., Collombet, M., Tisserand, D., Gratier, J.-P., 2007. Enhanced deformation of limestone and sandstone in the presence of high pCO_2 fluids, Journal of Geophysical Research 112, B05421.

Leonard, R.B., Signor, D.C., Jorgensen, D.G., Helgesen, J.O., 1983. Geohydrology and hydrochemistry of the Dakota aquifer, central United States. Water Resources Bulletin, American Water Resources Association, vol. 19, no. 16, pp. 903-911.

Levin, H.L., 1981. Contemporary Physical Geology. CBS College Publishing.

Littke, R., Scheck-Wenderoth, M., Brix, M.R., Nelskamp, S., 2008. Subsidence, inversion and evolution of the thermal field. In: Littke, R., et al. (Eds), Dynamics of Complex Intracontinental Basins – the Central European Basin System. Springer – Verlag Berlin Heidelberg.

Li, Z., Dong, M., Li, S., Huang, S., 2006. CO_2 sequestration in depleted oil and gas reservoirs – caprock characterization and storage capacity. Energy Conversion and Management, vol. 47, pp. 1372-1382.

Lo, T-W., Conyer, K., Toksoz, N.M., 1986. Experimental determination of elastic anisotropy of Berea sandstone, Chicopee shale, and Chelmsford granite. Geophysics, vol. 51, no. 1, pp.164-171.

Lucier, Amie Marie, 2007. Geomechanical Analysis Applied to Geological Carbon Dioxide Sequestration, Induced Seismicity in Deep Mines, and Detection of Stress-induced Velocity Anisotropy in Sub-salt Environments. PhD Dissertation, Stanford University.

Lyklema, J., 1995. Fundamentals of Interface and Colloid Science: Solid-Liquid Interfaces. Academic Press.

Lyons, W.C., Plisga, G.J., 2005. Standard Handbook of Petroleum & Natural Gas Engineering. 2nd Edition. Elsevier Inc.

Ma, C, Eggleton, R.A., 1999. Cation exchange capity of kaollinite. Clays and Clay Minerals. 47(2), pp. 174-180.

Macdougall, J.D., 2004. Frozen Earth: the Once and Future Story of Ice Ages. Regents of the University of California.

Malinin, S.D., 1959. The system water-carbon dioxide at high temperatures and pressures. Geochemistry (3), pp. 292-306.

Manrique, E.J., Muci, V.E., Gurfinkel, M.E., 2007. EOR field experiences in carbonate reservoirs in the United States. SPE 100063. SPE Reservoir Evaluation & Engineering, pp. 667-686.

Marini, L., 2007. Geological Sequestration of Carbon Dioxide: Thermodynamics, Kinetics, and Reaction Path Modeling. Elsevier B.V.

Marsala, A.F., Figoni, F., Brignoli. M., 1998. Transient method implemented under unsteady-state condition for low and very low permeability measurements on cuttings. SPE/ISRM paper 47202, presented at SPE/ISRM Eurock'98 held in Trondheim, Norway, July 8-10.

Mathias, S.A., Hardisty, P.E., Trudell, M.R., Zimmerman, R.W., 2009. Screening and selection of sites for CO_2 sequestration based on pressure buildup. International Journal of Greenhouse Gas Control, vol. 3, pp. 577-585.

McClay, K.R., 1977. Pressure solution and Coble creep in rocks and minerals: a review. Journal of the Geological Society, vol. 134, pp. 57-70.

McKee, B.N., 2005. Discussion paper from the task force for reviewing and identifying standards with regards to CO_2 storage measurement (version 2). Carbon Sequestration Leadership Forum-Technical Group-2005-9.

McLennan, J.D., Hasegawa, H.S., Roegiers, J-C., Jessop, A.M., 1986. Hydraulic fracturing experiment at the University of Regina Campus. Can. Geotech. J. vol. 23, pp. 548-555.

McTavish, G.J. Vigrass, L.W., 1987. Salt dissolution and tectonics, south-central Saskatchewan.Proc. 5th International Williston Basin Symposium, Saskatchewan. Geol. Soc. Special Pub. 9, Carlson and Christopher (Eds.), pp. 157–168.

McTigue, D.F., 1986. Thermoelastic response of fluid-saturated porous rock. Journal of Geophysical Research, vol. 91, no. B9, pp. 9533-9542.

Merino, E., 1987. Textures of low temperature self-organization. In: Rodriguez-Clemente, R., Tardy, T. (Eds), Geochemistry of the Earth's Surface. Cons. Sup. Invesrigaciones Cientificos (Spain) and Center National Recherches Scientifique (France), Madrid, pp. 597-610.

Metcalfe, R.S., 1982. Effects of impurities on minimum miscibility pressures and minimum enrichment levels for CO_2 and rich gas displacements. SPE Journal, vol. 22, no. 2, pp. 219-25.

Miall, A.D., Tyler, N. (Eds), 1991. The Three-Dimensional Facies Architecture of Terrigenous Clastic Sediments and Its Implications for Hydrocarbon Discovery and Recovery. Society of Sedimentary Geology, SEPM Concepts in Sedimentology and Paleontology, Tulsa, OK.

Michael, K., Golab, A., Shulakova, V., Ennis-King, J., Allinson, G., Sharma, S., Aiken, T., 2010. Geological storage of CO_2 in saline aquifers – a review of the experience from existing storage operations. International Journal of Greenhouse Gas Control, vol. 4, pp. 659-667.

Miller, M.C., Rasin, T.M., Donald L.K.,1966. Effect of Adjacent Expansible Fluids and Caprock Leakage on Build-up and Drawdown Behavior of Wells in an Aquifer. SPE Journal, vol. 6, no. 3, pp. 239 - 246

Mollema, P.N., Antonellini, M.A., 1996. Compaction bands: a structural analog for anti-mode I cracks in aeolian sandstone. Tectonophysics, vol. 267, pp. 209-228.

Moore, C.H., 2001. Carbonate Reservoirs: Porosity Evolution and Diagenesis in a Sequence Stratigraphic Framework. Elsevier Science B.V.

Morgan, P., Gosnold, W.D., 1989. Heat flow and thermal regimes in the continental United States, in: Pakiser, L.C., Mooney, W.D. (Eds), Geophysical Framework of the Continental United States: Boulder, Colorado, Geological Society of America Memoir 172.

Morris, J. P., McNab, W. W., Johnson, S. M., Hao, Y., 2009. Coupled hydromechanical and reactive transport processes with application to carbon sequestration. Presented at the 43rd US Rock Mechanics Symposium and 4th U.S.-Canada Rock Mechanics Symposium, held in Asheville, NC June 28th – July 1.

Muldoon, M.A., Simo, J.A., and Bradbury, K.R., 2001. Correlation of hydraulic conductivity with stratigraphy in a fractured-dolomite aquifer, northeastern Wisconsin, USA. Hydrogeology Journal, vol. 9, pp.570-583.

Muller, T.M., 2006. Spatiotemporal pore pressure evolution due to fluid-mass point sources in dynamic poroelasticity. Geophysical Journal International, vol. 165, iss.3, pp. 906–912,

Murphy, E.C., Nordeng, S.H., Juenker, B.J., Hoganson, J.W., 2009. North Dakota Stratigraphic Column, ND Geological Survey, Miscellaneous Series 91.

Mutschler, T., Triantafyllidis, T., Balthasar, K., 2009. Geotechnical investigations of cap rocks above CO_2 reservoirs. Energy Procedia, vol. 1, iss.1, pp. 3375-3382.

Nason, R.D., Cooper, A.K., Tocher, D., 1968. Slippage on the Buena Vista thrust fault, in Geology and oil fields, west side southern San Joaquin valley. Presented at the 43rd annual meeting guidebook, AAPG, SEF, SEPM, Pacific sections: Los Angeles, Cal. American Association of Petroleum Geologists, pacific section, pp. 100-101.

Naterer, G. F. 2003. Heat Transfer in Single and Multiphase Systems. CRC Press LLC.

Nelms, R.L., Burke, R.D., 2004. Evaluation of oil reservoir characteristics to assess North Dakota carbon dioxide miscible flooding potential. Presented at the 12th Williston Basin horizontal well and petroleum conference, May 2-4. Minot, North Dakota, USA.

Nelson, R.A., 1981. Significance of fracture sets associated with stylolite zones. AAPG Bulletin, vol. 65, no. 11, pp. 2417-2425.

Newmark, R. L., Zoback, M. D., Anderson, R. N., 1984. Orientation of in situ stresses in the oceanic crust. Nature, vol. 311, pp. 424-428.

Nordbotten, J.M., 2004. Sequestration of Carbon in Saline Aquifers: Mathematical and Numerical Analysis. PhD Dissertation. Department of Mathematics, University of Bergen, Norway.

Nguyen, Thanh Son, 1995. Computational Modeling of Thermal-Hydrological-Mechanical Processes in Geological Media. PhD Dissertation, McGill University.

Nguyen, Vinh Xuan, 2010. Dual-Porosity and Dual-Permeability Poro-Mechanics Solutions for Problems in Laboratory and Field Applications. PhD Dissertation, University of Oklahoma.

Oldenburg, C.M., Unger, A.J.A., 2003. On leakage and seepage from geologic carbon sequestration sites: unsaturated zone attenuation, Vadose Zone Journal, vol. 2, pp. 287-296.

Oldenburg, C.M., Lewicki, J.L., 2005. On leakage and seepage of CO_2 from geologic storage sites into surface water. Environmental Geology, 50(5), pp. 691-705.

Ouchterlony, F., 1988. Suggested methods for determining fracture toughness of rock. International Journal of Rock Mechanics & Mining Science Geomechanic Abstract, vol. 25(3), pp. 71-96.

Pariseau, W.G., 1988. On the concept of rock mass plasticity. In: Cundall et al. (Eds), Key Questions in Rock Mechanics. Balkema, Rotterdam, pp. 291-302. Presented at the 29th U.S. Symposium on Rock Mechanics (USRMS), June 13 - 15, Minneapolis, MN.

Park, Anthony J. 2001. A Multi-process Basin and Reservoir Simulator: Effect of Multi-Mineralic Diagenesis, Pressure Solution, and Textural Dynamics. PhD Dissertation, Indiana University.

Park, W.C., Schot, E.H., 1968. Stylolites: their nature and origin. Journal of Sedimentary Petrology, vol. 38, no. 1, pp. 175-191.

Penner, L., 2006. Evidence linking surface lineaments, deep-seated faults and fracture-controlled fluid movement in the Williston Basin. Presented at the 14th Williston Basin Petroleum Conf. & Prospect Expo. May 7-9, Minot, ND, USA.

Perkins, E.H., Gunter, W.D., 1995. Aquifer disposal of CO_2-rich greenhouse gases: Modeling of water–rock interaction paths in a siliciclastic aquifer. In: Kaharaka, Y.K., Chudeav, O.V. (Eds.), Water–Rock Interactions. Brookfield, Rotterdam, pp. 895–898.

Phillips, Frs. O.M., 2009. Geological Fluid Dynamics: Sub-surface Flow and Reactions. Cambridge University Press.

Pinder, G.F., Gray, W.G., 2008. Essentials of Multiphase Flow and Transport in Porous Media. John Wiley & Sons, Inc.

Pine, R.J., Harrison, J.P., 2003. Rock mass properties for engineering design. Quarterly Journal of Engineering Geology and Hydrogeology, Geological Society of London. vol. 36, pp. 5-16.

Pokrovsky, O.S., Golubev, S.V., Schott, J., 2005. Dissolution kinetics of calcite, dolomite and magnesite at 25 °C and 0 to 50 atm pCO_2. Chemical Geology, vol. 217, pp. 239–255.

Pomar, L., Hallock, P., 2008. Carbonate factories: a conundrum in sedimentary geology. Earth-Science Reviews, vol. 87, pp. 134-169.

Portier, S., Rochelle, C., 2005. Modeling CO_2 solubility in pure water and NaCl-type waters from 0 to 300 °C and from 1 to 300 bar. Application to the Utsira Formation at Sleipner. Chemical Geology, vol. 217, pp. 187–199.

Pratt, W.E., Johnson, D.W., 1926. Local subsidence of the Goose Creek oil field. Journal of Geology, vol. 34, pt. 1, pp.577-590.

Prentice, I.C., Farquhar, G.D., Fasham, M.J.R., Goulden, M.L., Heimann, M., Jaramillo, V.J., Kheshgi, H.S., LeQuéré, C., Scholes, R.J. and Wallace, Douglas W.R., 2001. The carbon cycle and atmospheric carbon dioxide In: Houghton, J.T., Ding, Y., Griggs, D.J., Noguer, M., van der Linden, P.J., Dai, X., Maskell, K. and Johnson, C.A. (Eds), Climate Change 2001: the Scientific Basis. Contributions of Working Group I to the Third Assessment Report of the Intergovernmental Panel on Climate Change. Cambridge University Press.

Price, L. 2000. Origins and characteristics of the basin-centered continuous reservoir unconventional oil-resource base of the Bakken source system, Williston Basin. Available at UND EERC website: http://www.undeerc.org/price/. Accessed at April 2, 2009.

Pruess, K., Spycher, N., 2007. ECO2N—A fluid property module for the TOUGH2 code for studies of CO_2 storage in saline aquifer. Energy Conversion and Management, vol. 48, pp. 1761-1767.

Reasenberg, P.A., Simpson, R.W., 1992. Response of regional seismicity to the static stress change produced by the Loma Prieta earthquake. Science 255, pp. 1687-1690.

Renard, F., Gundersen, E., Hellmann, R., Collombet, M., Le Guen, Y., 2005. Numerical modeling of carbon dioxide sequestration on the rate of pressure solution creep in limestone: Preliminary results. Oil, Gas Science & Technology 60, pp. 381-389.

Rosenbauer,R.J., Koksalan, T., Palandri, J.L., 2005. Experimental investigation of CO_2–brine–rock interactions at elevated temperature and pressure: Implications for CO_2 sequestration in deep-saline aquifers. Fuel Processing Technology 86, pp. 1581– 1597.

Rostron, B.J., Holmden, C., 2003. Regional variations in oxygen isotopic compositions in the Yeoman and Duperow aquifers, Williston basin (Canada-USA). Journal of Geochemical Exploration 78-79, pp. 337-341.

Roundtree, R., Eberhard, M., Barree, R., 2009. Horizontal, near-wellbore stress effects on fracture initiation. SPE 123589, presented at the SPE Rocky Mountain Petroleum Technology Conference held in Denver, Colorado, April 14-16.

Rusnak, J.A., Mark, C., 1999. Using the point load test to determine the uniaxial compressive strength of coal measure rock. Presented at the 19th Int. Conference on Ground Control in Mining, pp. 362-371.

Rutqvist, J. Birkholzer, J.T., Cappa, F., Tsang, C.-F., 2007. Estimating maximum sustainable injection pressure during geological sequestration of CO_2 using coupled fluid flow and geomechanical fault-slip analysis. Energy Conversion and Management, vol. 48, iss. 6, pp. 1798-1807.

Rutqvist, J., Birkholzer, J.T., Tsang, C-F., 2008. Coupled reservoir–geomechanical analysis of the potential for tensile and shear failure associated with CO_2 injection in multilayered reservoir–caprock systems. International Journal of Rock Mechanics and Mining Sciences, vol. 45, iss. 2, pp. 132-143.

Rutqvist, J., Vasco, D.W., Myer, L., 2010. Coupled reservoir-geomechanical analysis of CO_2 injection and ground deformations at In Salah, Algeria. International Journal of Greenhouse Gas Control, vol. 4, iss. 2, pp. 225-230.

Rutter, E.H., 1983. Pressure solution in nature, theory ad experiment. Journal of the Geological Society, vol. 140, pp.725-740.

Sakashita, H., Kumada, T., 1998. Heat transfer model for predicting thermal conductivity of highly compacted bentonite. J Japan Atom Soc, vol. 40, pp. 235–240.

Sanford, R. J., 2003. Principles of Fracture Mechanics. Pearson Education, Inc

Sasaki, K., Fujii, Y., Niibori, Y., Ito, T., Hashida, T., 2008. Numerical simulation of supercritical CO_2 injection into subsurface rock masses. Energy Conversion and Management, vol. 49, pp. 54-61.

Schiff, J.L., 1999. The Laplace Transform: Theory and Applications. Springer-Verlag New York, Inc.

Schreier, S., 1982. Compressible Flow. John Wiley & Sons, Inc.

Seeber, L., Armbruster, J.G., Kim, W.Y., 2004. A fluid-injection-triggered earthquake sequence in Ashtabula, Ohio: implications for seismogenesis in stable continental regions. Bulletin of the Seismological Society of America, vol. 94, no. 1, pp.76-87.

Segall, P., 1989. Earthquakes triggered by fluid extraction. Geology, vol. 17, pp.942-946.

Seifritz, W., 1990. CO_2 disposal by means of silicates. Nature, 345, June.

Selley, R.C., 1976. Subsurface environmental analysis of North Sea sediments. AAPG Bulletin, vol. 60, no. 2, pp. 184-195.

Sengul, M., 2006. CO_2 sequestration – a safe transition technology. SPE 98617, presented at the SPE International Conference on Health, Safety, and Environment in Oil and Gas Exploration and Production held in Abu Dhabi, UAE, April 2-4.

Shafeen, A., Croiset, E., Douglas, P.L., Chatzis, I., 2004. CO_2 sequestration in Ontario, Canada. Part I: Storage evaluation of potential reservoirs. Energy Conversion and Management, 45(17), pp. 2645-2659.

Sinha-Roy, S., 2002. Kinetics of differential stylolite formation. Current Science, vol. 82 no. 8, (25 April), pp. 1038-1046.

Skempton A. W., 1954. The pore-pressure coefficients A and B. Geotechnique, vol. 4, pp. 143-147.

Sloss, L. L. 1988. Forty years of sequence stratigraphy. Geological Society of America Bulletin, vol. 100, pp. 1661-1665.

Smith, S.A., McLellan, P., Hawkes, C., Steadman, E.N., Harju, J.A., 2009. Geomechanical testing and modeling of reservoir and cap rock integrity in an acid gas EOR/Sequestration project, Zama, Alberta, Canada. Energy Procedia, vol. 1, pp. 2169-2176.

Tapp, B., Cook, J., 1988. Pressure solution zone propagation in naturally deformed carbonate rocks. Geology, Feb., vol. 16, pp. 182-185.

Taron, J., 2009. Geophysical and Geochemical Analyses of Flow and Deformation in Fractured Rock. Ph.D. Dissertation, the Pennsylvania State University, 2009, 199 pages.

Taron, J., Elsworth, D., 2009. Thermal-hydrologic-mechanical-chemical processes in the evolution of engineered geothermal reservoirs. International Journal of Rock Mechanics & Mining Sciences, doi:10.1016/j.ijrmms.2009.01.007.

Terzaghi, K., Peck, R.B., 1967. Soil Mechanics in Engineering Practice. 3rd Ed. Wiley, New York.

Tiab, D., Donaldson, E.C., 2004. Petrophysics: Theory and Practice of Measuring Reservoir Rock and Fluid Transport Properties. 2nd Ed. Elsevier, Inc.

Townend, J., Zoback, M.D., 2000. How faulting keeps the crust strong. Geology, vol. 28, no. 5, pp. 399-402.

Towse, D., 1957. Petrology of Beaver Lodge Madison limestone reservoir, North Dakota. AAPG Bulletin, vol. 41, no. 11, pp. 2494-2507.

Turkenburg W.C., 1997. Sustainable development, climate change, and carbon dioxide removal (CDR). Energy Conversion and Management, vol. 38, supple. 1, pp. S3-S12.

Uhlig, F., 2002. Transform Linear Algebra. Prentice-hall, Inc.

U.S. DOE., 2002. CO_2 Capture and Storage in Geologic Formations. A white paper prepared for the National Climate Change Technology Initiative.

USGS Fact Sheet FS 026-03, 2003. Geologic sequestration of carbon dioxide – an energy resource perspective.

Vallejo, L.E., Walsh, R.A., Robinson, M.K., 1989. Correlation between unconfined compressive and point load strength for Appalachian rocks. Proc. 30th US Symp. Rock Mech. pp.461-468.

Vavra, C.L., Kaldi J.G., Sneider, R.M., 1992. Geological applications of capillary pressure–a review. AAPG Bulletin, vol. 76, pp. 840–850.

Vidal-Gilbert, S., Nauroy, J-F., Brosse, E., 2009. 3D geomechanical modeling for CO_2 geologic storage in the Dogger carbonates of the Paris Basin. International Journal of Greenhouse Gas Control, vol. 3, pp. 288-299.

Vidal-Gilbert, S., Tenthorey, E., Dewhurst, D., Ennis-King, J., van Ruth, P., Hillis, R., 2010. Geomechanical analysis of the Naylor Field, Otway Basin, Australia: Implications for CO_2 injection and storage. International Journal of Greenhouse Gas Control, vol. 4, pp. 827-839.

Wang, H.F., 2000. Theory of Linear Poroelasticity with Applications to Geomechanics and Hydrogeology. Princeton University Press.

Wang, J.A., Park, H.D., 2002. Fluid permeability of sedimentary rocks in a complete stress-strain process. Engineering Geology, vol. 63, pp. 291-300.

Wang, Q.Z., Jia, X.M., Wu, L.Z., 2004. Wide-range stress intensity factors for the ISRM suggested method using CCNBD specimens for rock fracture toughness tests. International Journal of Rock Mechanics & Mining Sciences, vol. 41, pp. 709-716.

Wang, Q.Z., 2010. Formula for calculating the critical stress intensity factor in rock fracture toughness tests using cracked chevron notched Brazilian disc (CCNBD) specimens. International Journal of Rock Mechanics & Mining Sciences, vol. 47, pp. 1006-1011.

Warpinski, N.R., Schmidt, R.A., Cooper, P.W., Walling, H, C., Northrop, D.A., 1979. High-energy gas frac: Multiple fracturing in a wellbore. Proceedings of the 20th US Symposium on Rock Mechanics, pp.143-151.

Weaver, C.E., 1989. Clays, Muds, and Shales. Developments in Sedimentology 44. Elsevier Science Publishers B.V.

Wetmiller, R.J., 1986. Earthquakes near Rocky Mountain House, Alberta, and their relationship to gas production. Canadian Journal of Earth Sciences, vol. 23, pp. 172-181.

White, C.M., Smith, D.H., Jones, K.L., Goodman, A.L., Jikich, S.A., Lacount, R.B., Dubose, S.B., Ozdemir, E., Morsi, B.I., Schroeder, K.T., 2005. Sequestration of carbon dioxide in coal with enhanced coalbed methane recovery – a review. Energy & Fuels, vol. 19, no. 3, pp. 659-724.

White, D.J., 2011. Geophysical monitoring of the Weyburn CO_2 flood: Results during 10 years of injection. Energy Procedia, vol. 4, pp. 3628–3635.

Whitehead, R.L., 2009. Ground water atlas of the United States, Montana, North Dakota, South Dakota, Wyoming. U.S. Geological Survey. HA 730-I.

Yale, D.P., Crawford, B., 1998. Plasticity and permeability in carbonates: dependence on stress path and porosity. SPE/ISRM 47582, presented at the SPE/ISRM Eurock ’98 held in Trondheim, Norway, July 8-10.

Yasuhara, H., 2005. Thermo-Hydro-Mechanic-Chemical Couplings That Define the Evolution of Permeability in Rock Fractures. PhD Dissertation, the Pennsylvania State University.

Yousef, A.M., Elkanzi, E.M., Singh, H., 2001. Prediction of supercritical CO_2 solubility using the Krichevsky–Ilinskaya equation with an adjustable parameter. Journal of Supercritical Fluids, vol. 20, pp. 105–112.

Yu, H-S., 2006. Plasticity and Geotechnics. Springer Science & Business Media, LLC.

Zeng, Z., Roegiers, J-C., 2000. Derivation of formulae for fracture toughness determination by CDISK test. Internal report, the University of Oklahoma.

Zeng, Z., 2002. Laboratory Imaging of Hydraulic Fracturing Using Microseismicity. PhD Dissertation, University of Oklahoma.

Zeng, Z., Grigg R.B., Gupta, D.B., 2004. Laboratory investigation of stress-sensitivity of non-Darcy gas flow parameters. SPE 89431, presented at the SPE/DOE 14th Symp. Improved Oil Recovery, Tulsa, Oklahoma, April 17-21.

Zeng, Z., Jakupi, A., Bigelow, T., Grigg, R.B., Kringstad, J., Belobraydic, M., Zhou, X.J., 2008. Laboratory observation of CO_2 phase transition induced seismic velocity change. ARMA 08-329, presented at the 42nd US Rock Mechanics Symposium and 2nd U.S.-Canada Rock Mechanics Symposium, held in San Francisco, June 29-July 2.

Zerai, B., 2006. CO_2 Sequestration in Saline Aquifer: Geochemical Modeling, Reactive Transport Simulation and Single-Phase Flow Experiment. PhD Dissertation, Case Western Reserve University.

Zhang, J., 2008. Ontology and Knowledgebase of Fractures and Faults. PhD Dissertation, Stanford University.

Zhang, Q., 2004. A Boundary Element Method for Thermo-Poroelasticity with Applications in Rock Mechanics. MS Thesis, the University of North Dakota.

Zhou, Q.L., Birkholzer, J.T., Tsang, C.F., Rutqvist, J., 2008. A method for quick assessment of CO_2 storage capacity in closed and semi-closed saline formations. International Journal of Greenhouse Gas Control, vol. 2, pp. 626-639.

Zhou, X.J., 2007. Numerical Modeling of Shotcrete Behavior under the ASTM C-1550 Test with the Distinct Element Method of PFC3D. MS Thesis, Montana Tech of the University of Montana.

Zimmerman, R.W., 2000. Coupling in poroelasticity and thermoelasticity. International Journal of Rock Mechanics & Mining Science, vol. 37, pp. 79-87.

Zoback, M.L., Zoback, M.D., 1980. State of stress in the conterminous United States. Journal of Geophysical Research, vol. 85, pp. 6113-6156.

Zoback, M.L., Zoback, M.D., Adams, J., Assumpção, M., Bell, S., Bergman, E.A., Blümling, P., Brereton, N.R., Denham, D., Ding, J., Fuchs, K., Gay, N., Gregersen, S., Gupta, H.K., Gvishianil, A., Jacob, K., Klein, R., Knoll, P., Magee, M., Mercier, J.L., Müller, B.C., Paquin, C., Rajendran, K., Stephansson, O., Suarez, G., Suter, M., Udias, A., Xu, Z.H., Zhizhin, M., 1989. Global patterns of tectonic stress. Nature, vol. 341, pp. 291-298.

Zoback, M.D., Zinke, J.C., 2002. Production-induced normal faulting in the Valhall and Ekofisk oil fields. Pure and Applied Geophysics, vol. 159, pp. 403–420.

Zoback, M.D., 2007. Reservoir Geomechanics. Cambridge University Press.